3D temperature modeling for the South China Sea using remote sensing data

D.J.Twigt

Master of Science Thesis

April 18, 2006

Z3966.10

Delft University of Technology

WL | Delft Hydraulics

3D temperature modeling for the South China Sea using remote sensing data

Master of Science Thesis

For obtaining the degree of Master of Science in Aerospace Engineering at Delft University of Technology

D.J.Twigt

April 18, 2006

TU Delft
Delft University of Technology

WL | Delft Hydraulics

CLIENT:	
TITLE:	3D temperature modeling for the South China Sea using remote sensing data

ABSTRACT:

This project has been carried out at WL | Delft Hydraulics to obtain a M.Sc. degree at the Faculty of Aerospace Engineering, Delft University of Technology. Its overall objective is first to assess the large-scale three-dimensional temperature and salinity characteristic behaviour of the South China Sea, based on information from literature and data. The second goal is to develop a model which represents these large-scale processes. Synoptic temperature and water-level data from remote sensing datasets and climatological atlases play an essential role. The project builds on experience gained at WL | Delft Hydraulics during the SAT2SEA and REST3D projects.

The present report describes the results of the large-scale South China Sea temperature assessment and modeling. It is subdivided into four separate parts:

Part I describes the assessment of the large-scale South China Sea temperature based on an overview of literature and of available data. Phenomena that are investigated are the large-scale interaction with the East Asian monsoon, the basin-scale circulation system and the seasonal surface heat flux, temperature and mixed-layer depth cycles.

Part II describes the data acquisition and data quality assessments. Remote sensing data used are water level (DUACS) and sea surface temperature (AVHRR / Pathfinder, Reynolds OI SST) data. Non-remote sensing data used include climatological (World Ocean Atlas 2001) and in-situ (ASIAEX, SCSMEX) temperature data.

Part III describes the Delft3D-FLOW model setup, based on the large-scale processes identified in part I and forcing and validation data discussed in part II. A model sensitivity analysis on relevant model parameters and model forcing is carried out. To further increase model accuracy, a data assimilation technique known as sea surface temperature nudging has been implemented and tested in Delft3D-FLOW.

Part IV provides a summary of conclusions and recommendations. The main conclusion is that the model represents the large-scale seasonal temperature and mixed-layer cycles with reasonable accuracy. Without nudging a mean difference with measurements of 1.75 ^{o}C is obtained. With nudging this difference decreases by 15 % to 1.5 ^{o}C.

REFERENCES: WL | Delft Hydraulics project Z3966.10
Basisfinanciering V2W/OC2W; Research cluster Data Model Integratie

VER	AUTHOR		DATE	REMARKS	REVIEW		APPROVED BY	
0.5	D.J.Twigt		January 2006	Draft version	H. Gerritsen, E.D. de Goede, E.J.O. Schrama			
1.0	D.J.Twigt		April 2006	Final version	H. Gerritsen, E.D. de Goede, E.J.O. Schrama			

PROJECT NUMBER:	Z3966.10		
KEYWORDS:	Hydrodynamic modeling, temperature, remote sensing, climatological atlases, South China Sea		
NUMBER OF PAGES:	227		
CONFIDENTIAL:	☐ YES	☒ NO	
STATUS:	☐ PRELIMINARY	☐ DRAFT	☒ FINAL

DELFT UNIVERSITY OF TECHNOLOGY
DEPARTMENT OF
ASTRODYNAMICS AND SATELLITE SYSTEMS

This Master of Science Thesis is approved by:

Prof.dr.ir. B.A.C. Ambrosius

The graduation committee:

Prof.dr.ir. B.A.C. Ambrosius	Delft University of Technology (Chairman)
Dr.ir. H. Gerritsen	WL | Delft Hydraulics
Dr. E.D. de Goede	WL | Delft Hydraulics
Dr.ir. E.J.O. Schrama	Delft University of Technology
Ir. M.C. Naeije	Delft University of Technology

Dated: April 18, 2006

Executive summary

Background of the project: The goal of the SAT2SEA2 project is to assess and model the three-dimensional (3D) temperature cycle of the South China Sea (SCS). This is motivated by potential end-user interests because knowledge of water temperature and stratification is of great importance to a variety of water quality issues. Processes such as sediment transport, nutrient distribution and primary production highly depend on the 3D transport and mixing for which the temperature distribution is an essential parameter. Due to the significant spatial extent of the region and the small number of long term in-situ monitoring stations available, remote sensing (RS) data will play a crucial role in this project. SAT2SEA2 builds upon experience gained during the REST3D and SAT2SEA projects. In these projects the benefits of combining RS and model data were used to integrate RS Sea Surface Temperature (SST) into a 3D North Sea temperature model and into a 2D SCS tidal model using altimeter data, respectively.

Objectives of the project: The two main objectives of the SAT2SEA2 project are (1) to assess the large-scale, seasonal SCS temperature behavior based on information from literature and on available RS and in-situ data, and (2) to develop and validate a Delft3D-FLOW based 3D temperature and salinity model for the SCS and to assess whether the large-scale, seasonal temperature processes can be represented accurately by this model. The model will integrate RS SST and altimeter data and various in-situ data products, among which climatological atlases.

Overview project area: The SCS region is characterized by a combination of deep and shallow basins. Large-scale processes in the region are to a large extent governed by the East Asian monsoonal system. The seasonally varying monsoon has a large effect on both the large-scale circulation and the 3D temperature distribution. From literature a number of processes associated with this system were identified that are important for the seasonal temperature cycle: (1) seasonal changes in net heat flux at the free surface; (2) large-scale monsoon driven circulation, characterized by cold water boundary currents along the Chinese and Vietnamese coastlines during the NE monsoon and by large-scale Rossby wave dynamics in the North SCS; (3) seasonally varying stratification; (4) upwelling of sub-surface water due to the large-scale circulation system and bathymetry constraints and (5) cold water influx through Taiwan Strait and warm water influx through Luzon Strait.

Data acquisition and assessment: A number of remote sensing and in-situ datasets were acquired for this project. These were used for model forcing and validation. Remote sensing products used were altimeter elevation data from the DUACS dataset and SST data from the AVHRR / Pathfinder and Reynolds IO SST datasets. In-situ temperature data was obtained from the ASIAEX and the SCSMEX projects. Also, climatological temperature and salinity data was obtained from the World Ocean Atlas 2001 (WOA01). Finally, meteorological data was obtained from the ECMWF ERA-40, NCEP/NCAR Re-analysis and COADS datasets. Data from these different datasets was assessed and compared in order to determine the most suitable data for model forcing and validation. This comparison indicated substantial differences between the meteorological datasets. From these datasets, the ECMWF ERA-40 showed the most realistic values. A comparison of RS SST data indicated that on a sub-monthly time scale the usefulness of this product is severely limited by cloud cover. When compared with monthly AVHRR / Pathfinder SST composites, a higher (weekly) temporal resolution was achieved using the blended

Reynolds OI SST data. Finally, a comparison between in-situ and climatological temperature data from the WOA01 indicated that, concerning seasonal SCS processes on a significant spatial scale, climatological WOA01 data was a useful product to validate non-climatological model results.

3D temperature modeling - Model setup: For the SAT2SEA2 project the SAT2SEA 0.25×0.25 degree spherical SCS model was adapted to include both temperature and salinity transport and vertical processes. Similarly to the SAT2SEA project, the model bathymetry was truncated by using a reduced-depth approach. This means that the maximum model depth is 300 meters. In the vertical direction 20 layers were applied with a uniform spacing of 15 meters in the central SCS basin. The surface heat flux was prescribed using the Delft3D-FLOW Ocean heat flux model. This model computes the net surface flux based on space and time-varying meteorological fields. Lateral temperature and salinity transport forcing, obtained from the WOA01, was prescribed at the open boundaries. Momentum forcing was applied by space and time-varying wind and pressure fields at the free surface and by non-tidal water-level elevation (Sea Surface Anomaly) at the open boundaries, which was derived from altimeter data. The model does not resolve tidal forcing.

3D temperature modeling - Sensitivity analysis: A model sensitivity analysis was performed on the following subjects (see chapter 9 and 10): (1) *Delft3D-FLOW temperature modeling and stratification coefficients:* from this analysis it was concluded that both the transfer coefficients of the heat flux model (Stanton and Dalton numbers) and the Ozmidov length scale, representing additional vertical mixing by internal waves, had a significant effect on model results ($\pm 0.5°$C each). For both the Stanton and Dalton numbers optimum values were found to be 2.1×10^{-3}. For the Ozmidov length scale an optimum value of 7 cm was found. (2) *temperature forcing:* from this analysis it was concluded that wind and cloud cover are the most important meteorological input fields. Also, compared with climatological forcing at a monthly temporal resolution, model results improved significantly when non-climatological data at a 6 hrs temporal resolution was used (increasing the goodness-of-fit by $\pm 0.3°$C). Furthermore, lateral transport forcing at the open boundaries had significant effects along the China Continental Shelf. In the shallow SCS regions the model accuracy was significantly lower than in the central SCS basin. (3) *momentum forcing:* based on a comparison between model and altimeter elevation data, it was concluded that in the central SCS basin sub-tidal elevation was primarily controlled by the atmospheric pressure. In the shallow model regions the sub-tidal elevation was primarily controlled by the monsoon winds. Over the shallow China Continental Shelf it was primarily controlled by intrusions through Taiwan Strait. These large-scale features were identified as the aforementioned boundary currents and Rossby waves, and were taken into account by the model with regard to their effect on the seasonal, large-scale temperature cycle.

3D temperature modeling - Data assimilation by SST nudging: To further improve model results, RS SST data was assimilated into the model using a nudging method (chapter 10 and appendix D.3). A correction term was added to the net temperature equation (equation 10.2), based on the difference between modeled and observed SST values. This term forced the model results towards the observed values. For this project Reynolds OI SST data was used as nudging input data, because of its high temporal resolution compared to AVHRR SST data. The magnitude of the correction term was tuned by a nudging coefficient.

3D temperature modeling - Validation: By comparing model and RS SST it was concluded that the seasonal SST cycle was resolved well by the model (see chapter 11). In the central SCS all characteristic, large-scale features observed from measurement data were represented by the model. Also, they had the correct order of magnitude. This was independent of whether SST nudging was applied or not. In the central SCS region the modeled mixed-layer temperature had an average difference of $\pm 1.5°$C with respect to climatological validation data. Based on the uncertainty in this validation data a maximum accuracy of $\pm 1°$C could have been achieved. Furthermore, a comparison with historical in-situ data indicated a mean model accuracy of $\pm 1.75°$C. In the shallow model regions the solution improved considerably if SST nudging was applied. Without SST nudging the model heated excessively in these regions, which resulted in a local mixed-layer temperature difference of $\pm 2.5°C$ with respect to climatological data. This was attributed to an excessively large surface heat flux. Also, in these regions the horizontal model grid was too coarse to adequately model effects of upwelling against the continental shelves and flow through shallow straits, such as Malacca Strait. An improvement in model accuracy was achieved at these locations by applying SST nudging, reducing the difference with climatological data to $\pm 1.5°C$. This resulted in an increase in total model accuracy of 15 % with respect to climatological data.

Evaluation of results: It is concluded that the model resolved both the seasonal SST and stratification cycle accurately. In both cases the model showed the correct seasonal variations, with an expected accuracy of $\pm 1.5°C$. This result can be attributed mainly to the forcing of the Delft3D-FLOW model with RS SST and altimeter data, and with climatological data from the WOA01. For the first time a Delft3D-FLOW temperature model was applied in deep waters and for a very large basin, with reasonable results. This indicated that Delft3D-FLOW is a suitable tool for large-scale temperature modeling in deep regions like the SCS.

Preface

This report presents the results of my M.Sc. Thesis project at the Faculty of Aerospace Engineering, Delft University of Technology. The project, named SAT2SEA2, is done in collaboration with WL | Delft Hydraulics, which is a research institute and specialist consultant for water-related issues. It is motivated by the potential and mutual benefits of assimilating remote sensing data in hydrodynamic models. The focus is on large-scale three-dimensional temperature and salinity modeling for the South China Sea.

I gratefully acknowledge WL | Delft Hydraulics for providing me with the opportunity to do this project.

I am grateful to Ernst J.O. Schrama (Delft University of Technology) for bringing me in contact with WL | Delft Hydraulics and for supervising me during the project.

I am grateful to Erik de Goede en Herman Gerritsen (both WL | Delft Hydraulics) for their enthusiastic response to the project and for their supervision during my stay at WL | Delft Hydraulics.

I would like to thank Ernst, Erik and Herman for their many useful comments and good advise throughout the project.

Finally, I would like to state it has been a great pleasure working on this project. It has been a invaluable learning experience.

Daniel Twigt

Table of Contents

List of Figures

List of Tables

List of Acronyms

3D three dimensional

ADT Absolute Dynamic Topography

ASIAEX Asian Seas International Acoustic Experiment

AVHRR Advanced Very High Resolution Radiometer

CLS Collecte Localisation Satellites

COADS Comprehensive Ocean-Atmosphere Data Set

CTD Conductivity/Temperature/Depth

DUACS Developing Use of Altimetry for Climate Studies

ECMWF European Centre for Medium-Range Weather Forecast

EM Electro-Magnetic

EOF Empirical Orthogonal Function

ERA-40 ECMWF Re-Analysis Archive (40 years)

GoF Goodness-of-Fit

GHC Global Hydrographic Climatology

GRACE GGM02 Gravity Recovery and Climate Experiment - Grace Gravity Model 2002

IR Infra Red

MDT Mean Dynamic Topography

ML Mixed Layer

MODIS Moderate Resolution Imaging Spectroradiometer

M.Sc. Master of Science

NCEP National Center for Environmental Prediction

NCEP/NCAR National Center for Environmental Prediction / National Center for Atmospheric Research

NE North East

NOAA National Oceanic and Atmospheric Administration

OI Optimally Interpolated

PC Principal Component

PMEL Pacific Marine Environmental Laboratory

REST3D Remote sensing of Sea surface Temperature for 3D North Sea modeling

RMS Root Mean Square

RS remote sensing

SAT2SEA Satellite Altimetry on tides and Transport applied to South East Asian waters

SAT2SEA2 Satellite Altimetry on tides and Transport applied to South East Asian waters - 2

SCS South China Sea

SCSMEX South China Sea Monsoon Experiment

SH Steric Height

SOC Southampton Oceanography Centre

SSA Sea Surface Anomaly

SSH Sea Surface Height

SST Sea Surface Temperature

STD Standard Deviation

SVD Singular Value Decomposition

SW South West

T Temperature

TMSI Tropical Marine and Science Institute

TOA Tropical Ocean Array

T/P Topex / Poseidon

WL WL | Delft Hydraulics

WOA01 World Ocean Atlas 2001

WOD01 World Ocean Database 2001

WOD98 World Ocean Database 1998

Chapter 1

Introduction

This report describes the objectives, approach and results of the SAT2SEA2 project. This project deals with the development of a 3D hydrodynamic model to simulate the large-scale temperature distribution of the South China Sea. The main focus is on representing the basin-scale mixed layer temperature throughout the year.

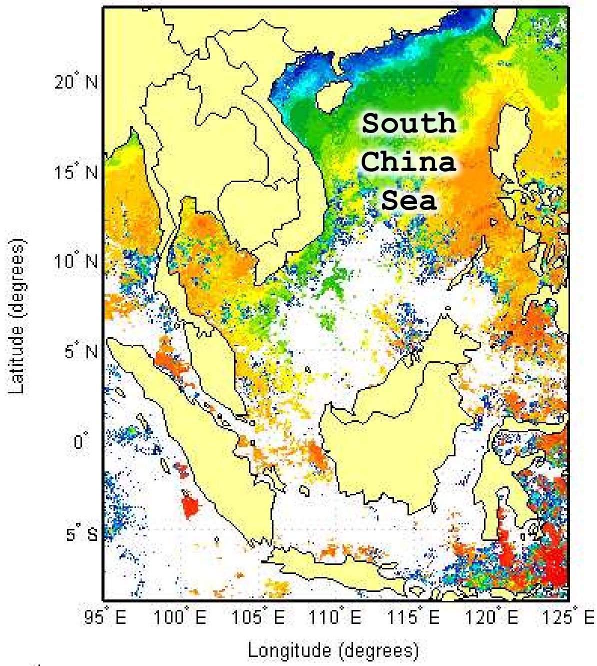

Figure 1.1: The South China Sea, project area of the SAT2SEA2 project. Satellite measurement of the sea surface temperature, which is blocked by clouds in some regions. Data from the AVHRR / Pathfinder dataset.

The South China Sea covers the region from the equator to 23°N and from 99°E to 121°N, bordering to among others Taiwan, The Philippines, China, Vietnam, Malaysia and Indonesia (see figure 1.1). Due to this large spatial extent, remote sensing (RS) will play an essential role in this project. Water level data measured by satellite altimeter and sea surface temperature (SST) data measured by satellite radiometer will be applied for model validation and forcing. Also, temperature climatologies like the World Ocean Atlas 2001 and atmospheric reanalysis datasets like the ECMWF ERA-40 will be applied. These datasets provide a synoptic coverage which, considering the large spatial scales of the SCS, is impossible with in-situ data.

Remote sensing, modeling and data

As indicated above, remote sensing data will be used because of its synoptic coverage. In this way both a large spatial area and a long temporal extent are covered. This is illustrated by figure 1.2, where the left panel shows the coverage of remote sensing (DUACS and AVHRR), climatological (WOA01) and atmospheric (ECMWF) datasets used with respect to the SCS scales. The right panel shows how to interpret this figure. Also included are in-situ measurements by ships and buoys. The focus of the SAT2SEA2 project is on processes on seasonal and basin-wide scales (the shaded region in the left panel of figure 1.2). From figure 1.2 it is observed that the sampling capability, or coverage, by the synoptic datasets is good at these scales.

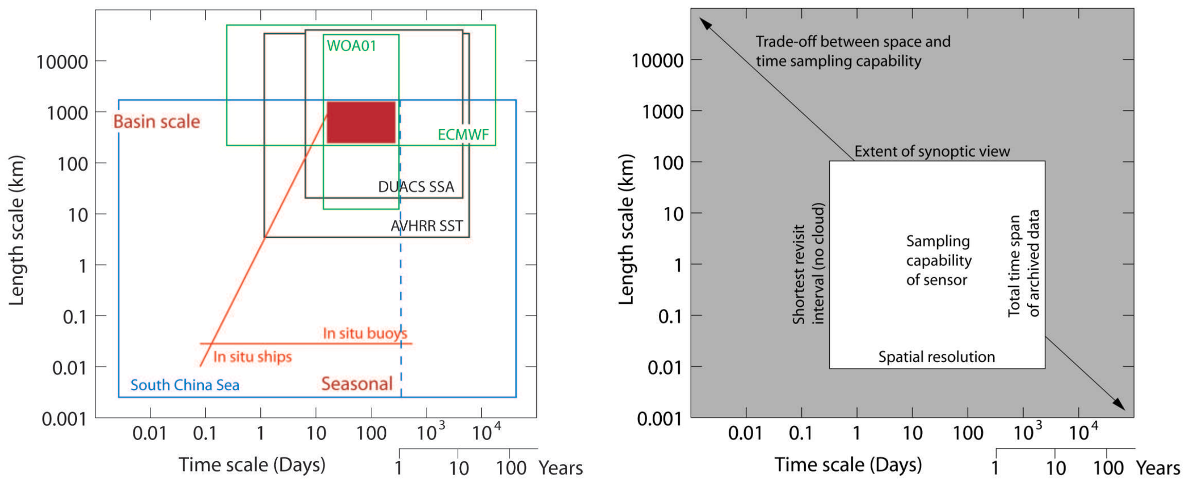

Figure 1.2: Overview of length and time-scales of in-situ and remote sensing sensors, compared with South China Sea scales.

From figure 1.1 it is seen that remote sensing measurements can be blocked by cloud coverage. This indicates one possible drawback of this measurement technique. Another possible drawback is that remote sensing sensors only directly measure surface (horizontal) variability. This can pose a problem if processes under investigation have significant vertical variability. A possible work-around to this problem is to combine data with models to assess the sub-surface variability. These model can provide a representation of reality. In order to do so they will require data for model forcing, to provide constraints within which the model finds this representation. Data is also required for model validation, to assess the quality of this representation.

Since water temperature shows significant sub-surface variability the combined use of remote sensing data and a model can provide an outcome. This will also require forcing and validation data which is not provided by remote sensing, explaining the need for temperature climatologies, describing the long-term mean water temperature state, and atmospheric datasets, describing the state of the atmosphere and required to impose atmospheric processes. These will also be assessed and used for modeling during this project.

Water temperature and modeling

Knowledge of water temperature is of great importance to a variety of marine issues. Chemical and biological processes are controlled to a large extend by the magnitude and distribution of the water temperature. Because of this, a good representation of the three dimensional (3D) temperature field is essential to model processes like substance transport, eutrophication and related oxygen depletion in water systems. As such, developing an accurate temperature model is an essential step toward modeling these processes. Such a model will be a valuable tool to forecast water quality processes like harmful algal blooms.

While the water temperature is governed primarily by surface phenomena, the temperature distribution has a significant vertical component caused by vertical mixing of surface layer water. This vertical mixing of water and substances can be limited by the existence of a thermocline, which is a water layer where the temperature changes rapidly with depth. Because water temperature and density are related, the thermocline can be considered as the separation zone between two layers of different densities. This stratified system is de-coupled to a large degree, and vertical exchange between these layers is small.

Because of this, surface processes like wind and wave induced mixing and the surface heat flux mainly effect the surface, or mixed layer. While this layer has a relatively uniform temperature, it can vary significantly over time. Below the thermocline, effects of the indicated processes are small. This is illustrated by figure 1.3, which shows a possible temperature (left panel) and density(-gradient) (middle panel) cycle. In the upper water layer a significant seasonal temperature cycle is observed. In deeper regions, this cycle diminishes. Furthermore, since the thermocline is situated in the region where the density gradient is largest, a seasonal thermocline depth cycle is observed also.

Since the most significant temperature variability occurs in the mixed layer region, the SAT2SEA2 project will focus on this region mainly. As indicated earlier, it will be assessed on a seasonal and basin-wide scale. This implies that the processes governing the 3D temperature in this region, like stratification, should be resolved by the model.

As illustrated, the sea surface temperature can be measured by satellite. This data can be applied as model surface forcing, providing a constraint for the model equations. Based on these constraints and on its internal dynamics, the model will give a representation of the true state. Data is also required to assess the quality of this representation.

To give a good representation of the required processes, the models discretization should be able to resolve these. Also, it should be forced is such a way that these processes are imposed. This illustrated the need to identify those processes that governing phenomena which have to be resolved by the model. Within the scope of SAT2SEA2, this indicates that the processes governing the SCS mixed layer temperature cycle have to be identified.

Furthermore, these processes have be imposed by model forcing or should result from the models response to this forcing. This requires the acquisition and assessments of the data needed for model forcing. Also, model results have to be validated, requiring the acquisition and assessments of model validation data. Finally, the models response, or sensitivity to the applied forcing data should be assessed. Based on this assessment the model setup, and as such its representation, can be optimized with respect to validation data. These steps will be described in this report.

Finally, it should be noted that there are different ways to force models or to optimize their representation of reality. Of these, methods that combine observations with models to improve the model state are known as data assimilation. During SAT2SEA2, an assimilation methodology known as nudging will be used to improve the models temperature accuracy.

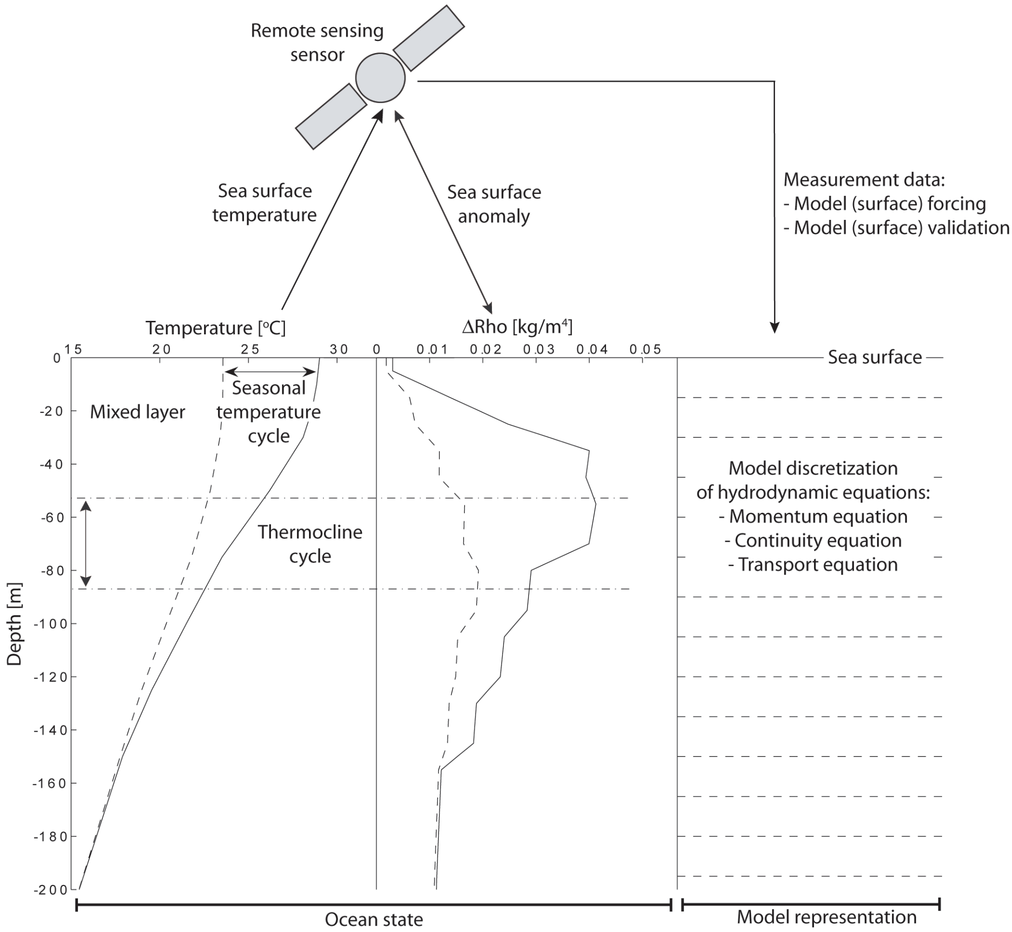

Figure 1.3: Schematized overview of vertical temperature and mixed layer (thermocline) variability and model representation.

SAT2SEA2 background

The SAT2SEA2 project builds upon experience gained during the REST3D and SAT2SEA projects, both performed by WL | Delft Hydraulics. In these projects the benefits of combining RS and model data were used to integrate RS Sea Surface Temperature (SST) into a 3D North Sea temperature model and into a 2D SCS tidal model using altimeter data, respectively. The results obtained during these projects would have been impossible without RS: the synoptic RS products provided a vital source of model validation and forcing data which, considering the large spatial scales of the models used, would have been impossible with in-situ data. As such, RS will be considered a key component of this project. SAT2SEA2 is a follow-up on the SAT2SEA project. Whereas SAT2SEA only focused on water level modeling for the SCS, SAT2SEA2 will expand this to 3D temperature and salinity modeling.

1.1 Project goals

The motivation for this project is based on the importance of the 3D temperature distribution for water quality and on the relevance of the SCS region. Knowledge of water temperature is of great importance to a variety of marine issues. Processes such as sediment transport, nutrient distribution and primary production highly depend on the three-dimensional transport, in which the temperature distribution is essential. Furthermore, information about these processes is of importance to a number of end-users in the SCS region, which has become a region of increasing economical importance over the past decade. Among these end-users are dredging, off-shore and consulting companies and economic centers such as Singapore and Hong Kong. As such, WL | Delft Hydraulics' interest is to model temperature and water quality processes using its in-house hydrodynamical package for open waters. Such a temperature model will be a valuable tool for scenario analysis and forecasting.

The goals of the SAT2SEA2 project are:

1. To assess the large-scale South China Sea (SCS) temperature behavior based on information from literature and on available remote sensing (RS) and in-situ data.

2. To expand the SAT2SEA model to a 3D temperature and salinity model and to assess whether the large-scale temperature processes can be represented accurately by this model. The primary focus will be on representing the seasonal, basin-scale mixed layer temperature cycle. The model will integrate remote sensing SST and altimeter data and various in-situ data products, among which climatological atlases.

To achieve this goal the following activities will be carried out:

1. The physical system of the SCS is studied by means of a detailed literature study. In particular the 3D temperature distribution on a seasonal and basin-wide scale is studied. Processes assessed are the large-scale circulation and transport, attributed to monsoon forcing, western boundary currents along the Vietnamese and Chinese coastlines, Rossby wave dynamics in the North SCS, upwelling due to bathymetry contraints and intrusions through Luzon and Taiwan Strait. Furthermore, the large-scale surface heat flux, mixed layer and thermocline cycles are assessed.

2. The necessary data for model forcing and validation is acquired. Emphasis will be on RS data (SST data from AVHRR / Pathfinder and Reynolds OI SST and water level data from DUACS), on climatological temperature atlases (the World Ocean Atlas 2001) and on atmospheric re-analysis archives (the ECMWF ERA-40 archive and the NCEP/NCAR Re-analysis). This is because of the advantageous synoptic coverage of these datasets with regard to the large model domain and the goal to model large-scale processes. Acquired data will be compared and controlled for quality.

3. A 3D temperature model is setup which is suited to represent the processes governing the seasonal, basin-scale temperature cycle. This model will be able to resolve the large-scale mixing and transport governing the seasonal temperature cycle. It will also resolve the large-scale heat flux at the free surface and the large-scale stratification. Furthermore, it will resolve upwelling attributed to bathymetry constraints and the seasonal intrusions though Luzon and Taiwan Strait. Finally, the model will not resolve tides, nor will it resolve meso-scale eddies.

4. The importance of different model parameters and forcing on the seasonal SCS temperature cycle is assessed by means of a model sensitivity analysis.

5. RS SST data is assimilated into the model using a nudging methodology in order to further improve the models temperature accuracy.

1.2 Scope of the SAT2SEA2 project

SAT2SEA2 focuses on improving the 3D hydrodynamic and temperature modeling for the South China Sea primarily. The Indonesian Archipelago is also included in the model domain, but the model performance and quality in this region are of secondary importance in this project.

WL | Delft Hydraulics' in-house hydrodynamic modeling package Delft3D-FLOW is used in the SCS temperature simulations. This package has a number of standard features to include pre-processed forcing data at model boundaries. A routine to force the model using RS SST at the free surface was included for this project specifically. This routine applies a data assimilation technique known as nudging: a correction term is added to the surface flux. This term is based on the difference between modeled and observed SST and corrects model forcing to minimize this difference.

In this report, the activities stated in the previous section are subdivided over three parts. Conclusions and recommendations are included in a separate, fourth part:

- Part I: Assessment of the SCS region and of the processes governing 3D temperature variability.
- Part II: Acquisition of RS and in-situ forcing and validation data, and assessment of data quality.
- Part III: Setup of the 3D temperature model, assessment of model parameters and forcing (including nudging) by means of a model sensitivity analysis and model validation.
- Part IV: Conclusions and recommendations.

These contents of these parts is described in more detail below.

Also, background information is provided in a set of appendices. Appendix A gives an overview of dataset providers. Appendix B gives some notes on computer scripts and data management. Appendices C till F describe methodology and background of applied temperature modeling and data assimilation methods. Appendices G till I provide tables and figures related to parts I till IV of this report.

1.2.1 Part I: Assessment of the project area

A first step in developing the 3D temperature model for the SCS is to examine the project area and the processes governing 3D temperature variability on a basin-wide and seasonal scale. In part I of this report an overview of processes governing the seasonal SCS temperature cycle is given, describing the large-scale circulation and transport attributed to monsoon forcing, western boundary currents along the Vietnamese and Chinese coastlines, Rossby wave dynamics in the North SCS, upwelling due to bathymetry constraints and intrusions through Luzon and Taiwan Strait. Furthermore, the large-scale surface heat flux, mixed layer and thermocline cycles are assessed. This assessment is partially based on data from the datasets described in part II. This is done to present a graphical overview of and to elaborate further on processes described in literature. Furthermore, SCS SST variability is assessed by means of a statistical Empirical Orthogonal Function (EOF) analysis. This method tries to find spatial patterns of variability, their time variation and their relative importance based on statistical properties.

Based on this overview the key processes controlling the seasonal SCS temperature (mixed layer) cycle are identified. These processes have to be resolved by the model to reproduce this cycle. As such, they have to be imposed by forcing or should result from the models internal dynamics.

1.2.2 Part II: Data acquisition and assessment

A wide range of datasets are acquired and processed for this project (see appendix H.1 for an overview). This data can be subdivided into a number of categories:

1. Climatological atlases containing temperature and salinity data (data from the World Ocean Atlas 2001). These atlases describe the long-term mean behavior and are obtained by interpolating available in-situ data to a fixed grid.
2. In-situ temperature and salinity measurements from the ASIAEX and SCSMEX projects.
3. Relevant meteorological data for surface heat flux, wind and pressure forcing, in the form of gridded numerical weather prediction model data (data from the ECMWF ERA-40, NCEP/NCAR Re-analysis and COADS datasets).
4. Altimeter water level data from the DUACS dataset (Sea Surface Anomaly, Absolute Dynamic Topography and geostrophic circulation).
5. Sea surface temperature from the AVHRR / Pathfinder and Reynolds OI SST datasets.

Based on assessments and comparisons of these different data and on their availability, decisions are made on model forcing and validation data and on the modeling period.

Due to the small amount of long-term SCS in-situ data obtained for this project, little historical data is available to validate the models vertical temperature distribution and stratification. To circumvent this, two approaches are assessed:

1. Climatological temperature profiles from the World Ocean Atlas 2001 (WOA01) are used for historical (year 2000) model validation. The project goal is to model large-scale, long-term temperature processes, and these are resolved well for the SCS by the climatological data.
2. Second, a method described by [Nardelli & Santoleri, 2004] is used to construct synthetic temperature profiles. This method uses information about the water column contained in surface RS observations (SST and SSA) to 'update' climatological temperature profiles. These synthetic profiles are reported to give a more accurate estimate of historical temperature values. This method is assessed in this part of the report.

1.2.3 Part III: Model setup, sensitivity analysis and validation

A 3D temperature model is setup using the Delft3D-FLOW hydrodynamic modeling environment. Based on the models discretization and forcing is should resolve the large-scale processes identified in part I of this report. This is done using data described in part II of this report. The SAT2SEA model is used as a starting point. This model is extended to include temperature and salinity processes and to resolve vertical variability.

A sensitivity analysis is performed to assess effects of model parameter settings and forcing. This analysis is subdivided into a number of steps:

1. A sensitivity analysis on the model parameters for the temperature modeling and stratification. Model results are assessed based on a Goodness-of-Fit (GoF) with WOA01 temperature data.
2. A sensitivity analysis on model temperature forcing, assessing heat flux forcing at the free surface and lateral transport forcing at the open boundaries. Model sensitivity is assessed based on a GoF with WOA01 temperature data.

3. A sensitivity analysis on model momentum forcing. Effects of momentum forcing at the free surface (wind and pressure forcing) and at the open boundaries (water level forcing) are assessed based on the correlation between model water level and altimeter SSA data.

4. A sensitivity analysis on the models nudging term. Effects of changing the nudging coefficient, which specifies the relative strength of the nudging term, are assessed by a comparison with WOA01 profile data.

Based on the results of this sensitivity analysis choices on model parameterization and forcing are made for the final model. Model results are validated using in-situ, climatological (WOA01) and RS temperature data for the year 2000. Based on this, conclusions about model performance and accuracy are drawn.

1.3 Summary of contents

Part I (chapters 2 and 3) gives a description about SCS temperature processes: in chapter 2 an overview of the processed governing 3D temperature variation as described in literature and observed from data is made. This overview is extended with a statistical analysis of temperature data in chapter 3.

In part II (chapters 4 till 7) data acquisition and assessment are discussed: chapter 4 gives an overview of non-RS data acquisition, followed by an overview of acquired RS data in chapter 5. This is followed by a comparison between the different datasets in chapter 6. Subsequently, a method used to construct synthetic temperature profiles is assessed in chapter 7.

Part III (chapters 8 till 11) focuses on setup, sensitivity analysis and validation of the 3D temperature model: chapter 8 provides an overview of model setup and modeling choices. This is followed by a sensitivity analysis on models temperature parameters in chapter 9. Subsequently, in chapter 10 model forcing is assessed, focusing on effects of temperature forcing, momentum forcing and SST nudging. This is followed by model validation in chapter 11.

Part IV presents conclusions in chapter 12 and recommendations in chapter 13.

Finally, appendix A provides acknowledgments to dataset providers. Appendix B gives some notes on computer scripts and data management. Appendices C till F subsequently describe the methodology and background of applied temperature modeling and data assimilation techniques. Appendices G till I provide tables and figures related to part I till IV of this report.

PART I: Assessment of the project area

In this part of the report a summary of relevant SCS temperature processes as described in literature is given. This summary is extended by an assessment of these processes based on the data described in part II of this report. This is done to present a graphical overview of and to elaborate further on processes described in literature. Assessed processes are:

- The monsoon system (section 2.2).
- Surface layer circulation (section 2.3).
- Exchange processes with other seas and oceans (section 2.4).
- Temperature distribution and transport, including stratification (section 2.5).

First, a short description about the SCS hydrography is provided in section 2.1.

Also, SCS SST variability is assessed by means of a statistical Empirical Orthogonal Function (EOF) analysis in chapter 3. This method tries to find spatial patterns of variability, their time variation and their relative importance based on statistical properties.

Based on the overview in this part the key processes controlling the seasonal SCS temperature cycle are identified. These processes have to be resolved by the temperature model to re-produce this cycle.

Finally, it should be noted that the assessment in this part will only focus on the surface and mixed-layer variability. Deeper layer processes will not be assessed during this project.

Chapter 2

Overview of the project area

As defined in chapter 1 the goal of the SAT2SEA2 project is to model SCS temperature and salinity variability on a seasonal timescale and a basin-wide spatial scale. This goal is further specified as to model the seasonal mixed-layer temperature. This seasonal temperature cycle is governed by, among others, large-scale ocean-atmosphere interaction, transport (advection) by large-scale circulation and seasonal stratification of the water column.

In this chapter the importance and characteristic scales of these processes are assessed for the SCS. This is important because the seasonal, basin-scale processes governing the mixed-layer temperature cycle have to be resolved by the model . The processes identified in this chapter have to be imposed by model forcing or should result from the models internal dynamics.

The assessment of the large-scale, seasonal SCS cycle in this chapter is based on an overview of the relevant processes as described by literature. This overview is complimented with data from the various datasets described in part II of this report. This is done in order to verify and study the information found in literature and to present a graphical overview of the processes. In chapter 3 this assessment is complemented with a statistical analysis of SCS temperature data. Following these assessments, chapter 8 (part III) will discuss the implications of the processes on model setup and forcing.

This chapter will start with an overview of the SCS hydrography in section 2.1. This is followed by an assessment of the monsoon wind system in section 2.2 and of basin-scale circulation in section 2.3. Subsequently, section 2.4 will discuss large-scale exchange with surrounding systems. Finally, the implications of these processes on the seasonal SCS temperature variability are discussed in section 2.5.

2.1 South China Sea hydrography

The South China Sea (SCS) is the largest sea bordering the Northwest Pacific Ocean and forms a semi-enclosed basin with a mean depth of 1800 m and a maximum depth of over 5400 m. It covers a region from the equator to 23°N and from 99°E to 121°E. The surface area of the SCS is about 3.5 million square kilometers. A topographic map of the SCS region is provided in appendix G.1. Appendix G.2 shows a SCS bathymetry chart.

As observed from appendix G.2, the deep (central) SCS basin is enclosed by two continental shelves with depths shallower than 100 m. The northern shelf, which includes the area of South China, extents from Taiwan southwestwards to 13°N. On the northern shelf, the exchange of water between the SCS and the East China Sea occurs through Taiwan Strait, which has a mean depth of 60 m. Exchange of water between the SCS and the Pacific Ocean occurs mainly through Luzon

Strait, which has a depth of over 2 kilometers, allowing the exchange of deeper layer and colder water. The southern shelf consists of the Gulf of Thailand and the Sunda Shelf between Malaysia and Borneo. The Sunda Shelf is connected to the Indian Ocean through the Strait of Malacca. On the eastern side, the SCS is separated from the Pacific Ocean by the Phillipines and Palawan. The slope between the continental and ocean shelves is steep at this interface. There are three openings on the eastern boundary, the widest and deepest of which is the above mentioned Luzon Strait, which is the major pathway of the Pacific water to the deep basin. Two narrower passages to the north and south of the Palawan Island connect the SCS to the Sulu Sea [Gerritsen *et al.* , 2001] [Qu, 2001].

2.2 East Asian Monsoon

According to literature, dynamic processes in the SCS are governed to a large extent by the Asian monsoon system. In this monsoon system a distinction can be made between the North East (NE) monsoon (also called winter or dry monsoon) and the South West (SW) monsoon (also called the summer or wet monsoon). This system follows the following annual cycle [Wyrtki, 1961]:

- From September till April the NE monsoon prevails. This monsoon is fully developed in January, during which a NE wind, often exceeding wind force 5 (8.0 - 10.7 m/s), prevails over the entire SCS domain. From February onwards, the NE monsoon will weaken in force, but it will prevail until April.
- From May till August the NE monsoon is succeeded by the SW monsoon. During May the NE winds over the SCS collapse, and a SW wind succeeds. It will increase in force over the following months, reaching full development in July and August, when at open sea wind force 4 (5.5 - 7.9 m/s) is often exceeded. From September onwards, however, NE winds occur over the North SCS, while in other regions the SW monsoon still prevails. From October onwards, the NE winds prevail over the entire SCS.

From wind data a similar annual cycle is observed. Figure 2.1 shows monthly-mean wind fields for January and August (the NE and SW monsoon highs). These fields are obtained from a 13 year climatology of monthly-means for these months, determined from ECMWF ERA-40 data (see chapter 4). A more extensive overview of climatological, monthly-mean SCS wind fields is provided in appendix G.3 (NE monsoon) and G.4 (SW monsoon).

From figure 2.1 the inverted NE and SW monsoon wind directions are clearly visible. Furthermore, from the figures in appendices G.3 and G.4 it is observed that around April the NE monsoon collapses and is followed by the SW monsoon. This in turn collapses around October. Also, it can be observed that during the NE monsoon the wind magnitude is more or less uniform over the entire SCS basin. During the SW monsoon this is not the case and a higher wind magnitude is observed over the South SCS.

These spatial differences in wind conditions will result in a spatial difference in surface wind stress and in wind induced circulation. This can be observed from figure 2.2, which shows the surface wind stress calculated from the wind fields shown in figure 2.1. The wind stress (τ) is calculated by $\tau = C_d \rho_a |U_{10}|^2$ [Delft3D, 2005], where ρ_a is the air density, U_{10} the wind speed at 10 meters height and C_d the wind drag coefficient. For ρ_a a constant value of 1.2 kg/m^3 is used and for C_d a constant value of 2 $\times 10^{-3}$ [Open University, 1989].

Finally, figure 2.3 shown the area averaged SCS wind magnitude (velocity). This data is determined from the ECMWF ERA-40 climatology described above and represents the area averaged conditions over 100°E - 120°E, 5°S - 25°N. From this figure a maximum wind velocity is observed around December / January, when the NE monsoon is high. A second maximum is observed

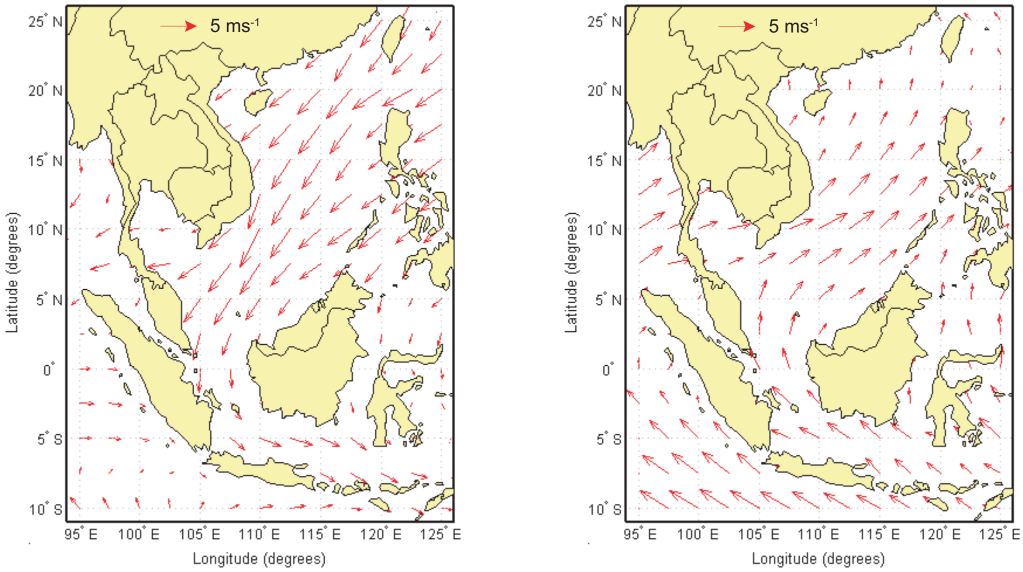

Figure 2.1: Monthly-mean wind climatology for January (left) and August (right). Obtained from ECMWF ERA-40 monthly wind composites averaged over 1983-2001. See appendix G.3 and G.4 for other months.

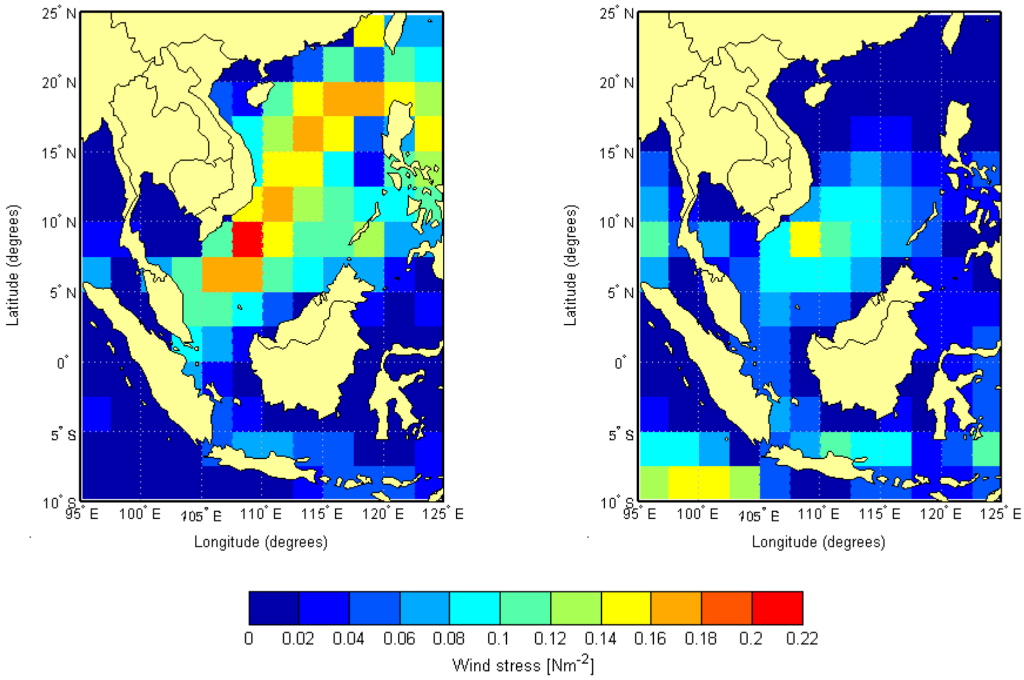

Figure 2.2: Monthly-mean surface wind stress for January (left) and August (right). Obtained from ECMWF ERA-40 monthly wind composites averaged over 1983-2001, using a wind drag coefficient of 2 $\times 10^{-3}$.

around July / September, when the SW monsoon is high. Around April and October minimum wind velocities are observed. These periods correspond with the transition periods between both monsoons. Furthermore, during the NE monsoon the wind has a mean magnitude of about 3.5 ms^{-1}. During the SW monsoon this magnitude is slightly lower, and is about 3 ms^{-1}.

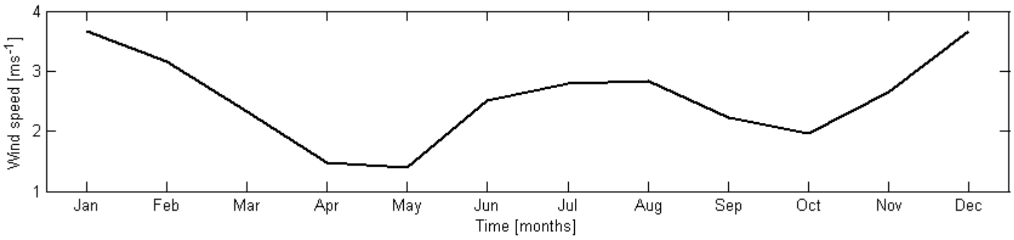

Figure 2.3: Monthly-mean wind magnitude, spatially averaged over 100°E - 120°E, 5°S - 25°N. Obtained from ECMWF ERA-40 monthly wind composites, temporally averaged over 1983-2001.

Based on these observations, the seasonal SCS monsoon cycle described by [Wyrtki, 1961] is confirmed. A NE / SW oriented monsoon system is identified with its peaks around January and August. During the NE monsoon the mean wind magnitude is higher than during the SW monsoon. In the transition between these periods the mean wind magnitude decreases. As such, the wind magnitude follows a seasonal cycle. Finally, during the NE monsoon wind conditions are similar over the entire SCS, while during the SE monsoon space dependent differences are observed between the North and South SCS.

Finally, the fact that the wind magnitude observed from ECMWF wind data is below that described by [Wyrtki, 1961] can be explained by the climatological and areal averaging performed on the data. As such, high wind velocity phenomena on smaller scales are unresolved (or underestimated) by the averaging procedures.

2.3 Basin-scale circulation

According to literature, upper-layer, basin-scale circulation in the SCS can be regarded as barotropic currents due to coastline constrains and wind stress forcing [Wang *et al.* , 2004]. Monsoon wind forcing is believed to play a leading role in this, and a seasonal circulation cycle is observed which follows the monsoon cycle [Wyrtki, 1961]. During this cycle, the NE monsoon drives basin scale cyclonic (counter-clockwise) circulation in the North SCS and South SCS. During the SW monsoon, weak cyclonic circulation is reported in the North SCS and anti-cyclonic (clockwise) circulation is reported in the South SCS [Liu *et al.* , 2001].

Also, during the NE monsoon, water piling up against the Chinese and Vietnamese coastlines is reported to result in strong western boundary currents. During the NE monsoon the largest part of this boundary current is turned to the east around 5°N [Chu *et al.* , 1998]. Furthermore, the basin scale gyre system in the North and South SCS is reported to form a west-to-east cross-basin current around 16°N [Chu *et al.* , 2002].

From figure 2.4 the basin-scale circulation conditions can be observed. This figure shows the monthly-mean Absolute Dynamic Topography (ADT) as determined from a 4 year climatology of DUACS altimeter data (see chapter 5). Fields are shown for the months January and August, identified in the previous section as the NE respectively the SW monsoon high. In appendix G.6 the monthly-mean ADT fields for monsoon transition periods (April and October) are shown as well. Furthermore, appendix G.5 shows monthly-mean Sea Surface Anomaly (SSA) fields for these months determined from a 14 year DUACS SSA climatology. These SSA fields describe variations in water-level only, whereas the ADT fields also take into account the mean dynamic topography (see chapter 5).

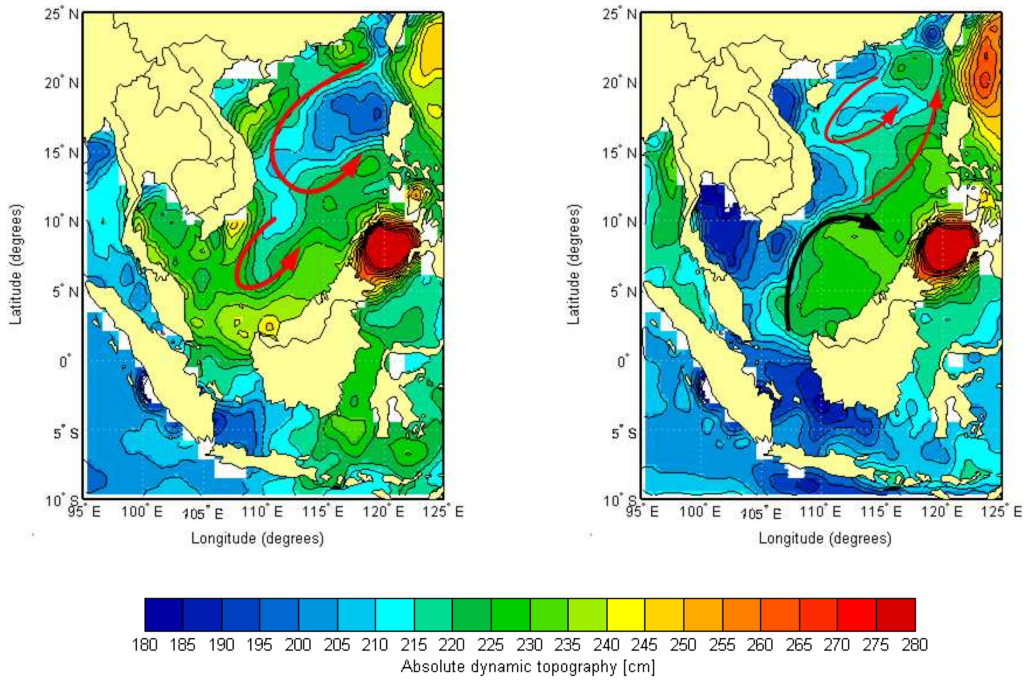

Figure 2.4: Monthly-mean absolute dynamic topography (ADT) for January (left) and August (right). Determined from a 4 year average of DUACS ADT data. The arrows indicate large-scale geostrophic circulation patterns. Red indicates cyclonic circulation and black indicates anti-cyclonic circulation. See appendix G.6 for other months.

From figure 2.4, large-scale cyclonic circulation is observed in both the North and South SCS during the NE monsoon. During the SW monsoon anti-cyclonic circulation is observed in the South SCS. In the North SCS weak cyclonic circulation is observed during this period. This confirms the large-scale circulation patterns described by [Liu *et al.* , 2001]. Note that with respect to SSA and ADT fields, geostrophic circulation follows iso-lines of equal height. The closer these lines are together, the higher the flow velocity. On the Northern Hemisphere the propagation direction will be such that the flow keeps high SSA (ADT) to its right and low SSA (ADT) to its left. On the Southern Hemisphere this direction is reversed (see appendix F).

The large-scale circulation in figure 2.4 follows the Chinese and Vietnamese coastlines during the NE monsoon. This confirms the western boundary current described by [Chu *et al.* , 1998]. Furthermore, during both the NE and SW monsoon a cross-basin current is observed which is centered around 16°N, confirming observation by [Chu *et al.* , 2002].

From figure 2.4 a significant increase in water level is observed in the Sulu Sea. Here, a dynamic topography of over 280 cm is observed, compared to a dynamic topography of around 230 cm in the adjacent SCS region. This high water level is not observed from the SSA fields in appendix G.5. These show a seasonal variability of around 15 cm in the Sulu Sea. Furthermore, figure E.2 in appendix E shows both the mean dynamic topography used for the DUACS ADT fields and the annual-mean steric height, calculated from World Ocean Atlas 2001 temperature and salinity data. Both these fields show a similar anomaly in the Sulu Sea. This suggests that the anomaly observed in this region from the ADT fields is the result of an anomaly in the mean dynamic topography, which was determined by CLS using among others the Levitus 1998 climatology (see appendix

H.4). As such, this anomaly can be explained by the anomaly observed from the World Ocean Atlas data. The origin of this anomaly is a subject for further study.

In literature, a number of explanations are given for the observed basin-scale circulation system. These explanations are consistent with each other, and indicate a strong correlation between the basin-scale circulation and the monsoon system. They are discussed below.

1. Basin-scale circulation by wind induced water-level tilting

The monsoon wind system is reported to cause a basin-scale 'tilting' of the SSA [Gerritsen *et al.* , 2001]. Due to the prevailing NE or SW wind directions, and because the ensuing wind-driven circulation will have an angle to this wind direction by the Coriolis force [Open University, 1989] (to the right on the Northern and to the left on the Southern Hemisphere), SCS water will pile up in either the western (NE monsoon) or eastern (SW monsoon) part of the basin. This is visualized schematically in figure 2.5.

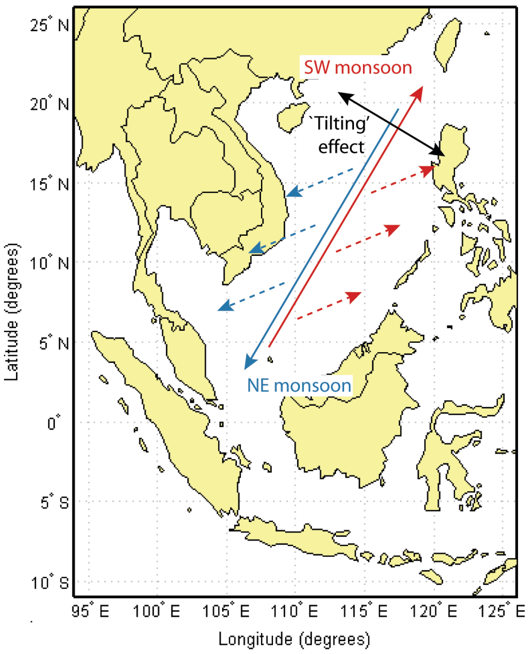

Figure 2.5: Schematic representation of Sea Surface Anomaly (SSA) tilting caused by the monsoon wind system. During the NE monsoon, wind forcing will cause water to pile up in the western part of the South China Sea (SCS) basin. During the SW monsoon wind conditions are reversed and water piles up in the eastern part of the basin.

From the monthly-mean SSA fields in appendix G.5 this behavior can be observed as well. During the NE monsoon a high SSA is observed in the western part of the SCS basin. In the eastern part of the basin a low SSA is observed. During the SW monsoon this situation has reversed. Also, from the SSA fields for April and October it is observed that this 'tilting' effect diminishes in the transition period between both monsoons. On the northern hemisphere, piling of water against a western coastline will result in a western boundary current which progresses along the coastline in counter-clockwise direction [Open University, 1989]. Because of this, the piling of water against the Vietnamese coastline during the NE monsoon will result in a western boundary current, which progresses southwards along the Vietnamese coastline. This provides an explanation for the western boundary current described by [Chu *et al.* , 1998]. Because of its relation with the described SSA tilting, and as such with the monsoon wind direction, this current has a one year period which follows the monsoon cycle.

In figure 2.13, the monthly-mean surface-layer salinity (obtained from the World Ocean Atlas 2001) is shown for January and August. A strong correlation between the large-scale circulation in figure 2.4 and these monthly-mean salinity fields can be observed. Using the salinity fields as 'tracer' for the large-scale circulation , it is observed that the western boundary current follows the Vietnamese coastline southwards. South of Vietnam the current continues over the shallow bathymetry of the Sunda Shelf. As such, it accounts for spatial variability in latitudinal direction from 15 °N till 5°N. In longitudinal direction, the wave itself is confined to the shallow Vietnamese coastline. From appendix G.2 it is observed that this is a narrow band only, between 0 and 50 kilometers in length at some points.

The 'tilting' effect also provides an explanation for the annual SSA cycle in the shallow SCS regions (Sunda Shelf), Gulf of Thailand and Java Sea. This can be observed from figure 2.6, which shows the correlation between the monthly-mean SSA and the wind direction. To determine this correlation the wind vector is projected on the NE monsoon wind direction (φ_w=225°) by θ^m_{NE}=cos(225 - φ^m_w), where θ^m_{NE} represents the projected wind direction, φ^m_w specifies the angle between the wind vector and the local North and m specifies the month number. Subsequently, the correlation is determined at each grid point from the covariance between the SSA and wind time-series, divided by the product of their respective standard deviations. SSA data used is obtained from a 10 year DUACS SSA climatology (see chapter 5). The wind direction is determined from the earlier mentioned ECMWF ERA-40 wind climatology. From figure 2.6, a high positive correlation is observed at the indicated regions (the Sunda Shelf and the China Continental Shelf), indicating the large-scale SSA cycle is similar to the large-scale monsoon cycle. As such, large-scale currents in these regions are modulated by this same cycle.

2. Basin-scale circulation forced by wind stress vorticity

According to [Wang *et al.* , 2004] there is a strong correlation between basin-scale SCS circulation and wind stress vorticity. This indicates the transfer of angular momentum by the surface winds, and as such the tendency to form vortices. Depending on their rotational direction, these vortices (or eddies) will result in either surface divergence or surface convergence. This will lead to a decrease (divergence) or an increase (convergence) in SSA [Open University, 1989]. A conceptual overview of these processes is given by figure 2.7. From this figure it is observed that positive vorticity is associated with to cyclonic winds and surface divergence, and negative vorticity is associated with anti-cyclonic winds and surface convergence (note that on the Southern Hemisphere these directions will be reversed).

Figure 2.8 shows the monthly-mean (surface-layer) atmospheric vorticity for January and August. These fields are obtained from a 13 year climatology of EMCWF ERA-40 vorticity data (see chapter 4). From this figure a negative vorticity is observed in the western part of the SCS basin during the NE monsoon. As described above, this will result in convergence and a higher SSA. In the eastern part of the SCS basin positive vorticity is observed, which will result in downwelling and a lower SSA. This corresponds to the January SSA field shown in appendix G.5. During the SW monsoon negative vorticity is observed in the eastern part of the SCS basin. This will result in surface convergence and a high SSA. Again, this is in line with the SSA as observed from appendix G.5. This confirms the correlation described by [Wang *et al.* , 2004]. This correlation is observed on similar temporal and spatial scales as the monsoon induced 'tilting' and the resulting SSA variability as described earlier. This indicates that, while the transfer of angular momentum by wind stress vorticity is a regional process, the large-scale patterns governing this transfer follow a similar monsoon related cycle.

3. Basin-scale circulation by Rossby wave dynamics

According to [Gerritsen *et al.* , 2001] a Rossby wave, originating from the Pacific Ocean, entered the SCS via Luzon Strait during the 1998 El Ninõ period. This wave crossed the North SCS basin with a phase speed of 3.5 degrees per month. A similar Rossby wave is described by [Yang & Liu, 2003]. Such a wave arises from the need to conserve potential vorticity when a

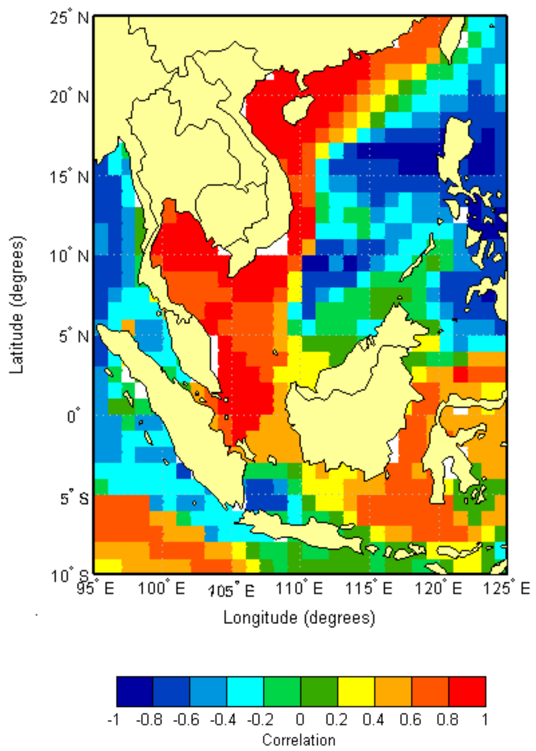

Figure 2.6: Correlation between monthly-mean Sea Surface Anomaly (SSA) and wind direction time series, calculated per grid location. The wind direction is specified by projecting the angle between the wind vector and the local North (φ_w^m) on the NE monsoon wind direction (φ_w=225°) by θ_{NE}^m=cos(225 - φ_w^m). SSA data is obtained from a 10 years DUACS climatology, wind data is obtained from a 13 year ECMWF ERA-40 climatology.

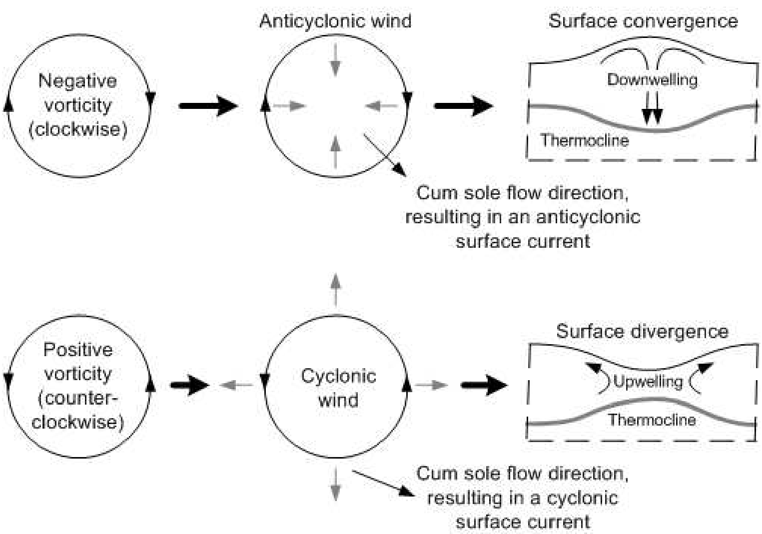

Figure 2.7: Conceptual representation of sea surface convergence or divergence caused by wind stress vorticity [Open University, 1989].

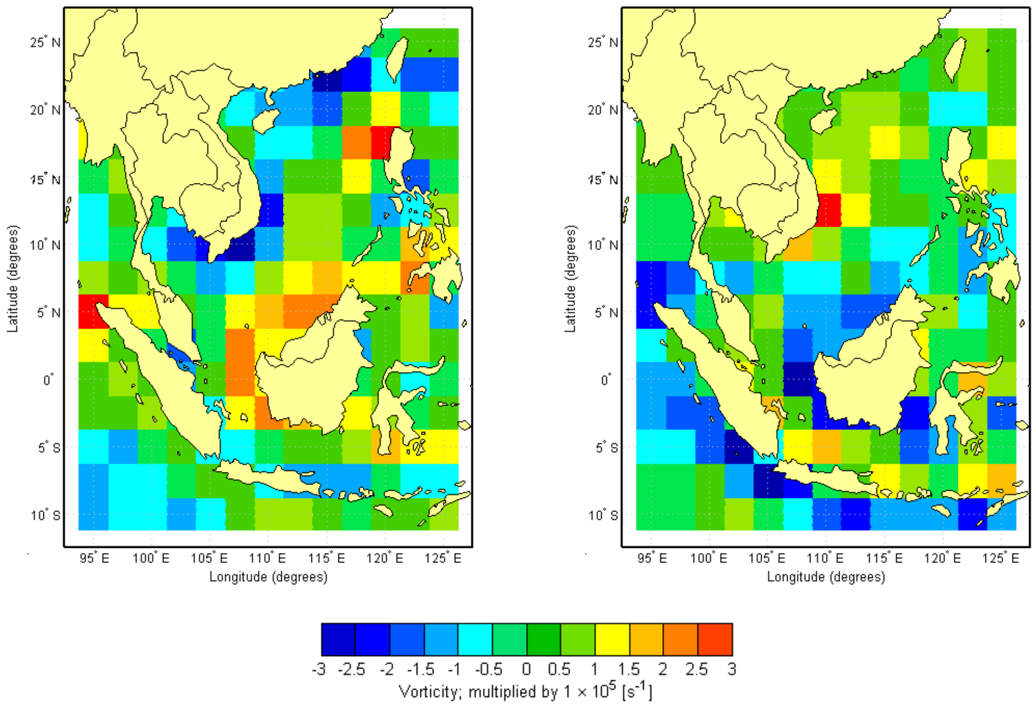

Figure 2.8: Monthly-mean (surface-layer) atmospheric vorticity for January (left) and August (right). Obtained from ECMWF ERA-40 monthly vorticity composites averaged over 1983-2001.

particle of water is displaced in latitudinal direction. This results in a latitudinal oscillation around the original latitude. The resulting wave-form will propagate westwards [Open University, 1989]. If the water particle moves southwards, it will gain positive (relative) vorticity. As indicated in figure 2.7 this leads to surface divergence and a lower SSA. If the water particle moves northwards, it gains negative relative vorticity. This will lead to surface convergence and a higher SSA.

From the January atmospheric vorcitity field in figure 2.8 a region of high positive vorticity is observed west of Luzon (around 17.5°N - 117.5°E). To assess possible effects of angular momentum transfer by this vorticity on the SCS circulation, figure 2.9 shows a Longitude-time SSA diagram at 18.5°N, 111°E - 120°E. This figure shows 3 years of DUACS SSA data (1999, 2000 and 2001) at the mentioned location. For comparison the annual cycle of atmospheric vorticity at 17.5°N, 117.5 °E is included in this figure, also. These values are obtained from a 13 year climatology of EMCWF ERA-40 data.

In figure 2.9 westward propagating waves are resembled by lines of constant SSA moving in north-western direction. Based on the time it takes a SSA feature to cross the longitudinal span in western direction, the propagation speed of a wave can be determined. From this figure a number of these waves can be distinguished. Most pronounced are an annually reoccurring positive SSA feature, originating at 120°E around July / August, and a negative SSA feature originating at 120°E around December / January. Both these features require about 15 weeks to cross the SCS basin from 120°E to 111°E, resulting in a phase speed of roughly 3 degrees per month. This could be interpreted as a Rossby wave crossing the North SCS basin. As observed, this wave has a one year period.

Furthermore, as observed from figure 2.9 the annual cycle of this wave is similar to that of the atmospheric vorticity at 17.5°N, 117.5 °E. This can provide an explanation about the origin of this wave: as explained a high atmospheric vorticity, as observed during the NE monsoon, results

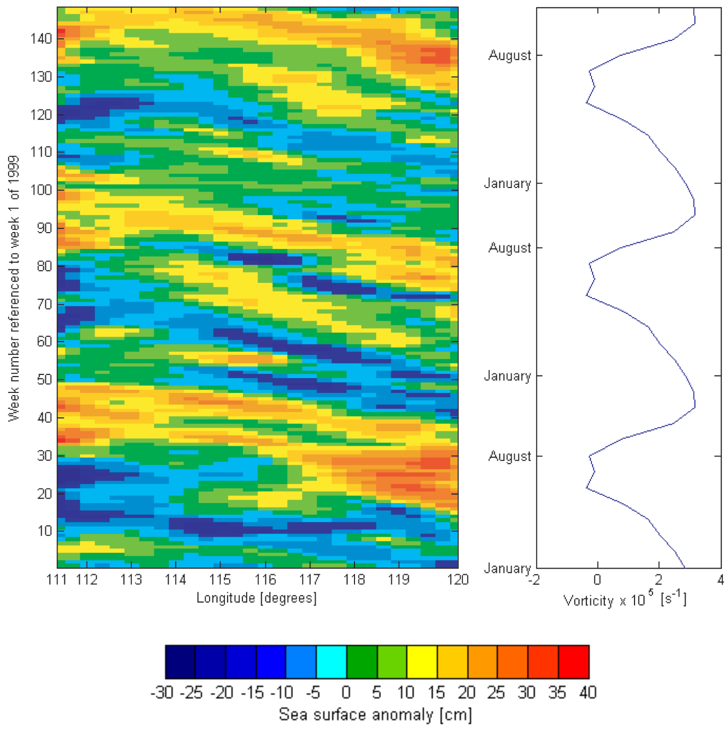

Figure 2.9: Longitude-time diagram at 18.5°N, 111°E - 120°E (left panel), representing SSA data from the DUACS dataset for 1999, 2000 and 2001. The right panel shows the annual cycle of monthly-mean atmospheric vorticity at 17.5°N, 117.5 °E. This data is obtained from a 13 year climatology of EMCWF ERA-40 data.

in surface divergence and a low SSA. Thus, a cyclonic eddy is formed west of Luzon. When the magnitude of the atmospheric vorticity decreases, this eddy may propagate westwards as a Rossby wave. This can explain the low SSA values observed in the North SCS during the NE monsoon. During the SW monsoon the reverse is observed. Atmospheric vorticity decreases until it reaches a negative maximum, forming a anti-cyclonic eddy. Again, this eddy may propagate westwards when the magnitude of the vorticity decreases. This can explain the high SSA values observed in the North SCS during the SW monsoon.

Based on this tentative explanation, it is suggested that the reoccurring Rossby wave observed from figure 2.9 is formed locally in the SCS by atmospheric forcing. This contrasts observations by [Gerritsen *et al.* , 2001], where a Rossby wave in observed to enter the North SCS from the Pacific Ocean. In support of that observation, SSA fields in appendix G.5 show a similar magnitude both east and west of Luzon Strait during January and August. Also, a similar SST is observed on both sides of this strait from January SST field in appendix G.7. This might indicate that SSA features both east and west of this strait originate from the same phenomenon. Based on these observations it is concluded that this is a subject for further study.

Finally, it is observed that the Rossby wave has a one year period. It is forced by processes on a significant time-scale, either locally by the atmosphere or originating from outside the SCS. In both cases a one year cycle is observed. Also, by a comparison with monthly-mean climatological salinity in figure 2.13 it is observed that this wave may account for variability in a significant part of the North SCS (in approximately a 5 x 10 degree region).

2.4 Exchange with surrounding systems

As described in section 2.1, Luzon Strait forms the only major connection between the SCS and other basins. This can be attributed to the significant depth of this Strait (over 2000 meters). Due to their shallow depths (around 100 meters) intrusions from the Sulu Sea, Java Sea or Malacca Strait have only marginal effects on the SCS system. As such, the SCS forms a semi-closed system [Chu *et al.* , 2002]. This can be observed from the SCS bathymetry map in appendix G.2.

According to [Liu *et al.* , 2001], Kuroshio intrusion through Luzon Strait plays a role in SCS circulation. This intrusion occurs by means of a so-called 'loop current' along Luzon Strait. At critical wind stress levels this loop current deflects into the SCS and influx occurs. This happens mainly during the NE monsoon when higher wind speeds are observed in the North SCS [Farris & Wimbush, 1996]. The Kuroshio influx causes mixing of Pacific and SCS waters in the Luzon and Taiwan Strait region.

In appendix G.6 monthly-mean Absolute Dynamic Topography (ADT) fields are shown. From these figures it is observed that from October till April (so during the NE monsoon and the transition periods) the iso-lines of dynamic height originating from the Kuroshio (Pacific Ocean) bulge into Luzon Strait before re-entering the Pacific southeast of Taiwan. During this period wind conditions are favorable to enter the SCS. As indicated in figure 2.5 and discussed in section 2.3, the mean wind-induced circulation will be to the west during the NE monsoon, making it easier to enter the SCS from the east at Luzon Strait. During the SW monsoon this situation is reversed.

From the SST fields in appendix G.7 the above mentioned loop current can be observed. From the December and January SST fields a small-scale warm-water tongue is observed at Luzon Strait. During this period the loop current is 1 to 2 degrees warmer than the surrounding SCS water. This loop current has only local effects on the SCS temperature, though. On both the eastern and the western sides of this strait the water is substantially colder.

On the SCS (western) side of Luzon Strait this colder water might be explained by cold water influx through Taiwan Strait. According to [Jacobs, n.d.] boundary currents propagate into the SCS through Taiwan Strait. From the SST fields in appendix G.7 cold water appears to enter the SCS from the East China Sea through this strait. This cold water is subsequently transport along the China Continental Shelf.

The above is shown in more detail by figures 2.10 and 2.11. These figures show SST and salinity fields for the Luzon and Taiwan Strait region (obtained from the World Ocean Atlas 2001 and from AVHRR / Pathfinder data, see chapters 4 and 5). Surface layer geostrophic circulation obtained from DUACS ADT data (see chapter 5) is imposted on these SST fields. For clarity, the large-scale circulation patterns are indicated by arrows.

From the SST fields in figure 2.10 both the warm water current at Luzon Strait and the cold water intrusion through Taiwan Strait are observed. From the circulation patterns it is observed that the large-scale Kuroshio circulation is parallel to Luzon Strait mainly. At this strait, small-scale mixing with colder SCS water is observed. Furthermore, south of Taiwan Strait large-scale mixing with cold water entering the SCS through this strait appears to play a more significant role. This large-scale mixing is also observed from the SST fields in appendix G.7.

From the salinity fields for both January and August it is observed that the salinity east of Luzon Strait is substantially higher than west of Luzon Strait (by about 0.5 ppt). At this strait, mixing of Kuroshio and SCS water can be observed from the salinity fields. This effect is larger during the NE monsoon, which can also be observed from the large-scale salinity fields shown in figure 2.13. During the NE monsoon high salinity water appears to enter the SCS. During the SW monsoon this is not observed.

The above confirms observations by [Farris & Wimbush, 1996], who state that Kuroshio intrusion occurs during the NE monsoon mainly. This cannot be attributed solely to the wind magnitude,

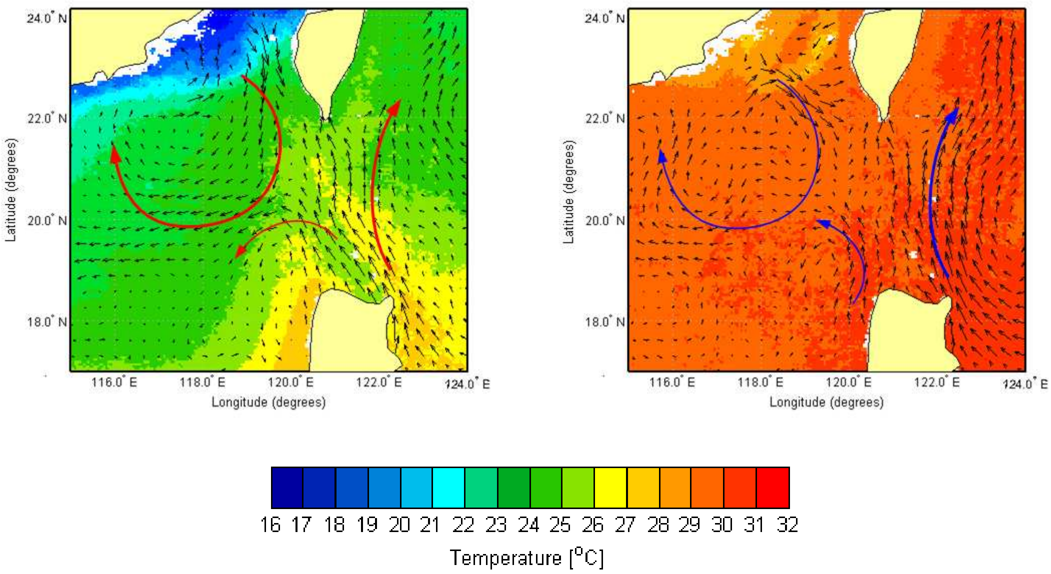

Figure 2.10: Monthly-mean sea surface temperature (SST) and geostrophic circulation at the Luzon and Taiwan Strait region for January (left) and August (right). Monthly SST composites obtained from AVHRR / Pathfinder. Geostrophic circulation obtained from DUACS sea surface anomaly and mean dynamic topography data.

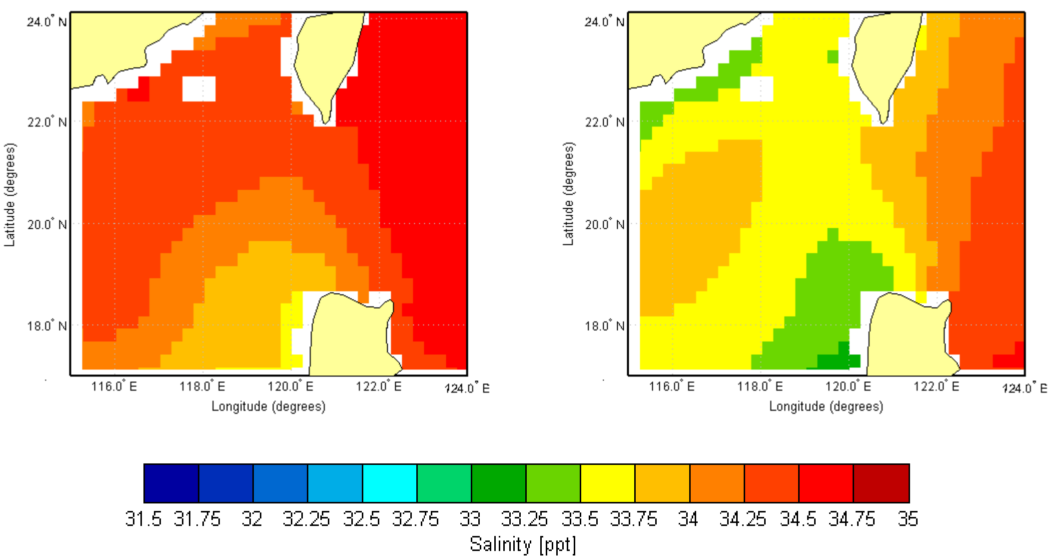

Figure 2.11: Monthly-mean surface layer salinity for January (left) and August (right). Obtained from the World Ocean Atlas 2001.

though, since the magnitude is higher during the SW monsoon than during the transition periods (see figure 2.3). Despite this, no intrusion is observed during the SW monsoon period while limited intrusion is observed during the transition periods based on the direction of the ADT iso-lines. As such, a favorable wind direction seems important as well. Based on these observations Kuroshio intrusion is primarily related to the monsoon winds direction and its magnitude, and occurs on a similar seasonal scale. Furthermore, salinity and temperature mixing of Kuroshio and SCS water is observed along the entire span of Luzon Strait. Furthermore, cold water intrusion through Taiwan Strait and mixing south of this Strait appear to have a more significant effect on the SCS temperature.

2.5 Temperature and salinity transport

2.5.1 Seasonal sea surface temperature variability

According to literature, the surface layer temperature in the SCS has a strong seasonal signal [Qu, 2001]. During the NE monsoon, the combined effect of the surface heat flux, sub-surface upwelling and wind-driven basin-scale circulation attributes to the formation of a bi-frontal thermal structure in the North SCS [Wang *et al.* , 2004]. A strong coastal front along the Chinese coast and a relatively weak and wide front across the SCS basin from the Vietnamese coast to the Luzon Islands are observed [Chu *et al.* , 2002]. These processes attribute to a seasonal amplitude of over 6°C in the North SCS. In the South SCS these effects are less pronounced, and the seasonal temperature amplitude is significantly lower (2.5°C - 4°C).

The principle mechanisms causing these variations are reported to be strong seasonal variation of the surface heat flux and dynamic processes associated with the monsoonal wind system [Wang *et al.* , 2004]. During the NE monsoon increased wind stress causes entrainment of colder and denser water in the mixed layer, resulting in a deeper mixed layer and a lower temperature. This effect is most pronounced near the southern coast of China. During the SW monsoon, wind stress decreases and heat gained from the atmosphere is trapped in the shallower mixed layer. This causes a rise in surface layer temperature [Qu, 2001].

Figure 2.12 shows monthly-mean Sea Surface Temperature (SST) fields for January and August. In section 2.2 these months were identified as the maximum of the NE and the SW monsoon, respectively. These fields are obtained from a 10 year climatology of monthly-mean AVHRR / Pathfinder SST composites (see chapter 5). In appendix G.7 and G.8 SST fields are shown for other months also. Next, an explanation is given for the characteristic SST features during both monsoon periods.

NE Monsoon SST

From figure 2.12 a frontal SST structure is observed during the NE monsoon. A first front is observed between Luzon and Vietnam, following the Vietnamese coastline (front 1). A second front is observed along the Chinese coastline (front 2). When compared with the August SST field, seasonal variation South of front 1 is limited, with an amplitude between 2°C and 4°C. Between front 1 and 2 the seasonal variation is more pronounced with an observed seasonal amplitude between 6°C - 7°C. Above front 2, in the narrow band of water following the Chinese coastline, a seasonal amplitude of over 7°C is observed. At the frontal interfaces horizontal mixing of temperature is observed.

In section 2.3 basin-scale circulation in the North SCS is explained by means of boundary current and Rossby wave dynamics. Both these processes are modulated by the monsoon cycle. By comparing the January SST field in figure 2.12 with the January ADT field in figure 2.4 it is observed that front 1 follows the dynamic topography in the central SCS. This can indicate that either the dynamic topography and the temperature are forced by the same mechanism, or that horizontal transport by the large-scale current system plays a role in the temperature cycle.

In section 2.4 it was observed that intrusion of cold water through Taiwan Strait has a significant effect on the SCS temperature. This cold water mixes with warmer SCS water south of this strait, and is transported along the China Continental Shelf by boundary currents. Subsequently, this

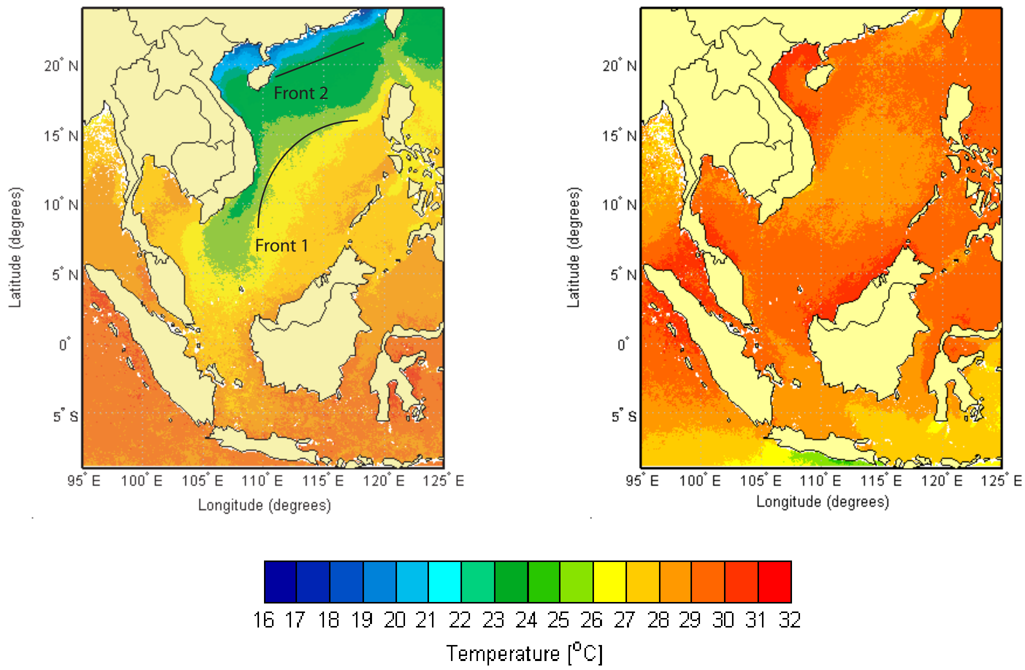

Figure 2.12: Monthly-mean sea surface temperature climatology for January (left) and August (right). Obtained from a 10 year (1994-2004) climatology of monthly-mean AVHRR / Pathfinder SST composites. See appendix G.7 and G.8 for other months.

colder water may be transported into the central SCS by the large-scale current system, explaining the correlation observed above.

Furthermore, in section 2.3 a tentative explanation about the North SCS water level cycle was given based on Rossby wave dynamics. Possibly, mixing by this wave will increase the North SCS's response to the intruding cold water during the NE monsoon. This, too, would explain the observed correspondence between the North SCS temperature and water level cycle.

This can also be observed from the surface-layer salinity fields in figure 2.13. During the NE monsoon high salinity values are observed in the region between front 1 and front 2. This can be explained by large-scale transport and mixing, possibly increased by the mentioned Rossby wave. This high salinity water is subsequently transported southwards along the Vietnamese coastline and onto the Sunda Shelf.

By comparing the shape of front 2 in figure 2.12 with the SCS bathymetry in appendix G.2 it is observed that this front closely follows the shallow Chinese coastline. From the monthly-mean climatological SST fields in appendix G.7 this colder water appears to originate from Taiwan Strait (see section 2.4). From this location it propagates into the SCS following the shallow bathymetry of the China Continental Shelf.

Furthermore, upwelling caused by the large-scale circulation system in the North SCS and by bathymetry constraints may contribute to the high salinity values observed south of the Chinese coastline. As observed from appendix G.6 North SCS circulation is cyclonic (counter clock-wise) all year round, following the China Continental Shelf in the northern regions. Possibly, this leads to upwelling of sub-surface water against this continental shelf, which would explain the higher salinity values observed along this shelf during the SW monsoon when no intrusion through Luzon and Taiwan Strait is observed. This may also contribute to the formation of the cold water fronts during the NE monsoon. Furthermore, figure 2.13 shows that from Hong Kong up till the Gulf of

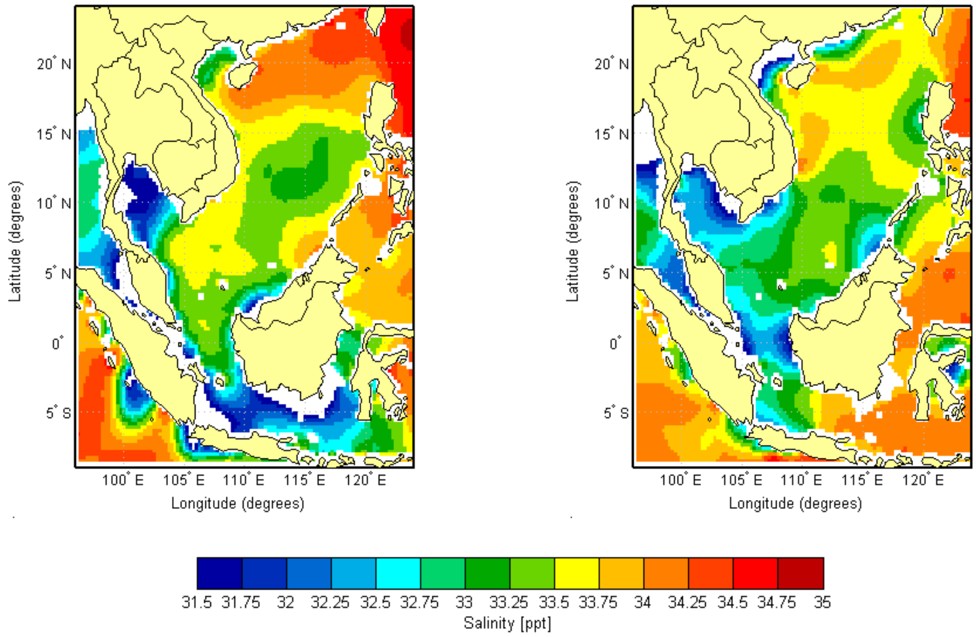

Figure 2.13: Monthly-mean surface layer salinity for January (left) and August (right). Obtained from the World Ocean Atlas 2001.

Tonking the surface layer salinity is lower than that observed in the Taiwan Strait region. This lower salinity may be explained by fresh water intrusions from the Pearl River near Hong Kong. This fresh water mixes with the water transported along the Chinese coastline and decreases its salinity.

Summarizing, the following explanation is given for the frontal temperature structure during the NE monsoon: First, the cold water north of front 2 intrudes into the SCS through Taiwan Strait. This cold water is transported along the Chinese and Vietnamese coastlines by western boundary currents. Subsequently, transport by the large-scale circulation system and large-scale mixing with the warmer North SCS water will attribute to cooling of the SCS water between front 1 and 2. Possibly, this mixing, and as such the cooling of the North SCS during the NE monsoon, is increased by a large-scale, annually reoccurring Rossby wave observed in this region. Below front 1, the temperature cycle is governed by the net heat flux mainly.

SW Monsoon SST

From figure 2.12 it is observed that when compared with the NE monsoon SST, the SCS temperature is more uniform during the SW monsoon. The frontal SST system observed during the NE monsoon has diminished completely and a SST between 28 and 32 degrees is observed over the entire SCS basin.

A characteristic feature observed during the SW monsoon period is the region of lower SST east of Vietnam. The shape of this region corresponds closely to that of the higher surface wind stress observed from figure 2.2. This can indicate that either a lower net surface heat flux or stronger vertical mixing by the higher wind speed attributes to this region of lower SST. This can be explained by the fact that at higher wind speeds the magnitude of both the evaporative and convective out flux will increase (see appendix C), resulting in a lower net surface flux. Furthermore, a higher wind speed will result in stronger vertical mixing and a deepening of the mixed-layer. This in turn results in upwelling of sub-mixed layer water and a lower mixed layer temperature.

Furthermore, from figure 2.13 a strong decrease in surface layer salinity can be observed southeast of Vietnam. This may be explained in part by fresh water influx from the Mekong river. Also, the prevailing current system during the SW monsoon can attribute to this. From figure 2.4 a strong current originating from the southern regions of the Sunda Shelf is observed during this period. This current may transport lower salinity water from the southern regions of the SCS and deflects to the northeast near Vietnam, which might explain the observed decrease in salinity in this region. This current may also cause upwelling of sub-surface water against the Vietnamese coastline, were a decrease in depth can be observed from appendix G.2. This may be supported by the standard deviation from the DUACS SSA climatology, shown in appendix H.6. A significant standard deviation from the monthly-mean is observed south of Vietnam during the SW monsoon (between 15 and 20 centimeters). This may be explained by water level changes attributed to effects of upwelling. This upwelling may also attribute to a decrease in surface-layer water temperature in this region. This colder water can subsequently be transported northeast by the prevailing current system.

Based on the above explanations the lower temperature east of Vietnam is attributed to processes on seasonal scales (wind forcing and basin-scale circulation) and to bathymetry constraints. As observed from appendix G.2 a decrease in depth of over 50 meters is observed south of Vietnam (with respect to a depth of 100 meters). Along the eastern Vietnamese coastline this decrease occurs over a horizontal span smaller than 100 kilometers.

Also, a region of lower SST is observed east of Taiwan. This may be attributed primarily to influx of colder water through Taiwan Strait, which mixes with the warmer SCS water. This can be observed from the SST fields in figure 2.10.

Summarizing, the surface layer temperature is more uniform during the SW monsoon. This is attributed to lower wind speeds and to the prevailing SW wind direction. As such, the dynamic processes governing the surface layer temperature during the NE monsoon will play no (significant) role during this period. The surface heat flux will cause a increase in SST during this period.

2.5.2 Seasonal surface heat flux

According to [Qu, 2001], the net surface heat flux shows a seasonal cycle over the SCS basin, with extremes during the intermediate periods between the NE and SW monsoons. During this period a significant positive influx is observed. During the monsoon period the net surface flux reduces to near zero, or a net outflux is observed.

Figure 2.14 shows the monthly-mean, area averaged surface heat flux (note that the plus and minus signs indicate the direction of the flux. Plus indicates influx, minus indicated outflux). This data is obtained from a 13 year climatology of ECMWF ERA-40 data (see chapter 4), area averaged over 100°E - 120°E, 5°S - 25°N. In appendix C it is explained that the net surface heat flux is the result of a number of physical processes at the ocean-atmosphere interface. These are the net influx of solar radiation (net shortwave flux), the effective long wave back radiation (longwave flux), heat exchange due to convection (convective heat flux) and heat exchange due to evaporation (evaporative flux). These individual components are included in figure 2.14. The magnitude of these components is governed by both the atmospheric state (air temperature, cloud coverage, relative humidity and wind speed) and by the state of the sea surface (surface temperature). The net balance between all components results in a net in- or outflux.

From this figure it is observed that the net shortwave flux has the most significant impact on the heat flux balance, with a mean magnitude between 150 and 250 W/m^2. This is followed by the evaporative flux, which is an order of magnitude smaller, between 100 and 150 W/m^2. Both the net shortwave flux and the evaporative flux have a distinguishable seasonal pattern, confirming conclusions by [Qu, 2001].

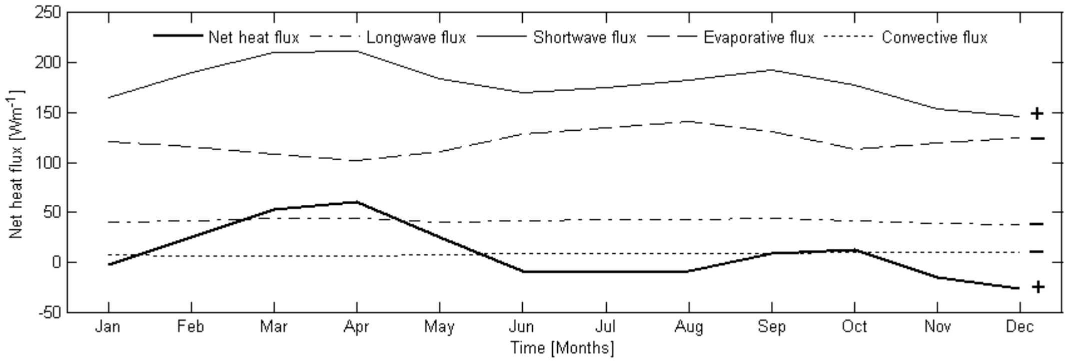

Figure 2.14: Monthly-Mean surface heat flux components: shortwave, longwave, convective, evaporative and net heat flux. Obtained from ECMWF ERA-40 monthly heat flux data, temporally averaged over 1983-2001 and spatially averaged over 100°E - 120°E, 5°S - 25°N.

In case of the net shortwave flux this can be explained by the combined cycles of the shortwave flux and the cloud coverage. This can be observed from figure 2.15, which shows the monthly-mean shortwave, cloud coverage and net shortwave cycles. For comparison all series are normalized with respect to their standard deviation. From this figure it is observed that the shortwave flux has an annual cycle with a maximum during the summer period and a minimum during the winter period. Furthermore, minimum cloud coverage is observed between February and April. From May till November cloud coverage is significantly higher. If this cycle is imposed on the shortwave flux cycle, a maximum net shortwave flux is observed during the period from February and April. Subsequently, by the high cloud coverage during the summer period the net shortwave flux decreases significantly. Finally, in chapter 6 an annual-mean cloud coverage of 74.8 % is observed over the SCS from ECMWF ERA-40 data. In the South SCS the coverage is higher than in the North SCS, however (80 % versus 70 %).

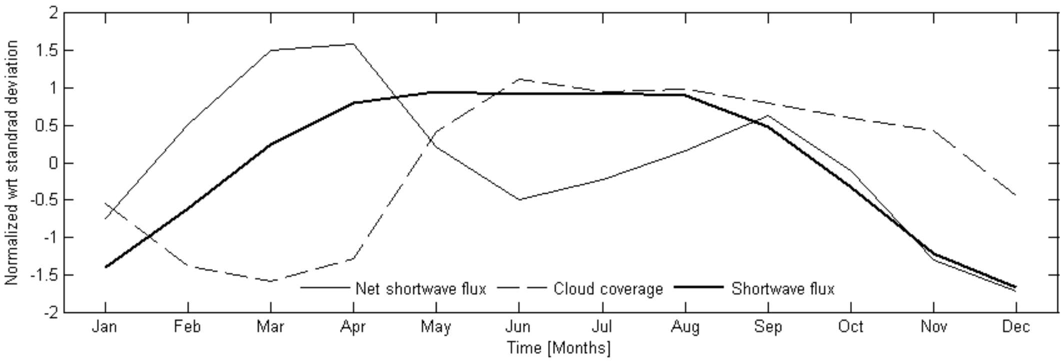

Figure 2.15: Monthly-mean shortwave flux, net shortwave flux and cloud coverage. Obtained from ECMWF ERA-40 monthly heat flux data, temporally averaged over 1983-2001 and spatially averaged over 100°E - 120°E, 5°S - 25°N. For comparison, each series is normalized with respect to its standard deviation.

In case of the evaporative flux the seasonal pattern can be explained by the relation with the wind magnitude (see appendix C). At high wind speeds, the magnitude of the evaporative flux will increase. At low wind speeds it will decrease. By comparing the evaporative flux cycle with the mean wind magnitude cycle shown in figure 2.3 it is observed that the evaporative flux follows a similar cycle: during the NE and SW monsoon maximums are observed. In the transition period between the monsoons minimum values are observed.

Furthermore, figure 2.14 shows that the (net) longwave flux is an order of magnitude smaller than the evaporative flux. It has a mean magnitude around 50 W/m^2, and no significant seasonal variation. Smallest is the convective heat flux. This component has a mean magnitude around 10 W/m^2 and no significant seasonal variation.

Combined, these components attribute to the net heat flux cycle observed from figure 2.14. This cycle has its maximums in transition periods between the monsoons. This is explained by the combined effect of a lower cloud coverage and a lower wind magnitude in these period, resulting in a large shortwave influx and a small evaporative outflux. During the monsoon periods minimums are observed. This is attributed to the combined effects of increased cloud coverage, increased wind magnitude and the annual shortwave flux cycle. From the monthly SST fields in appendix G.7 and G.8 the effect of this increased net surface flux can be observed from the June and October SST fields, where higher SST values are observed. This is most noticeable in those regions close to the equator. This annual cycle confirms conclusions by [Qu, 2001].

As explained above the net heat flux cycle will follow a seasonal temporal cycle, attributed to the seasonal cloud coverage, wind magnitude and shortwave flux cycles. In case of the shortwave flux, variations will be latitude dependent (due to latitude dependent differences in the solar elevation angle, see appendix C). For the monsoon wind, these variations are described in section 2.2. For the cloud coverage, large-scale spatial variations are observed between the North and South SCS.

2.5.3 Seasonal stratification

According to literature, there is a strong correlation between the SCS Sea Surface Temperature (SST) and the mixed layer depth [Qu, 2001]. An increase in temperature results in a decrease in mixed layer depth, and vise versa. This occurs on a seasonal time-scale, related to the monsoon [Wang *et al.* , 2004]. The thermocline follows a similar seasonal signal.

Furthermore, [Qu, 2001] reports that a maximum thermocline depth of 120 meters is observed in the central SCS basin. Here, continuous stratification is observed. In the shallow SCS regions over the Sunda Shelf and the China Continental Shelf stratification breaks down on a seasonal basis, following the seasonal cycle of the surface heat flux and the monsoon winds. Also, in the deep SCS following the the China Continental Shelf and Oceanic Plate interface only weak stratification is observed during the NE monsoon period. During the SW monsoon this stratification increases in intensity.

Figure 2.16 shows the annual-mean thermocline depth (left panel) and the bandwidth between the annual minimum and maximum thermocline depth (right panel). These values are determined from the maximum temperature gradient in monthly-mean World Ocean Atlas 2001 temperature profiles (see chapter 4). In this process a minimum bound of 0.05 $°\mathrm{Cm}^{-1}$ is specified. If no solution is found above this value it is assumed that the water column is well mixed. This process is repeated for all months. The mean thermocline depth is subsequently determined as the average of all values. The bandwidth around this mean value is defined as the difference between the minimum and maximum thermocline depths found. As such, this bandwidth defines the maximum seasonal thermocline variation.

From figure 2.16 a mean thermocline depth between 50 and 80 meters is observed in the central SCS. In the southern part of the deep SCS basin a mean value between 70 and 80 meters is observed. Here, a maximum seasonal variation between 20 and 40 meters is observed. In the northern part of the deep SCS basin the mean thermocline depth is lower, between 50 and 70 meters. The seasonal variation is larger, though, and ranges between 40 and 80 meters. Assuming a normal distribution of the observed bandwidth around the mean value, a maximum thermocline

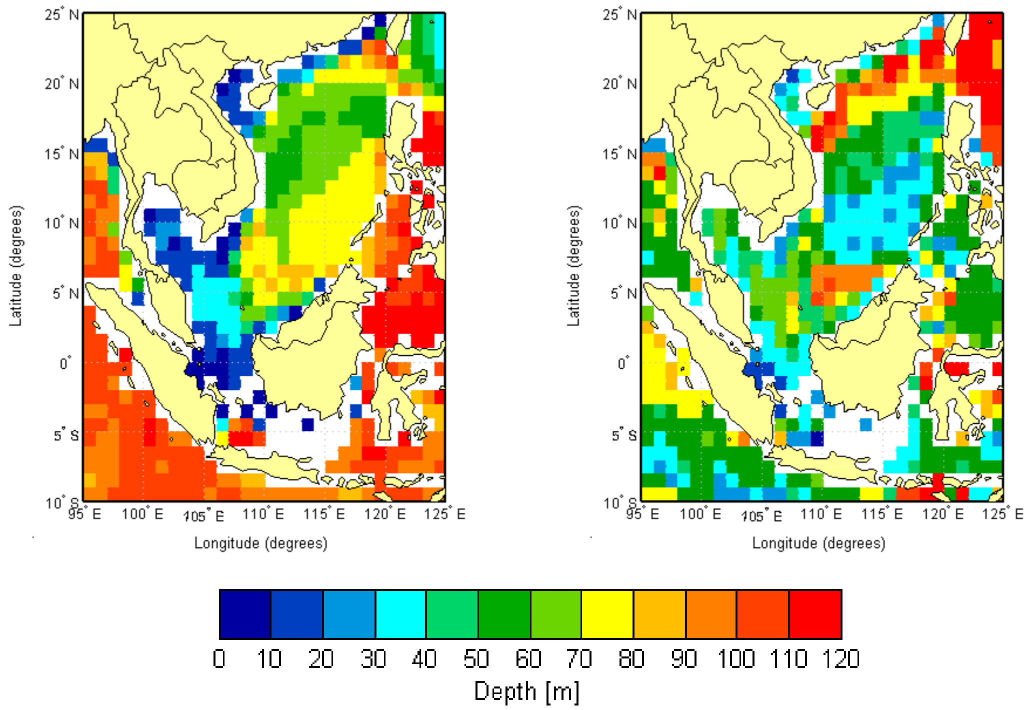

Figure 2.16: Annual mean thermocline depth (left) and bandwidth between minimum and maximum thermocline depth (right). Determined from the maximum temperature gradient of World Ocean Atlas 2001 monthly-mean temperature data, and specifying a minimum gradient of 0.05 $^{\circ}\mathrm{Cm}^{-1}$.

depth between 100 and 120 meters is observed in the central SCS. This confirms observations by [Qu, 2001].

Furthermore, in the shallow SCS regions over the Sunda Shelf a mean thermocline depth between 0 and 40 meters is observed. Subsequently, a seasonal amplitude between 30 and 70 meters is seen. When compared with the mean values this leads to the conclusion that the stratification breaks down during a part of the year. Similar values are observed and conclusions are drawn over the China Continental Shelf. This, again, confirms conclusions by [Qu, 2001].

Finally, in the deep SCS following the China Continental Shelf and Oceanic Plate interface a mean thermocline depth between 60 and 90 meters is observed. Here, a substantial seasonal amplitude is observed, between 70 and 120 meters. Compared with the mean values this leads to the conclusion that the flow is strongly stratified during one period of the year, and weakly stratified during another. In the first case, the thermocline depth is expected closer to the surface. In the second case, the maximum thermal gradient is found at larger depths. This corresponds with conclusions by [Qu, 2001].

To assess the seasonal thermocline variability observed above, figure 2.17 shows the monthly-mean net heat flux (upper panel, see section 2.5.2), wind magnitude (middle panel, see section 2.2) and thermocline depth (lower panel), area averaged over the deep SCS basin.

In section 2.2 the seasonal cycle of the monsoon wind system was discussed. The seasonal cycle of the net surface flux was discussed in section 2.5.2. From figure 2.17 it is observed that the minimum thermocline depth occurs when the maximum net heat flux and minimum wind velocities occur during the NE / SW monsoon transition period. This can be explained by the fact that at lower wind velocities the vertical mixing will decrease. Because of this, water heated by the increased surface flux will remain trapped in the upper water layer. Due to the significant rise in temperature

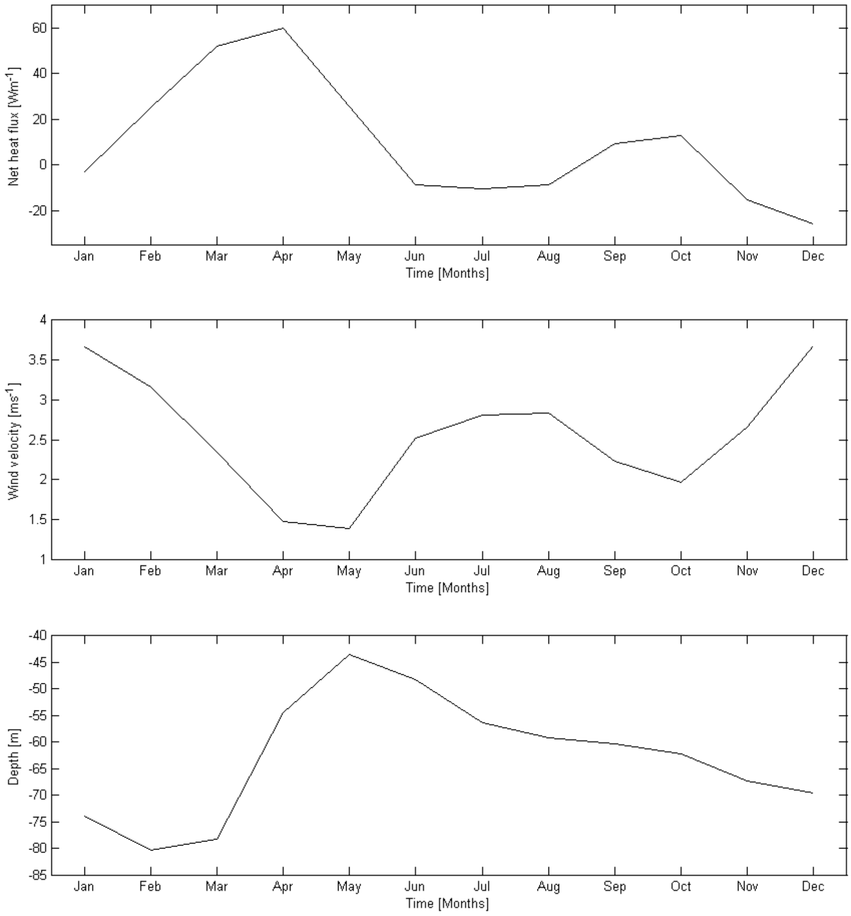

Figure 2.17: Monthly-mean net heat flux (upper panel), wind velocity (middle panel) and thermocline depth (lower panel) over deep SCS basin. Heat flux and wind data obtained from a 13 year climatology of ECMWF ERA-40 data, thermocline data obtained from the World Ocean Atlas 2001.

this will result in strong stratification. During the SW monsoon, the wind magnitude will increase and the net heat flux will decrease. This results in a deepening of the thermocline.

Note that during the SW / NE monsoon transition period the thermocline depth increases , while the wind velocity decreases in magnitude and the surface flux increases. Based on this, a decrease in thermocline depth would be expected. A tentative explanation about this phenomenon is based on the Rossby wave observed in the North SCS (see section 2.3). From August onwards this wave may attribute to surface convergence, downwelling and a deeper thermocline. If this effect is imposed on the wind and heat flux dependent thermocline cycle, the unexpected increase in thermocline depth in this period may be explained. During the NE monsoon the wind magnitude will reach it peak and the heat flux will be smallest. This will result in a further increase in thermocline depth. Furthermore, from January onwards the observed Rossby wave may cause surface divergence, upwelling and a shallower thermocline. As such, the mixed layer will respond to the increase in net heat flux and decreased wind speed faster during the March / April period, completing the seasonal cycle.

Based on this explanation the thermocline depth in the central SCS, and as such also the mixed layer temperature, will depend on the net heat flux, monsoon wind and possibly on mixing induced by the Rossby wave cycle. It will have the same characteristic scales as these processes. Also, the described Rossby wave attributes to variability in the North SCS only. As such, in the South SCS this process will not play a role in the seasonal heat flux cycle, which is governed by the wind magnitude and net heat flux only. This may explain the smaller seasonal amplitude observed in this region.

In the North SCS, following the China Continental Shelf and Oceanic Plate interface, the observed thermocline variability may be partially explained by large-scale cold water transport along the China Continental Shelf and by upwelling against the China Continental Shelf during the NE monsoon (see section 2.5.1). This will attribute to a lower temperature in the upper water layers, and as such a weaker stratification. During the SW monsoon these processes do not play a significant role and the increased heat flux will cause an increase in water temperature and a stronger stratification. This can explain the significant seasonal thermocline amplitude observed in this region.

In the shallow SCS regions over the Sunda Shelf the seasonal stratification is explained by the combined cycle of the net surface flux and wind magnitude. During the monsoon transition periods the increased surface flux and decreased wind magnitude will result in a stratified system. Due to the shallow depth in this region the thermocline will be shallow compared to the depth in the central SCS. During the monsoon periods this stratified system breaks down because of the increased wind magnitude, which causes mixing over the entire water column. This effect is more significant during the NE monsoon because of the higher wind velocities during this period.

Finally, in the shallow regions over the China Continental Shelf seasonal stratification can be explained by the combined effects of the net surface heat flux and horizontal temperature transport by a cold water boundary current originating from the Taiwan Strait. During the SW monsoon a stratified system is observed which can be attributed to the increase in water temperature by the net heat flux. During the NE monsoon this stratified system breaks down rapidly and a significant decrease in water temperature is observed. This temperature is uniform over the entire water column. This can be explained by the cold water transported along the Chinese coastline from the Taiwan Strait.

2.5.4 Vertical temperature transport

According to [Chu *et al.* , 2002] seasonal temperature variability is limited to the upper 300 m of the deep SCS basin. In figure 2.18, the monthly-mean temperature gradient is shown at a number of depth levels. These values are determined from monthly-mean World Ocean Atlas 2001 temperature profiles (see chapter 4).

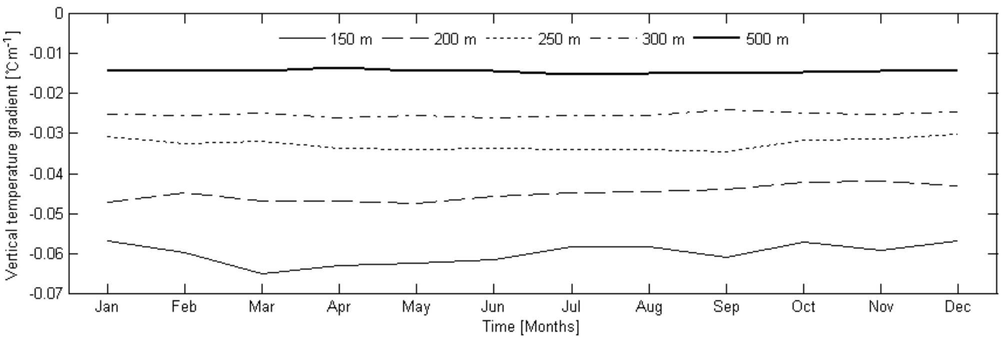

Figure 2.18: Monthly-mean vertical temperature gradient at 150 , 200, 250 , 300 and 500 meters depth, area-averaged over 110°E - 120°E, 10°N - 20°N. Data obtained from the World Ocean Atlas 2001.

From figure 2.18 seasonal temperature variability is observed at 150 meters depth. At 200 and 250 meters depth this variability is significantly less, though some variation is observed. At both 300 and 500 meters depth no significant variability is observed, indicating conditions are more or less constant throughout the year. This confirms measurement observations by [Chu *et al.* , 2002].

Furthermore, it is observed that the magnitude of the temperature gradient decreases with depth. At 150 meters the gradient is an order of magnitude larger than at 300 meters (approximately 0.06 $^{\circ}\mathrm{Cm}^{-1}$ versus 0.02 $^{\circ}\mathrm{Cm}^{-1}$). At 500 meters depth the gradient is again an order of magnitude smaller than at 300 meters depth (approximately 0.02 $^{\circ}\mathrm{Cm}^{-1}$ versus 0.01 $^{\circ}\mathrm{Cm}^{-1}$).

Chapter 3

Statistical analysis of SCS surface temperature

In this chapter the South China Sea (SCS) Sea Surface Temperature (SST) is analyzed using a statistical analysis method. This method, the so-called Empirical Orthogonal Function (EOF) analysis, analyzes the variability of a single field, and tries to find spatial patterns of variability, their time variation, and gives a measure of the 'importance' of each pattern [Bjornsson & Venegas, 1997]. These patterns can give insight in the dynamical behavior of a system. In this chapter it will be used to study seasonal, basin-scale SST dynamics. Together with the analysis of the project area in chapter 2, this assessment is used to identify the focal point of the temperature modeling effort during this project.

Background information on the EOF method is provided in section 3.1. Subsequently, a description on the data used for this method is given in section 3.2. Furthermore, it should be noted that while the EOF method breaks the data into 'modes of variability', these modes are data modes, and not necessarily physical modes. Whether they are physical will be a matter of subjective interpretation. As such, a comparison between the primary SST modes found and other (independent) data fields will be made in order to provide a physical interpretation of these modes. The results of this comparison are discussed in section 3.3.

3.1 EOF concept

The EOF method takes all the variability in a time evolving field, represented by data matrix F, and calculates the eigenvectors describing the maximum direction in the covariance matrix of F. Each of these eigenvectors (each EOF) is referred to as a mode of variability. Each of these modes has an associated series of expansion coefficients (called Principal Components (PC)) describing how they vary in time. Mathematically, this is described by:

$$F = \sum_{i=1}^{N} \vec{a}_i (EOF_i) \tag{3.1}$$

where F is the data matrix of time series and observations to analyze and $\vec{a}_i$ is the Principal Component (PC) time series for the eigenvector EOF_i.

Figure 3.1 shows a graphical representation of data matrix F. In this matrix each row contains all locations in the field (or map) assessed. Each column contains the time series of observations at each of these locations. F has size (number of observations (n), number of location (p)).

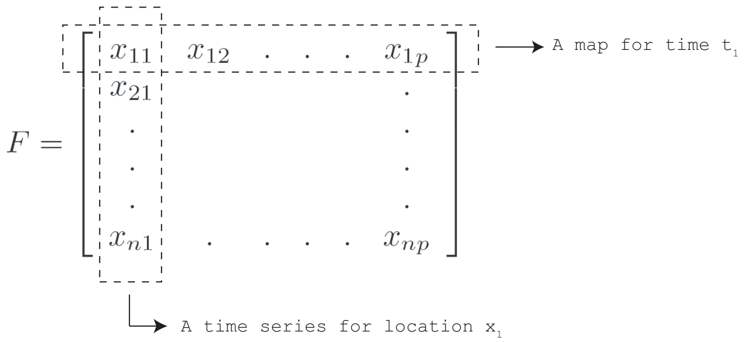

Figure 3.1: Schematization of data matrix F. Each row represents one map, and each column a time series of observations for a given location [Bjornsson & Venegas, 1997].

The system described by equation 3.1 is calculated by solving the eigenvalue problem for the covariance matrix of F. To form this covariance matrix, data matrix F is detrended (F_d) by removing the time average at each location:

$$F_d = \sum_{x=1}^{p}\sum_{t=1}^{n}(x_{np} - \frac{1}{n}\sum_{t=1}^{n} x_{np}) \tag{3.2}$$

Subsequently, the place dependent covariance matrix R is formed by:

$$R = F_d^T F_d \tag{3.3}$$

For covariance matrix R the eigenvalue problem is described by:

$$RC = C\Lambda \tag{3.4}$$

where Λ is a diagonal matrix containing the eigenvalues λ_i of R. The c_i column vectors of C are the eigenvectors of R corresponding to the eigenvalues λ_i. For each eigenvalue λ_i a corresponding eigenvector c_i is found.

Since the covariance matrix R is symmetric the eigenvalues and eigenvectors decompose R according to:

$$R = \lambda_1 c_1 c_1^t + \lambda_2 c_2 c_2^t + ... + \lambda_N c_N c_N^t \tag{3.5}$$

Based on this decomposition the variance of the system is given by a number (N) of uncoupled modes, of which often the first few dominate the others. The relative importance of, or 'amount of variance explained' by, each mode can be specified by the relative magnitude of the corresponding eigenvalue:

$$variance\,explained\,by\,mode\,i = \frac{\lambda_i}{\sum_{i=1}^{N}\lambda_i} \tag{3.6}$$

Finally, the PC describing the time evolution of mode i is obtained by projecting the detrended data matrix F_d onto the i-th EOF.

$$\vec{a}_i = F_d \times c_i \tag{3.7}$$

3.2 EOF data acquisition

In order to model temperature for the SCS, it is important to have a good understanding of the dynamical processes governing its temperature variability. While these processes have a significant vertical component, surface variability provides good insight into their origin. This is because the sea surface is the interface for coupled atmosphere-ocean dynamic processes, and these processes govern water temperature to a large degree. As such, the EOF method will be applied to SST fields. A substantial amount of SST data is available from both climatological and remote-sensing datasets (see appendix H.1 for an overview of data used during this project). A choice on SST data to use for this analysis is based on a number of issues:

- Temporal resolution: the primary goal of this project is to model seasonal, basin-scale temperature processes (see chapter 1). As such, the primary goal of the EOF analysis is to find the leading modes on these scales also, and the SST fields used should thus have a sufficiently high temporal resolution to show seasonal varying patterns.
- Spatial resolution: in the EOF method, the eigenvalue problem is solved for a full, symmetric matrix. A high spatial resolution will result in a large data matrix and an increase in processing time. This limits the maximum spatial resolution if the method is to be applied to the entire SCS domain.

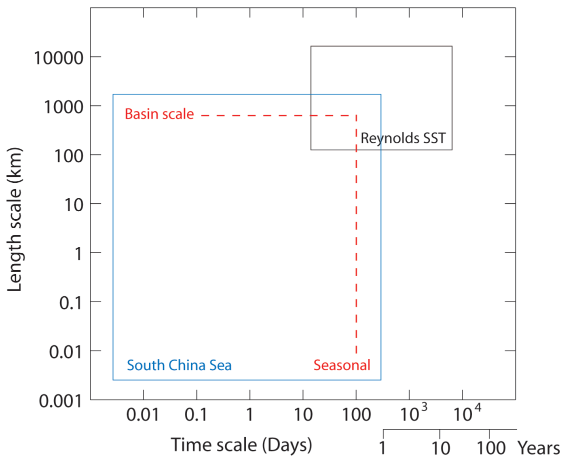

Figure 3.2: Spatial and temporal scales of monthly Reynolds SST data compared with the South China Sea scales.

Based on these reasons, the EOF analysis is performed on a climatological year of monthly SST fields from the Reynolds OI SST (Reynolds) dataset (see chapter 5). This climatology is obtained by averaging 23 years of monthly Reynolds SST data. In figure 3.2 the spatial and temporal scales of this dataset are shown graphically. Also, the SCS scales are included in this figure. From this it is observed that the sampling capability of the Reynolds SST data is sufficient to resolve basin-scale and seasonal temperature processes.

3.3 Results EOF analysis

The EOF method described in the previous section is applied to a climatological year of Reynolds SST data covering the entire SCS domain (95°E - 125°E, 5°S - 25°N). The data matrix F, discussed in the previous section, is constructed by arranging all non-land points in this domain sequentially in one row. This is repeated for each month.

The primary EOF modes found from this data matrix are summarized in table 3.1.

Mode	Variance (%)
1	67.5
2	30.5

Table 3.1: Primary modes obtained from EOF analysis on South China Sea Reynolds Sea Surface Temperature data

From table 3.1 it is observed that mode 1 and 2 together describe over 98% of the total SST variability found in the Reynolds data. Also, the contribution of mode 2 on the total variance is non-negligible.

According to [Bjornsson & Venegas, 1997], the EOF analysis can provide different solutions if the shape of the domain assessed is changed, or if this domain is split into several sub-domains. If this domain shape dependency occurs, the EOF decomposition is not robust. To test for this, the decomposition was performed on sub-domains of the SCS. Also, the location entries in the data matrix were changed to assess effects of domain shape. Both these tests provided similar results as those found during the initial analysis, indicating the decomposition is robust.

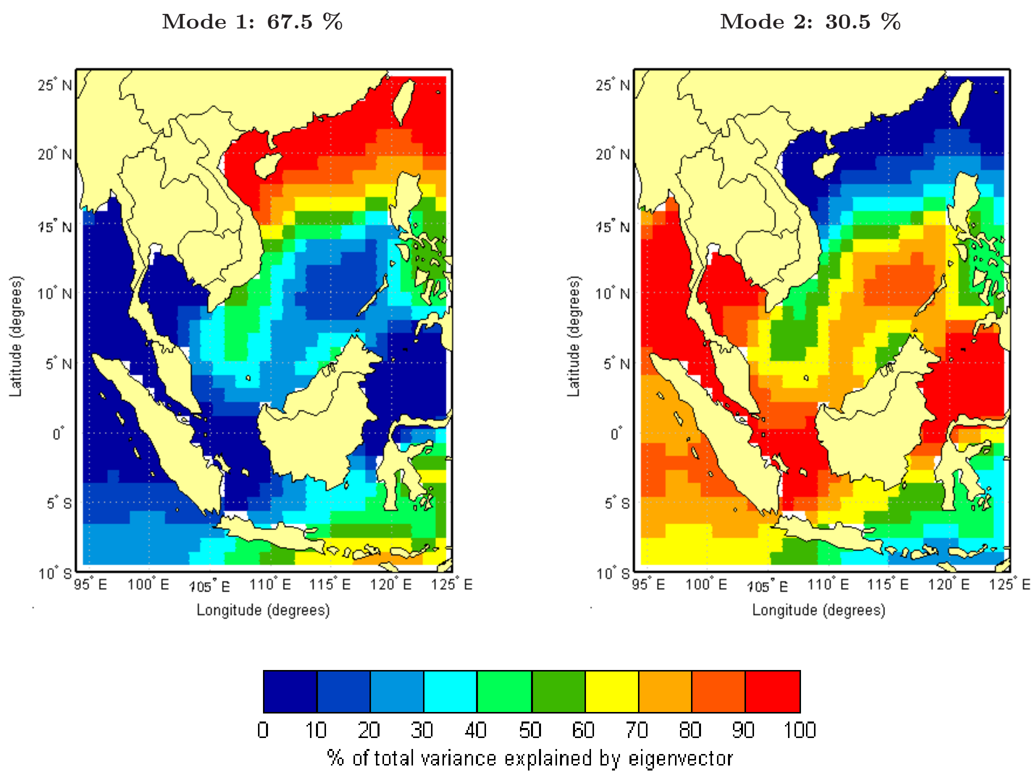

Figure 3.3: Percentage of signal variance explained by primary eigenvectors. Determined from an EOF analysis of monthly-mean Reynolds Sea Surface Temperature data.

The spatial patterns associated with the two primary SST modes are shown in figure 3.3. The temporal variation of these eigenvectors, represented by the expansion coefficients PC1 and PC2, is shown in figure 3.4. From figure 3.3 it is observed that mode 1 explains most of the variance in the region from Luzon Strait following the Chinese and Vietnamese coast. Subsequently, from figure 3.4 it is seen that this mode has a one year period, with extremes around January and July. From figure 3.3 it is observed that mode 2 explains most of the variance in the South SCS. From 3.4 it is observed that this mode is less periodic than mode 1. Maximum values occur around May and October, roughly the transition period between both monsoons.

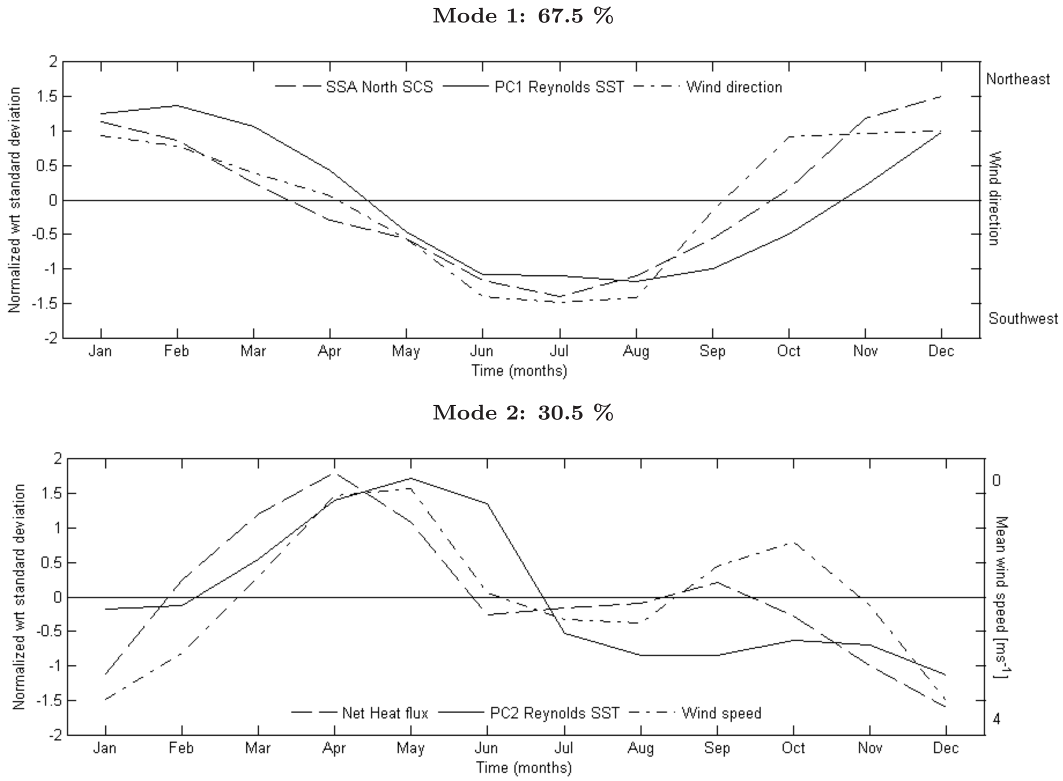

Figure 3.4: Principle components of primary modes, compared with sea surface anomaly data from the DUACS dataset, and net heat flux and wind data from the ECMWF ERA-40 archive.

In chapter 2 a description of the physical processes governing the seasonal SCS temperature cycle was given. To assess the physical significance of the data modes identified in this chapter, these are compared with the results from that chapter. To elaborate this comparison, the time evolution of the principle components is compared with Sea Surface Anomaly (SSA) data from the DUACS archive (see chapter 5) and net heat flux, wind direction and wind magnitude data from the ECMWF ERA-40 archive (see chapter 4). The wind direction is defined by projecting the wind vector on the NE monsoon wind direction (φ_w=225°) by θ_{NE}^m=cos(225 - φ_w^m), where θ_{NE}^m represents the projected wind direction, φ_w^m specifies the angle between the wind vector and the local North and m specifies the month number. The monthly mean time evolution of these quantities was determined for specific sub-domains of the SCS. These sub-domains were defined based on the regions of maximum variance explained by the eigenvectors, and are shown in figure 3.5.

The temporal variation of the ECMWF data was determined by averaging over the specified domain. The temporal variation of the SSA data was determined by an EOF analysis, in a similar way as described above for the Reynolds SST data. The principle component of the primary mode, which describes 80 % of the signal variance, is included in figure 3.4. Also, the temporal variation

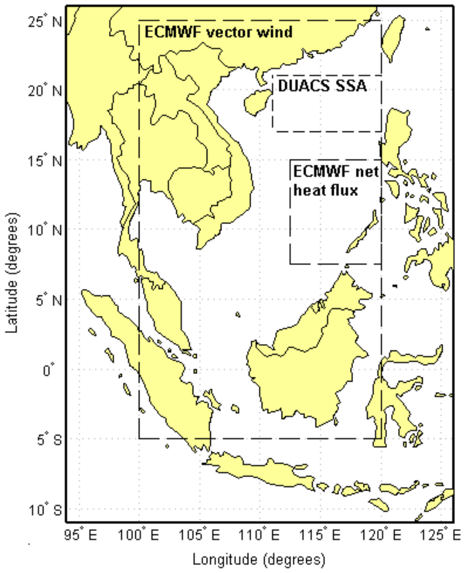

Figure 3.5: Domains used to average data from the ECMWF ERA-40 archive and the DUACS dataset, used for comparison with EOF modes.

of the ECMWF data is included in this figure. For comparison, all time series are normalized with respect to their standard deviation.

By comparing the time variation and location of mode 1 with results from chapter 2, it is observed that the location of mode 1 corresponds closely to that of the cold water fronts in the North SCS and along the Vietnamese coastline, observed from SST images during the NE monsoon (see figure 2.12). In chapter 2 these cold water fronts are explained by cold water influx into the SCS through Taiwan Strait. This cold water is transported along the Chinese and Vietnamese coastlines by boundary currents. Large-scale mixing at the China Continental Shelf / Oceanic Plate interface and transport by the large-scale circulation system will subsequently cool the North SCS temperature during the NE monsoon period. Possibly, this mixing and cooling is increased by an annually re-occurring Rossby wave observed in the North SCS. These dynamic processes (the cold water influx through Taiwan Strait, boundary currents and Rossby waves) follow an annual cycle related to the monsoon wind direction.

From the time series in figure 3.4 it is observed that the temporal cycle of mode 1 follows a similar annual cycle as the monsoon wind direction. The boundary currents described above can be explained by water level 'tilting' related to the monsoon direction, explaining the one year period of these currents (see section 2.3). A similar temporal relation is observed with the SSA in the assessed region. This annual SSA cycle might be explained by water level convergence and divergence attributed to the above mentioned Rossby wave (see section 2.3). From this it is concluded that the seasonal temperature cycle in the North SCS can be related to the boundary currents. Also, it can be related to the Rossby wave observed in the North SCS. These processes may explain the large-scale transport and mixing of cold water entering the SCS through Taiwan Strait during the NE monsoon. In the region indicated by mode 1 this will result in seasonal SST variability between 6°C and 8°C.

In chapter 2, the seasonal SST cycle in South SCS is explained by the seasonal cycle of both the net heat flux and the monsoon wind magnitude. The seasonal heat flux cycle is in turn explained by the net effect of the annual shortwave (solar) heat flux cycle, the seasonal cloud coverage cycle and the monsoon wind magnitude. The last modulates the seasonal evaporative flux cycle. Furthermore, the wind magnitude cycle plays an important role in the thermal stratification in this region. During the intermediate periods between the monsoons, the increased heat flux and the low wind magnitude will attribute to stratification of the water column. During both the NE and SW monsoon increased wind velocities will cause stronger vertical mixing and a breakdown of this stratified system, resulting in a decrease in surface layer temperature.

From the time series in figure 3.4 it is observed that mode 2 follows the same temporal cycle as both the net heat flux and the wind magnitude. This confirms the temporal relations described above and provides an explanation for the seasonal SST cycle in the regions governed by mode 2. Based on this it is concluded that the SST cycle in the South SCS can be explained by the annual shortwave heat flux, cloud coverage and wind magnitude cycles. Here, the wind magnitude modulates both the seasonal heat outflux and stratification of the water column. The combined effect of these processes attributes to a seasonal SST variability between 2°C and 4°C in the South SCS.

Summarizing, based on the results of this EOF analysis the SST in the North SCS and along the Vietnamese coastline follows an annual cycle, modulated by the monsoon wind direction. This cycle, and its spatial extent, is explained by boundary current dynamics and cold water influx through Taiwan Strait. Possibly, an annually reoccurring Rossby wave observed from altimeter SSA data increases mixing of this cold water into the North SCS basin. These processes attribute to a seasonal SST variability between 6°C and 8°C in the North SCS. In the South SCS the SST follows a seasonal cycle which is modulated by the monsoon wind magnitude and the net heat flux, which in turn is modulated by the annual shortwave flux, seasonal cloud coverage and seasonal wind magnitude cycles. These processes result in a seasonal SST variability between 2°C and 4°C in the South SCS.

Finally, based on the above results it is concluded that the EOF method is suitable to assess dynamic, large-scale temperature processes for the SCS. Note, however, that a thorough assessment and comparison with independent data is required to provide a physical interpretation of the statistical data modes found.

PART II: Data acquisition and assessment

A wide range of datasets were acquired and processed for this project (see appendix H.1 for an overview). These datasets can be subdivided into a number of categories:

1. Climatological atlases containing temperature and salinity data (the World Ocean Atlas 2001). These atlases describe long-term mean behavior and are obtained by interpolating available in-situ data to a fixed grid.
2. In-situ temperature and salinity measurements (the ASIAEX and SCSMEX datasets).
3. Relevant meteorological data from numerical weather prediction datasets (the ECMWF ERA-40, NCEP/NCAR Reanalysis and COADS datasets).
4. Altimeter data from the DUACS dataset (Sea Surface Anomaly, Absolute Dynamic Topography and geostrophic circulation data).
5. Sea Surface Temperature (SST) data from the AVHRR Pathfinder and Reynolds OI SST datasets.

In this part of the report the acquired datasets are described:

- Chapter 4 describes non-remote sensing datasets used (items 1 till 3).
- Chapter 5 describes remote sensing datasets used (items 4 and 5). For these datasets more background information on measurement methodology will be provided.

Furthermore, data from these different datasets is compared in chapter 6. Based on this comparison and on dataset properties as discussed in chapter 4 and 5, choices will be made on model forcing and validation data and on the modeling period.

Due to the small amount of long-term SCS in-situ data obtained for this project, little non-climatological data is available to validate the models vertical temperature distribution and stratification. To solve this, two approaches are assessed:

1. Climatological temperature profiles will be used for historical model validation. The project goal is to model large-scale, long-term temperature processes, and these are resolved well for the SCS by the climatological data.

2. A method described by [Nardelli & Santoleri, 2004] is used to construct synthetic temperature profiles. This method uses information about the water column contained in surface RS observations (SST and SSA) to 'update' climatological temperature profiles. These synthetic profiles are reported to give a more accurate estimate historical temperature values. This method is assessed in chapter 7.

Chapter 4

Data acquisition: non-remote sensing data

In this chapter an overview of acquired non-remote sensing (RS) datasets is given and some of their features are discussed. These non-RS datasets can be categorized under hydrological, in-situ and meteorological datasets, and will be described per category in this chapter.

In appendix H.1 an overview of dataset properties as discussed in this chapter is provided. Also, appendix H.2 gives an overview on the different dataset applications in this project.

Finally, in chapter 6 both the non-RS datasets discussed in this chapter and the RS datasets discussed in chapter 5 will be assessed for inter-dataset consistency.

4.1 Hydrological data: World Ocean Atlas 2001

The World Ocean Atlas 2001 (WOA01) is a climatological dataset containing global data statistics of several commonly measured oceanic variables at standard depth levels and on a fixed, equidistant grid. These fields have been derived from in-situ measurement data contained in the World Ocean Database 2001 (WOD01). This data is interpolated in both space and time to determine gridded climatological fields at annual, seasonal and monthly compositing periods [Conkright *et al.* , 2002]. Table 4.1 gives an overview of the data contained in the WOA01.

World Ocean Atlas 2001	
Spatial resolution (horizontal)	1 degree - 5 degrees
Depth levels (vertical)	33 (0 - 5500 m) (non-equidistant)
Temporal resolution	Annual, seasonal, monthly
Variables	Temperature, salinity, dissolved oxygen, apparent oxygen utilization, percent oxygen saturation, phosphate, nitrate, silicate, chlorophyll, plankton
Data statistics	Number of observations, analyzed mean, unanalyzed mean, standard deviation, standard error, grid points

Table 4.1: Overview of World Ocean Atlas 2001 dataset properties [Conkright *et al.* , 2002].

The WOA01 and WOD01 are the most recent in a series of World Ocean Atlas and World Ocean Database products. In addition to the 1 degree WOA01 dataset, 1/4 degree climatological fields were derived from the WOD01 by [Boyer *et al.* , 2004]. While this dataset is formally not a part of the WOA01, it will also be referred to as WOA01 in this report. A summary of this dataset is given in table 4.2. The main advantage with regard to the 1 degree WOA01 is an improved spatial resolution. Disadvantages are that this dataset contains less variables and no additional data statistics next to the analyzed mean fields.

World Ocean Atlas 2001 - 1/4 degree	
Spatial resolution (horizontal)	1/4 degree
Depth levels (vertical)	33 (0 - 5500 m) (non-equidistant)
Temporal resolution	Annual, seasonal, monthly
Variables	Temperature, salinity
Data statistics	Analyzed mean

Table 4.2: Overview of World Ocean Atlas - 1/4 degree dataset properties [Boyer *et al.* , 2004].

Since temperature and salinity are the only transport variables taken into account during this project, the 1/4 degree WOA01 dataset will be used for the majority of WOA01 applications in this project. In some cases where the higher computational load when working with the 1/4 degree WOA01 dataset poses problems, or where the additional data statistics included with the WOA01 provide additional information, the 1 degree WOA01 is used.

4.2 In-situ data

4.2.1 Asian Seas International Acoustics Experiment

In-situ temperature and salinity data was obtained from the Asian Seas International Acoustic Experiment (ASIAEX) dataset. The main objective of the ASIAEX project was to study shallow-water acoustics, physical oceanography and the bottom and sub-bottom structure of the South and East China Sea [Denner *et al.* , 2000]. The SCS component of this project focused on the region between Dongsha Island and Taiwan at the continental shelf break (see appendix G.1). As part of the measurement program in-situ along-track ship measurements were made in this region (centered approximately at 21.8°N, 117.3°E) between the 24th of April and the 17th of May 2000. Data obtained from Tropical Marine and Science Institute (TMSI) consisted of these cruise measurements (which are only a subset of the total program). Figure 4.1 shows the trajectory of this cruise (the track originates from Taiwan).

Along the track shown in figure 4.1 measurements were made using a towed SeaSoar data acquisition vehicle equipped to make Conductivity/Temperature/Depth (CTD) measurements. This vehicle was undulated from the surface to over 300 meter depth while making continuous measurements.

The provided data consists of depth-, time-, and location tagged measurements. In order to process these for applications in the SAT2SEA2 project it is assumed that the measurements were made on a fixed location, while in reality a varying track was followed over the measurement domain. Also, daily and weekly averages per depth point are assumed to represent mean conditions. In this averaging procedure, measurements showing an exceptionally large deviation from the mean were discarded.

Based on these assumptions temperature and salinity measurements were averaged into daily and weekly-mean 300 meter profiles centered at 21.8°N, 117.3°E. Properties of these profiles are summarized in table 4.3. Due to the small coverage period, a total of 3 weekly and 22 daily profiles were obtained this way.

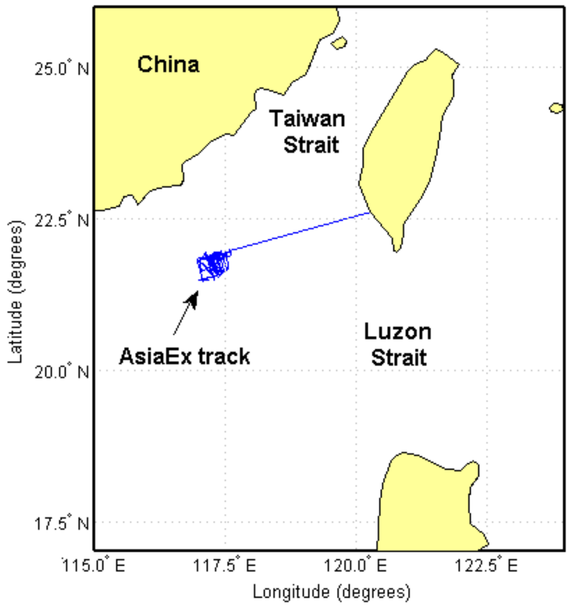

Figure 4.1: ASIAEX measurement track; along-track CTD measurements were made by a research vessel as part of the ASIAEX project.

Parameters used	Temperature, salinity
Period	24-4-2000 till 17-5-2000. 24 days of continuous measurements, averaged in 3 weekly or 22 daily profiles
Depth	0 - 300 m
Location	21.8°N, 117.3°E

Table 4.3: Overview of ASIAEX data used during the SAT2SEA2 project.

4.2.2 South China Sea Monsoon Experiment

In-situ temperature and salinity data was obtained from the South China Sea Monsoon Experiment (SCSMEX) dataset. The main goal of the SCSMEX was to study the water and energy cycles of the Asian monsoon regions in order to improve understanding of monsoon related processes [Lau, 1997]. Part of the project consisted of in-situ measurements using ATLAS mooring buoys in order to monitor the thermal gradient and vertical structure in the upper ocean and changes accompanying the onset of the Asian monsoon. These buoys were placed and maintained by the Tropical Ocean Array (TOA) group. This buoy measurement data is distribution by the National Oceanic and Atmospheric Administration (NOAA) Pacific Marine Environmental Laboratory (PMEL). Figure 4.2 shows the location of these buoys.

While all buoys were on location between the years 1997 and 2000, they measured only over subsets of this period. In appendix H.3 an overview of data availability per buoy is given. This consists of temperature, salinity and atmospheric data. While only temperature and salinity data will be used during this project, the atmospheric data has been added for completeness.

Table 4.4 gives a overview of this dataset. Note that the ATLAS buoys measure temperature and salinity continuously at specified depth points. For applications in this project, this data was averaged into daily means.

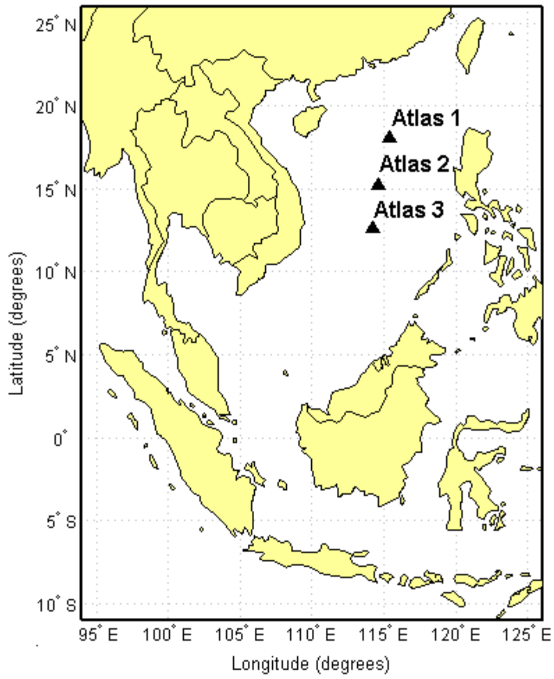

Figure 4.2: SCSMEX ATLAS mooring buoy locations.

Parameters used	Temperature, salinity
Period	1997 - 2000 (see appendix H.3)
Depth	0 - 500 m (non-equidistant)
Location	Atlas 1: 18.06°N - 115.36°E, Atlas 2: 15.21°N - 114.57°E, Atlas 3: 12.59°N - 114.25°E (see figure 4.2)

Table 4.4: Overview of SCSMEX ATLAS data used during the SAT2SEA2 project.

4.3 Meteorological data

4.3.1 ECMWF ERA-40 Archive

Meteorological data was obtained from the European Centre for Medium-Range Weather Forecast (ECMWF) ERA-40 dataset. This is a comprehensive set of global analysis describing the state of the atmosphere, land and oceans from September 1957 to August 2002 [1]. These fields are obtained from a numerical re-analysis of ECMWF archives and externally supplied in-situ and remote-sensing data [Kallberg *et al.* , 2004]. A summary of the ECMWF ERA-40 products used during this project is provided in table 4.5.

For this project ECMWF ERA-40 data was post-processed in a two ways. First, monthly-mean climatological fields were determined using 13 years of data. Second, data for the year 2000 was processed. Properties of these fields are summarized in table 4.6.

[1] Note that this coverage period suggests that 45 years of data are available, while the dataset name indicates it covers 40 years. No new data is added to the dataset, however.

Parameters used	Air temperature, wind speed, air pressure, relative humidity, cloudiness, heat flux data, atmospheric vorticity
Temporal resolution	6 hrs
Spatial resolution	2.5 degrees
Spatial coverage	Global
Temporal coverage (sensor)	Sep 1957 - Aug 2002

Table 4.5: Overview of ECMWF ERA-40 dataset properties [Kallberg *et al.* , 2004].

Climatological fields	
Parameters used	Air temperature, wind speed, air pressure, relative humidity, cloudiness, heat flux data, atmospheric vorticity
Temporal resolution	1 month
Spatial resolution	2.5 degrees
Spatial coverage	95°E - 125°E; 10°S - 30°N
Temporal domain	mean monthly data 1985 - 2001 (leap years excluded, resulting in 13 years of data)
Historical fields (year 2000)	
Parameters	Air temperature, wind speed, air pressure, relative humidity, cloudiness, heat flux data
Temporal resolution	6 hrs.
Spatial resolution	2.5 degrees
Spatial coverage	95°E - 125°E; 10°S - 30°N
Temporal domain	2000

Table 4.6: Overview of processed ECMWF ERA-40 products used during the SAT2SEA2 project.

4.3.2 NCEP/NCAR Reanalysis

Meteorological data was obtained from the National Center for Environmental Prediction / National Center for Atmospheric Research (NCEP/NCAR) Reanalysis dataset. An overview of products contained in this dataset can be found at [NCEP/NCAR, n.d.]. Similar to the ECMWF ERA-40 dataset, this data is produced by a numerical reanalysis using various types of model input data. Table 4.7 shows an overview of the NCEP/NCAR Reanalysis products used for this project.

Parameters used	Air temperature, wind speed, air pressure, relative humidity, cloudiness, heat flux data
Temporal resolution	1 month
Spatial resolution	2.5 degrees
Spatial coverage	95°E - 125°E; 10°S - 30°N
Temporal coverage (sensor)	Monthly-mean climatological data

Table 4.7: Overview of processed NCEP/NCAR Reanalysis products used during the SAT2SEA2 project.

4.3.3 Comprehensive Ocean-Atmosphere Data Set / SOC heat flux climatology

The Comprehensive Ocean-Atmosphere Data Set (COADS) contains a collection of global marine data observed from 1784 onwards. This data is edited and summarized statistically for each month [COADS, n.d.]. Table 4.8 gives an overview of the COADS products used for this project. Note that the COADS archive itself does not contain heat flux data. The heat flux data mentioned in table 4.8 was obtained from the Southampton Oceanography Centre (SOC) heat flux climatology [Simon *et al.* , 1999]. Heat flux data contained in this dataset was determined using COADS data.

Parameters used	Air temperature, wind speed, air pressure, relative humidity, cloudiness, heat flux data
Temporal resolution	1 month
Spatial resolution	1 degree
Spatial coverage	95°E - 125°E; 10°S - 30°N
Temporal coverage (sensor)	Monthly-mean data 1784 - close to present

Table 4.8: Overview of processed COADS / SOC products used during the SAT2SEA2 project.

Chapter 5

Data acquisition: remote sensing data

This chapter gives an overview of remote sensing (RS) datasets used in this project. These datasets can be grouped into two categories:

1. Altimetry datasets: water level data from the Developing Use of Altimetry for Climate Studies (DUACS) dataset.
2. Radiometry datasets: SST data from the Advanced Very High Resolution Radiometer (AVHRR) / Pathfinder and Reynolds Optimally Interpolated (OI) SST datasets.

For both categories an overview of the observation concept, data recovery and data acquisition is given.

In appendix H.1 an overview of dataset properties as discussed in this chapter is provided. Also, appendix H.2 gives an overview on the different dataset applications in this project.

Finally, in chapter 6 both the RS datasets discussed in this chapter and the non-RS datasets discussed in chapter 4 will be assessed for inter-dataset consistency.

5.1 Satellite altimetry

5.1.1 Altimetry: basic concept

The principle of satellite altimetry is that of an orbiting down-looking radar system. By means of such a system the response of the ocean is measured from a short hypothetical electro-magnetic pulse that bounces off the sea surface. The received information on board the satellite consists of radar waveform samples. Basically, they are histograms describing the distribution of power against time of the reflected signal.

Information retrieved from altimeter measurements is derived from these radar waveform samples, combined with auxiliary data which is either directly observed by satellite sensors or obtained from geophysical models. Derived directly from the waveform samples are:

1. The range between the phase center of the radar antenna and the mean range to the footprint of the ocean.
2. The significant wind-wave height in the footprint illuminated by the radar.

3. The signal strength of the radar pulse that bounces of the ocean surface.

Important auxiliary information added to these measurements are precise orbit information, atmospheric signal delay corrections and basic geophysical corrections that describe the sea state.

For an extensive overview of satellite altimetry and its applications the reader is referred to [Fu & Cazenave, 2001].

5.1.2 Altimetry: data recovery

Figure 5.1 gives a schematic overview the altimeter measurement. The Sea Surface Height (SSH) is defined as the difference between the measured range to the sea surface (R) and the satellites position with respect to a reference ellipsoid (S). This SSH consists of two components:

1. The geoid height (G). The geoid is the equipotential surface which coincides on average with the mean sea level. As such it represents the ocean 'at rest'.
2. The dynamic topography (η). The dynamic topography is the signal due to dynamic processes such as currents, temperature and salinity (steric) variations, tides and atmospheric pressure loading.

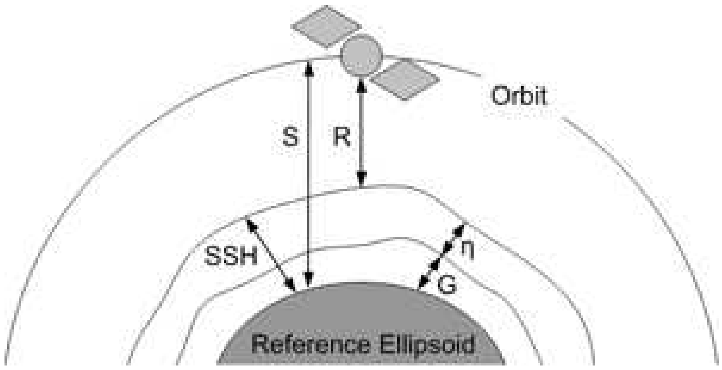

Figure 5.1: Conceptual overview of altimeter remote sensing.

This is summarized by equation 5.1:

$$SSH = S - R = G + \eta \tag{5.1}$$

Most commonly one is interested in η, which has an order of magnitude of over 1 meter. To determine η the local value of G, which can have an order of magnitude of up to 100 meter, has to be subtracted from the measured SSH. Due to this difference in magnitude, and by the fact that G is not known with enough precision, SSH cannot be accurately corrected for effects (errors) related to the geoid.

This problem can be avoided by using the repeat track method. This method works on the assumptions that the satellite repeats exactly the same ground track and that G does not vary (significantly) over time. For a given number of cycles, one can therefore compute the mean height $< SSH >$ along each satellite ground track:

$$< SSH >= G+ < \eta > \tag{5.2}$$

By subtracting the instantaneous measurement from the time mean of the measurements at that point the geoid is eliminated and a dynamic topography anomaly, or Sea Surface Anomaly (SSA), is obtained:

$$SSH - < SSH > = (G + \eta) - (G + < \eta >) = \eta - < \eta > = SSA \tag{5.3}$$

The SSA describes variations of the dynamic topography with respect to the mean component of the current, $< SSH >$, and can be determined with high accuracy (± 3 - 5 cm). It is useful for studying the transient processes of the ocean dynamics. The mean currents, which are removed from the SSA signal, can, however, play an important role in some energetic ocean processes. As such, it can be useful to derive an Absolute Dynamic Topography (ADT) from this SSA and a Mean Dynamic Topography (MDT), defined as the difference between the mean and geoid height:

$$ADT = SSA + < SSH > - G = SSA + MDT \tag{5.4}$$

There are several methods to derive the MDT while limiting the effect of inaccuracies in G. An overview of some of these methods is given in [Hernandez *et al.* , 2001].

Error sources in this measurement methodology can be subdivided into two classes [Fu & Cazenave, 2001], namely errors that influence the measurement of the ocean surface height and errors that influence the interpretation of these measurements. The origins of these errors can be separated into five categories, summarized in table 5.1. For reference, the error magnitude for the Topex / Poseidon (T/P) altimeters are included in this table [Gerritsen *et al.* , 2001]. Note that the altimeter data used during this project is from various missions and that as such these values may vary.

Error source	**Description**	**Order of magnitude**
Instrument error	altimeter noise	± 2 cm
Propagation medium corrections	EM bias, skewness, ionospheric and tropospheric correction	± 3.5 cm
Geoid modeling errors		± 1 m
Effects of temporal variations	solid earth and ocean tides, inverse barometric correction	± 1 cm
Spacecraft orbit determination error	orbital altitude	± 3.5 cm

Table 5.1: Altimeter error budget [Gerritsen *et al.* , 2001].

5.1.3 Data acquisition: DUACS

During this project a number of altimeter products from the DUACS dataset are used [DUACS, 2005] [DUACS, 2004]. In appendix H.4 an overview of the different products contained in this dataset is provided. For most applications in this project these products are post-processed to provide auxiliary information. Below, an overview of post-processing done for this project is given. Appendix H.2 summarizes where and how these post-processed product are used during this project.

As indicated in table 5.2 monthly-mean climatological SSA and ADT fields are determined from both the weekly 1/3 degree SSA and ADT data. Also, a 1 degree version of this climatology is processed. In appendices G.5 and G.6 these monthly-mean fields are shown for a number of selected

1. Climatological SSA fields - 1/3 degree	
Dataset	SSA - H
Mapping	Gridded, 1/3 degree
Satellite	Merged
Processing / Time frame	Monthly climatological means from all weekly DT maps in the period 1992 - 2001 and all NRT maps in the period 2002 - 2005 (14 years of SSA data). Also, the monthly-mean standard deviation from the climatological mean and the average signal error were determined.
2. Climatological SSA fields - 1 degree	
Dataset	SSA - H
Mapping	Gridded, 1 degree
Satellite	Merged
Processing / Time frame	Monthly climatological means from all monthly DT maps in the period 1992 - 2001 (10 years of SSA data).
3. Climatological ADT fields	
Dataset	ADT - H
Mapping	Gridded, 1/3 degree
Satellite	Merged
Processing / Time frame	Monthly climatological means from all weekly NRT maps in the period 2002 - 2005 (4 years of ADT data).

Table 5.2: Post-processing of DUACS altimeter products used during the SAT2SEA2 project.

months. Also, in appendix H.6 the standard deviation from the monthly-mean climatological SSA is shown. These fields were discussed in chapter 2. Climatological averaging is done by calculating the monthly-mean value according to equation 5.5. The standard deviation is calculated according to equation 5.6. In these equations α_m indicates whether a specific SSA_i sample was measured in month (m). Averaging periods are indicated in table 5.2.

$$\overline{SSA_m} = \frac{1}{N_{samples\ per\ month}} \sum_{i=1}^{All\ samples} \alpha_m SSA_i \tag{5.5}$$

$$SSA_{std,m} = \frac{1}{N_{samples\ per\ month} - 1} \sqrt{\sum_{i=1}^{All\ samples} \alpha_m (SSA_i - \overline{SSA_m})^2} \tag{5.6}$$

A similar averaging is performed on SSA error data. The annual average signal error, specified as a percentage of the total SSA signal, is calculated from 4 years of weekly error data. This field in shown in appendix H.5 and shows that the quality of the DUACS data decreases strongly near coastal regions. This effect is notable till 1 degree from the coastlines and can be attributed to altimeter sensor characteristics and correction techniques. This should be kept in mind when processing SSA data for modeling applications. Based on these characteristics and on interpolation methods applied, the realistic SSA resolution is expected to be around 1 degree.

Next to the climatological averaging, weekly 1/3 degree SSA data is used for historic water level forcing at the open model boundaries. The model boundaries are indicated in appendix I.1. At the end-points of these boundaries weekly SSA time-series are prescribed. Implications of this

SSA forcing on the modeling is discussed in chapter 8. Note that appendix H.5 indicates a mean signal error of over 30 percent at the Taiwan Strait boundary, which can reduce the quality of model forcing in this region.

Finally, geostrophic circulation fields were determined from 1 degree SSA data. DUACS does not provide geostrophic circulation for its 1 degree SSA products. Since the resolution of the 1/3 degree vector fields can be too high when plotted for a large spatial domain like the SCS (the plot becomes to dense with vector arrows), such a product is desirable. To determine these fields, 1 degree SSA data is added to the 1 degree CLS MDT (CLS-RIO3, see appendix E). Subsequently, using the gradient equation described in appendix F geostrophic circulation is calculated.

5.2 Remote sensing of sea surface temperature

5.2.1 Remote sensing of sea surface temperature: basic concept

The fundamental basis of remote sensing of Sea Surface Temperature (SST) is that all surfaces emit radiation, the strength of which depends on the surface temperature. The higher the temperature, the greater the radiated energy. By measuring the emitted radiation the temperature can be determined.

If the emitted radiation is not absorbed by the atmosphere, it can be measured from space using passive radiometer instruments. This is possible at several atmospheric windows where the influence of atmospheric interference on the radiated signal is small [Brown & Minnett, 1999]. Remaining atmospheric interference can be corrected with height accuracy by forming linear combinations of measurements on multiple frequencies. This property has been utilized by several generations of RS missions to determine SST with a good degree of accuracy.

The major disadvantage of measuring in the Infra-Red (IR) spectrum is that clouds pose a serious problem. They are non-transparent at IR frequencies and as such no SST measurements are possible over cloudy regions. There are several possibilities to reduce this problem, among which averaging of SST measurements in weekly or monthly composite maps or blending RS SST measurements with in-situ SST measurements.

5.2.2 Remote sensing of sea surface temperature: data recovery

Figure 5.2 gives an overview of radiation emitted by the sea surface in the mid- to far-infrared spectrum. The profiles in this figure represent radiation reaching the upper atmosphere at different atmospheric states. The upper profile indicates the radiated energy if no absorption occurs.

In this figure a number of peaks can be identified at which the radiation reaching the upper atmosphere is maximum. Of these, the peaks between 3.5 μm and 4.1 μm (band 1) and between 10.0 μm and 12.5 μm (band 2) are typically used for SST remote sensing. These peaks are chosen because SST has a typical emission peak between 9 and 11 μm (the emitted radiance is maximal around these values). Also, the emitted radiance varies rapidly with temperature in this range. As such this region is optimal for monitoring SST.

Furthermore, as observed from figure 5.2, none of the indicated bands are completely transparent, meaning the emitted radiation is partially absorbed by the atmosphere. By approximation this absorption is a function of wavelength only [Brown & Minnett, 1999]. As such, by measuring in multiple bands and by forming linear combinations of these measurements, atmospheric water vapor effects in the infrared can be corrected. The resulting linear measurement combination is represented by:

$$T_{SST} = a_0 + a_1 T_{band\ 1} + a_2 T_{band\ 2} \tag{5.7}$$

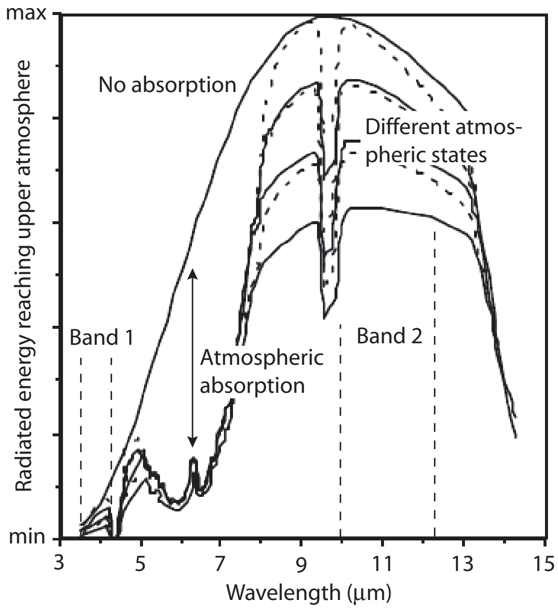

Figure 5.2: Conceptual overview of IR radiation emitted by the sea surface.

Where the constant a_0 is included as an overall adjustment for wavelength independent attenuation. The constants a_1 and a_2 can be determined both theoretically or empirically and are dependent on absorption in the two radiometer bands [Barton, 1992]. This methodology forms the basis of IR SST remote sensing and the coefficients a_0, a_1 and a_2 have been tuned for a large number of atmospheric states. Furthermore, adaptations can be made to improve the algorithm quality at high scanning angles and to generalize the algorithm into a non-linear structure:

$$T_{sst} = a'_0 + a'_1 T_{band\ 1} + a'_2(T_{band\ 2} - T_{band\ 1}) + a'_3(\sec(\theta) - 1) \tag{5.8}$$

Equation 5.8 forms the basis for the current state of IR SST remote sensing algorithms, such as those used for the current MODIS and AVHRR missions [Vazquez, 1999].

Figure 5.3 gives a schematic overview of IR SST remote sensing data recovery. From this figure a number of error sources in these measurements can be distinguished. These are cloud coverage, sun glint, water vapor absorption in the atmosphere, trace gas absorption and episodic variations in aerosol absorption due to volcanic eruptions and terragenous dust blown out to sea.

Of the mentioned error sources cloud coverage is most significant because clouds are non-transparent at IR frequencies. This can severely restrict the availability of RS SST measurements. For unclouded regions, the current state of infra-red remote sensing instruments is able to determine SST with an upper error bound of 0.5 °C [Brown & Minnett, 1999] [Vazquez, 1999].

An additional error source when using RS SST data is the so-called representation error; based on measurement methodology and sensor characteristics different SST products do not necessarily represent the same quantity. More attention to this error is given in appendix C. Also, the consequences of this error for this project are assessed in section 6.2.

5.2.3 Data acquisition: AVHRR Pathfinder

A wide range of RS SST datasets are available. In [Twigt, 2005] an overview of these datasets is provided. For this project the AVHRR / Pathfinder datasets is used (hereinafter called AVHRR).

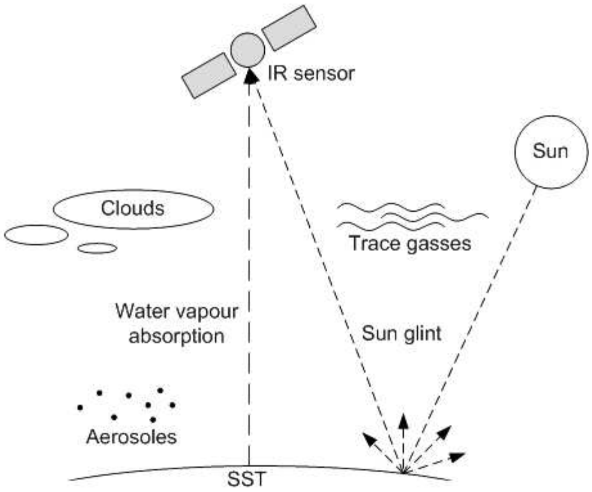

Figure 5.3: Conceptual representation of error sources in infra-red SST remote sensing.

This dataset combines data from a number of NOAA AVHRR satellites. Radiometer measurements by these satellites are calibrated according to equation 5.8, with algorithm coefficient determined by a regression with match-up buoy data. Finally, the calibrated measurements are mapped on a fixed grid.

This dataset was chosen because of its high temporal resolution (24 hrs) and a good spatial resolution (4.9 km). Also, it has a substantial coverage period (1985 - current) and is available free of charge. Furthermore, the AVHRR algorithm coefficients are determined empirically from a multiple regression with in-situ measurements. In this process the SST is corrected for the so-called skin-effect (see appendix C). As such, AVHRR SST data represents the bulk-temperature (top 1 meter of the water column) [Barton, 1998]. This should decrease the magnitude of the representation error when comparing AVHRR SST with other SST data sources (see section 6.2). Finally, quality assessment data is provided specifying the quality of each measurement and the number of measurements used to construct composite maps.

Table 5.3 shows a summary of AVHRR dataset properties [Vazquez, 1999]. Note that composite maps with a lower temporal resolution are available also.

AVHRR / Pathfinder dataset	
Spatial coverage	Global
Spatial resolution	4.9 km
Temporal coverage	1985 - current
Temporal resolution	24 hrs
Accuracy	0.3 - 0.5 K
Quality Assessment	0 (covered) - 7 (perfect measurement)

Table 5.3: Overview of AVHRR Pathfinder dataset properties.

In appendix H.2 an overview of AVHRR SST applications during this project is shown. For these applications a climatology of monthly-mean SST fields was determined using 10 years of AVHRR data (1994 - 2004). Using the associated quality products, only high quality SST data was used during the climatological averaging. This averaging is described by equation 5.9, where $Q_{m,i}$ indicates the quality index (which should be larger than 5) and $SST_{m,i}$ indicated SST for composite month m and year i.

$$\overline{SST_m} = \frac{1}{10}\sum_{i=1}^{10} Q_{m,i} SST_{m,i} \tag{5.9}$$

The reason for using monthly composite maps is based on the high cloudiness over the SCS domain. It is reported that at times up to 90% of this domain is covered by clouds [Farris & Wimbush, 1996]. This can also be observed by comparing daily, weekly and monthly SST fields (see appendix H.7) and by assessing cloudiness from meteorological datasets (see chapter 2).

5.2.4 Data acquisition: Reynolds OI sea surface temperature

The Reynolds OI Sea Surface Temperature dataset (hereinafter called Reynolds SST dataset) consists of SST fields derived using both in-situ and RS SST measurements (so called blended SST maps). Using an interpolation routine, these measurements are merged into weekly and monthly composite fields on a 1 degree grid [Reynolds *et al.* , 2002]. Table 5.4 gives a summary of this dataset. Also, appendix H.2 shows an overview of Reynolds SST applications in this project.

Reynolds OI SST dataset	
Spatial coverage	global
Spatial resolution (horizontal)	1 degree
Temporal coverage	1981 - current
Temporal resolution	Weekly, monthly
Accuracy	0.3 - 0.5 K

Table 5.4: Overview of Reynolds OI SST dataset properties.

Chapter 6

Assessment of consistency between datasets

This chapter describes comparisons between datasets discussed in chapter 4 and 5. This is done in order to assess the consistency between these datasets and in order to make choices on data usage for the modeling.

In section 6.1, ASIAEX in-situ temperature and salinity data (see section 4.2.1) is compared with climatological data from the World Ocean Atlas 2001 (WOA01, see section 4.1). This is done to validate the ASIAEX data processing and in order to study the usefulness of climatological WOA01 data for non-climatological modeling applications.

In section 6.2, SCSMEX in-situ Sea Surface Temperature (SST) data (see section 4.2.2) is compared with remote sensing (RS) and WOA01 SST data. Based on this comparison the RS SST dataset used for model SST nudging is determined (see appendix D).

In section 6.3, the atmospheric datasets described in section 4.3 are assessed. Based on this assessment a choice on data used for model atmospheric forcing is made.

Appendix H.1 provides an overview of properties of the above mentioned datasets.

6.1 Comparison of World Ocean Atlas 2001 and in-situ profile data

In appendix H.8 weekly-mean ASIAEX temperature and salinity profiles are compared with climatological data from the WOA01. The horizontal bars in these plots represent the standard deviation from the WOA01 climatological mean.

From this appendix it is observed that the WOA01 and ASIAEX temperature profiles show a reasonable degree of correspondence. In most cases the ASIAEX data fits well within the WOA01 standard deviation bounds. From this, it is concluded that the WOA01 climatological mean and its associated standard deviation give a good indication of the range in which non-climatological values are expected. This is confirmed by the layer averaged deviation between WOA01 and SCSMEX data shown in figure 7.3 (next chapter). This deviation has a mean value of about 1 degree. Based on this conclusion, WOA01 climatological temperature data (including its standard deviation) will be used for non-climatological model validation in chapters 10 and 11. The implications of using this validation data will be discussed in chapter 8.

Noteworthy is that the mean WOA01 temperature profiles show a smoother behavior than the ASIAEX profiles. In most cases, the temperature is too low in shallow regions (0 - 50 meters) and too high in deeper regions (50 - 150 meters). A similar behavior is observed when comparing WOA01 data with SCSMEX data in figure 7.4 (next chapter), which shows the difference between profiles from these two datasets. If this is a re-occurring WOA01 feature, this might be due to smoothing caused by the climatological averaging routines. This should be kept in mind when using WOA01 data for model validation, and when using the WOA01 dataset to determine thermocline variability.

Also, from the salinity profiles a significant discrepancy between WOA01 and ASIAEX salinity data is observed in the top layer (0 - 100 meter). Here, ASIAEX data is far outside the WOA01 standard deviation bounds. For deeper layers there is a better match. This difference might be explained in a number of ways:

1. Errors in the ASIAEX processing routines or in the assumptions made during the processing (see section 4.2.1). No programming errors were found, however, and the same routine was used for the ASIAEX temperature profiles which show a substantially better fit.
2. Errors in the ASIAEX measurements. This seems unlikely because the same salinity sensor is used for measurements at all depths and results below 100 show a good fit. Also, the low surface layer salinity is observed throughout the entire ASIAEX measurement period. Furthermore, the data is filtered for outlying and anomalous values.
3. Salinity phenomena unresolved in the WOA01 data: the ASIAEX measurement location was determined in order to study a number of dynamic processes in the North SCS, among which intrusion through Luzon and Taiwan Strait and interplay between these phenomena [Denner *et al.* , 2000]. According to [Jacobs, n.d.], fresh-water influx through Taiwan Strait occurs on a non-periodic basis. It is possible that these non-periodic, low-salinity intrusions are not resolved by the WOA01 because this data describes long-term mean behavior. Also, these low salinity values are observed in the top 0 - 100 meters only. This corresponds roughly with the depth of Taiwan Strait (see appendix G.2). Considering that salinity transport occurs mainly in the horizontal plane it is likely that salinity influx through Taiwan Strait will influence this depth range primarily. This also explains the better temperature fit, because temperature is primarily a vertical process driven by the surface flux.

   Furthermore, in section 5.1.3 a monthly-mean SSA climatology is discussed. In appendix H.6 the standard deviation from this climatology is shown for a number of months. From this appendix a substantial standard deviation is observed in the Taiwan Strait region (20 - 40 cm). While this may partially be explained by a significant SSA error (20 - 30 % of total signal, see appendix H.5), it can also indicate that non-periodic or high frequency (sub-monthly) phenomena occur frequently in this region. This supports the explanation that low salinity values in the ASIAEX data are caused by non-periodic salinity intrusions, or by phenomena unresolved on the WOA01 temporal scale.

From the above possibilities non-periodic salinity intrusions unresolved by long-term WOA01 averages seems most likely. The possible consequences of these non-periodic intrusions on transport modeling for the SCS will be discussed in chapter 8.

6.2 Comparison of in-situ, remote sensing and climatological sea surface temperature data

In chapter 5.2, two remote sensing SST datasets are described. These are the AVHRR / Pathfinder (AVHRR) and the Reynolds OI SST (Reynolds SST) datasets. To assess the consistency between these datasets they are compared with both in-situ buoy (SCSMEX, see section 4.2.2) and climatological WOA01 (see section 4.1) SST data. This comparison is made at each of the SCSMEX buoy locations.

Before this assessment is discussed it should be kept in mind that different sensors sample SST in different ways. As such, if data from different SST sources is compared this can lead to an error (representation error) because of differences between SST definitions. As indicated in section 5.2.3, AVHRR SST is determined by a match-up with in-situ buoys. This SST represents the temperature in the upper 0.3 - 1 meters of water [Vazquez, 2004]. A similar SST definition is used for Reynolds [Vazquez, 1999], WOA01 [Conkright *et al.* , 2002] and SCSMEX [TOA, n.d.] SST. From this it is concluded that the compared SST datasets represent the same SST quantity.

In figure 6.1 the different SST products are compared at the SCSMEX Atlas 1 buoy location (see appendix H.3). Similar figures at the Atlas 2 and 3 locations are shown in appendix H.9.

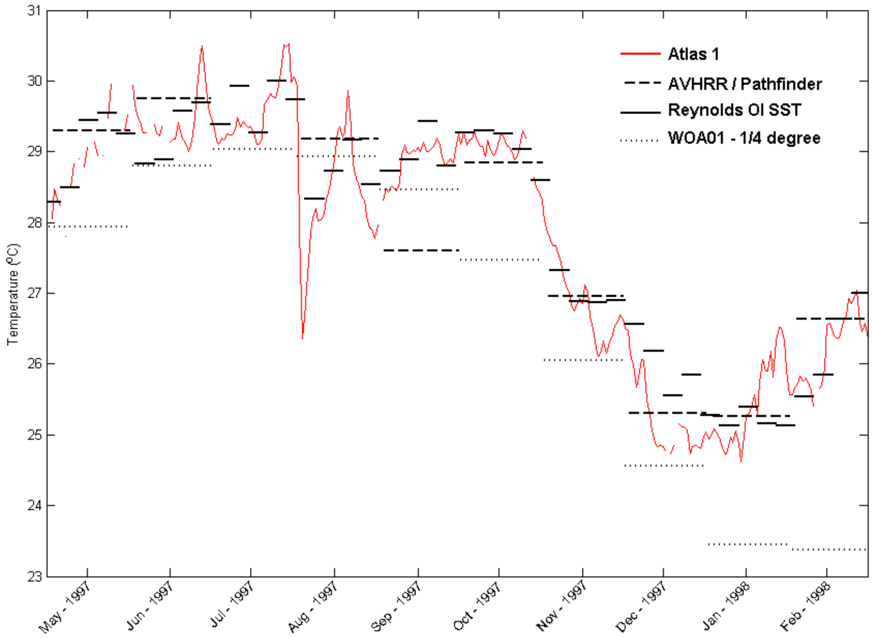

Figure 6.1: Sea Surface Temperature (SST) data comparison: in-situ buoy data from the SCSMEX project (Atlas 1: 18.06°N - 115.36°E), remotely sensed SST data from AVHRR Pathfinder and Reynolds OI SST and climatological SST data from the World Ocean Atlas 2001. See appendix H.9 for other Atlas buoys.

From these figures it is observed that there is a good correspondence between Reynolds and in-situ SST. A mean difference of 0.5 °C is observed. This good correspondence could indicate that SCSMEX in-situ data is used for the blended Reynolds SST. On the other hand, an inspection of COADS in-situ observations indicates that all SCSMEX buoys are located around busy shipping lanes between Luzon Strait and Singapore. As such, this good fit can also be attributed to sufficient in-situ measurements by ships-of-opportunity. Apart from this, the good correspondence between these datasets indicates their data was processed correctly. The difference between AVHRR and in-situ SST is larger, and has a magnitude of 1 °C. Also, during some months no AVHRR data is available due to cloudiness.

Furthermore, a significant difference between in-situ and WOA01 SST is observed. On average this is about 1.5 °C. In most cases, however, RS and in-situ SST data is within the WOA01 standard deviation bounds (these bounds were assessed separately from figure 6.1 and from the figures in appendix H.9. Including them results in overly crowded figures). An exception to this is the 1998 period, shown by the Atlas 3 buoy, where an average deviation of 2 °C is observed. This difference may be attributed to the 1998 El Ninõ, which caused a notable rise in SST in the central SCS

[Gerritsen *et al.* , 2001].

Finally, when compared with the monthly-mean SST data provided by AVHRR and the WOA01, intra-monthly SST variability can be substantial (up till 3 degrees). This variability is resolved better by the weekly Reynolds SST data.

In section 5.2.2 an overview of the AVHRR and Reynolds SST datasets was given. The difference in accuracy between these datasets, as described above, can be attributed primarily to processing methods and sensor characteristics as mentioned in that section. Summarizing, AVHRR provides high resolution SST data. Due to the measurement method this product can be severely limited by cloud coverage, which reduces the advantageous high temporal resolution considerably (see section 5.2.3). An assessment of AVHRR data in appendix H.7 indicates that monthly composite fields are required to obtain SST maps that are cloud free over most of the SCS. As observed from figure 6.1, even then data is not always available. Reynolds SST solves this problem by merging AVHRR and in-situ data in blended SST maps. In-situ data used comes primarily from ships-of-opportunity. While the high resolution of the original AVHRR data is reduced by this blending process (from 4.9 km to 1 degree), a better temporal resolution is achieved with respect to the potentially clouded AVHRR data (weekly instead of monthly).

Based on these properties and on the above conclusions on attainable accuracy (0.5 °C for Reynolds SST compared to 1 °C for AVHRR SST), Reynolds SST data will be used for SST nudging in part III of this report.

6.3 Atmospheric dataset comparison

In Delft3D-FLOW, the heat flux through the free surface can be imposed by input data prescribing the atmospheric state: momentum transfer at the free surface is prescribed by wind fields and the net surface heat flux is prescribed using air temperature, relative humidity and cloudiness fields. In appendix C an overview of heat flux modeling in Delft3D-FLOW is provided.

Since the model accuracy will partly depend on the quality of the forcing data applied, it is important to assess the quality of the atmospheric forcing data used. In chapter 4 a number of atmospheric datasets are described. In this section these datasets are compared in order to assess the consistency between them and to make an estimate of the dataset quality. Assessed datasets are the ECMWF ERA-40 dataset (ECMWF), the NCEP/NCAR Re-analysis (NCEP/NCAR) and the COADS / SOC dataset. These datasets contain gridded time-averages of the above-mentioned input fields. They also contain gridded time-averages of the individual heat flux components.

To assess the consistency between the datasets, climatological means of the relevant atmospheric fields are determined. These means are shown in table 6.1 and represent annual-mean, area averaged values over the domain indicated in figure 6.2. The EMCWF climatology was determined from 13 years of data (see section 4.3.1). For both the NCEP/NCAR and COADS/SOC climatologies all available data was used (see appendix H.1). Note that in this section meteorological wind fields are taken into account as parameter in the heat flux equation only.

Furthermore, climatological means of the heat flux components (shortwave, long wave, evaporative and convective flux, see appendix C) are determined. While these are not directly used for model forcing, they provide useful information in order to give a descriptive explanation of the dynamic processes controlling the heat flux at the free surface. Also, they are used to assess the relative magnitude and importance of the individual flux components (see chapter 2). Furthermore, they are used in this section to assess the quality of the atmospheric input data. The heat flux components are derived, among others, from the atmospheric state. As such, inconsistencies between these components among the datasets studied can also indicate inconsistencies between the atmospheric fields used for model forcing. In this manner, the quality of the heat flux components gives an indication on the overall quality of the dataset.

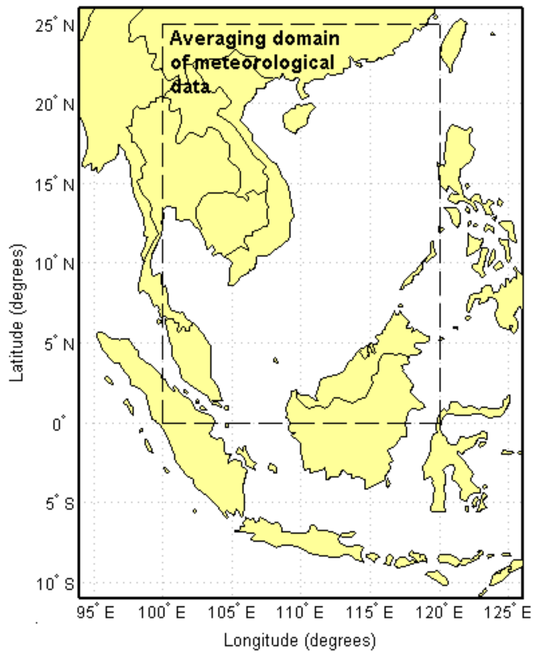

Figure 6.2: Averaging domain of meteorological data.

Table 6.1 shows an overview of the mean SCS atmospheric state (model input fields only) and the mean heat flux components from the mentioned datasets.

Component	Unit	ECMWF	NCEP/NCAR	COADS/SOC
Heat flux component				
Shortwave flux	W/m^2	177.3	179	213.8
Longwave flux	W/m^2	-40.95	-86.8	-43.9
Convective flux	W/m^2	-9.4	-31.6	-5.6
Evaporative flux	W/m^2	-119.3	-53	-101.6
Net flux	W/m^2	7.65	7.6	63
Atmospheric state components				
Air temperature (2 meter)	$^\circ C$	27.13	25.4	27.5
Relative humidity	%	80.8	85.2	81.2
Wind speed (10 meter)	m/s	4.39	4.08	6.7
Cloudiness	%	74.8	N.A.	64.4

Table 6.1: Mean atmospheric state and heat flux components: annual-mean values averaged over 100°E - 120°E, 0°N - 25°N. Data from ECMWF ERA-40, NCEP/NCAR Reanalysis, and COADS / SOC datasets.

From this table it is concluded that there are significant differences between the mean heat flux components obtained from these datasets. ECMWF and COADS longwave, convective and evaporative flux have a similar order of magnitude. Also, their relative magnitude is as expected from literature. The evaporative flux has the greatest magnitude and the convective the lowest [Emery *et al.* , 2006]. NCEP/NCAR values differ from this significantly, also in relative magnitude. In contrast to this, the ECMWF and NCEP/NCAR net flux are of comparable magnitude, while the COADS net flux is significantly larger. This can be attributed to a larger shortwave flux.

This can also be observed from figure 6.3, which shows the monthly-mean climatological heat flux for all datasets. It is seen that ECMWF and COADS have a similar temporal evolution while NCEP/NCAR data does not. In comparison, NCEP/NCAR variation seems excessively smooth.

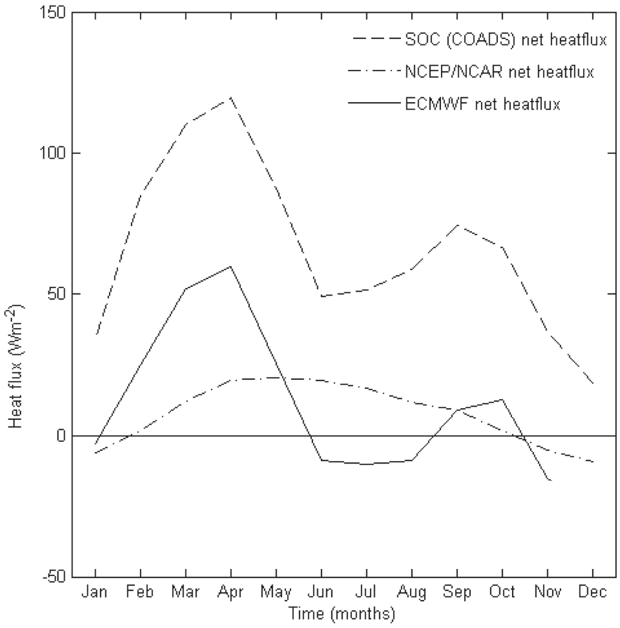

Figure 6.3: Climatological net heat flux series: monthly-mean values averaged over 100°E - 120°E, 0°N - 25°N. Data from ECMWF ERA-40, NCEP/NCAR Reanalysis, and COADS / SOC datasets.

To assess further differences between the ECMWF and NCEP/NCAR net heat flux data, the correlation between monthly-mean (m) time series of these datasets is determined over the SCS domain. This is done by determining the covariance of two time-series (ECMWF (E) and NCEP/NCAR (N)) at a specified location (lat, lon) and by dividing this by the product of the standard deviations (σ_E and σ_N) of these series:

$$Correlation(lat, lon) = \frac{\frac{1}{12-1}\sum_{m=1}^{12}(E_{(m,lat,lon)} - \overline{E_{(lat,lon)}})(N_{(m,lat,lon)} - \overline{N_{(lat,lon)}})}{\sigma_E \sigma_N} \tag{6.1}$$

Figure 6.4 shows the resulting correlation if this is done for all data-points. From this figure it is observed that the correlation is small at low latitudes (around the equator), but increases with latitude. In the North SCS a good correlation between these datasets is observed. As such, it seems likely that the quality of at least one of these datasets degrades at lower latitudes.

From the atmospheric state data in table 6.1 it is observed that ECMWF and COADS show a comparable air temperature while NCEP/NCAR data differs. As a test case it is assumed that SST follows the air temperature [Emery *et al.* , 2006]. An average SST of about 28°C is found from WOA01 data. Combined with the fact that the convective flux is outgoing (see figure 2.14, chapter 2) this indicates the mean air temperature is below the mean sea temperature. This is correct for all three datasets. The difference between NCEP/NCAR air temperature and mean WOA01 SST data is significant, however. The difference between ECMWF and COADS air temperature and mean WOA01 SST seems more realistic when compared with literature [Emery *et al.* , 2006].

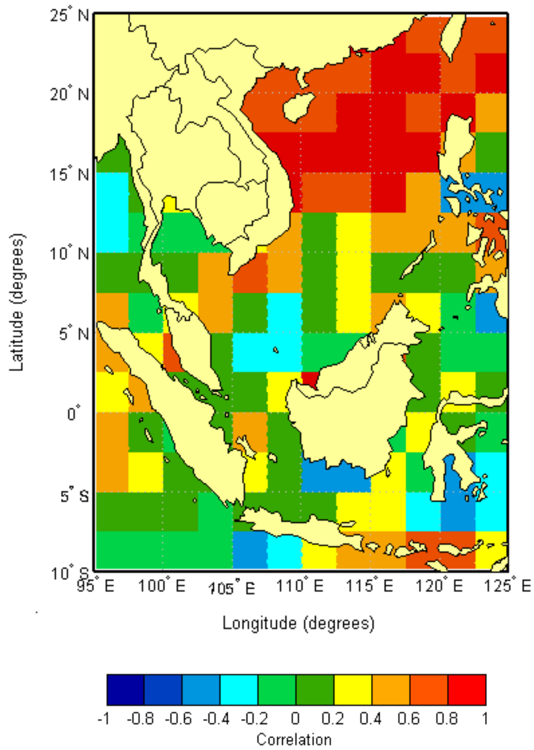

Figure 6.4: Correlation between monthly-mean heat flux data from the ECMWF ERA-40 and NCEP/NCAR Reanalysis datasets.

Furthermore, the ECMWF and NCEP/NCAR wind speed show a comparable order of magnitude, while the COADS magnitude is significantly larger. This may be partially due to the difference between vector and scalar wind fields. According to [Millar *et al.* , 1999] an additional term should be included to account for turbulent wind fluxes when calculating the wind magnitude from vector data. With this in mind, the scalar wind speed is expected to be higher than the mean vector wind speed. In table 6.1, NCEP/NCAR and COADS wind data is scalar, while ECMWF wind was calculated from vector data. This may partially account for the difference between the COADS and the ECMWF mean wind.

Finally, the NCEP/NCAR dataset does not provide cloud coverage data [NCEP/NCAR, n.d.]. This seems suspicious, since it is reasonable to assume that this parameter has to be taken into account in the reanalysis in order to model the shortwave and longwave flux components. This may explain the substantial longwave flux component of this dataset. A possible reason for omitting this data is described in the next paragraph.

Some of the differences between these datasets as discussed above can be attributed to how they were obtained. The ECMWF and NCEP/NCAR datasets are re-analysis archives, indicating a hind-cast was made using numerical weather models and a wide range of data sources. The COADS datasets contains statistical averages of in-situ measurements made primarily by ships-of-opportunity. This has a number of implications [Emery *et al.* , 2006].

First of all, the re-analysis fluxes are biased because they were calculated using numerical models optimized to produce accurate weather forecasts. Also, these models were optimized for specific regions (Europe, the USA). This may degrade the accuracy of the time-mean fluxes, most notably for other regions then those specified. This also results in substantial regional differences.

Secondly, the re-analysis flux quality is decreased by a significant error in the boundary-layer cloud coverage: generally, the numerical models used have a poor vertical resolution and as such the low-level cloud structure cannot be resolved adequately. This may explain the significant difference in cloud coverage between the ECMWF and COADS datasets. Also, this could be a reason for omitting this data in the NCEP/NCAR dataset.

Finally, the re-analysis models do not require that the net heat flux averaged over time and the Earth's surface to be equal to zero. According to [Emery *et al.* , 2006], the ECMWF dataset averaged over fifteen years gives a net heat flux of 3.7 W/m^2 into the ocean. From the NCEP/NCAR dataset a net heat flux of 5.8 W/m^2 out of the ocean is observed. Finally, the COADS dataset gives a net flux of 16 W/m^2 into the oceans.

Summarizing the above, it is concluded that for the SCS there are significant differences between the compared atmospheric datasets:

- The NCEP/NCAR heat flux data seems unrealistic in both magnitude and behavior: no distinct seasonal pattern is observed and the relative magnitude of individual components is incorrect when compared with values described by literature.
- The COADS net heat flux shows the expected seasonal pattern but has an offset due to a larger shortwave flux component.
- The ECMWF flux seems most realistic, both in terms of behavior, (relative) magnitude, and average net flux.

Assessment of net heat flux using the Ocean heat flux model

To assess the effect of these inter-dataset differences on temperature modeling, the mean atmospheric state as summarized in table 6.1 is used to calculate changes in water temperature for a test case:

Using the heat flux equations as formulated for the Delft3D-FLOW Ocean heat flux model (see appendix C.1.3) the net heat flux is calculated using the mean wind, air temperature, relative humidity and cloudiness as specified in table 6.1. Since these values are different per dataset, a different net heat flux is found for each dataset. It is assumed that the maximum difference between these inter-dataset heat flux values specifies a bandwidth which gives an indication about the uncertainty in the prescribed surface flux.

Subsequently, the annual change in water temperature over a 150 meters water column is calculated using this heat flux bandwidth as input data for equation 6.2. By doing so the uncertainty in surface heat flux is specified in terms of increasing or decreasing water column temperature.

$$\frac{\partial T_s}{\partial t} = \frac{Q_{tot}}{\rho_w c_p \Delta z_s} \tag{6.2}$$

In the above equation, Q_{tot} represents the net heat flux bandwidth. C_p specifies the specific heat capacity of sea water (3930 J/kgK), and ρ_w represents the water density. For ρ_w the average WOA01 value over the test domain is used, which has a magnitude of 1021 km/m^3. Finally, Δz_s specifies the thickness of the top water layer. It is assumed that the temperature is distributed evenly over the water column, which will not be the case in reality. Δz_s is assigned a value of 150 meters, since below this depth no seasonal thermocline variability is expected (see chapter 2).

Appendix C.1.3 describes that the magnitude of the Ocean heat flux models evaporative and convective heat flux equations is steered by a set of transfer coefficients, the Stanton (c_h) and Dalton (c_e) numbers. In chapter 9 a number of experiments are described to determine the value of these coefficients for the SCS. These experiments provided three sets of possible coefficients. The above described test is performed for each of these sets. Note that no cloud cover data is

Transfer coefficients	ECMWF	NCEP/NCAR	COADS	Heat flux bandwidth	Temperature uncertainty
$[-]$	$[W/m^2]$	$[W/m^2]$	$[W/m^2]$	$[W/m^2]$	$[°C]$
$c_h = 0.0009, c_e = 0.0015$	59	56 / 64	81	24	1
$c_h = 0.0009, c_e = 0.0024$	10	24/32	6	26	1
$c_h = 0.0021, c_e = 0.0021$	49	17/25	79	62	3

Table 6.2: Net heat flux and Temperature uncertainty due to inaccurate atmospheric forcing, as function of heat flux transfer coefficients. Data used from ECMWF ERA-40, NCEP/NCAR Reanalysis and COADS/SOC datasets.

provided by the NCEP/NCAR dataset, as such both the ECMWF and COADS cloudiness values are used for this dataset. This explains why two values are mentioned.

In table 6.2 the results of this test are shown. From these results it is observed that there are significant differences between the calculated net heat flux values. Also, these vary significantly for each set of transfer coefficients. As such, no conclusions on datasets quality can be drawn from these values. Furthermore, using the different heat flux values as uncertainty bandwidth results in a temperature uncertainty between 1 and 3 degrees.

Based on these results it seems reasonable to assume that the quality of the atmospheric forcing data will pose a constraint on attainable temperature model quality. Note, however, that this test is done to provide an indication of possible forcing data quality only, and a number of simplifying assumption have been made. For a more elaborate analysis these values may differ.

Finally, based on the conclusions in this section, ECMWF meteorological forcing data will be used for model forcing. A more elaborate assessment on model quality using this forcing data is made by means of a model sensitivity analysis in chapters 9 and 10.

Chapter 7

Synthetic temperature profiles from remote sensing data

This chapter describes a method to extrapolate vertical temperature profiles from RS surface data. This method is derived from a methodology described by [Nardelli & Santoleri, 2004] and [Guinehut *et al.* , 2004]. It is based on a technique for the identification of the coupled modes of variability between two datasets, known as coupled pattern analysis (also known as Singular Value Decomposition (SVD)) and on the hypothesis that few modes are needed to explain the major part of the co-variability. Subsequently, synthetic profiles are reconstructed from a limited number of modes and using the remotely sensed data as surface constraints.

The reason for assessing this method is based on the small amount of long-term, historic validation data found for the SCS during this project. The majority of the validation data obtained is either remotely sensed, describing surface variability, or climatological, describing long-term mean behavior. The only in-situ profile data obtained is from the ASIAEX and SCSMEX datasets and spans a limited spatial and temporal domain (see chapter 4). As such, the main goal of this method is to extent the number of semi-historic temperature profiles usable for model validation.

In this chapter the synthetic profile method will be tested at the spatial and temporal domain of the SCSMEX Atlas 1 buoy, since at this point independent validation data is available. If the method works satisfactorily, it will be used to obtain additional model validation data (see chapter 11).

7.1 Synthetic profiles concept

Figure 7.1 gives a schematic overview of the method used to derive synthetic profiles. The steps indicated in this figure will be discussed separately in subsections 7.1.1, 7.1.2 and 7.1.3.

As indicated in figure 7.1 the SVD method is applied on climatological steric height (SH) and temperature (T) fields determined from the WOA01. The reason for deriving coupled modes of variability between these fields is based on the relation between SH and temperature on the one hand, and the relation between SH and SSA on the other. SH variations are variations in sea surface height due to changes in water density over the whole water column (see appendix E). Since sea water density depends on water temperature (and salinity), changes is water temperature will subsequently result in changes in SH. As such, it is reasonable to assume there is a coupling between SH and temperature. Furthermore, these SH variations form a fraction of the SSA measured by altimeter (see chapter 5). By extracting this fraction from the total altimeter signal, SSA data contains information about the total temperature change in a water column. Since SST

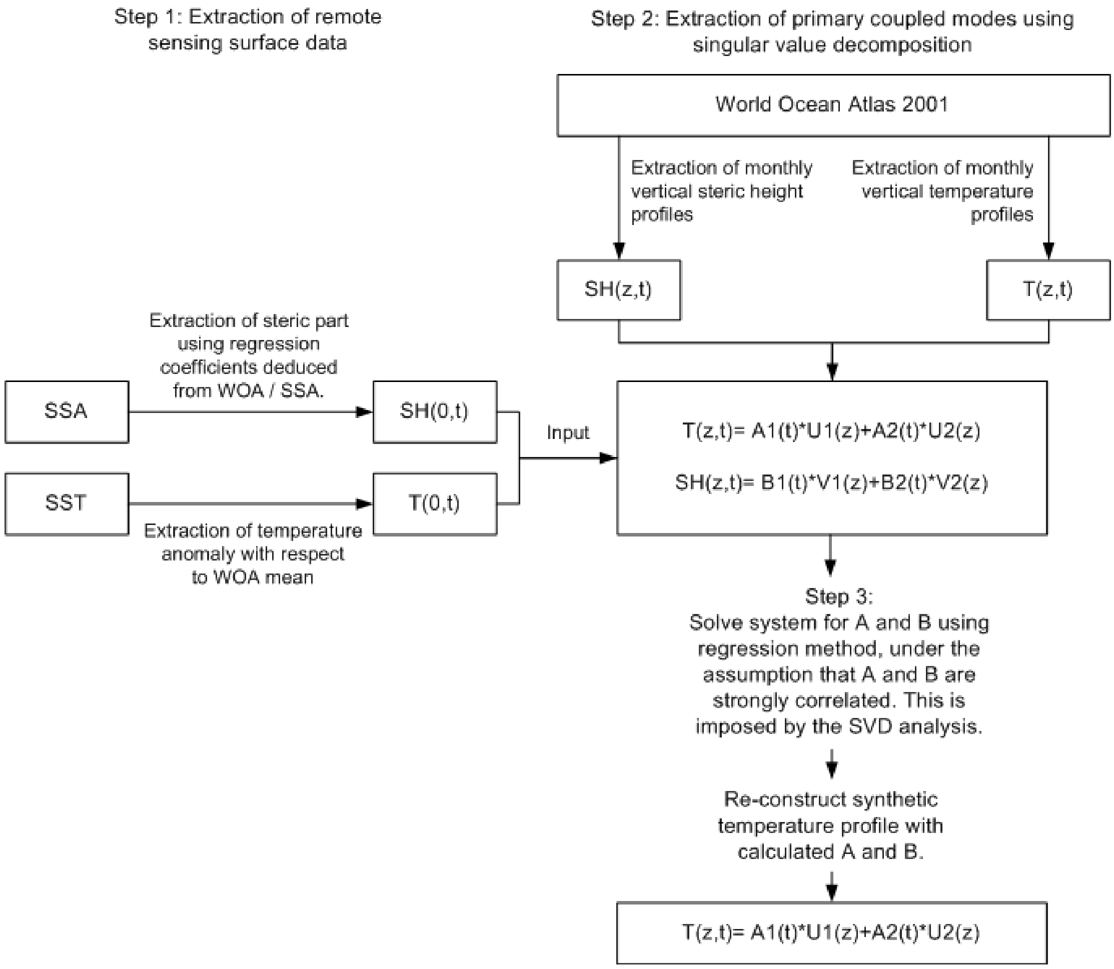

Figure 7.1: Methodology for synthetic profile extrapolation, based on the method described by [Nardelli & Santoleri, 2004].

can be measured directly from space (see chapter 5), we now have a second source of information related to temperature changes in the water column. The method applies these relations and uses both RS SSA and SST surface data to update SH and temperature profiles obtained from climatological data.

The above described method offers a number of advantages with respect to conventional use of remote sensing and climatological data. First of all, RS sensors only directly measure horizontal (surface) variability. This can pose a problem when the spatial distribution of a measured variable at the surface is significantly different from that deeper in the water column. Using this method, surface data is used to make an estimate of vertical variability, thus extending the useful domain of remotely sensed data. Also, climatological datasets generally suffer from low spatial and temporal resolutions (see chapter 4). Using this method, the spatial and temporal resolution of these datasets can be improved by 'updating' them with higher resolution RS data. Finally, as their name suggests, climatologies describe climatological mean fields. This may restrict the usefulness of this data for non-climatological applications. By 'updating' the climatological profiles with non-climatological RS data, they should give a better representation of non-climatological profiles.

On the downside, a number of factors limit the useful domain of this method. First of all, a strong correlation between SSA and SH is required in order to extract the SH part from the SSA signal. Secondly, it is dependent on the availability of RS data. In the case of SST data, this availability can be reduced by cloud coverage. Finally, if more than two dominant modes are found during the SVD analysis, the synthetic field is under-determined and no solution can be found.

7.1.1 Step 1: Data acquisition

As a test-case, synthetic temperature profiles are extracted at the SCSMEX Atlas 1 location. This domain is centered at 115.36°E, 18.06°N and spans a time period from May 1997 till February 1998 (see appendix H.3). As mentioned, the reason for using this domain is based on the availability of in-situ temperature and salinity validation data. Remotely sensed SST and SSA are also obtained and processed for this period and location.

RS SST data used is obtained from the Reynolds SST dataset (see chapter 5). This data has a temporal resolution of one week and a spatial resolution of 1 degree, which was interpolated to the Atlas 1 location. This data was chosen because of its high temporal resolution and its continuous availability. Furthermore, it has a similar temporal resolution as the SSA data used. In order to derive a temperature anomaly from the Reynolds data, the annual mean WOA01 surface temperature was subtracted from the weekly Reynolds values.

RS SSA data used is obtained from the DUACS dataset (see chapter 5). Similar to the Reynolds SST data, it has a temporal resolution of one week. The data has a spatial resolution of 1/3 degree, which was interpolated to the Atlas 1 location. Since the SVD is performed on SH data, the steric part has to be extracted from the SSA signal prior to insertion in the system of co-varying equations described in the next section. This is done using regression coefficients determined by a linear regression between a 10 year climatology of monthly-mean SSA values and monthly SH series derived from the WOA01 (see appendix E). The validity of this approach depends on a strong correlation between SSA and SH. Figure 7.2 shows the correlation between these two fields over the SCS domain. Due to the processing method for the SH anomalies this data is available for a limited section of the SCS only (see appendix E). At the test location, marked Atlas 1, the correlation is reasonable ($r = 0.71$).

7.1.2 Step 2: Singular value decomposition method

Similar to the EOF method discussed in chapter 3, the SVD method identifies modes of variability in data fields. The difference is that where the EOF method analyzes a single field, the SVD method identifies the coupled variability between two fields. It identifies spatial patterns and their temporal variation, with each pair explaining a fraction of the covariance between the two fields.

Prior to applying the SVD method, the SH and T data matrices are setup in a similar way as done for the EOF analysis described in chapter 3. Using these data matrices the temporal cross-covariance matrix C is formed.

$$C = T^t SH \tag{7.1}$$

The SVD of the cross-covariance matrix gives two spatial sets of singular vectors (spatial patterns analogous to the eigenvectors of the EOF method, but one for each variable) and a set of singular values associated with each pair of vectors (analogous to the eigenvalues of the EOF method). Each pair of spatial patterns describes a fraction of the square temporal covariance between the two variables. Mathematically, this comes down to solving the system described by equation 7.2.

$$C = \sum_{i=1}^{N} \vec{U}_i L(i,i) \vec{V}_i^t \tag{7.2}$$

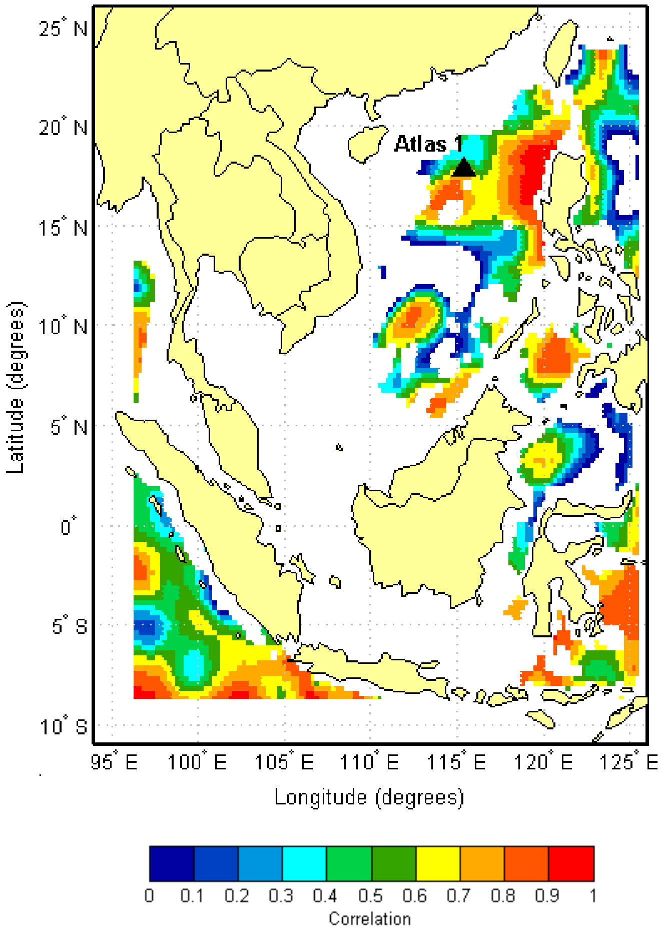

Figure 7.2: Correlation between monthly-mean steric height anomalies from the World Ocean Atlas 2001 and Sea Surface Anomalies from the DUACS archive. The methods test location is marked Atlas 1.

Here, U and V are two orthogonal matrices containing the singular vectors for T and SH, and L is a diagonal matrix containing the singular values. U and V are determined in such a way that the projection A_i of T on U_i has the maximum covariance with the projection B_i of SH on V_i. As such, each pair of singular vectors U_i and V_i describes a mode of co-variability between the T and SH fields. The relative importance of each mode can be assessed through its squared covariance (SCF):

$$SCF_i = \frac{L_i^2}{\sum L_i^2} \tag{7.3}$$

Subsequently, the expansion coefficients are retrieved by projecting the data onto the basis of singular vectors U or V:

$$\begin{aligned} \vec{A}_i &= T \times \vec{U}_i \\ \vec{B}_i &= SH \times \vec{V}_i \end{aligned} \tag{7.4}$$

Based on the hypothesis that only a few modes, in this case two, are needed to explain the major part of the co-variability between two fields, the original fields can be reconstructed by equation 7.5:

$$\begin{aligned} T(z,t) &= A_1(t)U_1(z) + A_2(t)U_2(z) \\ SH(z,t) &= B_1(t)V_1(z) + B_2(t)V_2(z) \end{aligned} \tag{7.5}$$

The above described analysis was applied on a year of monthly T and SH profiles derived from the WOA01 dataset. An overview of the primary coupled modes found from this data is given in table 7.1:

Mode	SCF	r
1	72.9	0.89
2	26.8	0.83

Table 7.1: Primary co-varying modes determined from a Singular Value Decomposition of World Ocean Atlas 2001 temperature and steric height data.

Table 7.1 shows that mode 1 and 2 together describe 99.7% of the co-variability found in the T and SH data. As such, reconstructing the original fields using these modes only, as is stated by equation 7.5, should give a realistic solution. Also, since mode 2 accounts for 26.8% of the co-variability between both fields it is non-neglidgible. From table 7.1 it is also observed that the expansion coefficients A_i and B_i show a strong correlation (described by r), which is as expected since this is the condition imposed by the SVD method. This property will be used to derive the synthetic profiles in the next section.

7.1.3 Step 3: Synthetic profile reconstruction

Table 7.1 shows that expansion coefficients A_i and B_i are strongly correlated. Based on this property they can be linearly related to each other:

$$\begin{aligned} A_1 &= \alpha_1 B_1 + \beta_1 \\ A_2 &= \alpha_2 B_2 + \beta_2 \end{aligned} \tag{7.6}$$

The coefficients α and β in equation 7.6 can be determined by means of a linear regression between the expansion coefficients found from the original (climatological) fields. Now, by substituting equation 7.6 in equation 7.5, the system of co-varying equations can be re-written for the surface layer as equation 7.7:

$$\begin{aligned} T(0,t) &= [\alpha_1 B_1(t) + \beta_1]U_1(0) + [\alpha_2 B_2(t) + \beta_2]U_2(0) \\ SH(0,t) &= B_1(t)V_1(0) + B_2(t)V_2(0) \end{aligned} \tag{7.7}$$

Using the remotely sensed $T(0,t)$ and $SH(0,t)$, equation 7.7 can be solved to obtain a new set of expansion coefficients, A_{new} and B_{new}. Using these coefficients, a new vertical profile of temperature anomalies can be reconstructed. By adding these to the initial mean temperature profile a new, synthetic temperature profile is determined:

$$T(z,t)_{synthetic} = A_{1-new}(t)U_1(z) + A_{2-new}(t)U_2(z) + T_{mean}(z) \tag{7.8}$$

7.2 Synthetic profile validation

Figure 7.3 shows synthetic temperature profiles derived at the test domain (lower panel). For comparison, temperature profiles from the SCSMEX Atlas 1 buoy (upper panel) and from the WOA01 (middle panel) are included also. Furthermore, figure 7.4 shown the deviation (or misfit) between the WOA01 (upper panel) and synthetic profiles (lower panel) with the SCSMEX validation data. Figure 7.5 subsequently shows the mean squared misfit in the upper 100 meters.

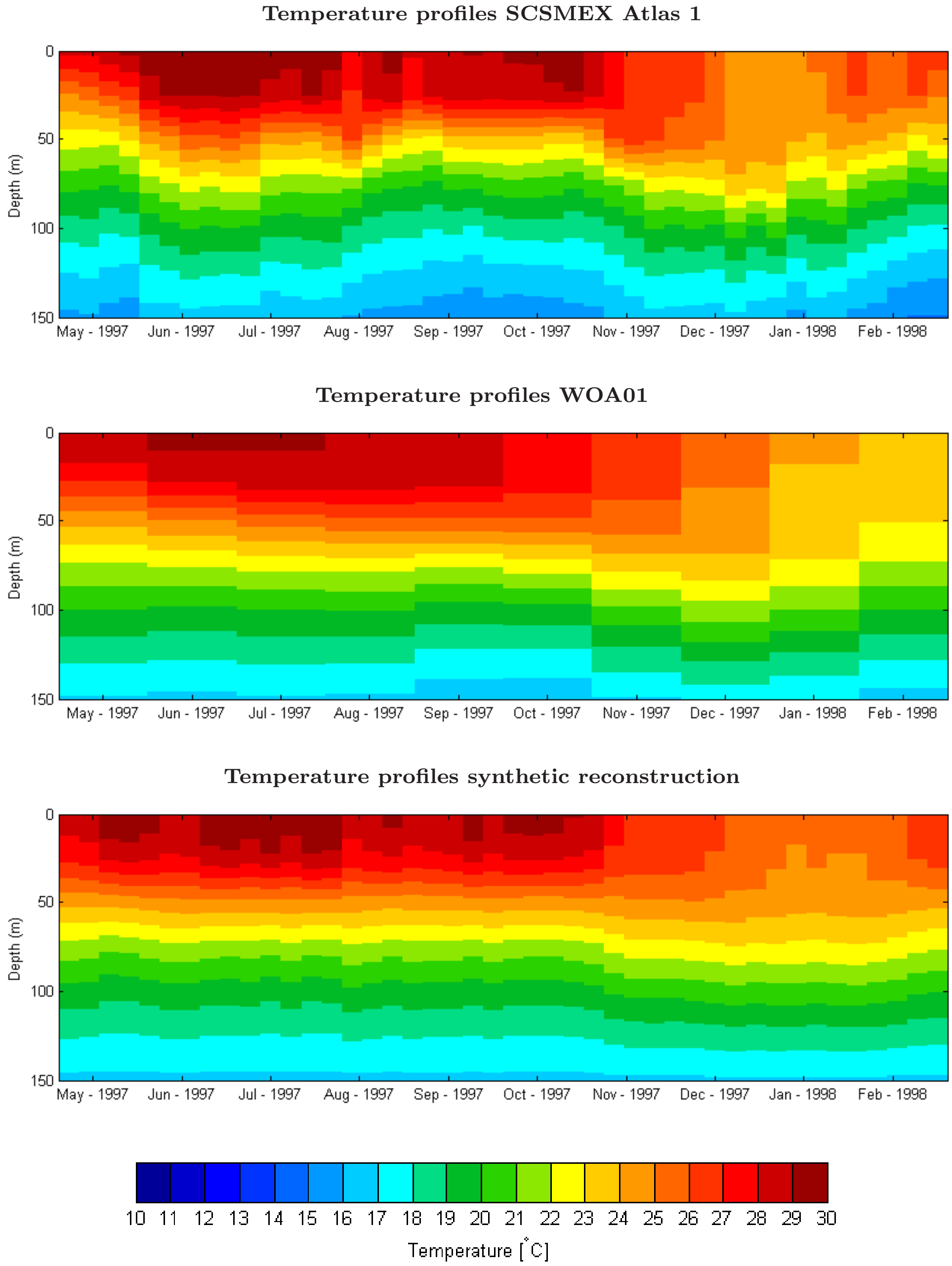

Figure 7.3: Time series of temperature profiles at 115.36°E, 18.06°N. Data obtained from SCSMEX buoys (upper panel), the World Ocean Atlas 2001 (middle panel) and by synthetic profile reconstruction (lower panel).

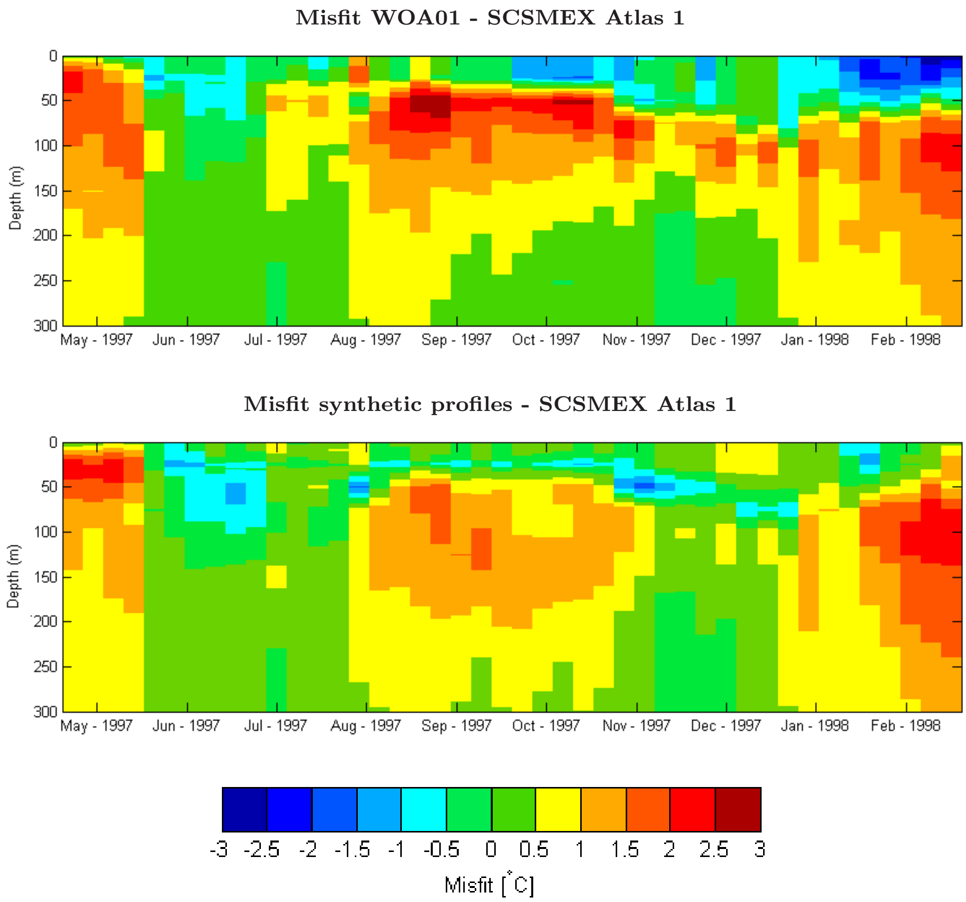

Figure 7.4: Temperature misfit between World Ocean Atlas 2001 and SCSMEX buoy data (upper panel) and synthetic profile and SCSMEX buoy data (lower panel) at 115.36°E, 18.06°N.

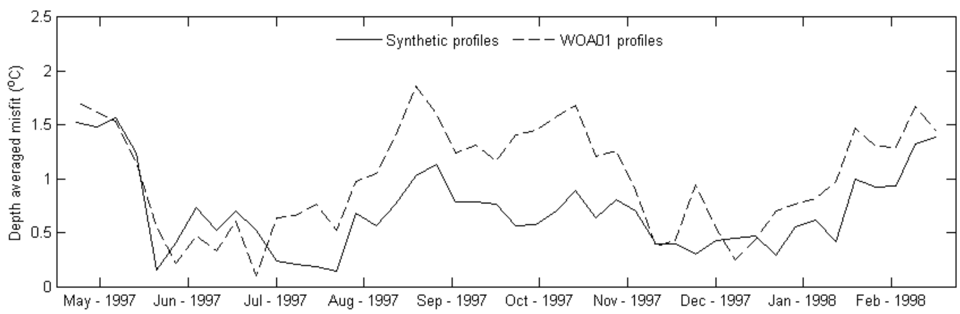

Figure 7.5: RMS between World Ocean Atlas 2001 and between SCSMEX buoy data and synthetic profile and SCSMEX buoy data for the upper 100 meters.

From figures 7.4 and 7.5 it is observed that the synthetic profiles have a smaller misfit (or a lower Root Mean Squared (RMS) error) than the climatological WOA01 profiles. For most periods, significant improvements are observed. On average, the RMS misfit decreases from 1 °C (WOA01) to 0.7 °C (synthetic profiles). In some periods, like October 1997, the averaged misfit halves.

Also, from figures 7.3 and 7.4 it is observed that improvements occur mainly in the upper 100 meters of water. Below this point, no significant improvements are observed. Since temperature processes like mixed layer or thermocline variability occur in the upper layer of water mainly (see chapter 2), this indicates that the synthetic profiling method is suitable to improve climatological temperature profiles to assess these processes.

Based on these results it is concluded that the method described by [Nardelli & Santoleri, 2004] can be used to construct synthetic profiles which are more accurate then those provided by the WOA01. As such, it is used to construct synthetic profiles at a number of points in the SCS. These profiles will be used for model validation in chapter 11. Note, however, that due to assumptions made the method is useful at a limited number of locations only. Also, because of the various types of input data required (RS SST and SSA, and climatological temperature and steric height profiles) it is labor intensive.

Part III: Model setup, sensitivity analysis and validation

In this part of the report model setup, sensitivity analysis and validation are discussed.

A 3D temperature model is setup using the Delft3D-FLOW hydrodynamic modeling package. This model should be able to resolve the processes identified in part I of this report, using forcing and validation data described in part II. It will use the SAT2SEA model as a starting point. This model is extended to include temperature and salinity processes and to resolve vertical variations. Similar as in SAT2SEA a so-called reduced-gravity approach is used. Furthermore, tides are not resolved by the model. The model setup is discussed in chapter 8.

A sensitivity analysis is performed to assess effects of relevant temperature modeling coefficients and model forcing data. This analysis is described in chapters 9 and 10 and is subdivided into a number of steps:

1. A sensitivity analysis on the relevant model coefficients for the temperature modeling and stratification. The model sensitivity is assessed based on a GoF with climatological temperature data (see chapter 9).
2. A sensitivity analysis on model temperature forcing, assessing heat flux forcing data at the free surface and open-boundary transport forcing data. Model sensitivity is assessed based on a GoF with climatological temperature data (see section 10.1).
3. A sensitivity analysis on model momentum forcing. Effects of momentum forcing at the free surface and at the open boundaries are assessed based on the correlation between model water level and altimeter SSA data (see section 10.2).
4. A sensitivity analysis on the models nudging coefficient. Effects of changing the nudging coefficient are assessed by a comparison with WOA01 profile data (see section 10.3). This coefficient specifies the relative strength of the SST nudging term (see appendix D).

In appendix I.4 an overview of model runs made during the sensitivity analysis is found.

Based on the results of this sensitivity analysis choices on model parameterization and forcing will be made for final model runs. Model results from these runs will be validated using in-situ, climatological (WOA01) and RS temperature data. Based on this, conclusions about model performance and accuracy will be drawn. This is done in chapter 11.

Chapter 8

Model Setup

In chapter 1 the goal of the SAT2SEA2 project is defined as to model South China Sea (SCS) temperature and salinity variability on a seasonal timescale and a basin-wide spatial scale. This goal is further specified as to model the seasonal mixed-layer temperature cycle. In part I of this report an overview of the processes governing this cycle was given. A summary of these processes is provided in section 8.1. These processes have to be imposed on the model by forcing data or have to result from the internal model dynamics in order to simulate the seasonal mixed-layer temperature cycle.

In order to model the processes summarized in section 8.1 data is required for model forcing and to validate model results. Where the processes provide a modeling requirement, forcing and validation data poses a model constraint. The applied data should have a sufficient spatial and temporal resolution to represent the required processes. In order to achieve this on a seasonal and basin-wide scale data is required with a synoptic coverage. As indicated in chapter 1 this coverage is provided by remote sensing and climatological datasets. In part II of this report a number of these datasets are assessed. In this chapter their application for model forcing or validation will be described.

A second constraint is posed by the model itself. The models internal dynamics should be able to resolve the relevant processes. It should also have a sufficient spatial and temporal resolution to represent these. Furthermore, it should be forced in such a way that these processes are resolved. In section 8.2, the SCS temperature model setup will be described based on these requirements.

In section 8.1 a summary is given of the large-scale processes governing the seasonal mixed-layer temperature cycle, described in more detail in part I of this report. In section 8.2 an overview of the model setup used to resolve these processes is given.

8.1 Overview of relevant processes and characteristic scales

In part I of this report the seasonal mixed-layer temperature cycle is assessed. The goal of this assessment is to identify those processes governing the seasonal SCS temperature cycle and to identify their characteristic scales. This is done based on an overview of these processes as described by literature, complemented with an assessment of available data. From this overview it is concluded that the seasonal temperature cycle of the SCS is governed by the following processes (see chapters 2 and 3):

1. **The monsoon wind system**: the SCS is governed by the monsoon wind system. From September till April the northeast (NE) monsoon prevails, with its peak in December /

January. From May till August the southwest (SW) monsoon prevails, with its peak in July / August. During the NE monsoon, wind conditions will by uniform over the entire SCS basin. During the SW monsoon the mean wind velocity over the South SCS will be higher than that over the North SCS. Furthermore, the mean wind velocity will be higher during the NE monsoon than during the SW monsoon. In the transition periods between both monsoons the mean wind velocity is smallest.

2. **Large-scale transport**: The monsoon wind will cause piling of water on the western side of the SCS basin during the NE monsoon. During the SW monsoon it will cause piling of water on the eastern side of the SCS basin. During the NE monsoon piling of water against the Vietnamese and Chinese coastlines may attribute to western boundary currents which transports colder water from the North SCS to the shallow Sunda Shelf region, following the shallow bathymetry east of Vietnam. During the NE monsoon a boundary current entering the SCS through Taiwan Strait transports cold water along the China Continental Shelf. Finally, during the SW monsoon a large-scale current originating from the Sunda Shelf will transport colder water into the central SCS.

3. **Rossby wave dynamics in the North SCS**: A Rossby wave with a one year period, which crosses the North SCS, is observed from altimeter data. In chapter 2 two tentative explanations are given about the origin of this wave. The first is based on an observed relation with atmospheric vorticity west of Luzon. The second places its origin in the Pacific Ocean. In the first case, this wave is forced locally the atmosphere, in the second case it is forced by processes outside the SCS. This Rossby wave is observed to have a one year period, synchronous with the monsoon, and attributes to large-scale water level variations in the North SCS. During the NE monsoon mixing attributed to this wave might increase the North SCS's response to cold water influx through Taiwan Strait.

4. **The surface heat flux**: Warming or cooling of surface water by the surface heat flux follows a seasonal cycle, related mainly to the annual shortwave, seasonal cloud coverage and seasonal monsoon wind cycles. The net effect of these contributers results in a net flux which has maximums during the monsoon transition periods and minimums during the monsoon highs. During the NE / SW monsoon transition period a maximum influx is observed. This heat flux will have the characteristic scales of its forcing processes. As such, it is latitude dependent based on its relation with the shortwave flux and spatially dependent based on its relation with the wind magnitude and cloud coverage. In both cases, higher values are observed in the South SCS during the SW monsoon.

5. **Influx through Luzon and Taiwan Strait**: At Luzon Strait temperature and salinity mixing with the Kuroshio current is observed. This mixing is stronger during the NE monsoon which can be attributed to advantageous wind conditions. Because of this, the Kuroshio bulges into the SCS south of Taiwan. Furthermore, cold water enters the SCS via Taiwan Strait during the NE monsoon. This water is transported westwards over the shallow China Continental Shelf by a boundary current. This boundary current has a one year period, synchronous to the monsoon.

6. **Upwelling due to bathymetry constraints**: The large-scale circulation system will cause upwelling of sub-surface water due to bathymetry constraints. During both the NE and SW monsoons upwelling is observed along the China Continental Shelf / Oceanic Plate interface. During the SW monsoon, upwelling of colder water is observed along the southern Vietnamese coast.

7. **Variations in mixed layer depth due to stratification**: In the central SCS stratification is observed throughout the year. In the southern regions the stratification shows a seasonal signal modulated by the seasonal wind magnitude and heat flux cycles. In the northern regions mixing caused by the observed Rossby wave may play a role also. A mean thermocline depth between 45 and 80 meters is observed in this region. In the shallow SCS regions over

the Sunda Shelf stratification occurs on a seasonal basis, modulated by the monsoon wind and the heat flux. During the monsoon transition periods stratification is observed, which can be attributed to lower wind speeds and a larger heat flux. During the monsoon periods, this stratified system breaks down due to the increased wind speed and the decreased heat flux. Finally, in the shallow SCS regions over the China Continental Shelf seasonal stratification is modulated by the heat flux and by horizontal temperature transport. During the SW monsoon period stratification is observed. This stratified system breaks down rapidly during the NE monsoon onset due to temperature transport originating from Taiwan Strait.

It should be noted that the focus of this project is on seasonal mixed-layer temperature on a basin-wide scale. This implies that processes on a smaller spatial and temporal scales which do not effect this cycle significantly are not taken into account (see chapter 1). Among these processes are tides and influx from the Mekong and Pearl River.

Similarly, only the large-scale temperature transport and mixing at Luzon and Taiwan Strait is assessed. Processes on smaller scales, like mesoscale eddies entering the SCS through Luzon Strait, are not taken into account.

Furthermore, the large-scale circulation and transport described above is assessed with regard to its role in the seasonal temperature cycle. Because of this an accurate representation of these processes in themselves is not a goal of this project. The boundary currents along the Chinese and Vietnamese coastlines are assessed with regard to transport of colder water in these regions only. Similarly, the Rossby wave in the North SCS is assessed with regard to large-scale mixing effects influencing the upper-layer temperature only. A more detailed assessment of this wave is a study in itself and as such beyond the scope of this project.

Also, stratification is assessed with regard to its influence on the mixed-layer temperature. Because of this an accurate representation of the thermocline depth is not a goal in itself. In a similar manner, the lower-level water temperature below the thermocline is of secondly importance with regard to the mixed-layer temperature.

Finally, upwelling of sub-surface water against the Continental Shelves is assessed with regard to its influence on the mixed-layer temperature cycle. An accurate representation of this process will require a detailed model grid in these regions due to the steep incline at the Continental Shelf / Oceanic Plate interface. For practical reasons the model grid resolution used during this project will be insufficient to resolve this at some locations (see section 8.2.3).

Summarizing, the model should be able to simulate items 1, 2, 4, 5 and 7. The model grid is too coarse to accurately model item 6. Furthermore, modeling of item 3 is a study in itself and beyond the scope of this project.

8.2 Model setup

In the previous section the processes governing the SCS mixed-layer temperature cycle are described. In order to model this cycle these processes have to be resolved by the model. This has several implications on the models setup. It should have a sufficient spatial and temporal resolution to represent the desired processes. Also, it should be forced in such a way that these processes are resolved. Furthermore, the models setup should be such that its internal dynamics provide an adequate representation of these processes. In this section these issues will be addressed.

First, an overview of requirements on Delft3D-FLOW needed to resolve the seasonal mixed layer cycle is given in section 8.2.1. This is based on the physical processes governing this cycle described in section 8.1. Second, model boundary forcing and validation using the datasets described in part II will be discussed in section 8.2.2. The availability and resolution of this data poses a constraint on the processes the model will able to resolve, thus placing a constraint on the model setup. Based on these constraints the models spatial resolution, both in horizontal and vertical direction, will be addressed in section 8.2.3. The models temporal resolution is subsequently assessed in section 8.2.4. Finally, in section 8.2.5 a number of relevant model parameters influencing its forcing and internal representation are described.

8.2.1 Delft3D-FLOW process representation

To model the SCS mixed-layer temperature cycle the Delft3D-FLOW modeling package will be used. This package solves the three-dimensional shallow water equations describing free-surface flows [Delft3D, 2005]. Using Cartesian rectangular coordinates in the horizontal and σ-coordinates in the vertical, the momentum equations are described by [Delft3D, 2003]:

$$\frac{\partial u}{\partial t} + u\frac{\partial u}{\partial x} + v\frac{\partial u}{\partial y} + \frac{\omega}{d+\zeta}\frac{\partial u}{\partial \sigma} - fv = -\frac{1}{\rho}P_u + F_u + \frac{1}{(d+\zeta)^2}\frac{\partial}{\partial \sigma}\left(\nu_v\frac{\partial u}{\partial \sigma}\right) \tag{8.1}$$

$$\frac{\partial v}{\partial t} + v\frac{\partial v}{\partial x} + v\frac{\partial v}{\partial y} + \frac{\omega}{d+\zeta}\frac{\partial v}{\partial \sigma} + fu = -\frac{1}{\rho}P_v + F_v + \frac{1}{(d+\zeta)^2}\frac{\partial}{\partial \sigma}\left(\nu_v\frac{\partial v}{\partial \sigma}\right) \tag{8.2}$$

The vertical velocity ω in the σ-coordinate system is computed from the continuity equation

$$\frac{\partial \zeta}{\partial t} + \frac{\partial[(d+\zeta)U]}{\partial x} + \frac{\partial[(d+\zeta)V]}{\partial y} = Q \tag{8.3}$$

by integrating in the vertical from the bottom to a level σ (-1 $\leq \sigma \leq 0$). In the above equations $u(x,y,\sigma,t)$, $v(x,y,\sigma,t)$ and $w(x,y,\sigma,t)$ are the velocity components in the horizontal x,y and vertical σ-directions, respectively; $\zeta(x,t)$ is the water level above a reference plane; $d(x,y)$ is the depth below this plane; $H(x,y) = d(x,y)+\zeta(x,y)$ is the total water depth; t is the time and f is the Coriolis parameter; P_u and P_v describe horizontal pressure terms; F_u and F_v describe horizontal viscosity terms; ν_v is the vertical eddy viscosity coefficient, which is determined by a turbulence closure model. Furthermore, Q represents the contribution per unit area due to the discharge or withdrawal of water, precipitation and evaporation and U and V represent the depth-averaged velocities.

Delft3D-FLOW solves the transport of matter and heat by an advection-diffusion equation in three coordinate directions. Source and sink terms are included to simulate discharges and withdrawals. In Cartesian coordinates in the horizontal and in σ-coordinates in the vertical, the transport equation reads:

$$\begin{aligned} \frac{\partial[(d+\zeta)C]}{\partial t} + \frac{\partial[(d+\zeta)uC]}{\partial x} + \frac{\partial[(d+\zeta)vC]}{\partial y} + \frac{\partial(\omega C)}{\partial \sigma} = \\ \left[\frac{\partial}{\partial x}\left(D_h(d+\zeta)\frac{\partial C}{\partial x}\right) + \frac{\partial}{\partial y}\left(D_h(d+\zeta)\frac{\partial C}{\partial y}\right)\right] + \frac{1}{d+\zeta}\frac{\partial}{\partial \sigma}\left[D_v\frac{\partial C}{\partial \sigma}\right] - \\ \lambda_d(d+\zeta)C + (d+\zeta)(q_{in}C - q_{out}C) + Q_{tot} \end{aligned} \tag{8.4}$$

where concentration C represents either dissolved substances, salinity or heat; D_h and D_v indicate the horizontal and vertical diffusivity, respectively; λ_d represents first order decay processes and Q_{tot} represents the exchange of heat through the free surface.

Based on the physical processes described in section 8.1, Delft3D-FLOW should meet the following requirements:

1. It has to take into account the space and time varying wind and atmospheric pressure system. This is done in Delft3D-FLOW by imposing free surface boundary conditions for the momentum equations:

$$\frac{v_H}{H}\frac{\partial u}{\partial \sigma}\bigg|_{\sigma=0} = \frac{1}{\rho_0}\left|\vec{\tau_s}\right| cos(\theta) \tag{8.5}$$

$$\frac{v_H}{H}\frac{\partial v}{\partial \sigma}\bigg|_{\sigma=0} = \frac{1}{\rho_0}\left|\vec{\tau_s}\right| sin(\theta) \tag{8.6}$$

   where θ is the angle between the wind stress vector and the local coordinate direction; $\vec{\tau_s}$ represents the wind shear-stress. Both θ and $\vec{\tau_s}$ are prescribed by space and time varying wind fields.

   Atmospheric pressure forcing is imposed by the horizontal pressure terms in equations 8.1 and 8.2 as prescribed by equations 8.7 and 8.8. The atmospheric pressure gradients dominate the external forcing at peak winds during storm events [Delft3D, 2005]. Similar to the wind fields, atmospheric pressure is prescribed by space and time varying fields.

2. It should be able to resolve temperature and salinity transport (equation 8.4). Delft3D-FLOW takes into account baroclinic flow, attributed to non-uniform density distributions, by the horizontal pressure gradients in equations 8.1 and 8.2:

$$\frac{1}{\rho}P_u = g\frac{\partial \zeta}{\partial x} + \frac{1}{\rho_0}\frac{\partial P_{atm}}{\partial x} + g\frac{d+\zeta}{\rho_0}\int_{\sigma}^{0}\left(\frac{\partial \rho}{\partial x} + \frac{\partial \sigma}{\partial x}\frac{\partial \rho}{\partial \sigma}\right) d\sigma' \tag{8.7}$$

$$\frac{1}{\rho}P_v = g\frac{\partial \zeta}{\partial y} + \frac{1}{\rho_0}\frac{\partial P_{atm}}{\partial y} + g\frac{d+\zeta}{\rho_0}\int_{\sigma}^{0}\left(\frac{\partial \rho}{\partial y} + \frac{\partial \sigma}{\partial y}\frac{\partial \rho}{\partial \sigma}\right) d\sigma' \tag{8.8}$$

   where ρ_0 represents the ambient density of water; the first term in equation 8.7 and 8.8 represents the barotropic effect; the second term the effects of atmospheric pressure forcing; the third term describes the baroclinic influence.

3. It should be able to resolve the net heat flux cycle at the free surface (Q_{tot} in equation 8.4). Q_{tot} is determined by the Delft3D-FLOW Ocean heat flux model from space and time varying atmospheric input fields (see appendix C.1).

4. It should be able to resolve (lateral) transport forcing and circulation forcing at the open boundaries. In Delft3D-FLOW open boundary forcing can be prescribed by both water level (ζ) and velocity (U) data. These are prescribed in a time varying way at the open boundary end-points and act as boundary conditions for equations 8.1, 8.2 and 8.3. In a similar way, (lateral) transport forcing is imposed by specifying time varying values of concentration C at the open boundary end-points. These act as boundary conditions for equations 8.4.

5. It has to resolve large-scale effects attributed to bathymetry constraints. In Delft3D-FLOW bathymetry constraints are imposed by closed model boundaries representing coastlines. The flow component normal to these boundaries is set to zero and acts as a boundary condition to equations 8.1 and 8.2. The model depth is prescribed by space varying bathymetry data. Shear-stress at the bed level can be prescribed by a number of formulations (see [Delft3D, 2005]).

6. It has to resolve vertical temperature variability and stratification of the water column. In Delft3D-FLOW vertical layers can be applied using a σ grid convention (see section 8.2.3). Vertical temperature transport over the model layers is determined from the advection-diffusion relations in equation 8.4. Stratification subsequently follows from the models vertical density representation, which is determined from the models temperature and salinity

based on the equation of state. Vertical mixing through the thermocline is determined by a turbulence-closure model.

8.2.2 Model forcing and validation

With regard to the processes indicated in the previous section, model forcing should be applied to impose those processes which originate from outside the model domain. These processes are the momentum transfer and pressure loading at free surface, the heat exchange at the free surface and momentum and transport forcing at the open boundaries. The characteristic scales of the data used to force these processes should be sufficient to resolve the physical processes identified in section 8.1. Below, the model forcing data applied to resolve these processes is described. An overview of the datasets from which these data are obtained in provided in part II or this report.

Wind and pressure forcing

As indicated in section 8.1, space and time varying wind forcing should be applied to resolve the large-scale monsoon driven circulation. Also, this data is required to determine the net heat flux at the free surface.

Based on a data comparison study in part II, space and time dependent ECMWF ERA-40 wind and pressure data will be applied for model forcing. This data has a spatial resolution of 2.5 by 2.5 degrees, and a minimum temporal resolution of 6 hrs. Based on the assessment in chapter 2, these resolutions are sufficient to resolve the large-scale monsoon system and its seasonal cycle. Also, these resolutions are sufficient to resolve the large-scale seasonal heat flux cycle. Furthermore, these resolutions are sufficient to impose the basin-scale water level 'tilting', which follows a seasonal cycle. It should also enable the formation of large-scale eddies (around 300 kilometers) by atmospheric forcing.

As described in part II two sets of ECMWF wind and pressure forcing data are applied (see chapter 4). The first consists of monthly composites representing climatological condition over the period 1983-2001. The other consists of forcing data for the year 2000 at 6 hrs intervals. In both cases, the large-scale monsoon cycle is resolved. In the case of the monthly-mean fields variability on smaller time-scales is unresolved, though. In chapter 10 differences between these forcing data are assessed by means of a model sensitivity analysis.

Heat flux forcing

In Delft3D-FLOW, the surface heat flux is calculated using a heat flux model. A number of different heat flux models are implemented in this package. In this project, the Ocean heat flux model will be used. This model is considered the 'best of' in Delft3D-FLOW and provides the possibility to apply the required space and time dependent heat flux forcing. In appendix C an overview of this model is provided.

As indicated in section 8.1, the net heat flux governs the seasonal temperature cycle in the South SCS. The seasonal cycle of the heat flux is modulated by the shortwave flux, cloud coverage and monsoon wind cycles. The heat flux model calculates the shortwave flux based on theoretical relations which are latitude dependent. As such it resolves the shortwave flux cycle. Space and time varying cloud coverage and wind are applied as input fields. Furthermore, the Ocean heat flux model requires the air temperature and relative humidity as input fields. These, too, are applied in a space and time dependent way.

Similar to the wind and pressure forcing, ECMWF ERA-40 data will be applied for heat flux forcing (see chapter 4). This data has a spatial resolution of 2.5 by 2.5 degrees and a minimum temporal resolution of 6 hrs. These resolutions are sufficient to resolve the large-scale, seasonal heat flux cycle.

Again, two sets of ECMWF wind and pressure forcing data are applied. The first consists of monthly composites representing climatological condition over the period 1983-2001. The other consists of forcing data for the year 2000 at 6 hrs intervals. In both cases, the large-scale heat flux cycle is resolved. In chapter 9 differences between these forcing data are assessed by means of a model sensitivity analysis.

Transport forcing at the open boundaries

As described in section 8.1, exchange with surrounding systems occurs through Luzon and Taiwan Strait. At Luzon Strait, mixing with warmer, high salinity Kuroshio water is observed during the NE monsoon. During this period, the Kuroshio bulges into the SCS, which can be explained by the prevailing wind conditions. This effect is most pronounced south of Taiwan. At Taiwan Strait, cold water intrudes into the SCS. During the NE monsoon, this water is transported along the shallow Chinese coastline, forming a front of cold water. During the SW monsoon, effects of this intrusion are less significant.

At both boundaries, temperature and salinity transport forcing has to be applied to account for large-scale mixing and influx processes. From the datasets assessed in part II, the World Ocean Atlas 2001 (WOA01) is the only one able to provide data at these scales and describing lateral temperature and salinity variations. The latter is required due to the significant depth at Luzon Strait (Note that the model is truncated at 300 meters depth, see section 8.2.3). Applying uniform transport forcing at this boundary will result in large discrepancies at either upper of lower depth levels. At Taiwan Strait these discrepancies will be smaller due to the shallower depth. The WOA01 provides monthly-mean climatological data with a maximum resolution of 0.25 degrees. These resolutions are sufficient to resolve the observed seasonal cycles at these boundaries. They are insufficient to resolve intrusions on smaller scales, like heat eddies entering the SCS via Luzon Strait. Furthermore, with regard to the dimensions of these Straits (over 2 degrees each) the spatial resolution is sufficiently high.

WOA01 data is prescribed at fixed depth levels, the spacing of which increases with depth. This data is linearly interpolated to the model grid in both the horizontal and vertical directions. It is subsequently prescribed as vertical profiles in Delft3D-FLOW [Delft3D, 2005]. This means that at the open boundary end-points temperature and salinity are prescribed with time and vertically varying data. Delft3D-FLOW subsequently calculates temperature and salinity values at non-end point cells by means of linear interpolation between the boundary end points. This implies that small scale intrusions are unresolved by this forcing data. For the described large-scale intrusions this does not pose a problem, since in the case of Luzon Strait effects are most significant south of Taiwan (or, on the northern edge of the Strait). In the case of Taiwan Strait large-scale temperature variations occur over the entire span of the strait.

Finally, it should be noted that this transport forcing consists of climatological mean data. As such, using this forcing data can result in discrepancies between model and historic data. This approach is justified, however, because obtaining historical transport forcing with a sufficient temporal and spatial coverage for all open boundaries of the SCS will be extremely difficult. Certainly when considering the sparse amount of in-situ data available. As such, using climatological data is believed to be the only realistic alternative.

Momentum forcing at the open boundaries

Next to transport forcing, momentum forcing is applied at the Luzon and Taiwan Strait boundaries to account for large-scale circulation interaction with the surrounding systems. As described in section 8.1, the Kuroshio bulges into the SCS during the NE monsoon. This effect is most pronounces at the northern edge of this strait. At Taiwan Strait the flow conditions are less clear, which might partially be explained by the lower quality of the altimeter data in this region. Literature reports on a boundary current entering the SCS through this strait during the NE monsoon (see chapter 2).

To account for momentum forcing at the open boundaries water level forcing is applied at these locations. This forcing is obtained from altimeter data and is applied to at the edges of these straits. As such, small-scale intrusions are unresolved by this forcing data. Furthermore, the quality of this data will be of lesser quality at the Taiwan Strait boundary, due to the larger error in the altimeter measurements in this region.

Initially, water level forcing from the SAT2SEA project will be used. This forcing data is obtained from Topex/Poseidon altimeter data [Gerritsen *et al.* , 2001]. The data as applied during this project has a temporal resolution of one month and is determined by averaging 6 years of SAT2SEA data (1993 - 1999, without the 1998 El Ninõ year). This is sufficient to model the large-scale processes at these boundaries. Furthermore, water level forcing is obtained from the DUACS dataset (see chapter 5). This data has a temporal resolution of one week. It is prescribed at the end-points of each boundary. Because of this small scale variability occurring between these boundaries remains unresolved.

In chapter 10 the differences between the SAT2SEA and DUACS forcing data are assessed by means of a model sensitivity analysis.

Model validation data

The model temperature will be assessed using climatological data from the WOA01 (see chapter 4). This is motivated by the synoptic coverage of this dataset, enabling the validation of basin-scale temperature behavior on seasonal time-scales. It is also motivated by the small amount of SCS in-situ data obtained during this project. The WOA01 data represents monthly-mean climatological conditions, and has a maximum spatial resolution of 0.25 degrees. As such, temperature variability on smaller spatial and temporal scales cannot be validated. This is not a problem considering the scales of interest to this project.

In part II climatological WOA01 data is compared with historic in-situ data to assess the possibility of applying WOA01 data for historic model validation (see chapter 6). From this comparison it is concluded that WOA01 data is suitable for historic model validation if the WOA01 standard deviation is included in the analysis. This standard deviation gives realistic bounds for historic values. This holds for temperature mainly. For salinity a significant discrepancy with historic values is observed. Note that the 0.25 degree WOA01 dataset has no accompanying standard deviation data. As such, the 1 degree WOA01 dataset is used when the standard deviation data provided extra information.

Also, WOA01 data is specified at fixed depth levels. These pose a constraint on the ability to validate vertical temperature variability. This is assessed in section 8.2.3.

DUACS Altimeter data will be used to assess the large-scale model circulation (see chapter 5). The data used has a 1 degree resolution, which is interpolated to the model grid, and consists of monthly-mean conditions. As such, water level variability on small temporal (below seasonal) and spatial (below 1 degree) scales cannot be validated using this data. This is not a problem because this project assesses processes on seasonal and basin-wide scales.

Furthermore, in-situ data from the ASIAEX and SCSMEX projects is used for model validation (see chapter 4). In both cases, data is available for the year 2000. As such, historic model runs will be done for this year. This data is available at a small number of points only (see appendix I.5). As such, it will only be used to obtain an estimate of model accuracy. Large-scale model behavior is not assesses using this data. Also, in chapter 7 a method to determine synthetic temperature profiles from remote sensing and climatological data is discussed. This method is used to determine synthetic profiles at a limited number of model locations. These profiles are determined for the year 2000 and will be used in a similar way as the in-situ data.

Finally, remotely sensed SST fields, obtained from the AVHRR / Pathfinder dataset (see chapter 5), are used to assess the models surface temperature variability. This data has a high temporal resolution (4.9 km). Due to high cloud coverage over the SCS it has a useful temporal resolution of 1 month. As indicated in chapter 5 a so-called representation error can occur when comparing this data with other surface layer temperature data. This error occurs because AVHRR SST data represents the temperature of the upper 1 meter of water. In the next section it is described that the model will have a maximum surface layer thickness of 15 meters. As such, the models surface layer temperature will be underestimated with respect the the AVHRR SST. From a comparison of climatological monthly-mean AVHRR SST data with monthly-mean WOA01 data a mean error smaller than 1 °C is observed over the SCS basin.

8.2.3 Model spatial resolution: grid and vertical layering

As mentioned in chapter 1, SAT2SEA2 is a follow on of the SAT2SEA project. The SCS model grid used during that project is used as a starting point in this project. Table 8.1 gives a summary of the geographical extent and the horizontal resolution of this model.

SAT2SEA South China Sea grid	
Model domain West-East direction	between 95° E.L. and 126° E.L
Model domain South-North direction	between −9° N.L. and 24° N.L.
Grid	
Grid spacing	1/4° by 1/4° (spherical)
Number of grid points West-East direction	124
Number of grid points South-North direction	133
Origin of grid	(−8.875 N.L. 95.125 E.L.)

Table 8.1: Overview of the geographical extent and the horizontal resolution of the SAT2SEA Delft3D-FLOW grid.

Geographic extent and horizontal resolution

In appendix I.1 a graphic overview of the geographic extent of this grid is shown. From this appendix and from the values in table 8.1 it is observed that the grid includes both the SCS and the Indonesian Archipelago. The grid has open boundaries at all straits indicated in appendix I.1.

As summarized in section 8.1 the focus of the SAT2SEA2 project is on the SCS. As such, temperature variability in the Indonesian Archipelago will not be assessed. Furthermore, Luzon and Taiwan Strait were identified as the only open boundaries with a significant influence on the SCS mixed-layer temperature cycle. As such, the focus of open boundary forcing is at these boundaries primarily.

The SAT2SEA grid has a uniform horizontal grid size of 27.7 km (0.25 degrees). According to [Delft3D, 2005] 5 grid cells are required to adequately resolve a geometric or hydrodynamic phenomenon. Furthermore, to resolve horizontal circulation the grid size should be 1/10 th or less of the size of the circulation. With these guidelines in mind, the following is concluded about the processes described in section 8.1:

First, this resolution is sufficient to represent the large-scale, space-varying monsoon and heat flux cycles. As explained in chapter 2, these show variations on a ‘sub-basin’ scale (different in North and South SCS). Also, both the wind and heat flux forcing data used have a 2.5 degree spatial resolution. With regard to this resolution a higher model resolution will not provide more realistic results.

Second, the resolution of continental shelves along the Chinese and Vietnamese coastlines is coarse (2 to 5 grid points in the direction toward the Oceanic Plate). The boundary currents run parallel to these coastlines, though. In this direction the resolution is sufficient to represent boundary currents forced by large-scale events, like piling of water against the western SCS boundaries during the NE monsoon.

Third, the resolution at the open model boundaries at Luzon and Taiwan Strait is sufficient to represent the large-scale circulation and transport processes indicated in section 8.1 (over 10 grid points each). Note that this resolution is too coarse with regard to small scale features entering the SCS. With regard to the transport and circulation forcing data at these boundaries (monthly or weekly means prescribed at the boundary end-points) a higher resolution will not provide more realistic results.

Fourth, the resolution is too coarse to represent the steep incline at Continental Shelf and Oceanic Plate interfaces. As observed from figure I.1, a decrease in depth of over 200 meters is observed over a horizontal span of 2 grid points. In reality, this incline will be even steeper since the model bathymetry is truncated. This implies that the effects of upwelling of colder sub-surface water against these boundaries may be inadequately represented. The impact of this on the model results will be assessed in chapter 11. This coarse resolution is accepted on the basis that a substantial increase in model resolution will be required to improve it, which will result in a strong increase in model computation time. Since the project focus is on modeling large-scale mixed-layer this is unrealistic.

Finally, the model results will be validated using 0.25 degree WOA01 temperature data and 1 degree DUACS water level data, mainly. These resolutions are insufficient to validate features on smaller spatial scales. Because of this, small-scale model variability resolved by an increase in horizontal resolution beyond 0.25 degrees cannot be validated.

Reduced-gravity approach and vertical model resolution

Similar as in SAT2SEA a so-called reduced gravity approach is used. This means that the models bathymetry is truncated at a specified depth. Because of this truncation the propagation speed $\sqrt{gH}$ of barotropic waves decreases, which distorts the propagation of barotropic processes like tides. This is permitted because the effects of tides are not taken into account during this project (see section 8.1). Furthermore, this is justified because the phase speed of motions in quasi-geostrophic balance is reduced negligibly [Gerritsen *et al.* , 2001].

In the reduced-gravity approach it is assumed that below the level of the thermocline vertical transport is limited. By truncating the model below this level, unresolved energy dissipation to deeper levels is assumed negligible. This assumption is required because Delft3D-FLOW imposes a zero-flux condition at the bed level, which in this case is the truncation interface. During SAT2SEA the model was truncated at 150 meters depth on the basis that the thermocline is always above this level.

The reduced-gravity approach is required because of the significant SCS depth: at the basin center a depth of over 4 kilometer is reached (see appendix G.2). If this bathymetry is included in the model, a small time step will be required to keep the Courant number within bounds. By truncating the model at a shallower depth the Courant number is reduced significantly, allowing for a larger time step.

In chapter 2 it is confirmed that the SCS thermocline is always above 150 meters depth. It is also shown, however, that at this depth level the vertical temperature gradient has a seasonal signal. From 300 meters depth onwards no seasonal signal is observed. As such, two truncation depths will be assessed in chapter 9. One at 150 meters, based on the assumption that the thermocline is always above this level. The other at 300 meters, based on the assumption that at this depth no seasonal temperature variability occurs. Note that in both cases a vertical temperature gradient is still observed. Heat transfer to lower levels by this gradient is unresolved by the model, which can lead to a build-up of heat in lower model layers. This is justified because the main focus of this project is on mixed-layer temperature, and a possible build-up of heat will occur below the thermocline level.

In appendix I.1 the models bathymetry, truncated at 300 meters, is shown. This data is used for the model truncated at 300 meters, and is obtained from the ETOPO5 dataset (the official, public US Navy bathymetry [ETOPO5, n.d.]). For the model truncated at 150 meters the bathymetry provided by the SAT2SEA project is used. This originates from a so-called blended dataset (data from multiple sources was used).

An additional argument in favor of the reduced gravity approach is based on the requirement to model vertical temperature variability. The models vertical resolution should be sufficient to represent the seasonal, basin-scale cycle of the mixed-layer temperature. For the Delft3D-FLOW model a so called σ layer convention is used to specify this vertical resolution, meaning it is defined per grid point as a percentage of the total depth. This percentage is fixed over the entire model domain. Due to the large differences in depth over the SCS domain this will result in significant differences in vertical resolution if the true depth is included in the model. To solve this either more layers should be included, increasing the computation time, or the layer distribution in the shallow model regions becomes coarse.

In chapter 2 a mean thermocline depth between 45 and 80 meters in observed in the central SCS. Furthermore, a maximum thermocline depth between 100 and 120 meters is observed in this region. Since the mixed layer is situated above the thermocline the model should have sufficient resolution to represent variability in this region. Furthermore, WOA01 temperature profiles will be used to validate modeled temperature. This data is specified at fixed depth level. In the upper water column these levels are defined at 0, 10 , 20, 30, 50, 75, 100, 125 and 150 meters. Since this data is rather coarse in the regions were seasonal thermocline variability is observed an accurate representation of the thermocline depth is of secondary importance as long as the seasonal stratification cycle is resolved. In the deep SCS basin an equidistant vertical layer spacing of 15 meters is applied, resulting in 10 layers in the upper 150 meters of the water column. Based on conclusions in [De Goede *et al.* , 2000] this resolution is sufficient to resolve the large-scale stratification (while it is too coarse to provide an accurate representation of the thermocline depth). In the mixed-layer region this layer distribution result in 3 to 6 layers. Since the temperature is relatively uniform in this region due to mixing [Mellor, 1996], it is concluded that this resolution is sufficient to resolve large-scale vertical variability in the mixed-layer. Also, in this region validation data is available at 6 depth levels only. As such, variability on smaller vertical scales cannot be validated. Because of the σ layer convention used a layer depth of 15 meters in the central SCS results in a total of 10 layer for the truncation depth of 150 meters (10 % of the total depth per layer). For the truncation depth of 300 meters this will result in a total 20 layer (5 % of the total depth per layer). In both cases this spacing will result in a higher vertical resolution in the shallow model regions over the continental shelfs. While the higher resolution in these regions may be sufficient to accurately resolve the thermocline depth, the validation data is too coarse to validate this. In chapter 9 differences between the 150 and 300 meters truncation depth will be assessed.

8.2.4 Model temporal resolution: time step, initial conditions and spin-up

Model timestep

Delft3D-FLOW poses a number of limitations on the allowable model step size due to stability and accuracy requirements for the time integration of the shallow water equations. These requirements are different for barotropic and baroclinic processes.

As described in section 8.2.1, baroclinic flow resulting from a non-uniform density distribution should be resolved. Because of this the model step size should adhere to the baroclinic stability requirement, specified by [Delft3D, 2005] as:

$$2\Delta t\sqrt{\frac{\Delta\rho}{\rho}gH\left(\frac{1}{\Delta x^2}+\frac{1}{\Delta y^2}\right)} < 1 \tag{8.9}$$

Furthermore, barotropic wind-driven flow should be resolved at the shallow model regions over the Sunda Continental Shelf (see section 8.2.1). In these regions no truncation is applied and barotropic wave propagation can be resolved if the accuracy requirement for barotropic flow is met. This requirement is specified by [Delft3D, 2005] as:

$$C_f = 2\Delta t\sqrt{gH\left(\frac{1}{\Delta x^2}+\frac{1}{\Delta y^2}\right)} < 10 \tag{8.10}$$

In equations 8.9 and 8.10, Δx and Δy indicate the model grid dimensions. As described in section 8.2.3, a grid size of 27.7 km in both directions is applied. Furthermore, H denotes the model depth. For the baroclinic stability the maximum depth at the deep SCS basin provides a maximum bound. This depth is specified at either 150 or 300 meters (see section 8.2.3). For the barotropic mode a maximum bound is specified by the shallow bathymetry over the continental shelves, which is below 100 meters mostly. Subsequently, g indicates the gravitation constant which has a value of 9.8. In equation 8.10, C_f indicates the Courant number for wave propagation. For practical barotropic application in Delft3D-FLOW a Courant number below 10 is advised for accuracy [Delft3D, 2005].

Furthermore, in equation 8.9, $\frac{\Delta\rho}{\rho}$ indicates the fraction between the density gradient and the density. The maximum value of this fraction specifies the upper bound of the stability requirement for the baroclinic mode. This value is determined from WOA01 temperature and salinity data. Using an algorithm described in appendix E the monthly-mean density is calculated at all model grid points and layers. Subsequently, the maximum density gradient is determined using a central differencing scheme. This data is used to determine the maximum value of $\frac{\Delta\rho}{\rho}$. A maximum of $4.2 \times 10^{-4} m^{-1}$ is found this way.

For the truncation depth of 150 meters a maximum time step of roughly 7 hrs is found from the baroclinic requirement. The barotropic requirement allows a maximum time step of about 1 hrs and 40 minutes. For the truncation depth of 300 meters a maximum time step of roughly 5 hrs is obtained from the barotropic requirement. Again, the barotropic requirement allows for a maximum time step of about 1 hrs and 40 minutes. In both cases, an upper time step bound results from the barotropic requirement. Based on these results a time step of 2 hrs will be applied, since in most cases the model depth will be shallower than 100 meters over the shallow model regions.

According to [Delft3D, 2005] at least 40 time steps are required per wave period of a feature. As such, features with a wave period larger then 3 days are resolved by the model. Since the processes mentioned in section 8.1 occur on seasonal temporal scales this temporal resolution is sufficient.

As indicated in section 8.2.2 and discussed in part II, a limited amount of in-situ validation data (ASIAEX and SCSMEX datasets) is available for the year 2000. Furthermore, it is described that climatological WOA01 data will be used for model validation. Based on this, model runs will be performed for both a climatological year (using climatological forcing data) and for the historic year 2000.

Finally, it should be noted that for initial model runs (HF-C1a till HF-H1e, see appendix I.4) a time step of 45 minutes was used, based on an incorrect calculation of the barotropic criterion. All other runs (HF-H1f till N-F) apply a time step of 2 hrs.

Model initial conditions and spin-up

According to [Wang *et al.* , 2004] SCS salinity has a circulation period of about 50 years. High salinity water enters the SCS via Luzon Strait and follows a 50 years cycle through the SCS before exiting though Luzon Strait again. Based on these conclusions, a significant model spin-up time will be required before a steady state is achieved when uniform initial model conditions are used and salinity transport forcing is applied at Luzon Strait. Note that for temperature this problem will be smaller, since temperature is primarily a vertical processes forced at the free surface, while salinity is primarily a horizontal process, forced at the open boundaries. Since the horizontal dimensions of the grid are significantly larger than its vertical dimensions, salinity spin-up will take considerably longer.

To decrease the spin-up time the models initial conditions are obtained from the WOA01 (see chapter 4). Annual-mean climatological temperature and salinity fields from the WOA01 are linearly interpolated to the model grid, averaged over each model layer based on the local depth and the applied layer definition and subsequently prescribed as initial conditions. As such, the model will start from the annual-mean SCS state, which decreases the spin-up time considerably, saving computation time. Also, the cumulative effect of forcing errors is reduced due to a smaller spin-up period. Bases on the assumption that the model circulation will spin-up rapidly it will start from rest conditions [Delft3D, 2005].

Model test runs using climatological ECMWF heat flux, wind and pressure forcing and SAT2SEA water level forcing (see section 8.2.2) indicate that a spin-up time of one year if sufficient to suppress transient model startup effects related to discontinuities between the annual-mean initial conditions and January boundary forcing. In the model regions above the thermocline a steady state is achieved after this period. In the model regions below the thermocline a build-up of temperature is observed and no steady state conditions are reached at this point (this will be discussed in chapter 11). To minimize this effect a one-year spin-up period is used for model runs in subsequent chapters.

Finally, using 20 vertical layers and a time-step of 2 hrs, a one year model run takes 3 hrs on a 3.6 GHz PC running on a Linux Operating System.

8.2.5 Model coefficients important for the SCS temperature model

Delft3D-FLOW specifies a number of coefficient by which the magnitude of model forcing or the representation of internal model processes can be controlled. A number of these coefficients are assessed in this project based on their relevance to the applied model forcing and (temperature) mixing due to turbulent processes. These are:

1. The Stanton number (c_h), a transfer coefficient which controls the magnitude of the convective heat flux (see appendix C.1).

2. The Dalton number (c_e), a transfer coefficient which controls the magnitude of the evaporative heat flux (see appendix C.1).

3. The Ozmidov length scale (L_{inf}), which specifies the magnitude of turbulent mixing by internal waves (see appendix C.2).

4. The wind drag coefficient (C_d), which specifies the magnitude of the surface wind stress τ according to $\tau = C_d \rho_a |U_{10}|^2$ [Delft3D, 2005].

5. The horizontal diffusivity and viscosity, which specify the magnitude of turbulent mixing on a sub-grid scale, based on a turbulence closure model. During this project the k-ϵ model is used [Delft3D, 2005].

These coefficients will assessed by means of a model sensitivity analysis. In chapter 9 the Stanton and Dalton number will be assessed. Also, the Ozmidov length scale, horizontal diffisivity and horizontal viscosity will be assessed in this chapter. The wind drag coefficient is assessed in both chapters 9 and 10.

Finally, for the bottom roughness a Manning coefficient of 0.026 (in both directions) is applied, based on conclusions in [Gerritsen *et al.* , 2001].

Chapter 9

Sensitivity analysis on model coefficients

In section 8.2.5 the most relevant model coefficients were described by which the magnitude of model forcing or the representation of internal model processes can be controlled. In this chapter these coefficients are assessed and optimized for this SCS model by means of a sensitivity analysis.

The coefficients assessed in this chapter are:

1. The Stanton number (c_h), a transfer coefficient which controls the magnitude of the convective heat flux (see appendix C.1).
2. The Dalton number (c_e), a transfer coefficient which controls the magnitude of the evaporative heat flux (see appendix C.1).
3. The Ozmidov length scale (L_{inf}), which specifies the magnitude of turbulent mixing by internal waves (see appendix C.2).
4. The horizontal diffusivity, which specify the magnitude of turbulent mixing on a sub-grid scale, based on a turbulence closure model.
5. The wind drag coefficient (C_d), which specifies the magnitude of the surface wind stress.

Of these coefficients, the Stanton and Dalton numbers are used to control the heat flux forcing. The Ozmidov length scale and horizontal diffusivity influence the magnitude of turbulent mixing.

To determine the models sensitivity to these parameters and to optimize them for the SCS, the following approach is followed:

First, c_h and c_e as described in literature are studied in order to determine their most commonly specified magnitude (section 9.1).

Second, c_h and c_e are calibrated by determining the optimum fit between SST changes caused by a prescribed net surface flux and SST changes as observed from climatological data (section 9.2).

Third, c_h, c_e and L_{inf} are calibrated using a small-scale test basin forced by ECMWF atmospheric data. The optimized settings are determined iteratively using the Goodness-of-Fit (GoF) method described in appendix D (section 9.3). The SCS model sensitivity to the different coefficients found is subsequently assessed by means of the GoF routine, also. The settings providing the smallest misfit with WOA01 reference data are used for the final model (section 9.4).

Furthermore, the models sensitivity to the horizontal diffusivity (section 9.5) and the wind drag coefficient (section 9.6) is assessed using the GoF method. Again, the settings providing the smallest misfit with WOA01 reference data are used for the final model.

9.1 Overview of Stanton and Dalton numbers found in literature

In literature a wide range of Stanton (c_h) and Dalton (c_e) numbers are applied. This can be explained by the fact that these coefficients are determined by comparing empirical measurements with reference data, and therefore have only limited physical meaning. Also, in previous projects at WL | Delft Hydraulics different values for these coefficients were used. Table 9.1 shows an overview of the different coefficients found in studied literature. It should be noted that most of the sources mentioned in table 9.1 describe research at high latitudes in the Northern Hemisphere (North-America, North-Sea). An exception to this found in [Kernkamp & Smits, 2000], which describes temperature modeling for Lake Malawi. Since the SCS climate should be closer to that of Lake Malawi, more similarity with these values is expected. Furthermore, a climatological, annual-mean wind speed of $4.39ms^{-1}$ is observed over the SCS (see section 6.3). During the monsoon highs, however, substantially higher wind speeds are achieved, often above $8ms^{-1}$ [Wyrtki, 1961]. According to [Millar *et al.* , 1999] this implies that the value of c_h should be increased to account for turbulent conditions associated with higher wind-speeds.

Source	Stanton number	Dalton number
[Gill, 1982]	0.83×10^{-3} (stable), 1.1×10^{-3} (unstable)	1.5×10^{-3}
[Millar *et al.* , 1999]	$0.79 \times 10^{-3}(*)$	1.5×10^{-3}
[Smith *et al.* , 1996]	$1.1 \times 10^{-3}(*)$	$1.32 \times 10^{-3}(*)$
[Simon *et al.* , 1999]	1.0×10^{-3}	1.2×10^{-3}
[Emery *et al.* , 2006]	1.0×10^{-3}	1.2×10^{-3}
[Lane, 1989]	N.A.	$1.33 \times 10^{-3}(*)$
[De Goede *et al.* , 2000]	1.45×10^{-3}	1.2×10^{-3}
[Kernkamp & Smits, 2000]	2.255×10^{-3}	1.885×10^{-3}

Table 9.1: Overview of Stanton and Dalton numbers specified by literature.

(* Values determined using the climatological, annual-mean atmospheric state described in table 6.1)

Since the formulation of the heat flux equations described in appendix C is largely based on those described by [Gill, 1982], c_h and c_e as specified by this source are assumed representative. A Stanton number of 0.9×10^{-3} will be used to account for unstable wind conditions also [Millar *et al.* , 1999]. These values are summarized in table 9.2.

Stanton number (c_h, convective flux)	0.9×10^{-3}
Dalton number (c_e, evaporative flux)	1.5×10^{-3}

Table 9.2: Stanton and Dalton numbers representative for values found in literature.

9.2 Optimization of Stanton and Dalton numbers by a heat exchange comparison

A second approach used to determine the magnitude of the Stanton and Dalton numbers is by minimizing the misfit between SST change due to heat exchange calculated by the heat flux model, and the surface layer temperature change observed from climatological data (WOA01, see chapter 4). By changing the values of c_e and c_h the magnitude and temporal evolution of the net heat flux can be changed. It is assumed that a minimum misfit is found at a certain combination of these coefficients.

As described in appendix C the temperature change caused by the net heat flux can be written as:

$$\frac{\partial T_s}{\partial t} = \frac{Q_{tot}}{\rho_w c_p \Delta z_s} \tag{9.1}$$

with Q_{tot} specified as:

$$Q_{tot} = Q_{sn} + Q_{an} - Q_{br} - Q_{ev} - Q_{co} \tag{9.2}$$

Since the magnitude of Q_{ev} can be steered by c_e and the magnitude of Q_{co} by c_h equation 9.1 can be written as:

$$\frac{\partial T_s(c_e, c_h)}{\partial t} = \frac{Q_{sn} - Q_{eb} - Q_{ev}(c_e) - Q_{co}(c_h)}{\rho_w c_p \Delta z_s} \tag{9.3}$$

Temperature change described by the WOA01 is used as a second set of temperature data. Now the misfit between both series is specified as:

$$Misfit = \left| \frac{\partial T_{WOA01}}{\partial t} - \frac{\partial T_s(c_e, c_h)}{\partial t} \right| = \left| \frac{\partial T_{WOA01}}{\partial t} - \frac{Q_{sn} - Q_{eb} - Q_{ev}(c_e) - Q_{co}(c_h)}{\rho_w c_p \Delta z_s} \right| \tag{9.4}$$

For varying values of c_e and c_h the outcome is quantified by the magnitude of this misfit. In this sense a smaller misfit indicates a better solution.

Furthermore, in equation 9.4 it is assumed that the heat exchange by advective and diffusive processes can be neglected. To justify this, the method is applied at a location in the SCS where the surface heat flux is the primary process for the seasonal temperature change. This location (115°E, 10°N) is determined based on the results of an EOF temperature analysis in chapter 3. Furthermore, in equation 9.4 Δz_s specifies the thickness of the top layer. Assuming temperature change is limited to the mixed layer and a mean mixed layer depth of 75 m at the test domain (see chapter 2), Δz_s is prescribed as 75 m. The WOA01 temperature data also represents the mean temperature change over this layer. As a final simplification, ρ_w is assumed constant and its value represents the annual-mean ρ_w at the test location as calculated from the WOA01.

Finally, monthly-mean climatological ECMWF ERA-40 data is used for heat flux forcing (see chapter 4). Figure 9.1 shows the resulting mitfit for c_e and c_h ranging between 0 to 5×10^{-3} and using a step size of 1×10^{-5}.

Figure 9.1 shows an optimum (a minimum misfit) around $c_h = 2.4 \times 10^{-3}$, $c_s = 0.9 \times 10^{-3}$. Also, a stronger dependency on the Dalton number is observed. This can be explained by the fact that the evaporative flux is an order of magnitude larger than the convective heat flux over SCS (see chapter 2). Because of this the Dalton number will have a more significant role in the net heat flux balance. Furthermore, for the optimized values a significant improvement is noted with respect to the values suggested by the majority of literature (over 0.5 °C). The optimized values are summarized in table 9.3.

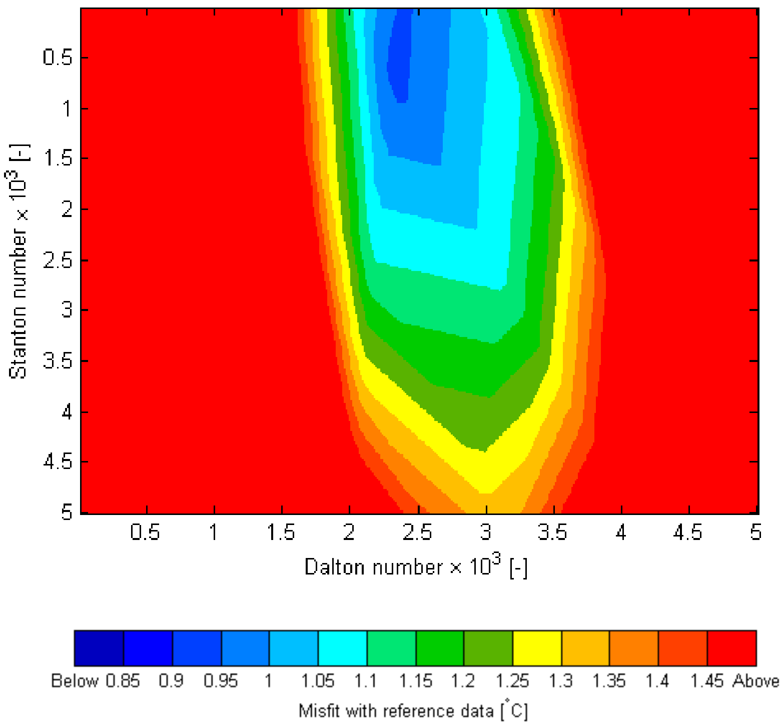

Figure 9.1: Misfit between World Ocean Atlas 2001 temperature data and temperature calculated using the Ocean heat flux model and ECMWF ERA-40 forcing data, for varying Stanton and Dalton numbers. At location 115°E, 10°N.

Stanton number (c_h, convective flux)	0.9×10^{-3}
Dalton number (c_e, evaporative flux)	2.4×10^{-3}

Table 9.3: Optimized Stanton and Dalton numbers found by minimizing the misfit between World Ocean Atlas 2001 temperature data and temperature calculated using the Ocean heat flux model and ECMWF ERA-40 forcing data.

9.3 Optimization of Stanton and Dalton numbers using a test basin

As a third approach to optimize the heat flux model, the optimum Stanton and Dalton values are determined by minimizing the misfit between the temperature modeled by a simple test basin and WOA01 temperature data. An advantage of this method is the possibility to include coefficients that influence vertical temperature transport as calibration parameters. Also, by using a test basin instead of the large-scale SCS model, model run time is significantly reduced allowing a substantial number of test runs with different parameter settings.

Similar as in the atmospheric / climatological flux comparison described in the previous section, large-scale advective temperature processes are neglected in this approach. This is justified by locating the test basin in a sub-domain of the SCS where the heat flux through the free surface is the primary contributor to large-scale temperature cycle. This location is determined by studying the processes described in chapter 2 and is placed at 114°E - 120°E, 8°N - 14°N. In appendix I.2 the test basin extent is shown graphically. Note that grid points in the Sulu Sea are not taken into account in the optimization process decsribed below. The basin has closed boundaries, a fixed depth of 150 meters and applies the same vertical spacing as the SCS model. As explained in appendix C.2, the Ozmidov length scale will be used to optimize vertical temperature transport during this project. This coefficient is also included in the optimization process in this section.

The test basins heat flux model is forced using climatological ECMWF data (see chapter 4). No additional boundary forcing is included. Reference data from the WOA01 is interpolated to the basin grid. The misfit between the model temperature and reference temperature is determined using the GoF routine described in appendix D. In this section the upper 6 layers (corresponding to the upper 90 meters) obtain an increased weight factor in the GoF routine (1.5 instead of 1) since most dynamic temperature processes occur in this depth range.

The resulting misfit for a range of Stanton and Dalton numbers is shown in figure 9.2. For these runs an Ozmidov length scale of 5 cm is applied. This value was chosen based on initial test runs.

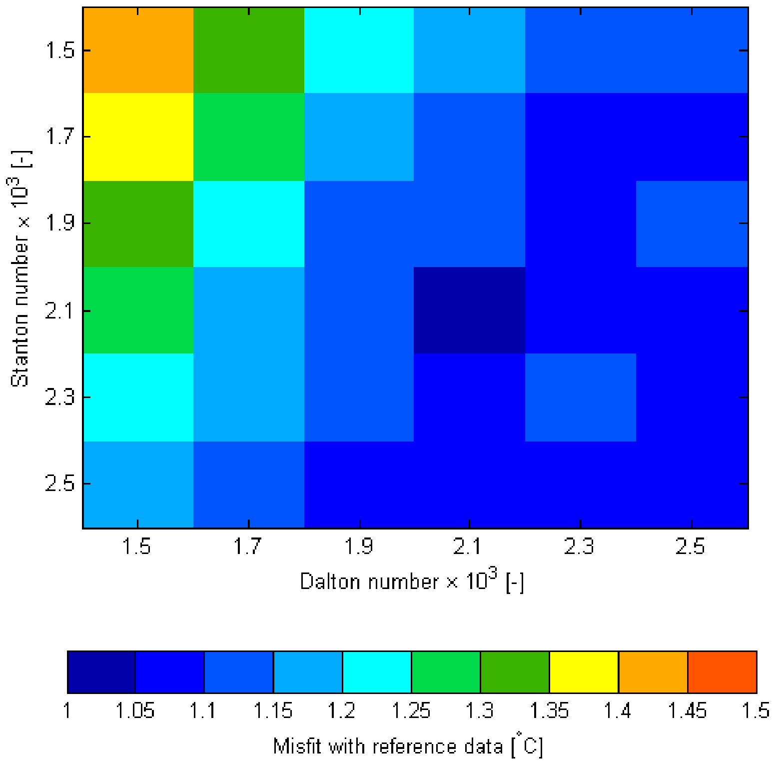

Figure 9.2: Mean misfit between World Ocean Atlas 2001 temperature data and temperature calculated using Delft3D-FLOW and ECMWF ERA-40 forcing data, for varying Stanton and Dalton numbers. Using a test basin located at 114°E - 120°E, 8°N - 14°N.

From figure 9.2 an optimum (minimum misfit) is observed at $c_h = 2.1 \times 10^{-3}$ and $c_e = 2.1 \times 10^{-3}$. For these values the observed misfit is roughly 0.5 °C lower than for the values commonly used in literature. Using these c_h and c_e values the Ozmidov length scale (L_∞) is subsequently varied between 1 and 9 cm. The resulting misfits are visualized in figure 9.3.

In this figure an optimum is found at $L_{\text{inf}} = 7$ cm. It is also observed that a decrease in misfit of about 0.5 °C is achieved with respect to the maximum misfit value observed. This improvement has a similar order of magnitude as the improvement achieved by optimizing the c_h and c_e coefficients. This can indicate that if no L_{inf} value is specified, too little vertical mixing through the thermocline

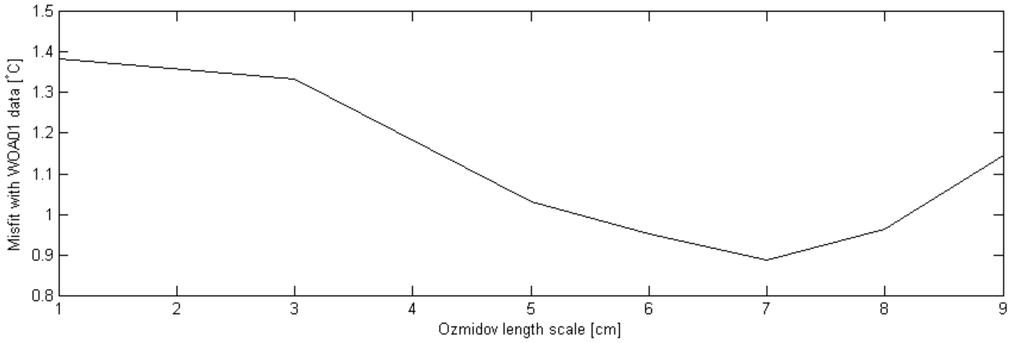

Figure 9.3: Mean misfit between World Ocean Atlas 2001 temperature data and temperature calculated using Delft3D-FLOW and ECMWF ERA-40 forcing data, for varying Ozmidov length scales. Using a test basin located at 114°E - 120°E, 8°N - 14°N. A Stanton number of 2.1 $\times 10^{-3}$ and a Dalton number of 2.1 $\times 10^{-3}$ gave a minimum misfit.

occurs. This will cause a build-up of heat in the mixed layer region. Adversely, if the specified value is too high, too much mixing occurs and too much heat is transported to lower water layers. This explains the optimum curve observed in figure 9.3.

The optimized settings found using the test basin are summarized in table 9.4.

Stanton number (c_h, convective flux)	0.9×10^{-3}	[-]
Dalton number (c_e, evaporative flux)	1.5×10^{-3}	[-]
Ozmidov length scale (L_{inf})	7	[cm]

Table 9.4: Optimized Stanton and Dalton numbers and Ozmidov length scale found by minimizing the misfit between World Ocean Atlas 2001 temperature data and temperature calculated using a Delft3D-FLOW test basin located at 114°E - 120°E, 8°N - 14°N. Climatological ECMWF ERA-40 data is used for test basin heat flux forcing.

9.4 Heat flux sensitivity runs

In table 9.5 the optimized Stanton, Dalton and Ozmidov numbers as determined in the previous sections are summarized. With these different values a number of sensitivity runs are done using the model as described in chapter 8. For these runs the models heat flux will be forced using climatological ECMWF ERA-40 data. Furthermore, climatological water level forcing and lateral WOA01 temperature and salinity forcing will be applied at the open model boundaries (see section 8.2.2). As such, the model is forced using climatological data only to ensure compatibility with the WOA01 validation data.

Furthermore, in section 8.2.3 two truncation depths are discussed. One at 150 and the other at 300 meters. The sensitivity runs described in this chapter will be applied on both these depths. This is done to study the effects of model truncation on the temperature representation.

In order to quantify model results the GoF method as described in appendix D is used. The results of the method are applied in two ways:

First, the annual-mean, spatially averaged value is determined to quantify the models performance. For this application it should be noted that initial test runs indicated a poor model quality in the shallow regions of the SCS domain. To prevent these low quality values from distorting the

	c_h	c_e	L_{inf}
	[-]	[-]	[cm]
Literature	0.9×10^{-3}	1.5×10^{-3}	N.A.
$\partial T/\partial t$ comparison	0.9×10^{-3}	2.4×10^{-3}	N.A.
Test basin	2.1×10^{-3}	2.1×10^{-3}	7

Table 9.5: Stanton, Dalton and Ozmidov values assessed by model sensitivity analysis.

GoF, this average is calculated over a subsection of the SCS domain. Appendix I.2 shows the spatial extent of this truncated domain. Also, for this application the models upper 6 layers have an increased weight (1.5 instead of 1) since most dynamic temperature processes occur in these layers. For consistency with the model truncated at 150 meters only the upper 10 layers of the model truncated at 300 meters are used for the GoF. This means that in both cases the upper 150 meters are assessed.

Second, the GoF method is used to determine annual-mean, layer-averaged maps showing the space dependent misfit. This is done in order to visually assess the space dependent model quality. Since these maps show the annual mean misfit they do no provide direct information on the models temporal behavior. Because of this it is assumed that a small misfit indicates that the model follows a similar temporal evolution as the reference data. This is justified by the significant seasonal temperature cycles observed over the SCS (see chapter 2). Furthermore, the average misfit is determined over the upper 6 layers only. This is done because the primary goal is to model temperature in this depth range (the mixed layer).

Run ID	**Truncation depth**	c_h	c_e	L_{inf}	**GoF**
		[-]	[-]	[cm]	[°C]
HF-C1a	150 m	0.9×10^{-3}	1.5×10^{-3}	N.A.	1.52
HF-C1b	300 m	0.9×10^{-3}	1.5×10^{-3}	N.A.	2.19
HF-C2a	150 m	0.9×10^{-3}	2.4×10^{-3}	N.A.	1.09
HF-C2b	300 m	0.9×10^{-3}	2.4×10^{-3}	N.A.	1.49
HF-C3a	150 m	2.1×10^{-3}	2.1×10^{-3}	7	1.08
HF-C3b	300 m	2.1×10^{-3}	2.1×10^{-3}	7	1.34

Table 9.6: Overview of heat flux sensitivity runs performed using the SCS model and the resulting mean temperature misfit with World Ocean Atlas 2001 validation data. See appendix I.5 for annual-mean GoF plots.

Table 9.6 shows an overview of model sensitivity runs performed using the coefficients specified in table 9.5. Also, the annually and spatially averaged misfit with WOA01 reference data is included in this table. In appendix I.5 the spatially dependent misfit is shown for these runs.

From these results it is concluded that runs HF-C2 and HF-C3 perform considerably better than run HF-C1. This implies that the Stanton and Dalton values specified by literature are too low for the SCS, resulting in an overestimation of the net heat flux.

Also, it is observed that the difference between runs HF-C2 and HF-C3 occur mainly in the shallow model regions like the Gulf of Thailand and the Java Sea. In those regions, the misfit of setup HF-C3 is approximately 1°C lower than that of setup HF-C2. This can be explained by the higher Stanton number used for run HF-C3. This coefficient determines the strength of the convective flux. While this flux is an order of magnitude smaller than the evaporative flux, governed by the Dalton number, it has a direct relation with the surface layer water temperature. As explained in appendix C, it is linearly related to the difference between the water and air temperature. This means that if the water temperature rises significantly the convective flux will work as a feedback mechanism, reducing the water temperature. As observed, the misfit in the indicated regions is large for all runs. In all cases this is due to excessive heating during the NE / SW monsoon transition period and during the SW monsoon. Because of the indicated feedback mechanism, this effect is smallest for run HF-C3.

A number of explanations can be given for this excessive heating in the shallow model regions. First, the heat flux coefficients are optimized for deeper model regions at higher latitudes. For the shallow regions other values may be required. This is not possible, however, since these parameters are fixed in Delft3D-FLOW (see appendix C).

A second explanation can be given based on conclusions in chapter 2. In the shallow model regions the seasonal temperature cycle is governed by the heat flux cycle primarily. This cycle, in turn, is governed by the annual shortwave flux cycle, the wind magnitude cycle and the cloud coverage cycle. In chapter 6, it is described that numerical weather prediction models, like those used for the ECMWF ERA-40 dataset, generally suffer from a low-quality cloud coverage representation. Furthermore, in chapter 2 it was concluded that over the southern regions of the SCS higher cloud coverage occurs than over the northern regions (a 10 % difference is observed from ECMWF ERA-40 data). The higher cloud coverage, stronger dependency on this cloud coverage and possibly the low quality of the cloud coverage forcing data used can explain the observed heating during the NE / SW monsoon transition period in these regions.

A third explanation is provided by Run HF-H1f (see section 9.6). For this run the magnitude of the wind stress coefficient is increased from 0.00083 (the SAT2SEA value) to 0.002 (suggested by [Open University, 1989]). This results in stronger currents in the shallow regions over the Sunda Shelf. These currents transport colder water into the Gulf of Thailand, decreasing the misfit. As such, an inaccurate representation of the large-scale current system can also attribute to the significant misfit observed for the runs described in this section.

Of the provided explanations, a combination of all three seems most likely. It should be noted, however, that with regard to values decribed by literature the used Stanton and Dalton numbers are already large. As such, higher values may be physically unrealistic. Increasing them, however, will decrease the net influx. This may require the application of space dependent values for these coefficients in Delft3D-FLOW. Where cloud cover forcing is concerned, it should be noted that of the meteorological datasets assessed in this report, the ECMWF ERA-40 performed best (see chapter 6). This forcing data will be studied in more detail in the next chapter. Finally, a more detailed assessment of the processes governing the seasonal temperature cycle in these local regions could attribute to a better representation of this cycle. In this project these regions are only studied as a sub-system of the SCS, and only the large-scale processes are assessed.

Furthermore, a significant misfit is observed in the Gulf of Tonking and along the southern Chinese coastline. In chapter 2 it is described that the seasonal temperature cycle in these regions is governed by a western boundary current transporting cold water from Taiwan Strait during the NE monsoon. While this current is observed from model results (see appendix I.10), it does not follow the China Continental Shelf past Hong Kong. This may be attributed to a coarse model grid in this region (see section 8.2.3). Furthermore, if this current follows the China Continental Shelf further westwards, the grid will be too coarse to enter the Gulf of Tonking. The dependency on large-scale horizontal temperature transport in this region is also observed from run HF-C3f (see section 10.1). In this run no boundary forcing is applied at Luzon and Taiwan Strait. This results in a strong decrease in model quality over the China Continental Shelf region. Concluding, it is likely that a refinement of the model grid is required to improve the model results in these regions, in specific were the temperature in the Gulf of Tonking is concerned.

It is also observed that the models truncated at 150 meters perform better than those truncated at 300 meters. This turned out to be caused by an error in the initial boundary transport forcing at Luzon Strait: too much heat entered the model at lower depths at this Strait. This warmer water subsequently follows the the China Continental Shelf west- and southwards, reducing the model quality in these regions. Due to the different layer definition for the 300 meter model the effects of this error are more pronounced here than for the 150 meter model. No time was available to redo these runs. Based on conclusions in chapter 2, however, better results are expected with the 300 meter truncation depth. At 150 meters a seasonal temperature signal is still observed. Also, the vertical temperature gradient is an order of magnitude larger at this depth than at 300 meters depth, which can result in a build-up of heat in lower model levels. Bases on these conclusions, the 300 meter truncation depth will be used for subsequent model runs.

Finally, an increasing misfit can be observed along the Continental Shelf / Oceanic Plate interface for the models truncated at 300 meters. This may be attributed to an effect called creep [Stelling & van Kester, 1994]. As described in chapter 8, a σ co-ordinate system is used for the vertical model layering. At large bottom gradients, like those at the mentioned interface, truncation errors generated by this system can cause artificial vertical diffusion, thus decreasing the model quality. It should be noted that Delft3D-FLOW provides an option to suppress creep, but an assessment of model results with this option turned on showed no improvements.

Concluding, of the models truncated at 300 meters run HF-C3b provides the smallest misfit. As such, these Stanton, Dalton and Ozmidov settings will be used for subsequent model runs in the following sections.

9.5 Horizontal diffusivity sensitivity runs

In this section the model sensitivity to different horizontal diffusivity values is assessed. This is done using the GoF method as described in the previous section and as formulated in appendix D. As described in the previous section the setup of run HF-C3b is used as a baseline for these runs. Table 9.7 gives an overview of runs performed and their mean misfit with WOA01 reference data. In appendix I.6 maps showing the spatially varying misfit are provided.

Run ID	D_h	**GoF**
	$[m^2/s]$	[°C]
HF-C3b	1	1.34
HF-C3c	10	1.33
HF-C3d	100	1.30
HF-C3e	250	1.25

Table 9.7: Overview of horizontal diffusivity sensitivity runs performed using the SCS model and the resulting mean temperature misfit with World Ocean Atlas 2001 validation data. See appendix I.6 for annual-mean GoF plots.

Based on these runs, it is concluded that increasing the horizontal diffusivity results in a smaller misfit. The effects of this are most significant at the Continental Shelf / Oceanic Plate interface, particularly in the North SCS. This decrease can be explained by the fact that an increase in horizontal diffusivity results in increased effects of turbulent mixing on sub-grid scales. In chapter 2, mixing of cold water entering the SCS through Taiwan Strait and warmer North SCS water was observed to play an important role during the NE monsoon period. As such, the increase in model quality when increasing the horizontal diffusivity may be explained by a better representation of these mixing processes.

A second explanation is based on the layering convention used. When applying a σ layer grid, the 'horizontal grid' is not necessarily horizontal. This means that horizontal mixing on a level plane can resemble vertical mixing when specified in depth instead of in layer number (the aforementioned creep). As such, increasing the horizontal diffusivity may mimic effects of upwelling against the continental shelves. Turbulent mixing on the horizontal plane, in this sense, resolves the process of upwelling against the continental shelf. As such, if the horizontal diffusivity is increased so will this the representation of this process. This may imply that upwelling against the continental shelf is resolved in an inconsistent way with respect to its actual forcing mechanisms.

Finally, it is concluded that 250 m^2/s is a realistic value for this coefficient, considering the grid used [Delft3D, 2005]. Also, in [Gerritsen *et al.* , 2001] an identical value is applied for the SCS grid. As such, this value will be applied for subsequent model runs.

9.6 Wind drag sensitivity runs

In Delft3D-FLOW the wind shear stress at the free surface is defined as [Delft3D, 2005]:

$$|\vec{\tau}| = \rho_a C_d U_{10}^2 \tag{9.5}$$

where ρ_a represents the air density, U_{10} the wind speed 10 meters above the free surface and C_d the wind drag coefficient, dependent on U_{10}. In literature, a great variety of relations are used to specify the magnitude of C_d. In most cases, functions dependent on U_{10} and on coefficients based on excessive wind conditions (like storm surges) are used. Since these coefficients are determined based on empirical relations they show a strong regional dependency.

During the SEA2SEA project a wind drag coefficient of $C_d = 8.3\times10^{-4}$ was used to model monsoon winds over the SCS. During this project this coefficient is used also. As indicated above, however, a variety of different coefficients can be found in literature. According to [Open University, 1989] a value of $C_d = 2 \times 10^{-3}$ provides realistic results. Following [Delft3D, 2005], $C_d = 2.5 \times 10^{-3}$ is a realistic value.

To assess the models sensitivity to this coefficient a value of $C_d = 2 \times 10^{-3}$ is prescribed for run HF-H1f. Furthermore, this run is forced using historic meteorological data and SAT2SEA water level forcing (see appendix I.4). The resulting annual-mean, space varying misfit with WOA01 validation data is shown in appendix I.6.

When comparing results with run HF-H1e, which is forced with similar data but with the above mentioned wind drag coefficient of 8.3×10^{-4}, a decrease in misfit is observed in the shallow model regions over the Sunda Shelf. Over the deep, central SCS a increase in misfit is noted. This difference in response may be explained by a regional dependence on C_d, as indicated above. This could imply that the large-scale wind driven circulation over the shallow model regions is under-estimated by the wind drag coefficient of 8.3×10^{-4}. Due to time constraints, this is not further investigated, and a value of 8.3×10^{-4} is used for the entire model domain. Furthermore, Delf3tD-FLOW does not provide the option to specify this coefficient in a space dependent way. As such it is not possible to distinguish between these regions.

Chapter 10

Sensitivity analysis on model forcing

In this chapter the models sensitivity to different forcing data is assessed (see section 8.2.2). This assessment is subdivided into a number of steps:

- An assessment of the models sensitivity to temperature forcing data (section 10.1). This is done using the GoF method.
- An assessment of the models sensitivity to momentum forcing at the free surface and at the open boundaries (section 10.2). The models sensitivity to this forcing is studied from the correlation between model water level and altimeter SSA data. Also, model water level and SSA time series are assessed at a number of model test stations.
- The models sensitivity to changes in the SST nudging coefficient (as described in appendix D) is assessed (section 10.3). This is done on a basin-wide scale using the GoF method and on a local scale by studying time series at a number of model test stations.

In appendix I.4 an overview of model runs discussed in this chapter is provided. Unless noted otherwise, all runs discussed in this chapter use the parameter settings applied for run HF-C3b as described in section 9.5.

Based on the results in this chapter choices are made on model forcing for the final model, which will be validated in chapter 11.

Finally, in this chapter historic model data is validated using climatological data from the World Ocean Atlas 2001 (WOA01). This is justified based on a comparison between WOA01 and in-situ data in chapter 6. The large-scale consistency between these climatological and historic datasets is of good quality for the SCS and as such a comparison with climatological data is believed to give an realistic indication about the quality of historic model results.

10.1 Sensitivity runs on model temperature forcing

In chapter 2 the role of the surface heat flux cycle on the SCS temperature is described. This cycle is seasonal and space dependent and has to be resolved by the model in order to represent the SCS temperature. Furthermore, chapter 8 describes that two sets of atmospheric ECMWF ERA-40 forcing data will be applied to achieve this. The first consists of monthly composites representing climatological condition over the period 1983-2001. The other consists of forcing data for the year 2000 at 6 hrs intervals.

As described in chapter 9 model setup HF-C3b is forced using the climatological atmospheric data. To study the models sensitivity to atmospheric forcing data, these forcing fields are changed from the climatological to historic. To assess their relative importance, different meteorological forcing fields are changed sequentially.

Furthermore, chapter 2 describes the role of lateral temperature influx through Luzon and Taiwan Strait. To resolve the seasonal cycle of this influx, lateral model transport forcing is applied (see chapter 8). The impact of this forcing assessed in this section also.

Table 10.1 shows an overview of the sensitivity runs described in this chapter, as well as their mean misfit with WOA01 validation data. In appendix I.7 space dependent misfit fields for these runs are shown.

Run ID	**Parameter changed**	**GoF**
		[°C]
HF-C3b	Reference run	1.34
HF-H1a	Historic 2 meter air temperature	1.33
HF-H1b	Historic relative humidity	1.38
HF-H1c	Historic cloud coverage	1.24
HF-H1d	Historic wind and pressure fields	1.03
HF-H1e	Historic forcing (all)	1.03
HF-C3f	No lateral temperature forcing	N.A.

Table 10.1: Overview of temperature forcing sensitivity runs performed using the SCS model and the resulting mean temperature misfit with World Ocean Atlas 2001 validation data. See appendix I.7 for annual-mean GoF plots.

From these runs it it observed that no significant improvement in model quality is achieved if historic, high resolution air temperature forcing is applied. A small improvement is observed in the Gulf of Thailand and the Java Sea. This improvement can be explained by means of the convective feedback mechanism explained in section 9.4. Similarly, no improvement is observed if historic, high resolution relative humidity fields are applied. Both these observations are as expected, since no significant role was attributed to these fields with regard to the large-scale SCS temperature cycle (see chapter 2).

A 7 % improvement in model quality is observed if historic, high resolution cloud cover forcing is applied. This improvement is observed over the entire model domain. Also, it results in an improvement in model quality in the Gulf of Thailand and the Java Sea, supporting the conclusion in section 9.4 that this misfit can partly be attributed to inaccurate cloud cover forcing. Overall, the improvement in model quality can be explained by the significant effect of cloud coverage on the net heat flux cycle (see chapter 2). This indicates that small-scale variability unresolved by the monthly-mean cloud cover forcing influences this cycle to some degree.

A 23 % improvement in model quality is observed if historic, high resolution wind and pressure forcing is applied. This improvement is observed over the entire model domain and is attributed to a number of reasons:

First, in chapter 2 it was described that the North SCS temperature cycle is governed to a large extent by seasonal mixing, possibly increased by Rossby wave dynamics. A tentative explanation about the origin of this Rossby wave was based on the large-scale atmospheric vorticity over the North SCS. This atmospheric vorticity will have a signal in both the wind and pressure forcing data and will attribute to the large-scale transfer of angular momentum. It will cause large-scale mixing which contributes to the seasonal temperature cycle. Based on these results it is concluded that this process has a temporal variability which is resolved better by the high resolution historic data.

Second, because of the climatological averaging and the lower temporal resolution, extreme wind and pressure conditions (like storm surges) will be unresolved by the monthly-mean forcing data.

Possibly, large-scale temperature mixing by these conditions, whether in vertical direction and causing upwelling of colder water or in horizontal direction, attributes to a better temperature representation. This is supported by conclusions in section 9.6, where a better temperature representation was observed in the shallow model regions for a higher wind drag coefficient. These extreme wind conditions are resolved by the high resolution non-averaged forcing data, explaining the model improvements in these regions.

Third, an underestimation of wind speeds by the climatological averaging result in a larger net heat flux (see appendix C). This can partially explain the significant model improvements in the shallow regions observed if historic, non-averaged data is applied.

If the historic forcing fields are combined an improvement similar to that of the 'historic wind only' forcing is observed. From this it is concluded that the improvements described above are not cumulative, indicating a degree of interaction between the different processes.

Finally, run HF-C3f shows model results if no lateral transport forcing is applied at Luzon and Taiwan Strait. If these results are compared with run HF-C3e, which uses similar atmospheric forcing and lateral boundary forcing, it is observed that this has a significant effect on the modeled temperature in the North SCS. This effect is most notable over the China Continental Shelf and southwest of Taiwan. In chapter 2 the large-scale temperature cycle in these regions is described by means of a cold-water boundary current originating from Taiwan Strait. Run HF-C3f confirms this conclusion. Also, this run indicates that this process follows a seasonal cycle which is resolved by monthly-mean lateral transport and water level forcing. Finally, it is concluded that these processes have no significant effect on the temperature cycle in the South SCS. This is in line with conclusions drawn about the seasonal temperature cycle in chapter 3.

10.2 Sensitivity analysis on model momentum forcing

In this section the modeled large-scale circulation is assessed based on a visual inspection of the correlation between model water level and altimeter SSA data. This is done in order to assess the models sensitivity to momentum forcing data and to assess the role of different processes attributing to the large-scale SCS circulation cycle.

The altimeter SSA data used in this section is obtained from the DUACS dataset (see chapter 5). It has a temporal resolution of 1 month and a spatial resolution of 1 degree. This data is compared with monthly-mean model data. Based on these resolutions, correlation found only apply to processes on significant time-scales. This is in accordance with the project goal, which is to model seasonal processes. The correlation is determined from model (D3D) and altimeter (SSA) time series describing the monthly-mean conditions (t) per grid-point (n,m), according to:

$$Correlation(n,m) = \frac{\frac{1}{12-1}\sum_{m=1}^{12}((D3D_{(t,n,m)} - \overline{D3D_{(n,m)}})(SSA_{(t,n,m)} - \overline{SSA_{(n,m)}}))}{\sigma_{D3D(n,m)} \times \sigma_{SSA(n,m)}} \tag{10.1}$$

where σ_{D3D} and σ_{SSA} indicate the standard deviations of both series and $\overline{SSA}$ and $\overline{D3D}$ indicate their annual-mean value.

Furthermore, model water-level and altimeter SSA data are compared for a limited number of test stations. Appendix I.3 shows an overview of these model stations. The station locations are defined to obtain a reasonable coverage of the model domain and are based in part on the relevant large-scale processes as summarized in chapter 8.

In chapter 2 a number of processes are identified as governing the large-scale SCS circulation cycle. These processes are attributed to wind and pressure forcing at the free surface and to intrusions through Luzon and Taiwan Strait. Also, these processes have a significant influence on the seasonal, large-scale temperature cycle. This indicates they have to be resolved in order to accurately represent this cycle. Table 10.2 shows an overview of model runs done to assess these processes and to assess model forcing data used to resolve them (see section 8.2.2). Furthermore, appendix I.8 shows the resulting correlation maps for these runs.

Run ID	Boundary forcing	Transport	Surface	Other
C-1	SAT2SEA	T/S	ECMWF - H	N.A.
C-2	DUACS	T/S	ECMWF - H	N.A.
C-3	SAT2SEA	T/S	ECMWF - C	N.A.
C-4	SAT2SEA	T/S	NCEP/NCAR - C	N.A.
C-5	SAT2SEA	N.A.	ECMWF - H	
C-6	N.A.	N.A.	ECMWF - H	Pressure forcing
C-7	N.A.	N.A.	ECMWF - H	Pressure and wind forcing
C-8	SAT2SEA	T/S	ECMWF - H	Increased wind drag coefficient

Table 10.2: Overview of momentum forcing sensitivity runs done using the SCS model*. See appendix I.8 for correlation plots.

(* T/S = Temperature and salinity included, H = historic, C = climatological, N.A. = not applied)

Based on the correlation maps in appendix I.8 a number of observations are made about the large-scale SCS water level cycle:

First, run C-6 applies atmospheric pressure forcing only. As described in chapter 8 this will cause variations in water column high by atmospheric pressure loading. Run C-6 shows that this relation explains a significant part of the large-scale water level cycle in the eastern part of the SCS. Also, a strong correlation is observed west of Luzon. Chapter 2 describes a tentative explanation about the large-scale water level cycle in the North SCS by Rossby wave dynamics. This wave is observed to follow a similar cycle as the atmospheric vorticity in this region. Run C-6 confirms a relation between the large-scale North SCS water level and atmospheric forcing. This large-scale water level cycle is resolved by the model to some degree using this forcing data. A more elaborate assessment on the mechanisms forcing this cycle and on the models representation of these processes is a study in itself, however, and as such beyond the scope of this project. In this report large-scale mixing in the North SCS is assessed with regard to its role in the large-scale seasonal temperature cycle only.

Second, run C-7 shows the resulting correlation if both atmospheric pressure and wind forcing are applied. When compared with run C-6 the correlation is improved in the shallow model regions over the Sunda Shelf. In chapter 2 this is explained by large-scale water level tilting forced by the monsoon winds. Based on run C-7 it is concluded that this large-scale tilting is resolved reasonably using the wind forcing data.

Run C-5 subsequently applies wind and pressure forcing at the model surface and monthly-mean SAT2SEA water level forcing at the Luzon and Taiwan Strait boundaries. When compared with run C-7 the large-scale features in the central and south SCS are still observed. Furthermore, a good correlation is observed along the Chinese and Vietnamese coastlines. This supports the conclusion drawn in the previous section that the large-scale circulation in this region is imposed by large-scale intrusions through Taiwan and Luzon Strait. It also indicates that these large-scale intrusions can be resolved from monthly-mean forcing data.

Furthermore, run C-1 shows that the correlations along the Chinese and Vietnamese coastlines improve if density variations due to temperature and salinity are resolved by the model.

Subsequently, runs C-3 and C-4 show the correlations if monthly-mean atmospheric forcing data is applied instead of forcing data with a temporal resolution of 6 hrs. It is observed that the large-scale water level cycle attributed to influx through Taiwan and Luzon Strait and to the monsoon wind system is resolved by this forcing data. The large-scale cycle in the North SCS is not, however. This supports the conclusion drawn in the previous section that the large-scale mixing is not resolved properly by the monthly-mean atmospheric forcing data.

From run C-2 it is subsequently observed that the model quality west of Luzon Strait decreases slightly if weekly DUACS water level forcing is applied. In the other model regions effects are unnoticeable. Based on this observation the SAT2SEA boundary forcing will be used for subsequent model runs.

Finally, run C-8 shows the correlation if the wind drag coefficient is increased from 8.3 $\times 10^{-4}$ to 2.0 $\times 10^{-3}$. This leads to a lower correlation in the central SCS basin. This corresponds with observations in section 9.6 were a decrease in model temperature representation is noted in this region if the wind drag coefficient is increased. This implies that a wind drag coefficient of 8.3 $\times 10^{-4}$ provides a better solution for the central SCS basin.

Appendix I.8 also shows water-level time series for a number of the above runs. From these series the following observations are made about the large-scale SCS water-level cycle:

Stations O6, O4 and O12 show the modeled water level and altimeter SSA data at the shallow model regions over the Sunda Shelf, Gulf of Thailand and Java Sea. From these series it is observed that the large-scale water level follows a cycle synchronous to the monsoon, with its peak during the NE monsoon high and its low during the SW monsoon. This relation with the monsoon wind is described in section 2 by means of monsoon induced water level tilting. It is also observed from the correlation maps described above. Furthermore, it is observed that the small scale variability is resolved reasonable by the model. Since this small-scale variability is not observed if monthly-mean atmospheric forcing data is used it is attributed to small-scale wind and pressure variability. This also indicates that small-scale mixing will not be resolved by the monthly forcing data, which may contribute to the lower model temperature accuracy as observed in this region for monthly-mean forcing data and discussed in the previous section.

Station O1 shows model water level and altimeter SSA series south of Hong Kong. From this station it is observed that the seasonal water level cycle at this location is resolved reasonably by the model. On a smaller time-scale the SSA data shows a wave-like signal which is not resolved by the model, however. Note that the rise in water level during the October period coincides with a rapid breakdown of the thermocline in this region (see appendix I.11). This may be explained by the large-scale transport of colder water from Taiwan Strait (see chapter 2). This dependency on large-scale temperature transport is also observed from temperature data in the previous section, and from the large-scale correlation between modeled water level and altimeter SSA data for run C-5 (see above).

Summarizing, it is concluded that atmospheric pressure forcing plays a significant role in the large-scale water level cycle in the North SCS. This cycle is resolved to some degree if pressure forcing data with a temporal resolution of 6 hrs is applied. Furthermore, the large-scale wind system governs the water level cycle in the South SCS. This large-scale cycle can be resolved by the model if monthly-mean wind and pressure forcing data is applied. The large-scale water level cycle along the Chinese and Vietnamese coastlines can be explained by intrusions through Taiwan and Luzon Strait. This large-scale cycle is resolved by the model if monthly-mean water level forcing is applied at these open model boundaries. Finally, it should be noted that an accurate representation of these features in themselves is not the goal of this project. They are assessed with regard to their respective roles in the seasonal SCS temperature cycle. This is done in more detail in chapter 11.

10.3 Sensitivity analysis on the SST nudging coefficient

In appendix D a SST nudging routine implemented in the Delft3D-FLOW model is discussed. This routine is similar to that used during the REST3D project [De Goede *et al.* , 2000], is included in the transport equation for temperature and is formulated as:

$$\frac{\partial T}{\partial t} = advection + diffusion + \frac{Q_{tot}}{\rho_0 c_{pw} \Delta z_s} - G \frac{\frac{\partial Q}{\partial T}(T_{SST} - T_s)}{\rho_0 c_{pw} \Delta z_s} \tag{10.2}$$

where $(T_{SST} - T_s)$ is the difference between model and measured SST. $\frac{\partial Q}{\partial T}$ is a term added for dimensional arguments. This term is calculated based on time and space varying model conditions. Because of this the relative magnitude of the nudging term is determined in a space and time varying way, also. Finally, G is a coefficient which can be tuned to specify the relative strength of the nudging term.

In this section the models sensitivity to varying values of G will be assessed. Based on arguments presented in chapter 6 weekly varying Reynolds SST data for the year 2000 is used as forcing data for the nudging routine.

Table 10.3 shows an overview of sensitivity runs performed using different nudging coefficients. Both the nudging and heat flux forcing data used is for the year 2000. Furthermore, parameter settings as defined for run HF-H1e are used.

Run ID	Nudging coefficient
N-1	1
N-2	5
N-3	10
N-4	25
N-5	50
N-6	100

Table 10.3: Overview of SST nudging coefficient sensitivity runs performed using the SCS model. See appendix I.9 for annual-mean GoF plots.

In appendix I.9 the annual-mean temperature misfit with WOA01 validation data is shown, along with time series for a selected number of test stations. The station locations are defined to obtain a reasonable coverage of the model domain and are based in part on the relevant large-scale processes as summarized in chapter 8 (see appendix I.3). Furthermore, all time-series are plotted for two depth levels. This is done to study differences between the impact of SST nudging on the models surface layer and lower level temperature. The second depth level is defined in the lower regions of the mixed layer. Note that this level varies per station.

From appendix I.9 it is observed that increasing the nudging coefficient results in a smaller misfit in shallow model regions. In deeper regions no significant improvement is observed. This can be explained by the lower model quality in the shallow model regions. In section 10.1 this lower model quality is attributed to a stronger dependency on the (inaccurate) net heat flux cycle and possibly to an incorrect representation of the large-scale current system in this region. In the shallow regions along the Chinese coastline and in the Gulf of Tonking the lower model quality is explained by a coarse model resolution. With regard to the improvement achieved by SST nudging this implies that in the shallow North SCS regions this is done an in inconsistent way with respect to the processes governing the temperature cycle. The unresolved horizontal transport is resolved by a stronger surface flux. For the shallow model regions over the Sunda Shelf this implies that if an inaccurate net heat flux is the main contributor to the observed temperature inaccuracy, the model temperature is improved in a consistent way with respect to its forcing mechanism.

As implemented during this project, the SST nudging routine alters the surface flux in order to optimize the model solution with respect to measurement (forcing) data. This results in better heat flux forcing over the Sunda Shelf region and an increase in model accuracy. If, however, large-scale circulation plays a role in this lower model quality the model temperature is resolved in an inconsistent way with respect to its forcing mechanism. This implies that caution is needed when applying the nudging method, because unresolved temperature features can be resolved in an inconsistent way with respect to their forcing mechanisms.

Furthermore, the run HF-C3e temperature accuracy is better in the central SCS basin than in the shallow regions described above. As such the improvement achieved by SST nudging will be smaller there.

Finally, from appendix I.9 it is observed that the models temperature representation improves if the nudging coefficient is increased. For an increase in coefficient from 0 to 50 the improvement is more significant than from 50 to 100.

From the time series shown in appendix I.9 similar conclusions are drawn. For the stations in the North SCS (Ex and A1) no significant improvement in model temperature is observed if the nudging routine is applied. For all runs and at both depth levels these stations show a similar seasonal cycle as the WOA01 reference data. In most cases the magnitude of the modeled temperature is well within the WOA01 standard deviation bounds.

For the stations at lower latitudes a significant improvement is observed if the nudging method is applied. While initial model results at these stations show a similar seasonal cycle as the WOA01 data, the magnitude differs significantly (up to 4 degrees). If the magnitude of the nudging coefficient is increased, the fit between between the model and WOA01 data improves for both the surface layer temperature and the temperature at lower depths. For a nudging coefficient of 50 the magnitude is within the WOA01 bounds most of the time. An additional improvement is noted for a coefficient of 100, though this improvement is substantially smaller.

Station S6 forms an exception to this. At lower depths the model temperature is below the WOA01 standard deviation bounds. This can indicate that too much vertical mixing occurs and too much heat is transported to lower model levels. Furthermore, in section 9.5 the lower model quality in the S6 region is attributed to an incorrect representation of sub-surface upwelling, possibly generated artificially by model creep. Finally, in chapter 8 it is explained that the model grid is too coarse to resolve the steep bathymetry incline at the Continental Shelf / Oceanic plate interface. This indicates that a grid refinement is required to resolve this process. Since the focus of this project is on the large-scale temperature, however, this was not investigated in more detail.

Finally, for subsequent nudging runs, done for model validation in the next chapter, a nudging coefficient of 100 will be applied.

Chapter 11

Model validation

In chapter 8 the general setup of the SCS temperature model is described. This model applies heat flux and atmospheric wind and pressure forcing at the free surface and water level and lateral transport forcing at the open boundaries. Subsequently, chapters 9 and 10 describe sensitivity analysis on relevant model coefficients and forcing data (an overview of model sensitivity runs is provided in appendix I.4). Based on the results of these sensitivity runs, two model setups are assessed to validate the model temperature representation. These are:

- A setup using the Ocean heat flux model as the only means of heat flux forcing (Run ID: HF-F).
- A setup were the Ocean heat flux model is extended with the SST nudging routine described in appendix D (Run ID: N-F).

The forcing and coefficients applied for these runs are summarized in table 11.1.

Run ID	**Parameters**				**Trunc.**	**Forcing**			**Nudging**
	c_e	c_h	L_∞	D_h		B.C.	B.T.	S.	G
	10^{-3}	10^{-3}	[cm]	$[m^2/s]$	[m]				
HF-F	2.1	2.1	7	250	300	SAT2SEA	WOA01	ECMWF-H	N.A.
N-F	2.1	2.1	7	250	300	SAT2SEA	WOA01	ECMWF-H	100

Table 11.1: Overview of model setups applied for model validation runs*. See appendix I.12 for annual-mean GoF plots.

(* See appendix I.4 for an explanation about abbreviation used in this table.)

In this chapter results from these runs are compared with the validation data as described in chapter 8.

11.1 Model SST validation using AVHRR / Pathfinder data

In appendix I.10 model and AVHRR surface temperature fields for the months January and August are shown. In chapter 2 these months are identified to correspond roughly with the maximums of the NE and SW monsoon periods. These fields are compared in this section to make an assessment of the modeled surface layer temperature. This assessment will focus on run HF-F. This is done because run N-F applies SST nudging and as such implicitly gives a good representation of the surface layer temperature.

From the AVHRR and HF-F fields in appendix I.10 it is observed that during the NE monsoon the model shows the large-scale bi-frontal thermal structure. In chapter 2 this bi-frontal structure is explained by means of cold water transport along the China Continental Shelf and by large-scale mixing and transport of this cold water into the North SCS. Based on results described in section 10.2 it is concluded that the large-scale circulation governing these processes is resolved by the model to some degree. This is supported by the modeled surface layer temperature, which shows both the cold water front attributed to the large-scale mixing, the boundary current along the Vietnamese coastline and partially shows the cold water boundary current along the Chinese coastline. This boundary current is not resolved west of Hong Kong, which is attributed to a coarse model resolution in section 9.4. This provides an explanation for the high temperatures observed in the Gulf of Tonking. Furthermore, the southwards cold water transport over the Sunda Shelf is observed from the model data.

The magnitude of the large-scale temperature in the North SCS has the correct order of magnitude during the NE monsoon period. As such, it is concluded that the large-scale temperature in the North SCS is resolved by the model to a reasonable degree. In the South SCS, however, excessive temperatures are observed. In section 9.4 this is attributed to an incorrect representation of the net heat flux and possibly to an incorrect representation of the large-scale circulation.

During the SW monsoon the SCS surface layer temperature is relatively uniform (see chapter 2). Distinguishable features during this period are the upwelling of colder water east of Vietnam and the large-scale cold water transport into the central SCS basin by a large-scale current system originating from the Sunda Shelf. Both these features are observed from the model results. Also, the spatial extend of these features corresponds roughly with that identified in chapter 2.

Furthermore, it is observed that the upwelling east of Vietnam is too strong, resulting in too low model temperatures. In section 9.4 it is described that this strong upwelling can be explained partly by the σ grid layering applied which may attribute to artificial upwelling.

Finally, it is observed that in the North SCS the model temperature shows the correct order of magnitude during the SW monsoon. In the South SCS observed temperatures are too high. Furthermore, with regard to the NE monsoon values in this region an increase in surface layer temperature is observed. This can be explained by excessive model heating by the surface heat flux during the NE / SW monsoon transition period. During this period maximum heat flux values are observed in chapter 2. In section 10.1 the incorrect representation of this process is explained by inaccuracies in cloud cover forcing data.

Based on these observation it is concluded that the model resolves the large-scale surface layer temperature cycle to a reasonable degree. Observed discrepancies can be attributed to a coarse model resolution along the China Continental Shelf and to inaccurate net heat flux forcing and circulation over the South SCS. The first discrepancy will require a refinement of the model grid (see section 9.4). The second will require better cloud cover forcing data and possibly a more accurate representation of the local current system (see sections 9.6 and 10.1).

11.2 Model mixed layer validation using WOA01 profile data

In appendix I.11 vertical temperature time-series for runs HF-F and N-F are compared with reference data from the WOA01. These time series are shown for a number of model test stations as indicated in appendix I.3. The station locations are defined to obtain a reasonable coverage of the model domain and are based in part on the relevant large-scale processes as summarized in chapter 8. Based on these series the models large-scale mixed layer temperature cycle is assessed. In chapter 2 an overview of this cycle is provided based on literature and data.

From these series the following is observed:

1. In the North SCS the mixed-layer cycle is governed by the seasonal heat flux cycle and by the large-scale circulation, transport and mixing (see chapter 2). Stratification will occur during the SW monsoon when the maximum heat influx occurs. De-stratification will occur during the NE monsoon due to stronger vertical mixing and large-scale horizontal cold water transport. These large-scale cycles attribute to a decrease in mixed layer depth during the SW monsoon and an increase in mixed layer depth during the NE monsoon. From stations O1 and Ex it is observed that the model resolves this large-scale cycle for both runs HF-F and N-F. Results for these runs are similar to a large degree, confirming the better model quality in the North SCS as indicated in the previous section. Furthermore, for station Ex the de-stratification can be explained by stronger vertical mixing imposed by atmospheric forcing and by large-scale horizontal mixing (see chapter 2). For station O1 this is explained by large-scale transport of colder water along the China Continental Shelf (see section 10.2). This explains the rapid break down of the stratified system during the October period.

2. In the central SCS the seasonal mixed layer cycle is governed by the surface heat flux and by the large-scale circulation (see chapter 2). In this region stratification is observed throughout the year. During the NE / SW monsoon transition period the net heat flux will cause an increase in mixed layer temperature. During the SW monsoon the increase in cloud coverage will cause a decrease in net heat flux and as such a decrease in water temperature. Furthermore, in the northern and western regions of the central SCS a Rossby wave observed from altimeter data may attribute to a seasonal increase or decrease in vertical mixing.

   From stations A2 and O3 this large-scale cycle is observed. The mixed layer temperature follows the net heat flux cycle and continuous stratification is seen. A maximum mixed layer temperature is observed around May. During this period the strongest stratification is observed. Furthermore, at station O3 a strong seasonal mixed layer depth cycle is observed. From July till November minimum values are observed. From December till June a sudden increase in depth is noted. This large-scale cycle is resolved by the model. Furthermore, it is observed that both runs HF-F and N-F provide similar results at these stations.

3. In the shallow regions of the South SCS the seasonal mixed layer cycle is controlled by the surface heat flux and the monsoon wind mainly. During the monsoon transition periods the heat flux will reach maximum values, resulting in an increase in water temperature. Furthermore, during these periods a minimum wind speed is observed. The combined effect of these processes will attribute to stratification. During the monsoon period the wind speed increases and the heat flux decreases. This attributes to stronger vertical mixing, de-stratification and a uniform water temperature over the water column (see chapter 2). This large-scale behavior is observed from stations O6, O4 and O11. Furthermore, at these stations a significant improvement is noted for run N-F. For run HF-F excessive temperatures are observed during the monsoon transition periods. This may be explained by an inaccurate net heat flux (see section 10.1). For run N-F this heat flux is ‘corrected’ using remotely sensed SST data. This results in a strong decrease in water temperature during the indicated period and a good agreement with the reference data.

Based on the above it is concluded that the model resolves the expected seasonal mixed layer cycle adequately at all stations assessed. This seasonal mixed layer cycle shows a good correspondence with WOA01 validation data. Furthermore, it is concluded that SST nudging improves results in the shallow Sunda Strait regions mainly. Here, a significant model improvement is observed if this method is applied.

Finally, at the stations over the truncation model region (stations A2, S6 and O3) the modeled temperature is too high in the deeper model layers. This may partly be explained by excessive mixing of warm water through the thermocline, imposed by the Ozmidov length scale. This will require a re-assessment of the value used, which is not possible during this project due to time constraints. Furthermore, this may be attributed to the reduced-gravity approach. As described in section 8.2.3 the model bathymetry is truncated at 300 meters depth. At this truncation interface

Delft3D-FLOW imposes a zero-flux condition, implying that the heat transfer to deeper water layers is unresolved. In chapter 2 a vertical temperature gradient is observed at the truncation interface. This unresolved gradient may cause a build-up of heat in the lower model regions. To resolve this Delft3D-FLOW should be extended with a feature to prescribe heat sinks at the models bathymety.

11.3 Model temperature validation using the GoF

In appendix I.12 the annual-mean, layer-averaged misfit with WOA01 validation data is plotted for runs HF-F and N-F. In table 11.2 the area-averaged misfit for these runs is shown.

Run ID	**GoF**
	[°C]
HF-F	1.75
N-F	1.5

Table 11.2: Annual-mean, area-averaged misfit between model results and World Ocean Atlas 2001 validation data.

Based on these results it is concluded that both runs provide similar results in the deep, central SCS region. In the shallow model regions a significant improvement is achieved when SST nudging is applied. This confirms conclusions in sections 10.3 and 11.2. This is explained by a coarse model grid along the China Continental Shelf and by inaccurate heat flux forcing and circulation over the Sunda Shelf.

Furthermore, both runs show an inaccurate model representation at the Continental Shelf / Oceanic Plate interface. This can be attributed to a coarse model grid in these regions (see chapter 9.4).

Also, both runs show a significant misfit in the North SCS. This misfit is largest northeast of Taiwan. The location corresponds roughly with that where strong temperature mixing is observed in chapter 2. As described in that chapter, this mixing may be increased Rossby waves crossing the North SCS. The large model misfit in this region indicates that this process is not resolved accurately by the model. Note, however, that the SST fields discussed in section 11.2 show a reasonable agreement with AVHRR validation data in this region.

Finally, run HF-F provides a mean misfit of 1.75 °C with respect to WOA01 validation data. A decrease in misfit of 0.25 °C, or an improvement in model accuracy of 15 % is observed if SST nudging is applied.

11.4 Model temperature validation using in-situ data

In appendix I.13 model results are compared with in-situ and synthetic validation data (see section 8.2.2) at a number of test stations:

1. Model results are compared with ASIAEX data at station Ex.

2. Model results are compared with SCSMEX data at station A2.

3. Model results are compared with synthetic profile data at station S6.

From the comparison with ASIAEX data an average misfit of 1.5 °C is observed in the upper model layers. At lower depths, the misfit increases to over 2 °C. At these depths the modeled temperature is too high. This supports conclusions in the previous sections. Also, in most cases there is no significant difference between results from run HF-F and N-F.

When compared with SCSMEX data the average misfit in the upper model layers is below 0.5 °C. At lower levels, however, it increases significantly to over 2 °C. Again, modeled temperature is too high at deep layers. No significant differences between results from run HF-F and N-F are observed.

Finally, when comparing model and synthetic results an average misfit of 1 °C is observed at shallow levels. At deeper levels this misfit increases to over 2 °C due to high synthetic temperatures around March. This increasing misfit may be attributed to both the model results and to inaccuracies in the synthetic profiles. In chapter 7 it is concluded that these profiles perform better at shallow depths. From July onwards, however, a smaller misfit is observed. Finally, when compared with the synthetic values run N-F performs better then run HF-F, providing an average misfit of 1 °C versus one of 1.5 °C.

Part IV: Conclusions and Recommendations

In this part of the report conclusions to the objectives stated in chapter 1 are summarized. These objectives are:

1. Study the physical system of the SCS by means of a detailed literature study. In particular the 3D temperature distribution on a seasonal and basin-wide scale is studied.
2. Acquire necessary data for model forcing and validation. Emphasis will be on RS data (SST and SSA), on climatological temperature atlases and on atmospheric re-analysis archives. This is because of the advantageous synoptic coverage of these datasets with regard to the large model domain and the goal to model large-scale processes. Acquired data will be compared and controlled for quality.
3. To setup a 3D temperature model which is suited to represent seasonal, basin-scale circulation and temperature and salinity transport. The original SAT2SEA model will be used as a starting point.
4. To assess the importance of different model parameters and forcing on SCS temperature transport and circulation by means of a sensitivity analysis.
5. To assimilate RS SST data into the model in order to further improve the models temperature accuracy.

The resulting conclusions to these objectives were obtained in parts I till III of this report, and are summarized in chapter 12.

Following the conclusions, recommendations will be provided in chapter 13.

Chapter 12

Summary and conclusions

As stated in chapter 1 of this report, the SAT2SEA2 project has the following goals:

1. To assess the SCS temperature behavior on a seasonal time scale and on a basin-wide spatial scale, and to identify the processes causing these variations.

2. To expand the SAT2SEA model to a 3D temperature and salinity model and to assess whether the large-scale temperature processes can be represented accurately by this model. The primary focus will be on representing the seasonal, basin-scale mixed layer temperature cycle. The model will integrate remote sensing SST and altimeter data and various in-situ data products, among which climatological atlas data.

These goals are subdivided into five objectives. In this chapter, conclusions with regard to these objectives are summarized. Also, final conclusions on the model results are given.

Objective 1: Study the physical system of the South China Sea (SCS) by means of a detailed literature study. In particular with regard to the 3D temperature distribution on a seasonal and basin-wide scale.

From this study, and by examining available data, the following key-processes governing the seasonal mixed-layer cycle were identified (see chapter 2):

1. **The monsoon wind system:** The SCS is governed by the monsoon wind system. From September till April the northeast (NE) monsoon prevails, with its peak in December / January. From May till August the southwest (SW) monsoon prevails, with its peak in July / August. The monsoon winds govern both the large-scale SCS circulation and contribute to the seasonal heat flux cycle (see section 2.2).

2. **Large-scale transport:** monsoon-induced circulation causes piling of water on the western side of the SCS basin during the NE monsoon. This forces western boundary currents which transport colder water from the North SCS to the shallow Sunda Shelf region (see section 2.3). Also, during the NE monsoon a boundary current entering the SCS through Taiwan Strait transports cold water along the China Continental Shelf (see sections 2.3 and 2.4).

3. **Rossby wave dynamics in the North SCS:** An annually reoccurring Rossby wave with a one year period crosses the North SCS. This wave attributes to large-scale water level variations in the North SCS. Also, mixing by this wave may increase the North SCS response to cold water influx during the NE monsoon (see section 2.3).

4. **Heat flux:** Warming or cooling of surface water by the surface heat flux follows a seasonal cycle, related mainly to the annual shortwave heat flux, seasonal cloud coverage and seasonal monsoon wind cycles. The net effect of these contributers results in a net flux which has maximums during the monsoon transition periods and minimums during the monsoon highs (see section 2.5.2).

5. **Influx through Luzon and Taiwan Strait:** At Luzon Strait large-scale temperature and salinity mixing with the Kuroshio current is observed. Furthermore, cold water enters the SCS via Taiwan Strait during the NE monsoon. This water is transported westwards over the shallow China Continental Shelf by a boundary current (see section 2.4).

6. **Upwelling due to bathymetry constraints:** The large-scale circulation system will cause upwelling of sub-surface water due to bathymetry constraints. This upwelling is observed along the China Continental Shelf / Oceanic Plate interface and east of Vietnam (see section 2.5).

These processes govern the seasonal SCS mixed-layer temperature cycle and follow seasonal cycles on significant scales. Their relative importance and magnitude will vary per region of SCS. In the North SCS these processes will attribute to a seasonal temperature cycle between 6 °C and 8 °C. In the South SCS this cycle is between 2 °C and 4 °C. With respect to this cycle, minimum temperatures are observed during the NE monsoon, and maximum temperatures during the SW monsoon.

The large-scale relations between these processes and the seasonal temperature cycle was confirmed by results from an EOF analysis performed on Reynolds SST data. The primary modes found during this analysis describe 67.5 % respectively 30.5 % of the total variance. The temporal and the spatial variability described by these modes shows a strong correlation with the processes described above (see chapter 3).

Objective 2: Acquire necessary data for model forcing and validation.

To model the large-scale processes described at *Objective 1*, forcing data is required to impose them on the model and validation data is required to assess the model representation. To this end, data from the following synoptic remote sensing and in-situ datasets is acquired:

1. **In-situ and climatological data:** World Ocean Atlas 2001 (WOA01), ASIAEX, SCSMEX (see chapter 4).

2. **Remote sensing data:** DUACS Sea Surface Anomaly (SSA) and Mean Dynamic Topography (MDT), AVHRR Sea Surface Temperature (SST), Reynolds Optimally Interpolated SST (blended remote sensing / in-situ data) (see chapter 5).

3. **Atmospheric data:** ECMWF ERA-40, NCEP/NCAR Re-Analysis, COADS (see chapter 4).

From assessments of these datasets the following is concluded:

1. **In-situ data:** The amount of long-term, in-situ temperature profiles found for the SCS is limited: in-situ profile data from the SCSMEX and ASIAEX datasets has a maximum, continuous measurement period of 10 months (see appendix H.3). This is at one measurement location only. This limits the possibility of model validation using non-climatological data. Furthermore, it is concluded that on large spatial and temporal scales the WOA01 climatology provides a good insight in the SCS temperature variability. Based on a comparison with in-situ data in chapter 6 it is concluded that climatological profiles contained in this dataset, along with their standard deviation, give an good estimate of non-climatological SCS values. Also, on the spatial scale of the SCS and on the temporal scales imposed by the modeling goal, WOA01 data is useful for lateral transport forcing (both temperature and salinity) and for the model initial conditions (see chapter 8).

2. **Remote sensing data:** Altimeter SSA data from the DUACS archive is of good quality for the larger part of the SCS domain (a mean error smaller than 10% of the total signal is observed). Near coastlines and in narrow model regions like Taiwan and Malacca Strait the quality of this data significantly deteriorates (see appendix H.5). This data has a maximum temporal resolution of 1 week and gives realistic results on a spatial resolution of 1 degree (see chapter 5). Based on the modeling scales, this makes it a suitable product for model forcing and validation (see section 10.2).

   Furthermore, AVHRR / Pathfinder provides SST data at a 4.9 km spatial and a 12 hours temporal resolution. Due to extensive cloudiness over the SCS region (up to 90 %), however, the useful temporal resolution deteriorates to one month. Monthly AVHRR composites provide a useful source of information for validation of the seasonal SST variability (see chapter 11). A better temporal resolution can be achieved using Reynolds SST data. Due to blending with in-situ data, this dataset has a useful temporal resolution of one week. The spatial resolution is smaller, though (1 degree instead of 4.9 km). A comparison with available in-situ data indicates that a higher SST accuracy, by about 0.5 °C, is achieved using this product. Also apparent from this comparison are higher SST values, by up to 2 °C, during El Ninõ events (see chapter 6).

3. **Atmospheric data:** A comparison of the ECMWF ERA-40, NCEP/NCAR Re-analysis and COADS data indicates significant inconsistencies between these datasets, with differences in net surface heat flux of up to 50 W/m^2. This is most pronounced in the net shortwave (solar) flux component, indicating cloud coverage data from these archives may be inaccurate. A sensitivity experiment using data from these archives indicates that their difference in net heat flux representation can amount to an annual temperature difference between 1 °C and 3 °C (see chapter 6). Furthermore, based on this comparison the ECMWF ERA-40 dataset is expected to provide the most accurate meteorological forcing data (see chapter 6).

Due to the limited amount of non-climatological profile data available a method to derive synthetic temperature profiles from climatological and remote sensing data was investigated. This method, proposed by [Nardelli & Santoleri, 2004], is assessed in chapter 7. It is based on the coupled variability of vertical temperature and steric height profiles described by climatological datasets like the WOA01. Based on statistical relations these profiles are reconstructed using remote sensing data as surface constraints. According to [Nardelli & Santoleri, 2004], these profiles offer a number of advantageous with respect to the original, climatological profiles from which they were derived. Firstly, the temporal resolution is increased with respect to that of the RS data used. Secondly, the synthetic profiles provide a better approximation of non-climatological in-situ profiles than the initial, climatological profiles [Guinehut *et al.* , 2004]. To assess this, the method was tested at the SCSMEX Atlas 1 location. Using weekly Reynolds SST and DUACS SSA data, WOA01 temperature and steric height profiles were reconstructed. From a comparison with in-situ SCSMEX data, the resulting synthetic profiles show a mean improvement of 0.3 °C with respect to climatological WOA01 data. This improvement is most significant in the upper water levels. Based on this conclusion, the method is applied for model validation.

Objective 3: Setup a 3D temperature model which is suited to represent seasonal, basin-scale circulation and temperature and salinity transport.

Using the SAT2SEA model as a starting point, a 3D temperature model was setup using the Delft3D-FLOW modeling package (see chapter 8). To resolve the seasonal mixed-layer temperature cycle, this model must resolve the large-scale processes summarized at *Objective 1.* To achieve this heat flux and momentum forcing are applied at the free surface, and lateral transport and water level forcing are applied at the open boundaries. Furthermore, both the forcing and validation data used must share the characteristic scales of the features to be forced. Based on the processes identified at *Objective 1* and the data assessed at *Objective 2*, the following data is applied for model forcing and validation (see section 8.2.2):

1. **Heat flux forcing:** Heat flux forcing will be achieved by space and time varying EMCWF ERA-40 data. Two sets of forcing data are applied, one describing monthly-mean climatological values, the other describing year 2000 values at a 6 hrs temporal resolution. In both cases, data has a spatial resolution of 2.5 degrees. This data will be used as forcing for the Delft3D-FLOW Ocean heat flux model.

2. **Surface momentum forcing:** Wind and pressure forcing will be applied by space and time varying EMCWF ERA-40 data. Again, two sets of forcing data are applied, one describing monthly-mean climatological values, the other describing year 2000 values at a 6 hrs temporal resolution. In both cases, data has a spatial resolution of 2.5 degrees.

3. **Lateral transport forcing**: Monthly-mean WOA01 temperature and salinity data is used for lateral temperature and salinity forcing at the Taiwan and Luzon Strait boundaries. This forcing data has a temporal resolution of 1 month and resolves vertical variations.

4. **Open boundary momentum forcing:** Monthly-mean water level forcing obtained from the SAT2SEA project is prescribed at the Taiwan and Luzon Strait boundaries. In a similar way, weekly DUACS data is applied.

5. **Model validation:** Model results will be validated using monthly-mean WOA01 temperature data with a spatial resolution of 0.25 degrees. Based on conclusions at *Objective 2* this data will be applied to validated historic model results, also. Furthermore, in-situ SCSMEX and ASIAEX data and synthetic temperature profiles are applied for model validation. The models surface variability will be validated using historic, monthly-mean AVHRR SST data. Finally, the models large-scale, monthly-mean water level cycle is assessed using monthly-mean, 1 degree DUACS SSA data.

Within the constraints posed by the required processes and the used data, the model is setup (see section 8.2). The model applies a reduced-gravity approach, meaning its bathymetry is truncated at the deep SCS basin. This is done to reduce computation time and is justified by truncating the model below the thermocline, where vertical transport is very small. During SAT2SEA a truncation depth of 150 was applied. From WOA01 data it is observed that the maximum thermocline depth is above this point (around 120 meters). Furthermore, from WOA01 data a seasonally varying temperature-gradient is observed at this depth ($\pm 0.06°\text{Cm}^{-1}$). At 300 meters depth no such signal is observed. Moreover, the magnitude of the temperature-gradient is an order of magnitude smaller at this depth ($\pm 0.013°\text{Cm}^{-1}$) (see chapter 2). Based on these conclusions two truncation depths were assessed. One at 150 meter, the other at 300 meter. Furthermore, because of this truncation the propagation speed of barotropic waves decreases. This is justified by not taking into account the effects of tides during this project.

The SAT2SEA model has an equidistant 1/4° by 1/4° spherical grid. Based on the spatial scales of the required processes and of the forcing data applied, this resolution is sufficient in most model regions. An exception to this are the steep bathymetry inclines at the Continental Shelf / Oceanic plate interface. To resolve regional upwelling effects at this interface a grid refinement will be required. Within the scope of this project this is unrealistic and unneeded. Furthermore, a σ layer convention is used in the vertical model direction, implying the layer-thickness is specified as a percentage of the total depth. A uniform percentage (5 %) is applied with a maximum vertical layer spacing of 15 meters. This amounts to 6 model layers in the mixed-layer region over the central SCS, which is sufficient to resolve large-scale mixed-layer variability. Furthermore, the WOA01 validation data used has a similar resolution.

The main focus is on density driven, baroclinic flow in the central SCS. Moreover, the propagation speed of barotropic waves is represented incorrectly in this region due to the model truncation. In the shallow, un-truncated model regions large-scale wind-driven circulation will play a larger role. As such, both the baroclinic and the barotropic time step criteria will be adhered to. This resulted in a time step of 2 hrs (see section 8.2.4). Furthermore, to decrease model spin-up time, annual-mean temperature and salinity fields from the WOA01 are used as initial conditions. Transient spin-up effects using these initial conditions are suppressed after one year. As such, a one year model spin-up time is used. Finally, based on the availability of in-situ validation data the year 2000 is defined as modeling period. To increase consistency with the WOA01 validation data the model will be run for a climatological year, also.

Finally, using 20 vertical layers and a time-step of 2 hrs, a one year model run takes 3 hrs on a 3.6 GHz PC running on a Linux Operating System.

Objective 4: Assess the importance of different model coefficients and forcing on SCS temperature transport and circulation by means of a sensitivity analysis.

Using the model setup as described at *Objective 3* a number of sensitivity analysis were conducted. These analysis assessed the role of model parameters influencing the heat flux and temperature transport (chapter 9), the model temperature forcing (chapter 10), the model momentum forcing (chapter 10) and the model nudging coefficient (see next section). From these analysis the following is concluded:

1. **Sensitivity analysis on heat flux and temperature transport coefficients:** During this analysis the models sensitivity to the Stanton number (c_h, a transfer coefficient for the convective heat flux), Dalton number (c_e, a transfer coefficient for the evaporative heat flux) and Ozmidov length scale (L_{inf}, specifying the magnitude of mixing by internal waves) were assessed (see chapter 9). This was done using a simplified test-basin located in the central SCS. In literature c_h and c_e are generally assigned values of 0.9 $\times 10^{-3}$ and 1.5 $\times 10^{-3}$. Based on sensitivity experiments it is concluded that values of 2.1 $\times 10^{-3}$ and 2.1 $\times 10^{-3}$ provide better results for the SCS, decreasing the misfit with WOA01 reference data by 0.5 °C. Furthermore, the model showed a stronger dependency on c_e, which can be explained by the observation that over the SCS the evaporative flux is an order of magnitude larger than the convective flux ($\pm 120 W/m^2$ versus $\pm 10 W/m^2$, see chapter 2). A similar improvement (0.5 °C) is observed if L_{inf} is specified at 7 cm instead of its default value of 0 cm.

   Also, the model sensitivity to horizontal diffusivity D_h is assessed. This analysis showed that the fit with WOA01 reference data improves if the magnitude of D_h is increased. At $D_h = 250\ m^2/s$ this improvement is ± 0.1°C. It is most significant in the North SCS region along the China Continental Shelf, where strong mixing with a cold water boundary current is observed in chapter 2.

   Finally, a sensitivity analysis on the wind drag coefficient indicated that the model solution improves by ± 1°C in the shallow model regions over the Sunda Strait if a larger wind drag coefficient is applied ($C_d = 2 \times 10^{-3}$ versus $C_d = 0.83 \times 10^{-3}$). In the central SCS this leads to a similar decrease in model solution, indicating the need for a spatial variations of this coefficient.

2. **Sensitivity analysis on model temperature forcing:** During this analysis differences between the monthly-mean, climatological atmospheric forcing and the 6 hourly year 2000 ECMWF ERA-40 atmospheric forcing were assessed (see section 10.1). From this analysis it is concluded that the 6 hourly wind and cloud cover fields provide a significantly better solution (resulting in a 23 % and a 8 % increase in accuracy, respectively). These effects are noticable over the entire model domain, but are most significant over the shallow Sunda Shelf regions where the temperature cycle is governed by the heat flux primarily. This indicates that small scale variability plays a role in the magnitude of this cycle and that this is unresolved by the monthly-mean forcing data.

   No improvements were observed for changes in air temperature and relative humidity forcing. From this it is concluded that these fields play a smaller role in the large-scale temperature cycle.

   Furthermore, the models sensitivity to lateral transport forcing at Luzon and Taiwan Strait was assessed. Not taking into account this forcing results in a strong decrease in model quality over the shallow China Continental Shelf (± 4 °C) and to a lesser extent in the North SCS (± 0.5 °C). From this it is confirmed that the cold-water boundary current following this shelf during the NE monsoon originates from outside the SCS. Also, it is concluded that this current is resolved by the monthly-mean lateral temperature forcing.

3. **Sensitivity analysis on model momentum forcing:** To assess the models sensitivity to momentum forcing at the free surface and at the open boundaries, the modeled water level is compared with altimeter SSA data (see section 10.2). From this comparison it is concluded that atmospheric pressure forcing plays a leading role in the large-scale water level cycle in the eastern regions of the SCS. Also, this forcing data attributes to the formation of large-scale eddies in the North SCS. Possibly, this is related to a Rossby wave observed in this region from altimeter data. A detailed assessment and an accurate representation of this wave is beyond the scope of this project, however.

   Also, it is concluded that the monsoon wind plays a leading role over the shallow Sunda Shelf. A large-scale correlation with the monsoon cycle is observed in this region. This behavior is resolved by both monthly-mean and 6 hourly forcing data.

   Furthermore, it is concluded that open boundary forcing at Luzon and Taiwan Strait plays a leading role in the water-level cycle over the China Continental Shelf. This supports the conclusion drawn earlier that the cold-water boundary current observed in this region originates from outside the SCS. This intrusion is resolved by the monthly-mean forcing data.

Objective 5: Assimilate RS SST data into the model in order to force the models surface layer temperature.

To improve model accuracy, remotely sensed SST data was assimilated into the model by adding a SST nudging term to the Delf3D-FLOW Ocean heat flux model; a correction term based on the difference between model and RS SST was added to the temperature equation (equation 10.2). The magnitude of this term is controlled by means of a nudging coefficient. The reason for this approach is that (see appendix D):

1. Forcing errors due to inaccurate atmospheric data can be reduced in this way.
2. The routine is easy to implement in Delft3D-FLOW. Adaptations are made to the surface heat flux equation only, so the models transport equations remain unaltered. They are steered indirectly by the nudging term in the temperature equation.
3. The routine requires almost no additional computation time.
4. Due to its efficiency and simplicity, both in terms of formulation and required input data, the routine is robust.
5. By increasing / decreasing the nudging coefficient, emphasis can be on model forcing by either RS SST or atmospheric surface flux data. This depends on the quality of both types of forcing data.

Input data used for the nudging routine consists of weekly-mean Reynolds SST data with a spatial resolution of one degree.

After implementing this routine in the model and by a comparison with WOA01 validation data (see section 10.3), it is concluded that the model accuracy increased if the strength of the nudging coefficient is increased. For a coefficient varying between 0 and 100, the most significant increase is observed in the coefficient range between 0 and 50 (±3°C in some model regions). The improvement between 50 and 100 is an order of magnitude smaller (±1°C in some model regions). In the shallow Sunda Shelf region this leads to a model improvement of ±4°C. In the northern SCS no significant improvement is observed.

This difference can be explained by the lower model quality in the Sunda Shelf region. This lower quality may be explained by the higher cloud coverage over the South SCS when compared with the North SCS (10 % higher, see chapter 2), the higher shortwave flux at lower latitudes and by the net heat flux being the primary driver behind the seasonal temperature cycle in the South SCS (see chapter 3). Because of this the model is more sensitive to inaccuracies in the cloud coverage forcing in the southern regions. Futhermore, according to [Emery *et al.* , 2006] the numerical reanalysis cloud coverage data used is likely to have a low accuracy. Since this will result in inaccuracies in the surface heat flux it is concluded that in this region the nudging method improves the model quality in a consistent way with respect to its forcing mechanism.

A similar improvement in model quality can be observed in the Gulf of Tonking. Here, the low model quality is attributed to an incorrect representation of the cold-water boundary current, explained by a coarse model grid. From this it is concluded that in this region the model temperature is improved in an inconsistent way with respect to its forcing mechanism. This leads to the overall conclusion that caution is required when using the nudging method, since it can obscure model inaccuracies and can resolve these in an inconsistent way.

Finally, it is concluded that the best temperature representation is achieved if a nudging coefficient of 100 is applied.

Model validation.

Based on results of the model sensitivity analysis, the final model is forced using 6 hourly ECMWF ERA-40 atmospheric forcing, lateral temperature and salinity forcing from the WOA01, and monthly-mean SAT2SEA water level forcing. With regard to the seasonal mixed layer temperature, the following is concluded about the model (see chapter 11).

During the NE monsoon the characteristic, large-scale temperature features are resolved reasonably by the model. These features include a bi-frontal temperature system in the North SCS and a boundary current along the Vietnamese coastline. Furthermore, these features can be attributed to cold water intrusions through Taiwan Strait and to the large-scale current system. During this period, boundary currents transport the intruding cold water along the Chinese and Vietnamese coastlines into the shallow Sunda Shelf region. In the North SCS mixing with this colder water causes a decrease in water temperature. This mixing may be increased by Rossby wave dynamics. Based on an assessment of model water-level data it was concluded that these large-scale features are resolved by the model to some degree. An accurate representation of these large-scale circulation features is beyond the scope of this project, however, and they are assessed with regard to their role in the large-scale temperature cycle only. From a comparison with AVHRR validation data it was observed that the large-scale cycle and its characteristic features are resolved in the North SCS. Also, their respective magnitude showed a good correspondence with the AVHRR data.

Discrepancies are observed in the shallow Sunda Strait regions ($\pm 2.5°$C too high) and west of Hong Kong, following the China Continental Shelf ($\pm 3°$C too high). It is concluded that in the shallow Sunda Strait regions this discrepancy is due to an inaccurate representation of the surface heat flux, possibly by inaccurate cloud cover data. Also, an incorrect representation of the local, wind-driven current system can play a role. In the region west of Hong Kong this discrepancy is attributed to the incorrect representation of the western boundary current, explained by a coarse model grid over narrow regions of the China Continental Shelf.

During the SW monsoon the characteristic, large-scale temperature features were resolved as well. These features involve the large-scale transport of colder water from the Sunda Shelf into the central SCS and the upwelling of colder water east of Vietnam. Furthermore, a uniform temperature distribution is observed.

During this period discrepancies are observed east of Vietnam, where upwelling of sub-surface water results in excessively cold surface layer temperatures ($\pm 3°$C too low). It is concluded that this upwelling is forced by turbulent mixing and bathymetry constraints. Combined with the grid layering used this can result in artificial upwelling, also known as creep. Furthermore, excessive temperatures are observed in the shallow Sunda Strait region (±2.5°C too high). This is attributed to inaccurate heat flux forcing.

It is concluded that in most regions the mixed layer depth is resolved adequately. The model resolves the seasonal stratification cycle and the mixed layer temperature has the required magnitude (similar to the surface layer temperature described above). A discrepancy is noted in the South SCS. Here, model temperatures are too low at shallow levels and too high at deeper levels. This can be explained by excessive mixing though the thermocline imposed by a high Ozmidov length scale. The coefficient was optimized for a different part of the SCS basin, and may result in an inaccurate representation in other regions. This may be solved by specifying this coefficient in a space dependent way, which is not possible in Delft3D-FLOW. Furthermore, the observed discrepancy may partly be attributed to the zero-flux condition imposed at the model truncation interface. Because of this condition, vertical heat transport to lowers level is underestimated, resulting in a build-up of heat in these regions.

If SST nudging is applied, the model quality improves in those regions where discrepancies were observed earlier. Over the Sunda Shelf this will result in a considerable improvement in mixed layer temperature representation (by ±4°C). In other regions effects are less notable.

Finally, based on a comparison with WOA01 data a mean model accuracy of 1.75 °C is observed if no nudging is applied. If nudging is applied an improvement of 15 % is observed (a mean accuracy of 1.5 °C). From a comparison with in-situ data similar magnitudes are observed. A misfit between 1.5 °C and 2 °C is observed with respect to ASIAEX data. With respect to SCSMEX data the misfit is between 0.5 °C and 2 °C. Finally, with respect to synthetic provide data the misfit is between 1 °C and 2 °C.

Overall, it is concluded that the model resolves the seasonal mixed layer temperature to a reasonable degree. It shows the correct seasonal variations with an expected accuracy between 1.5 °C and 2 °C. This implies that Delft3D-FLOW is a suitable tool to model (mixed layer) temperature in deep water systems and large basins like the SCS.

Chapter 13

Recommendations

For each of the objectives in this project (see chapter 1) we will now describe recommendations:

Objective 1: Study the physical system of the South China Sea (SCS) by means of a detailed literature study. In particular with regard to the 3D temperature distribution on a seasonal and basin-wide scale.

The North SCS water level cycle is governed to a large extent by an annually reoccurring Rossby wave. Large-scale mixing by this wave may attribute to the significant seasonal temperature cycle observed in this region. The forming mechanisms of this wave are unclear, however. A number of different explanations are possible, based on forcing by atmospheric vorticity or intrusions through Luzon Strait. Due to the possible relation between this wave to the North SCS temperature cycle a better insight in and representation of this wave is required to improve model quality in this region. This requires a closer study of this phenomenon.

Objective 2: Acquire necessary data for model forcing and validation.

During this project only a small amount of long-term in-situ temperature profile data was obtained. For future SCS temperature modeling projects, additional effort should be put in obtaining more data, in order to make are more realistic estimate of the models accuracy.

Objective 3: Setup a 3D temperature model which is suited to represent seasonal, basin-scale circulation and temperature and salinity transport.

During this project a reduced-gravity approach is used, indicating that the models bathymetry is truncated. This is done on the assumption that below the thermocline vertical transport is small. Depending on the truncation depth this will result in a build-up of heat in lower model levels. This implies that either a small spin-up time should be used to prevent the build-up of this error, or heat sinks should be added to the truncation interface. The latter is not possible in Delft3D-FLOW at this point.

The model grid is too coarse to adequately model temperature processes in certain regions. These effects are mainly noticed along the Continental Shelf / Oceanic Plate interface, in Malacca Strait and along the China Continental Shelf. For future SCS modeling applications it should be considered refining the grid at these locations. At this moment the coarse model resolution prevents a better temperature representation in these regions.

Artificial upwelling, or creep, is observed at some model locations. This might be explained by sigma grid truncation errors at the steep Continental Slope / Oceanic Plate boundaries. Possibly, a z-layering scheme would be better suited for these applications.

Objective 4: Assess the importance of different model coefficients and forcing on SCS temperature transport and circulation by means of a sensitivity analysis.

During this project choices on model setup, parameterization and forcing were made in a sequential way. For future model use, some modeling choices made (mainly on model coefficients) should be re-evaluated using the final model setup. This holds in particular for the horizontal diffusivity and Ozmidov length scale setting, because in some model regions artificial upwelling caused by excessive horizontal mixing or excessive mixing of warm water through the thermocline is observed.

Due to the significant spatial extent of the SCS grid there may be a strong regional dependence om model coefficient settings. This property is observed for both the wind drag coefficient and the Ozmidov length scale. At this point Delft3D-FLOW does not provide the option to implement these coefficients in a space dependent way. Should the goal be to obtain a good model representation over the entire SCS model domain, such an option would be advisable.

Objective 5: Assimilate RS SST data into the model in order to force the models surface layer temperature.

For the nudging routine implemented in Delft3D-FLOW during this project, Remote Sensing (RS) Sea Surface Temperature (SST) data has to be interpolated to the model grid before application. Also, no quality labels associated with the RS SST data are taken into account. For future use it should be considered to include these features. This will further increase the ease of using the method and will further improve its results.

Chapter 14

Bibliography

[Barton, 1992] Barton, I.J. 1992. Satellite-derived Sea Surface Temperatures - A comparison between operational, theoretical and experimental algorithms. *Journal of Applied Meteorology*, **31(5)**.

[Barton, 1998] Barton, I.J. 1998. Future Directions for Satellite Studies of Skin-bulk Temperature Differences. *Journal of Advanced Marine Science and Technology*, **4(2)**.

[Bjornsson & Venegas, 1997] Bjornsson, H., & Venegas, S.A. 1997. A Manual for EOF and SVD Analysis of Climatic Data. February.

[Boyer *et al.* , 2004] Boyer, T., Levitus, S., Garcia, H., Locarnini, R.A., Stephens, C., & Antonov, J.I. 2004. Objective Analyses of Annual, Seasonal, and Monthly Temperature and Salinity for the World Ocean on a $1/4^o$ grid. *International Journal of Climatology*.

[Brown & Minnett, 1999] Brown, O.B., & Minnett, P.J. 1999. *MODIS Infrared Sea Surface Temperature Algorithm: Algorithm Theoretical Basis Document*.

[Chu *et al.* , 1998] Chu, P.C., Chen, Y., & Lu, S. 1998. Wind Driven South China Sea Deep Basin Warm-Core Cool-Core Eddies. *Journal of Oceanography*, **54**.

[Chu *et al.* , 2002] Chu, P.C., Ma, B., & Chen, Y. 2002. The South China Sea Thermohaline Structure and Circulation. *Acta Oceanologica Sinica*, **21(2)**.

[COADS, n.d.] COADS. *International Comprehensive Ocean-Atmosphere Data Set (ICOADS)*. http://icoads.noaa.gov.

[Conkright *et al.* , 2002] Conkright, M.E., Locarnini, R.A., Garcia, H.E., O'Brien, T.D., Boyer, T.P., Stephens, C., & Antonov, J.I. 2002. *World Ocean Atlas 2001: Objective Analyses, Data Statistics, and Figures, CD-ROM Documention*. Tech. rept. National Oceanographic Data Center.

[De Goede *et al.* , 2000] De Goede, E.D., Roozekrans, J.N., De Kok, J.M., Vos, R.J., & Uittenbogaard, R.E. 2000. *REST3D - Remote Sensing Sea Surface Temperature for 3D North Sea Modelling*. WL | Delft Hydraulics Report, NRSP-2 00-16.

[Delft3D, 2003] Delft3D. 2003 (December). *Validation Document Delft3D-FLOW*. Gerritsen, H., De Goede, E.D., Genseberger, M., Uittenbogaard, R.E. Version 0.3.

[Delft3D, 2005] Delft3D. 2005 (January). *Delft3D-FLOW - User Manual*. Version 3.11.

[Denner *et al.* , 2000] Denner, W.W., Chiu, C.S., & Ramp, S.R. 2000. *Report on the Office of Naval Research Phase III International Workshop on Shallow-Water Acoustics*. Tech. rept. NPS-00-00-001PR. Naval postgraduate school.

[DUACS, 2004] DUACS. 2004. *SSALTO/DUACS User Handbook: (M)SLA and (M)ADT Near-Real Time and Delayed Time Products*. Tech. rept. CLS. CLS-DOS-NT-04.103.

[DUACS, 2005] DUACS. 2005. *DT CorSSH and DT SLA Product Handbook*. Tech. rept. CLS/C-NES. CLS-DOS-NT-05-097.

[Emery *et al.* , 2006] Emery, W.J., Talley, L.D., & Pickard, G.L. 2006. *Descriptive Physical Oceanography*. Elsevier. http://www-pord.ucsd.edy/ ltalley/sio210/.

[ETOPO5, n.d.] ETOPO5. *Data Announcement 88-MGG-02, Digital Relief of the Surface of the Earth.*

[Farris & Wimbush, 1996] Farris, A., & Wimbush, M. 1996. Wind-Induced Kuroshio Intrusion into the South China Sea. *Journal of Oceanography*, **52**.

[Fu & Cazenave, 2001] Fu, L.L., & Cazenave, A. 2001. *Satellite Altimetry and Earth Sciences*. Academic Press.

[Gerritsen *et al.* , 2001] Gerritsen, H., Schrama, E.J.O., Uittenbogaard, R.E., Van den Boogaard, H.F.P., & Van der Kaaij, Th. 2001. *SAT2SEA*. WL | Delft Hydraulics Report, X0242, NRSP-2 1-14.

[Gill, 1982] Gill, A.E. 1982. *Atmosphere-Ocean Dynamnics*. International Geophysical Series, vol. 30. Academic Press.

[Gosnell *et al.* , 1995] Gosnell, R., Fairall, C.W., & Webster, P.J. 1995. The Sensible Heat of Rainfall in the Tropical Ocean. *Journal of Geophysical Research*, **100(C9)**.

[Gouretski & Koltermann, 2004] Gouretski, V.V., & Koltermann, K.P. 2004. *WOCE - Global Hydrographic Climatology*. Tech. rept. NR.35. Bundesamtes fur Seeschiffahrt und Hydrographie.

[Guinehut *et al.* , 2004] Guinehut, S., Le Traon, P.Y., Larnicol, G., & Philipps, S. 2004. Combining Argo and Remote-Sensing Data to Estimate the Ocean Three-Dimensional Temperature Fields - A First Approach Based on Simulated Observations. *Journal of Marine Systems*.

[Hernandez *et al.* , 2001] Hernandez, F., Schaeffer, P., Rio, M.H., Tamagnan, D., & Le Traon, P.Y. 2001. Mean Dynamic Topography for Satellite Altimetry: Two Approaches, from Oceanographic Data or Satellite Gravimetry.

[Jacobs, n.d.] Jacobs, G.A. Jason-1 Monitoring and Prediction Capabilities on the Continental Shelf. http://jason-1.jpl.nasa.gov.

[Kallberg *et al.* , 2004] Kallberg, P., Simmons, A., Uppala, S., & Fuentes, M. 2004. *The ERA-40 Archive*. Tech. rept. ECMWF.

[Kernkamp & Smits, 2000] Kernkamp, H.W.J., & Smits, J.G.C. 2000 (February). *Preparation Preliminary Model Lake Malawi/Nyasa*. University of Waterloo, UNU/INWEH, WL | Delft Hydraulics, T2380.

[Lane, 1989] Lane, A. 1989. *The Heat Balance of the North Sea*. Tech. rept. Report No. 8. Proudman Oceanographic Laboratory.

[Lau, 1997] Lau, W.K.M. 1997. *The South China Sea Monsoon Experiment (SCSMEX)*. Tech. rept. NASA/GSFC.

[Liu *et al.* , 2001] Liu, Q., Jin, W., Wang, X., & Yang, H. 2001. On the Annual Cycle Characteristics of the Sea Surface Height in the South China Sea. *Advances in Atmospheric Sciences*, **18(4)**.

[Mellor, 1996] Mellor, G.L. 1996. *Introduction to Physical Oceanography*. American Institute of Physics.

[Millar *et al.* , 1999] Millar, S., Mupparapu, P., Brown, W.S., & Bub, F.L. 1999. *Convex Air-Sea Heat Flux Calculations*. Technical Report UNH-OPAL-1999-004. Ocean Process Analysis Laboratory.

[Nardelli & Santoleri, 2004] Nardelli, B.B., & Santoleri, R. 2004. Reconstructing Synthetic Profiles from Surface Data. *Journal of Atmospheric and Oceanic Technology*, **21**.

[NCEP/NCAR, n.d.] NCEP/NCAR. *NCEP/NCAR Reanalysis Monthly Means and Other Derived Variables*. http://www.cdc.noaa.gov.

[NOAA, n.d.] NOAA. *Wet-bulb Temperature and Dewpoint Temperature from Air Temperature and Relative Humidity*. www.srh.noaa.gov.

[Open University, 1989] Open University. 1989. *The Open University: Ocean Circulation*. Pergamon Press.

[Panaconi *et al.* , 2003] Panaconi, C., Marrocu, M., Putti, M., & Verbunt, M. 2003. Newtonian Nudging for a Richards Equation-based Distributed Hydrodynamic Model. *Advances in Water Resources*, **3(26)**.

[Pond & Pickard, 1983] Pond, S., & Pickard, G.L. 1983. *Introductory Dynamical Oceanography*. 2nd edn. Elsevier.

[Qu, 2001] Qu, T. 2001. Role of Ocean Dynamics in Determining the Mean Seasonal Cycle of the South China Sea Surface Temperature. *Journal of Geophysical Research*, **106(C4)**.

[Reynolds *et al.* , 2002] Reynolds, R.W., Rayner, N.A., Smith, T.M., Stokes, D.C., & Wang, W. 2002. An Improved In-Situ and Satellite SST Analysis for Climate. *Journal of Climate*, **15**.

[Rio & Hernandez, 2003] Rio, M., & Hernandez, F. 2003. *CLS Combined Mean Dynamic Topography*.

[Simon *et al.* , 1999] Simon, A.J., Kent, E.C., & Taylor, P.K. 1999. *The Southampton Oceanography Centre (SOC) Ocean - Atmosphere Heat, Momentum and Freshwater Flux Atlas*. Tech. rept. Southampton Oceanography Centre.

[Smith *et al.* , 1996] Smith, S.D., Fairall, C.W., Geernaert, G.L., & Hasse, L. 1996. Air-Sea Fluxes: 25 Years of Progress. *Boundary-Layer Meteorology*, **78**.

[Stelling & van Kester, 1994] Stelling, G.S., & van Kester, J.A.Th.M. 1994. On the approximation of horizontal gradients in sigma co-ordinates for bathymetry with steep bottom slopes. *Int. J. Num. Meth. Fluids*, **18**.

[Tapley *et al.* , 2005] Tapley, B., Ries, J., Bettadpur, S., Chambers, D., Cheng, M., Condi, F., Gunter, B., Kang, Z., Nagel, P., Pastor, R., Pekker, T., Poole, S., & Wang, F. 2005. GGM02 - An Improved Earth Gravity Field Model from GRACE. *Journal of Geodesy*. DOI 10.1007/s00190-005-0480-z.

[TOA, n.d.] TOA. *TOA Sensor Specifications*. http://www.pmel.noaa.gov.

[Tomczak & Stuart Godfrey, 2001] Tomczak, M., & Stuart Godfrey, J. 2001. *Regional Oceanography An Introduction*. Pergamon.

[Twigt, 2005] Twigt, D.J. 2005. *Temperature Modeling for the South China Sea using Remote Sensing*. Internship report. WL | Delft Hydraulics and Delft University of Technology.

[Vazquez, 1999] Vazquez, J. 1999. *NCEP Reynolds Optimally Interpolated Sea Surface Temperature Data Set*.

[Vazquez, 2004] Vazquez, J. 2004. *AVHRR Ocean Pathfinder - Sea Surface Temperature Data Sets*.

[Villars *et al.* , 2003] Villars, N., Gerritsen, H., & Boon, J.G. 2003. *DMI for Modelling of Total Suspended Matter in the North Sea*. WL | Delft Hydraulics Report, Z3293.

[Wang *et al.* , 2004] Wang, D., Du, Y., Wang, W., Chen, J., & Xie, Q. 2004. Progress in Studies on the Circulation and Regional Air-Sea Interaction in the South China Sea during 1998-2002.

[Willis *et al.* , n.d.] Willis, J., Roemmich, D., & Cornuelle, B. *Combining Altimetric Height with Broadscale Profile Data: A Technique for Estimating Subsurface Variability*. http://www.jason.oceanobs.com.

[Wyrtki, 1961] Wyrtki, K. 1961. *Scientific Results of Marine Investigations of the South China Sea and the Gulf of Thailand 1959-1961*. NAGA Report - Volume 2.

[Yang & Liu, 2003] Yang, H., & Liu, Q. 2003. Forced Rossby Wave in the Northern South China Sea. *Deep Sea Research*, **50**.

Appendix A

Overview of data sources

A wide range of RS, in-situ and meteorological datasets have been used during this project. These were provided by the following institutes:

The DUACS altimeter products were produced by SSALTO/DUACS as part of the Environment and Climate European Enact project (EVK2-CT2001-00117) and distributed by AVISO, with support from CNES, at http://www.aviso.oceanobs.com/.

The AVHRR Oceans Pathfinder SST data was obtained from the Physical Oceanography Distributed Active Archive Center (PO.DAAC) at the NASA Jet Propulsion Laboratory, Pasadena, CA. http://podaac.jpl.nasa.gov/.

The NCEP Reynolds OI SST data was obtained from the Physical Oceanography Distributed Active Archive Center (PO.DAAC) at the NASA Jet Propulsion Laboratory, Pasadena, CA. http://podaac.jpl.nasa.gov/.

The World Ocean Atlas 2001 data was provided by the Ocean Climate Laboratory (OCL), division of the National Oceanographic Data Center (NODC), at http://www.nodc.noaa.gov/.

The ECMWF ERA-40 data used in this project have been provided by ECMWF, Reading, The United Kingdom, at http://www.ecmwf.int/.

The NCEP/NCAR Reanalysis data was provided by the NOAA-CIRES ESRL/PSD Climate Diagnostics branch, Boulder, Colorado, USA, from their Web site at http://www.cdc.noaa.gov

The COADS data was provided by the NOAA-CIRES Climate Diagnostics Center, Boulder, Colorado, USA, from their Web site at http://www.cdc.noaa.gov/.

The Southampton Oceanography Centre (SOC) surface flux climatology was obtained from the Southampton Oceanography Centre (SOC), at www.soc.soton.ac.uk/

The ASIAEX dataset was provided by the Tropical Marine and Science Institute (TMSI), Singapore, at http://www.tmsi.nus.edu.sg/.

The SCSMEX dataset was provided by the Tropical Atmosphere Ocean (TOA) Project Office, at www.pmel.noaa.gov/tao/.

Appendix B

Computer scripts and data management

During this project a wide range of computer scripts were written, mostly in the MATLAB environment. These scripts were used, among others, to (1) process and visualize data from the datasets described in part II of this report (WOA01, DUACS, AVHRR / Pathfinder, Reynolds OI SST, SCSMEX, ASIAEX, ECMWF ERA-40, NCEP/NCAR Reanalysis, COADS); (2) process and visualize Delft3D-FLOW results described in part III of this report; (3) perform the EOF method described in chapter 3; (4) perform the synthetic profile method described in chapter 7 and (5) to perform the goodness-of-fit method described in appendix D. For future use and reference these scripts have been put on a cd-rom.

Also, data from the datasets described in part II of this report (WOA01, DUACS, AVHRR / Pathfinder, Reynolds OI SST, SCSMEX, ASIAEX, ECMWF ERA-40, NCEP/NCAR Reanalysis, COADS) has been converted from dataset dependent formats (ASCII, Binary, NetCDF, HDF) to the MATLAB format. Both the conversion scripts and the datasets in MATLAB format have been put on a cd-rom.

Note that these datasets are provided by the institutions mentioned in appendix A. Most of these datasets are available free of charge when (1) data is used for research purposes (2) reference to the data providing institution is made. Those datasets for which this is not the case (ASIAEX) have not been included on the cd-rom.

For usage at WL | Delft Hydraulics the above mentioned cd-roms are available through:

Herman Gerritsen	herman.Gerritsen@wldelft.nl
Erik de Goede	erik.deGoede@wldelft.nl

Appendix C

Temperature modeling in Delft3D-FLOW

In this chapter an overview of temperature modeling in Delft3D-FLOW is given. In this chapter, only those features relevant to temperature modeling for the SCS will be discussed. For a more complete description of this package, the reader is referred to [Delft3D, 2005].

C.1 Heat flux modeling in Delft3D-FLOW

C.1.1 Heat flux balance

The exchange of heat at the sea surface is determined by a number of physical processes. Figure C.1 gives a schematic overview of these processes. The total flux through the free surface can be formulated by equation C.1.

$$Q_{tot} = Q_{sn} + Q_{an} - Q_{br} - Q_{ev} - Q_{co} \tag{C.1}$$

where

Q_{tot}	=	net heat flux [W/m^2]
Q_{sn}	=	net incident solar radiation (short wave) [W/m^2]
Q_{an}	=	net incident atmospheric radiation (long wave) [W/m^2]
Q_{br}	=	back radiation (long wave) [W/m^2]
Q_{ev}	=	evaporative heat flux (latent heat) [W/m^2]
Q_{co}	=	convective heat flux (sensible heat) [W/m^2]

Note that in equation C.1 and in literature multiple names are used for each component. Hereinafter the following names will be used to avoid confusion: shortwave flux, (net) longwave flux, evaporative flux and convective flux.

The change in surface layer temperature due to the net heat flux described by equation C.1 is formulated as:

$$\frac{\partial T_s}{\partial t} = \frac{Q_{tot}}{\rho_w c_p \Delta z_s} \tag{C.2}$$

where

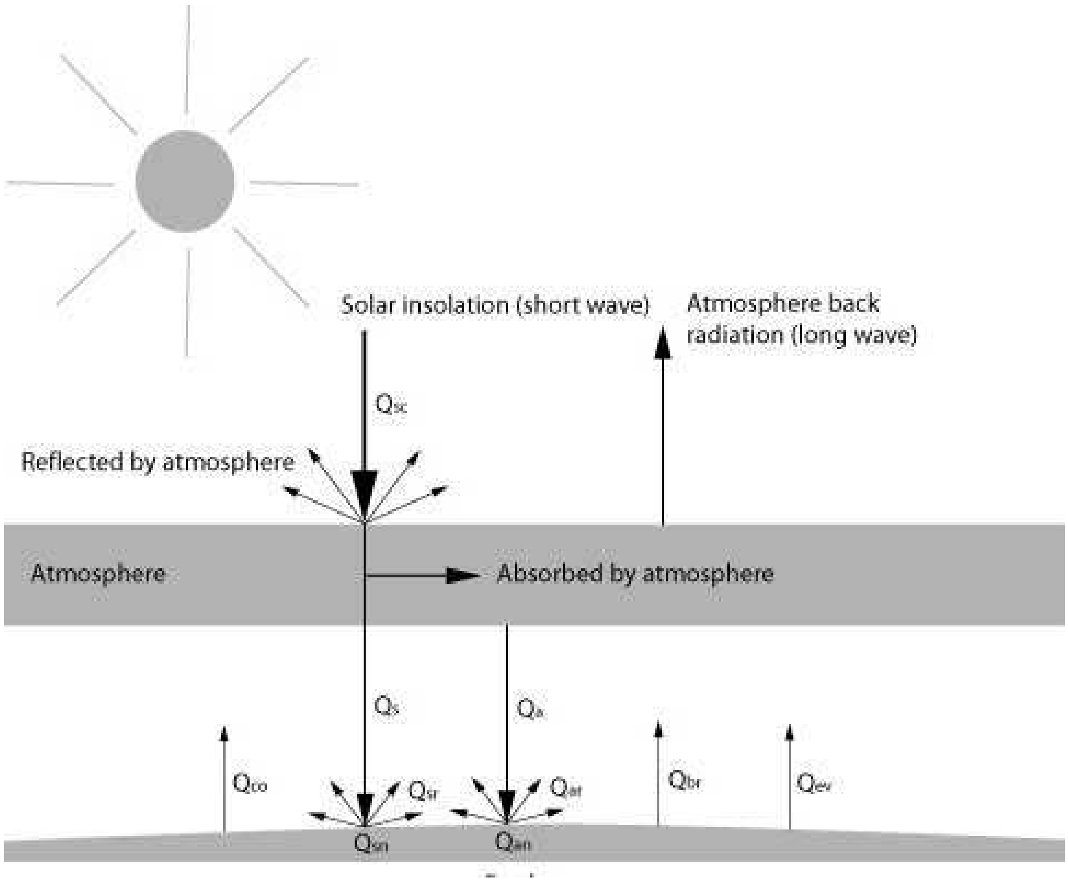

Figure C.1: Schematic overview of heat exchange processes at the water surface

Q_{tot} = net heat flux through the free surface [W/m^2]
c_p = the specific heat capacity of sea water [m^2/(s^2°C)]
ρ_w = specific density of water [km/m^3]
Δz_s = thickness of the top water layer [m]

The right-hand side of equation C.2 is added to the transport equation, which consists of advective and diffusive terms, in order to calculate the total net temperature change:

$$\frac{\partial T_s}{\partial t} = advection + diffusion + \frac{Q_{tot}}{\rho_w c_p \Delta z_s} \tag{C.3}$$

C.1.2 Delft3D-FLOW heat flux models

The Delft3D-FLOW model takes the separate effects of shortwave and net-longwave radiation and heat exchange due to evaporation and convection into account (see equation C.1). A great variability of formulations to calculate these components can be found in literature (see [De Goede *et al.* , 2000]). A number of these formulations are available in Delft3D-FLOW calibrated for different applications [Delft3D, 2005]. For the SCS temperature model the so-called Delft3D-FLOW Ocean heat flux model will be used. The term ‘Ocean’ is somewhat confusing because the model has shown to be accurate in seas, such as the North Sea, as well. This model calculates the net short wave solar radiation for a clear sky based on the declination between the Sun (incoming solar radiation) and the Earth’s surface. The total long wave atmospheric and back radiation and the heat losses due to evaporation and convection are computed by the model based on prescribed meteorological fields describing the state of the atmosphere [Delft3D, 2005]. This model offers a number of advantages when compared with the other heat flux formulations implemented in Delft3D-FLOW:

First,the short wave flux is prescribed using time and latitude-dependent relations and an average solar flux. As such, this formulation provides a higher temporal and spatial short wave flux resolution than those prescribed by atmospheric datasets (see chapter 4), prescribing clear day-night variation. Due to the latitude dependency of this model, it is applicable for large water bodies and as such suitable for regions like the SCS, spanning over 30 degrees in latitudinal direction.

Second, using this model, space-varying meteorological surface forcing can be prescribed. As such, the total net flux calculated by the model is both time and space dependent which is a desirable property considering the dimensions of the modeling domain (see chapter 8). Also, this is required to model the relevant temperature processes (see chapter 2)

Finally, this heat flux model is considered as the 'best model' of available temperature models in Delf3D-FLOW due to practicallity, robustness and simplicity. It has been applied with success in projects for the North Sea and Lake Malawi [De Goede *et al.* , 2000] [Kernkamp & Smits, 2000].

C.1.3 Ocean heat flux model

This section describes the individual terms in equation C.1 as formulated in the Ocean heat flux model. For a more extensive description see [De Goede *et al.* , 2000], [Delft3D, 2005] or [Gill, 1982].

Short wave radiation

The Ocean heat flux model calculates the short wave flux based on the geographical position and the local time: the incoming shortwave flux at the water surface depends on the declination between the Sun (incoming radiation) and the Earth's surface. This in turn depends on the geographical position and the local time. From these parameters the solar elevation angle γ is calculated. Assuming the incoming short-wave solar radiation through a clear sky at ground level is 76% of the flux incident at the top of the atmosphere and an average solar flux S (called the solar constant), the total short wave flux at the surface is calculated by:

$$Q_{s0} = \begin{cases} 0.76S sin(\gamma) & sin(\gamma) \geq 0; \\ 0 & sin(\gamma) < 0. \end{cases} \quad [W/m^2] \tag{C.4}$$

from equation C.4 it is seen that day-night variation in imposed on the shortwave flux by the solar elevation angle γ.

A part of the radiation that reaches the sea surface is reflected. This fraction is represented by the Albedo coefficient α, which depends on latitude and season. In the Ocean heat flux model α has a constant value of 0.06. According to an overview of latitude dependent Albedo coefficients in [Lane, 1989] it is concluded that this value is realistic for the SCS area. Also, cloud coverage reduces the magnitude of short wave flux reaching the sea surface. The correction factor for cloud cover $f(F_c)$ is an empirical formula based on the fractional cloud cover faction F_c. The net short wave flux is now described by:

$$Q_{sn} = (1-\alpha)Q_{s0}f(F_c) \ \ [W/m^2] \tag{C.5}$$

For the Ocean heat flux model, $f(F_c)$ is formulated as $f(F_c) = 1 - 0.4F_c - 0.38F_c^2$.

Long wave radiation

The sea radiates heat back into the atmosphere at longer wavelengths than the incident shortwave radiation (hence the name longwave radiation). Part of this longwave radiation is absorbed and re-emitted by the atmosphere. Therefore, the effective longwave radiation flux Q_{eb} from the sea surface is expressed as back radiation from the sea Q_{br} minus the longwave atmospheric radiation Q_{an}. In the Ocean heat flux model the effective back radiation is calculated as a product of the radiation by a black body at sea surface temperature, the emissivity of water, a correction factor for cloud cover and the amount of water vapour in the air:

$$Q_{eb} = Q_{br} - Q_{an} = \epsilon\sigma T_s^4(0.39 - 0.5\sqrt{e_a})(1 - 0.6F_s^2) \;\; [W/m^2] \tag{C.6}$$

In equation C.6, e_a (actual vapor pressure) is formulated as a function of relative humidity (r_{hum}) and air temperature (T_a).

Evaporative heat flux

Evaporation is a process that takes place at the boundary surface between water and the air above it. It depends on the conditions in the immediate vicinity of the free surface, and occurs until the air above the sea surface is saturated. The transport of the water vapor into the air proceeds by turbulent exchange, which depends on the wind velocity.

In the Ocean heat flux model the evaporative flux is calculated using a so called bulk formula which is based on empirical relations. It is assumed that the heat loss of sea water due to evaporation depends on the difference between the specific humidity ($q_a(T_a)$) and the specific humidity of saturated air ($q_s(T_s)$) at a prescribed atmospheric state, the air density (ρ_a), the latent heat of vaporation (L_v), and the entrainment rate $f(W)$:

$$Q_{ev} = L_v\rho_a f(U_{10})(q_s(T_s) - q_a(T_a)) \;\; [W/m^2] \tag{C.7}$$

$f(U_{10})$ is a wind speed function defined as:

$$f(U_{10}) = c_e U_{10} \tag{C.8}$$

where U_{10} is the wind speed 10 meters above the water surface and c_e is a dimensionless constant (transfer coefficient) called the Dalton number. The Dalton number is an input parameter of the Ocean heat flux model and can be used to tune the magnitude of the evaporative flux (and thus also of the net heat flux). Chapter 9 describes the optimization of this parameter for the SCS temperature model.

Convective heat flux

The Ocean heat flux model calculates the convective heat exchange through the water-atmosphere interface using a bulk formula. It assumes that the heat loss of sea water due to convection depends on the entrainment rate $g(W)$, the temperature difference between the air (T_a) and the sea (T_s) and the heat capacity of the air (c_a):

$$Q_{co} = \rho_a c_a g(U_{10})(T_s - T_a) \;\; [W/m^2] \tag{C.9}$$

$g(U_{10})$ a wind speed function defined as:

$$g(U_{10}) = c_h U_{10} \tag{C.10}$$

where U_{10} is the wind speed 10 meters above the water surface and c_h is a dimensionless constant (transfer coefficient) called the Stanton number. The Stanton number is an input parameter of the Ocean heat flux model and can be used to calibrate the magnitude of the convective flux (and thus of the net heat flux). Chapter 9 describes the optimization of this parameter for the SCS temperature model.

C.2 (Vertical) Temperature transport

In Delft3D-FLOW, temperature is transported by advective and diffusive processes: heat entering or leaving at the open model boundaries (by either the heat flux at the free surface or prescribed transport at the lateral boundaries) is transported to other regions of the model domain by these processes. In cartesian coordinates (and neglecting other source and sink terms), the transport equation for temperature can be written as [Pond & Pickard, 1983]:

$$\frac{\partial T}{\partial t} = \ advection \ + \ D_h(\frac{\partial^2 T}{\partial x^2} + \frac{\partial^2 T}{\partial y^2}) + D_v(\frac{\partial^2 T}{\partial z^2}) + Q_t \tag{C.11}$$

Where D_h and D_v are the horizontal and the vertical eddy diffusivity coefficient, and Q_t is the net heat flux calculated by the heat flux model. In Delft3D-FLOW D_v is defined as $D_v = D_{3D} + D_{mol}$. D_{3D} is referred to as the three-dimensional turbulence and is related to the turbulent eddy viscosity, which is determined by a turbulent closure model. D_{mol} represents molecular diffusion. [Delft3D, 2005]

In [De Goede *et al.* , 2000] it was shown that in strongly stratified flows problems can occur using the above definition of D_v: the turbulent eddy diffusivity at the bottom of the mixed layer (interface) reduces to zero and the vertical mixing reduces to molecular diffusion only. Because of this it can occur that too much heat remains trapped in the models top layers. This is physically not realistic because internal waves will cause additional mixing through the interface. Two approaches are possible to account for this process:

- A background mixing coefficient D_{back} can be specified in order to prescribe a minimum vertical diffusivity which accounts for all unresolved forms of mixing:

  $$D_v = D_{mol} + max(D_{back}, D_{3D}) \tag{C.12}$$

  In [De Goede *et al.* , 2000] a background eddy diffusivity of $7 \times 10^{-5} m^2/s$ was applied in order to model stratified flow in the North Sea.

- The minimum diffusivity can be specified by the Ozmidov length scale L_∞ , which prescribes mixing caused by internal waves calculated by the Brunt Väisälä frequency [Delft3D, 2005] (Also known as the buoyancy frequency, since it produces a vertical oscillation caused by buoyancy force, which induces vertical mixing [Gill, 1982]):

  $$D_v = D_{mol} + max(0.2 L_\infty^2 \sqrt{\frac{-g}{\rho}\frac{\partial \rho}{\partial z}}, D_v) \tag{C.13}$$

Both methods will cause additional mixing through the interface. They can be used to calibrate the models vertical temperature transport and stratification behavior to match reference data. Calibration parameters are summarized in table C.1. It should be noted that the Brunt Väisälä frequency has a foundation in physics, while the background diffusivity coefficient does not (and plainly forces extra mixing through the interface at all instances). As such, the Ozmidov length scale will be used as a calibration parameters in this project.

Background mixing coefficient	D_{back}
Ozmidov length scale	L_{∞}

Table C.1: Overview of Delft3D-FLOW vertical transport calibration parameters.

C.3 Error sources in temperature modeling

In sections C.1 and C.2 the processes governing surface heat flux and temperature transport were described. In these processes a number of possible error sources can be identified. These error sources can be subdivided into two groups:

- Errors due to model forcing (input) and setup.
- Errors due to model parameterization.

In this section there error sources will be discussed qualitative.

C.3.1 Errors due to model forcing and setup

The Delft3D-FLOW Ocean heat flux model calculates the net heat flux using a set of theoretical and empirical equations and space and time varying input fields prescribing the atmospheric state. Table C.2 summarizes the input fields for each of the components in this model:

Q_s	F_c
Q_l	F_c, r_{hum}, T_a
Q_{ev}	T_a, P_{atm}, ρ_a, U_{10}
Q_{co}	T_a, U_{10}

Table C.2: Required forcing data for the Ocean heat flux model

In general, errors in model forcing are the greatest contributor to the total model error [Fu & Cazenave, 2001]. As such, chapter 6 provides an assessment on the quality of different atmospheric datasets usable for model forcing. Based on this assessment a choice on forcing data is made.

It should also be noted that the temporal and spatial resolution of all atmospheric datasets under consideration is substantially lower than that of the SCS temperature model. Therefore, small(er) scale heat exchange processes might not be taken into account adequately, which can lead to an additional modeling error.

Also, errors arise due to the way in which Delf3D-FLOW is setup (or represents reality). A number of representation errors influencing model temperature are summarized below:

1. Delft3D-FLOW does not account for temperature changes due to precipitation. Only the change in water volume caused by this process is taken into account. In table C.3, the annual mean change in water temperature of a 150 meters water column due to precipitation is calculated for the SCS. Annual precipitation and evaporation values are obtained from ECMWF ERA-40 data (see chapter 4). The rain temperature is subsequently calculated based on the wet-bulb temperature [NOAA, n.d.] [Gosnell *et al.* , 1995]. From this table it is observed that the temperature error due to the neglect of precipitation is small. Also noteworthy is a annual increase in water height of nearly 1 meter when taking the difference between precipitation and evaporation. Effects of evaporation and precipitation are not taken into account in this project, however.

Annual precipitation	m	2.3
Annual evaporation	m	1.3
Mean rain temperature	°C	25.8
Mean column temperature	°C	26.2
Column temperature change	°C	0.02

Table C.3: Assessment of water column temperature change due to precipitation: annual water temperature change of a 150 meter water column with a mean temperature of 26.2 degrees, attributed to rainfall.

2. Delft3D-FLOW uses a number of vertical layer definitions, specifying either the absolute (z layering) or the relative thickness (σ layering) of each layer. In both cases it may occur that the surface layer has a significant depth. The surface layer temperature is the average temperature over this depth. This can pose problems in a number of ways:

   - When comparing model SST with SST from other sources such as in-situ, remote sensing and climatological SST. In a numerical model like Delft3D-FLOW, SST indicates the temperature in the top layer of the numerical grid. As such it is dependent on the vertical resolution. This differs from RS or in-situ SST: in general, RS SST sensors measure the the so-called skin temperature (T_s), indicating the upper film-layer of water which contributes to the ocean / atmosphere heat and moisture fluxes. Because of evaporative cooling, T_s is generally lower than the interior temperature [Barton, 1998]. In-situ SST sensors generally measure temperature at depths between 0.3 and 1 meter. This is generally called the bulk temperature (T_b).
   - When calculating the heat exchange through the free surface. A number of heat flux components (longwave and evaporative flux) depend on the model SST. Since these processes occur at the sea-atmosphere interface, SST here indicates the temperature at this interface, which is different from the temperature averaged over the model surface layer. As such, the SST temperature used to calculate the heat flux is likely to be under-estimated, resulting in an over-estimated net flux. This again will result in a over-estimated temperature in the model surface layer (as such it forms a feedback mechanism).

3. In Delft3D-FLOW, the heat exchange to the bottom is assumed to be zero. This may lead to over-prediction of the water temperature in deeper model layers where the SCS model depth is truncated to 150 / 300 meters.

C.3.2 Errors due to model parameterization

Processes governing surface heat flux and temperature transport can be subdivided into two sets:

- Those based on theory: the magnitude of a certain property is calculated from theoretical functions, often using a set of assumptions or simplifications.
- Those based on empirical measurements: the magnitude of a certain property is calculated using functions based on empirical measurements.

In both cases, a modeling error will occur due to:

- The assumptions and simplifications made.
- The empirical nature of the functions.

In most cases, parameters can be calibrated in order to minimize this error. In some cases, however, parameters are fixed and cannot be changed. Table C.4 gives an overview of these parameters for each component of the heat flux balance and for the parameters influencing vertical temperature transport. It also indicates whether these parameters are fixed in Delft3D-FLOW or if they can be used to calibrate the model.

Q_s	$f(F_c)$, α	Fixed, fixed
Q_l	$f(F_c)$	Fixed
Q_{ev}	c_e (Dalton)	Calibration
Q_{co}	c_h (Stanton)	Calibration
Vertical transport	D_{mol}, D_{back}, L_∞	Fixed, calibration, calibration

Table C.4: Overview of Delft3D-FLOW heat flux and vertical temperature transport model coefficients.

Important is that in Delft3D-FLOW all parameters in table C.4 are uniform over the model domain. As such, values calibrated for one part of the domain might not be realistic for another part. This may pose a problem for SCS temperature modeling: the model domain encompasses a number of regional seas and straits spread out over 30 degrees in latitudinal and longitudinal direction (see chapter 2). Moreover, these seas vary significantly in depth. As such it is reasonable to assume vertical mixing and stratification behavior will differ over the model domain.

Of the parameters summarized in table C.4, C_e, C_h and L_∞ will be assessed by means of a model sensitivity analysis in chapter 9.

Appendix D

Data assimilation

This chapter describes two data assimilation methods used to optimize the 3D temperature distribution of the SCS temperature model. Prior to this description some conceptual background information on data assimilation and on the various error sources encountered when assimilating data will be discussed in section D.1. Based on this discussion, a Goodness-of-Fit (GoF) routine used for model calibration will be described in section D.2. A routine implemented to nudge remotely sensed SST into the Delft3D-FLOW model will subsequently be discussed in section D.3. This chapter only provides background information on these methods and on their implementation. In part III and IV of this report results obtained with these methods will be discussed.

D.1 Data assimilation concept

Data assimilation is a procedure that combines observations with models. The combination aims to better estimate and describe the state of the dynamic system. Estimates of the dynamic system are improved by correcting model errors with observations. Also, in addition to the state of the ocean, data assimilation provides a framework to estimate and improve model parameters, external forcing, and open boundary conditions. In [Fu & Cazenave, 2001] a clear overview on the subject of data assimilation is provided. The discussion below will closely follow this work.

Mathematically, the data assimilation problem can be described by equation D.1, where the unknowns $\mathbf{x}_i$ are dependent variables of the model. The knowns, $\mathbf{y}_i$ include all observations. The functional $\mathbf{H}_i$ describes the relationships between the knowns and the unknowns. All variables and functions are assumed to be discretizised in time and space.

$$\mathbf{y}_i \approx \mathbf{H}_i(\mathbf{x}_i) \tag{D.1}$$

In addition to equation D.1, the model algorithm provides a constraint on the temporal evolution of the model state described by equation D.2:

$$\mathbf{x}_{i+1} \approx \mathbf{F}_i(\mathbf{x}_i) \tag{D.2}$$

Here functional $\mathbf{F}_i$ describes a discretization of the equations of ocean physics and integrates the model state in time from instant i to instant $(i+1)$.

By solving the data equation D.1 and the model equation D.2 simultaneously, the simulation seeks a solution (model state) that is consistent with both data and model equation. Considering the dimensions of the problem at hand, this will result in a significant computational task. As such, within the scope of this project two methods are used which are related to, but don't actually solve the above described system of equations. In these equations, the following error sources are encountered.

1. **Model state error**: The models true state is described by a functional representation of the 'real ocean':

$$\overline{\mathbf{x}} = \mathbf{P}(\mathbf{w}) \tag{D.3}$$

Here $\overline{\mathbf{x}}$ describes the model true state, $\mathbf{w}$ the 'real' ocean, and functional $\mathbf{P}$ relates the complete and exact state of the ocean to its representation in the finite and approximate space of the model. $\mathbf{P}$ includes both spatial averaging as well as truncation and/or approximation of the physics. These operations will result in an error (ϵ_{state}) between $\mathbf{x}$ and $\mathbf{P(w)}$ described by:

$$\epsilon_{state} = \overline{\mathbf{x}} - \mathbf{P}(\mathbf{w}) \tag{D.4}$$

Apart from its dependence on errors in the initial conditions and assimilated data, $\mathbf{P}$ contains an error due to time-integration of the process noise $\mathbf{q}_i$ of equation D.2:

$$\mathbf{q}_i = \overline{\mathbf{x}}_{i+1} - \mathbf{F}_i(\mathbf{x}_i) \tag{D.5}$$

$\mathbf{q}_i$ includes inaccuracies in the numerical algorithms, as well as errors in external forcing and boundary conditions.

2. **Observation Error**: During observations properties of the real ocean are measured, which can be described by:

$$\mathbf{y} = \mathbf{E(w)} + \epsilon_{obs} \tag{D.6}$$

Here $\mathbf{y}$ describes the measured value, $\mathbf{E}$ represents the measurements sampling operation of the real ocean $\mathbf{w}$, and ϵ_{obs} denotes the measuring instruments error. Generally, functional $\mathbf{E}$ differs from the models equivalent $\mathbf{H}$ in equation D.1.

Using this description of error sources, equation D.1 can be re-written as:

$$\mathbf{y} = \mathbf{H(x)} + (\mathbf{E(w)} - \mathbf{H(P(w))}) + \epsilon_{obs} \tag{D.7}$$

Here $(\mathbf{E(w)} - \mathbf{H(P(w))})$ is called the representation error. This error is caused by the difference between the model representation error $\mathbf{H(P(W))}$, which is largely caused by spatial and physical truncation errors in $\mathbf{P}$, and by incorrect model forcing and the data representation error $\mathbf{E(w)}$, which is primarily caused by the observation system not exactly measuring the intended property. ϵ_{obs} denotes the measuring instrument error.

D.2 Goodness-of-Fit

In general, the reason for using a Goodness-of-Fit (GoF) is to measure the difference or agreement between model results and observations. It is a method of comparing two different data sources and quantifying the difference in an objective and reproducible way, reducing this difference to a single number or a set of numbers [Villars *et al.* , 2003].

Mathematically, the GoF can be described as quantifying the difference between the observation $\mathbf{y}$ and its model equivalent $\mathbf{H(X)}$ in equation D.7:

$$\mathbf{y} - \mathbf{H}(\mathbf{x}) = (\mathbf{E}(\mathbf{w}) - \mathbf{H}(\mathbf{P}(\mathbf{w}))) + \epsilon_{obs} = GoF \tag{D.8}$$

Because this is done in an objective and reproducible way, the magnitude of the GoF gives an indication of the quality of the model: since the data representation error $\mathbf{E(w)}$ and the measuring instrument error ϵ_{obs} are constant, changing model parameters or forcing will result in changes in the model representation error $\mathbf{H(P(W))}$, which are quantified by the GoF procedure. As such, by minimizing the GoF the model representation error is minimized with respect to the observed data. As such, differences between the compared properties are not resolved. Also, the instrument error ϵ_{obs} provides a lower bound for the GoF, causing a large instrument error to limit the usefulness of this method.

For this project, a GoF routine is used to compare WOA01 (see chapter 4) and modeled 3D temperature and salinity profiles. As described above, the GoF may suggest variations in model set-up and parameters, which iteratively may lead to a decrease of the GoF, corresponding to an improvement of the model representation. In this manner, the GoF can be used to optimize the model. This process is schematised in figure D.1.

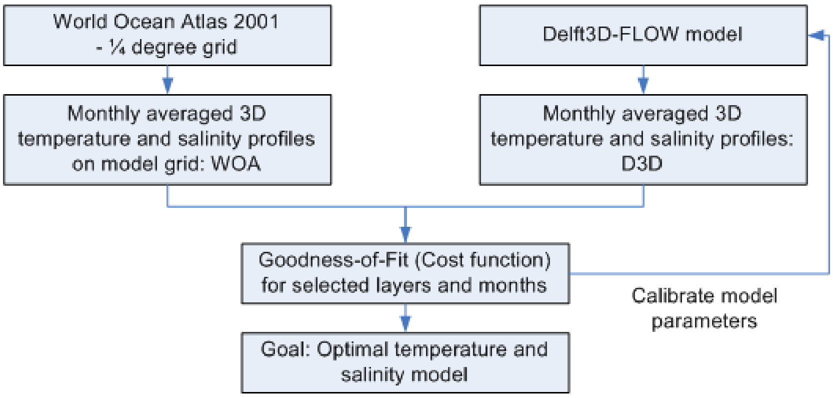

Figure D.1: Schematic diagram Goodness-of-Fit concept.

In the above process, a GoF value ($GoF_{t,\sigma,n,m}$) is determined for each grid cell at specified time instances. $GoF_{t,\sigma,n,m}$ is specified as the absolute difference between WOA01 and model data:

$$GOF_{n,m} = |D3D_{t,\sigma,n,m} - WOA_{t,\sigma,n,m}| \tag{D.9}$$

This definition implies a better agreement when the GoF is smaller. A single GoF model value follows from summation over the specified model domain (n,m), time (t) and the model layers (σ):

$$GOF_{model} = \frac{\left\{\sum_t \sum_\sigma \sum_{n,m} \{W_{t,\sigma,n,m} * GoF_{t,\sigma,n,m}\}\right\}}{\left\{\sum_t \sum_\sigma \sum_{n,m} \{W_{t,\sigma,n,m}\}\right\}} \tag{D.10}$$

As described in equation D.10 weights ($W_{t,\sigma,n,m}$) are applied in this GoF formulation. In this way, emphasis can be placed on specific regions of the model domain.

It should be noted that the WOA01 data fields describe climatological means at standard layers and a fixed grid. These fields were obtained by interpolation of in-situ measurements. As such, the measurement error ϵ_{obs} in equation D.8 can be seen as a combination of the measurement errors in the original data and the interpolation routine. Over the SCS domain this error has an average magnitude of 0.96 °C for temperature and of 0.16 ppt for salinity. Since these errors are constant at each grid point in the routine, they will have the same impact on all compared results and as such will not restrict the usefulness of this routine. They do, however, place a bound on the achievable model accuracy when using this method. Also, it should be taken into account that the temperature as described by the model and by the WOA01 represents different quantities:

- The SCS temperature model uses a layer definition in which layer depth is defined as a percentage of the total depth. As such model temperature represents the average temperature over a water layer, the thickness of which is defined by the local depth.
- In the WOA01 climatological mean monthly temperature is defined at standard layers and a fixed grid.

In order to minimize the magnitude of this representation error, WOA01 temperature data is interpolated to the model grid. Also, the data is interpolated in vertical direction to the model layers based on its layer definition. Finally, monthly averages of model temperature were used for this comparison for consistency with the WOA01 data. In Delft3D-FLOW these were obtained using Fourier files [Delft3D, 2005].

D.3 Nudging

This section will describe the theoretical background of a temperature nudging routine implemented in Delft3D-FLOW for this SCS project. A short conceptual description on nudging (also called Newtonian relaxation) is given in section D.3.1, followed by a more thorough description on SST nudging, its implications and its implementation in Delft3D-FLOW in section D.3.2.

D.3.1 Nudging concept

Nudging is a data assimilation method in which observation data is blended with models by adding a Newtonian relaxation term to the model equation D.2. The aim is to continuously force the model state toward that of the observations. Mathematically, this can be described by:

$$\mathbf{x}_{i+1} \approx \mathbf{F}_i(\mathbf{x}_i) - \gamma(\mathbf{H}(\mathbf{x}) - \mathbf{y}) \tag{D.11}$$

Here the nudging coefficient (γ) is a relaxation coefficient that is typically a function of distance and time between model variables and observations. Using equation D.7, the relaxation term in equation D.11 can be re-written as:

$$\gamma(\mathbf{y} - \mathbf{H}(\mathbf{X})) = -\gamma(\mathbf{E}(\mathbf{w}) - \mathbf{H}(\mathbf{P}(\mathbf{w}) + \epsilon_{obs}) \tag{D.12}$$

By introducing an additional forcing term based on the difference between model and observation data, the nudging routine aims to minimize the magnitude of the representation error. The method, however, gives no insight in the origin of this error and changes in model forcing are not necessarily physically consistent. Also, the method can be used for hind-casting only and has no predictive capabilities.

Despite these drawbacks, a nudging approach was chosen for this project because of its simplicity with respect to other data assimilation methods and due to the computational efficiency of the method. Moreover, the method is robust and easy to use.

D.3.2 SST nudging

In this project, SST nudging is applied to thermal forcing at the model surface boundary. RS SST data will be nudged into the model in order to improve the models 3D temperature distribution. The approach used is similar to the one described during the REST3D project for a North Sea temperature model [De Goede *et al.* , 2000] and can be applied in two ways:

1. **Forcing by a nudging term only**: The temperature at the models surface layer is prescribed using SST data. Changes in surface temperature are described by:

$$\frac{\partial T}{\partial t} = advection + diffusion + \gamma(T_{SST} - T_s) \tag{D.13}$$

   The quality of the solution using this approach depends on a number of factors:

   - The quality of the SST forcing at the free surface: SST data is available from a number of sources (see appendix H.1). Each of these sources has associated instrument errors. Also, they can represent different quantities.
   - Averaging effect: SST fields available from these sources represent temporal and areal averages by both the sensor characteristics and post-processing. This can lead to inconsistencies between computed heat flux and measured SST (different representation).
   - Data availability: the availability of remotely sensed SST can be severely hampered by cloudiness. As described in chapter 2 an average cloudiness of up to 80% can occur over the SCS domain. As such, the high temporal resolution characteristic of remotely sensed SST strongly deteriorates. Appendix H.7 shows that for both daily and weekly composite SST maps, a substantial part of the SCS domain is obscured by clouds. Only for a monthly compositing period the entire domain is mostly cloud free.

2. **Nudging as a correction term in the heat flux equation**: The heat flux model described in appendix C is extended with a SST nudging term to correct the surface heat flux:

$$\frac{\partial T}{\partial t} = advection + diffusion + \frac{Q_{tot}}{\rho_0 c_{pw} \Delta z_s} - \gamma \frac{\frac{\partial Q}{\partial T}(T_{SST} - T_s)}{\rho_0 c_{pw} \Delta z_s} \tag{D.14}$$

   This formulation offers a number of advantages with respect to the methods using the heat flux model (equation C.3) or nudging term only (equation D.13):

   - The high spatial resolution of the remotely sensed SST is used to prescribe heat flux forcing on a smaller spatial scale than the meteorological forcing applied, allowing a more realistic representation of heat exchange phenomena on a small(er) spatial scales.
   - The observed SST is used to correct for inadequates in the heat flux forcing data.
   - The high temporal resolution of the meteorological forcing (6 hrs, see chapter 4) is used to prescribe temporal variability unresolved in the weekly or montly composite SST maps.
   - The model provides a solution when there is no remote sensing data available and so improves on the remotely sensed SST solution.
   - By including the $\frac{\partial Q}{\partial T}$ term the magnitude of the nudging term is specified in a time and space varying way.

Equation D.14 prescribes the heat flux as the sum of two components, namely a prescribed heat flux based on meteorological data and a correction term proportional to the difference between the measured T_{sst} and the model temperature T_s. This difference is multiplied by a relaxation term, which is formulated by:

$$Relaxation\ term = \gamma \frac{\frac{\partial Q}{\partial T}}{\rho_0 c_{pw} \Delta z_s} \tag{D.15}$$

Here $\partial Q/\partial T$, added for dimensional arguments, is the temperature derivative of the heat flux equation described in appendix C. This equation is determined in a space and time varying way, and is specified by a number of components (shortwave, longwave, convective and evaporative flux):

$$Q_{tot} = Q_s - Q_l - Q_e - Q_c \tag{D.16}$$

Differentiating equation D.16 with respect to temperature gives:

$$\frac{\partial Q}{\partial T} = \frac{\partial Q_s}{\partial T} - \frac{\partial Q_l}{\partial T} - \frac{\partial Q_e}{\partial T} - \frac{\partial Q_c}{\partial T} \tag{D.17}$$

where

$$\frac{\partial Q_s}{\partial T} = 0 \tag{D.18}$$

$$\frac{\partial Q_l}{\partial T} = f(U_{10}) L_v \frac{\epsilon \rho_a}{P_{atm}} e_s(T) ln(\frac{0.03153}{(1+0.00412T)^2} \tag{D.19}$$

$$\frac{\partial Q_e}{\partial T} = 4\epsilon\sigma T^3 (0.39 - 0.05\sqrt{e_a})(1 - 0.6F_c^2) \tag{D.20}$$

$$\frac{\partial Q_c}{\partial T} = \rho_a c_p g(U_{10}) \tag{D.21}$$

It was described in section D.3.1 that the relaxation coefficient γ is typically a function of distance and time between model variables and observations. Following [Panaconi *et al.* , 2003] it can be formulated as:

$$\gamma = GW(\mathbf{x}, t)\epsilon(\mathbf{x}) \tag{D.22}$$

Where G determines the relative strength of the nudging term with respect to the physical forcing. When specifying G it should be taken into account that this term is multiplied by $\partial Q/\partial T$, which in effect also changes the relative strength of the nudging term in a space and time varying way based on changes in the prescribed heat flux. $W(\mathbf{x}, t) = W1(x, y)W2(z)W3(t)$ describes weights as functions of space and time in order to specify the magnitude of the nudging term. Finally, $\epsilon(\mathbf{x})$ reflects the accuracy of the observations. For a perfect measurement ϵ should equal 1. If no data is available ϵ should be set to 0. If ϵ is set to 0, the heat flux will be calculated based on the meteorological forcing solely.

To account for day-night variation unresolved by most RS SST products an additional term specifying this variation can be included in equation D.14:

$$T_{day-night} = -T_a cos(2\pi \frac{(t_{hour} - t_p)}{24}) \tag{D.23}$$

where T_a specifies the amplitude of day-night variation, and t_p specifies the time-of-day at which the maximum correction should occur.

The routine implemented in Delft3D-FLOW for this project makes some simplifications with regard to the formulations as described above. Due to time limitations the weight function, quality index and day-night variation were not included. As such, the thermal forcing equation with SST nudging reads:

$$\frac{\partial T}{\partial t} = advection + diffusion + \frac{Q_{tot}}{\rho_0 c_{pw} \Delta z_s} - G \frac{\frac{\partial Q}{\partial T}(T_{SST} - T_s)}{\rho_0 c_{pw} \Delta z_s} \tag{D.24}$$

Chapter 10 of this report describes a sensitivity analysis on the nudging term G for the SCS temperature model. Chapter 6 describes a comparison study on RS SST datasets under consideration as forcing data.

Appendix E

Steric Height

This chapter describes the background of the steric height profiles used to derive synthetic temperature profiles in chapter 7. Section E.1 provides theoretical background and section E.2 describes the used processing methodology. Section E.3 subsequently describes the validation of the described algorithm.

E.1 Steric height concept

The sea level at a particular ocean location can be associated with the water density in the whole ocean column at that point. Assuming the mass of a water particle is constant, an increase in density will result in a decrease in volume, and visa versa. Under the assumption that volume changes only occur along the column direction, this can be formulated as:

$$M = \rho V \rightarrow \delta M = \delta\rho V + \rho\delta V = 0 \rightarrow \frac{\delta z}{z} = -\frac{\delta\rho}{\rho} \tag{E.1}$$

In equation E.1, the density is calculated as a function of temperature, salinity and pressure using the Equation of State [Gill, 1982]:

$$\rho = \rho(T, S, p) \tag{E.2}$$

Equations E.1 and E.2 state that changes in temperature, salinity or pressure result in changes in column height. The difference between this column height and that of a reference state is generally referred to as steric height. Changes in density due to changes in temperature and salinity will result in changes in steric height.

Using this property, temperature and salinity fields from climatological datasets like the WOA01 (see chapter 4) can be used to calculate steric height fields. To this end equation E.1 can be rewritten as:

$$Steric\ Height\ =\ h(z_1, z_2) = \int_{z_1}^{z_2} \frac{\Delta\rho(T, S, p)}{\rho_0(p)} dz \tag{E.3}$$

Where $\rho_0(p) = \rho(0, 35, p)$ and $\Delta\rho(T, S, p) = \rho_0(p) - \rho(T, S, p)$. This equation describes the height by which a column of water between z_1 and z_2 with reference temperature T=0°C and salinity S=35.0 ppt expands if its temperature and salinity are changed to the observed values

[Tomczak & Stuart Godfrey, 2001]. These height variations are described between isobaric surfaces. This has some important implications. When calculating steric height it is assumed that the sea surface is isobaric. It can, however, not be used as a reference surface. Because of this, the assumption is made that a constant pressure surface which does not vary with depth can be found somewhere in the ocean (a 'depth of no motion'). Now it is possible to map the steric variation of every isobaric surface with respect to this depth of no motion. This property is used in the next section to derive steric anomaly fields.

E.2 Steric height derivation

The previous section describes that steric height variations are variations in water column height due to changes in temperature and salinity. The reasons for studying these variations are two-fold:

- Steric height is strongly correlated with the heat content of a water column. Based on this property maps of heat content and storage can be determined from estimates of steric height [Willis *et al.* , n.d.].
- A large portion of the Sea Surface Anomaly (SSA) variability measured by altimeter is caused by steric variations (density changes) in the top-most kilometer of the water column, since most dynamic temperature and salinity processes occur in this region [Willis *et al.* , n.d.].

SSA variations measured by altimeter contain information about sub-surface density and associated temperature and salinity variations. [Guinehut *et al.* , 2004] and [Nardelli & Santoleri, 2004] describe methods to use this information in order to construct synthetic sub-surface temperature profiles. This method, based on coupled patterns of variability in steric height and temperature fields, is assessed in chapter 7.

Steric height anomalies used in this method are calculated from the WOA01 dataset (see chapter 4). This dataset contains monthly gridded fields of temperature and salinity at fixed depth levels. Figure E.1 shows the processing method used to derive steric anomaly maps from this data.

1. Temperature and salinity profiles from the WOA01 are interpolated from specified depth levels to 1 meter vertical spacing at each grid point.
2. The WOA01 does not contain information about pressure at the specified depth levels. As such, the equation of state (equation E.4) and the hydrostatic pressure equation (equation E.5) are used to calculate pressure from the surface downwards:

$$\rho_{(0-1)} = \rho(T(0), S(0), p(0)) \tag{E.4}$$

$$p(1) = \rho_{(0-1)} g h \tag{E.5}$$

   It is assumed that the pressure at the surface is known, and the density is constant over 1 meter intervals. Subsequently, a new pressure is calculated after each 1 meter step using the hydrostatic equation. Using this pressure, a new density is calculated from the equation of state. This is repeated for each layer. The value of g used in the hydrostatic equation is obtained from the GRACE GGM02 Gravity Model and is specified per grid point [Tapley *et al.* , 2005].

3. Using the 150 bar isobaric surface (which lies slightly above 1500 m depth) as a reference surface (the 'depth of no motion'), the steric height variations in the water column are calculated using equation E.3. The reason for choosing this reference surface is based on its frequent use in literature about steric height [Gouretski & Koltermann, 2004] [Rio & Hernandez, 2003]. As such, the calculated fields can be compared with literature sources for validation.

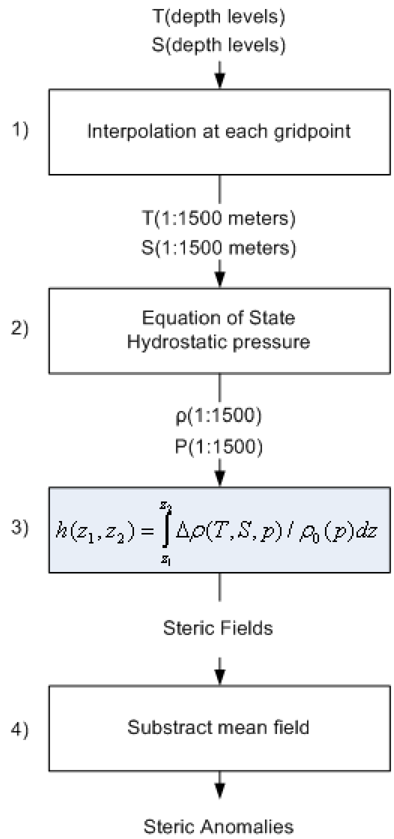

Figure E.1: Flowchart representing the algorithm used to derive steric height from World Ocean Atlas 2001 temperature and salinity data, referenced to the 150 bar surface.

4. Steric anomalies are calculated by subtracting the annual mean steric height.

In the above process, steric height fields are computed with respect to the 150 bar reference surface. As such they will only be calculated for central SCS basin (over the Oceanic Plate), and not over the shallow Continental Plate regions.

E.3 Steric height validation

In figure E.2 the annual-mean steric height calculated using the above described algorithm is compared with the MDT calculated by [Rio & Hernandez, 2003]. This MDT was calculated from a multi-variate analysis using hydrographic data, surface drifter velocities and altimetry. The first guess is based on both the CLS01 MSS - EIGEN2 (CHAMP) geoid and the Levitus '98 climatology (referenced to 150 bar) [Rio & Hernandez, 2003]. While this procedure is different from the one described above, the reference level for the hydrographic data is similar (150 bar). As such results should be comparable. Due to this choice of reference surface steric height is only computed for grid points with a depth larger than 1500 meter. Therefore, no values are available at shallower points.

From figure E.2 the following is concluded:

- Both dynamic heights show more or less similar features.

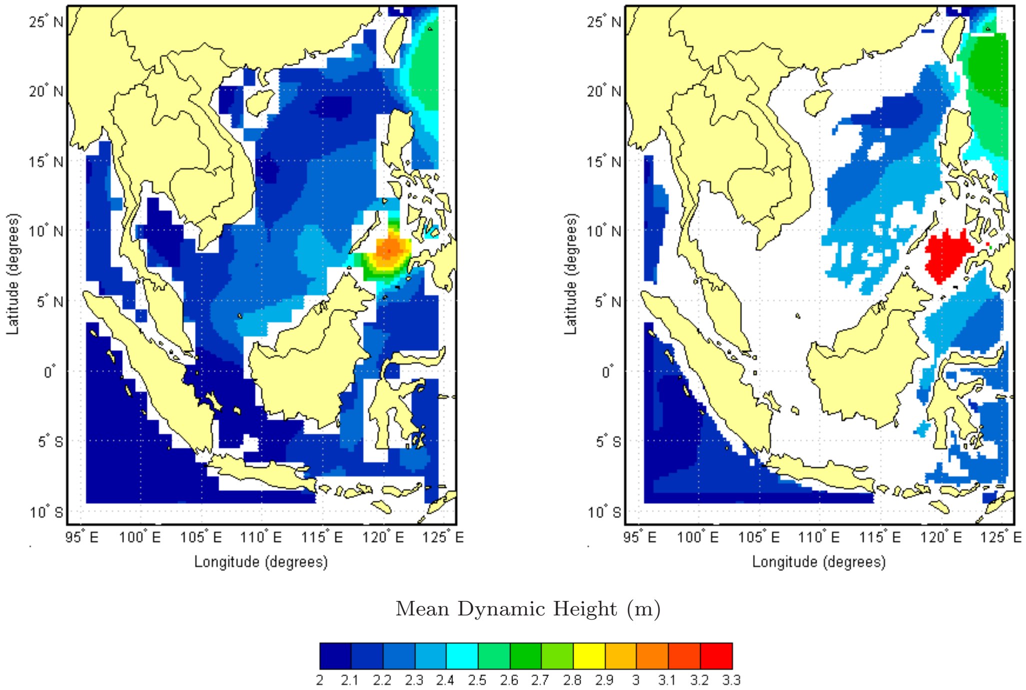

Figure E.2: Mean Dynamic Topography (left) and Mean Steric Height (right): Mean Dynamic Topography obtained from CLS [Rio & Hernandez, 2003]. Mean Steric Height determined from World Ocean Atlas 2001 temperature and salinity data.

  - Increasing height in the Pacific waters East of Luzon strait.
  - An anomalous high in the Sulu Sea.
  - A slight increase in height following the Borneo, Palawan and Luzon Islands.
  - A significantly lower height in the Indian Ocean

- The order of magnitude of these features is also similar. Exception is the anomalous high in the Sulu Sea, which is significantly higher in the steric field (see chapter 2).

Based on these similarities the steric height fields are assumed to be sufficiently accurate for applications in this project.

Appendix F

Geostrophic Currents

This chapter will provide background information on geostrophic circulation and on obtaining these fields from altimeter SSA and ADT data. In this project geostrophic circulation fields will be used to assess the SCS circulation in chapter 2.

Altimetric dynamic topography can be used to derive geostrophic current maps. Differences in dynamic topography between two points result in differences in pressure at a given depth level, resulting in a horizontal pressure gradient. This happens because of the fact that the pressure at a given depth is essentially caused by the weight of the above water column (hydrostatic principle), and is illustrated in figure F.1:

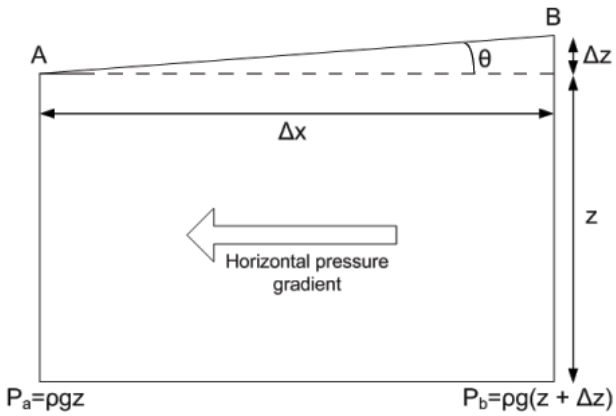

Figure F.1: Schematic overview geostrophic flow [Open University, 1989]

The difference in pressure between points A and B is given by:

$$\Delta p = p_b - p_a = \rho g z(z + \Delta z) - \rho g z = \rho g \Delta z \tag{F.1}$$

where p indicates pressure, ρ indicates density and z indicates the height above a reference surface. If points A and B are a distance Δx apart, the horizontal pressure gradient between them is given by:

$$\frac{\Delta p}{\Delta x} = \rho g \frac{\Delta z}{\Delta x} = \rho g \tan\theta \tag{F.2}$$

Per unit mass of seawater this becomes:

$$\frac{1}{\rho}\frac{\Delta p}{\Delta x} = g \tan\theta \tag{F.3}$$

Due to this pressure gradient water particles flow from high to low pressure regions. The force balance between this force and the Coriolis force experienced by a moving water particle is called the geostrophic equilibrium:

$$mg \tan\theta = mfu \tag{F.4}$$

From this equation the geostrophic flow velocity can be determined as:

$$u = \frac{g}{2\Omega \sin\varphi}\frac{\Delta h}{\Delta x} \tag{F.5}$$

where Δh is the difference in SSA between two locations, Δx is the horizontal distance between these locations, φ specifies the latitude and Ω the Earths rotation speed.

The resulting current is called a geostrophic current and will flow in perpendicular direction to the pressure and Coriolis force, following isolines of dynamic height. The direction along these lines is such that the flow leaves higher SSA to its right in the northern hemisphere, and to its left on the southern hemisphere [Open University, 1989].

To achieve a real geostrophic equilibrium, the flow should be steady and the pressure gradient and Coriolis force should be the only forces acting on the water (other then the attraction due to gravity). While this will not be the case in reality, most currents can be assumed geostrophic to a first degree, and geostrophic current maps give a realistic approximation of actual currents.

Appendix G

Assessment of project area

G.1 South China Sea topography

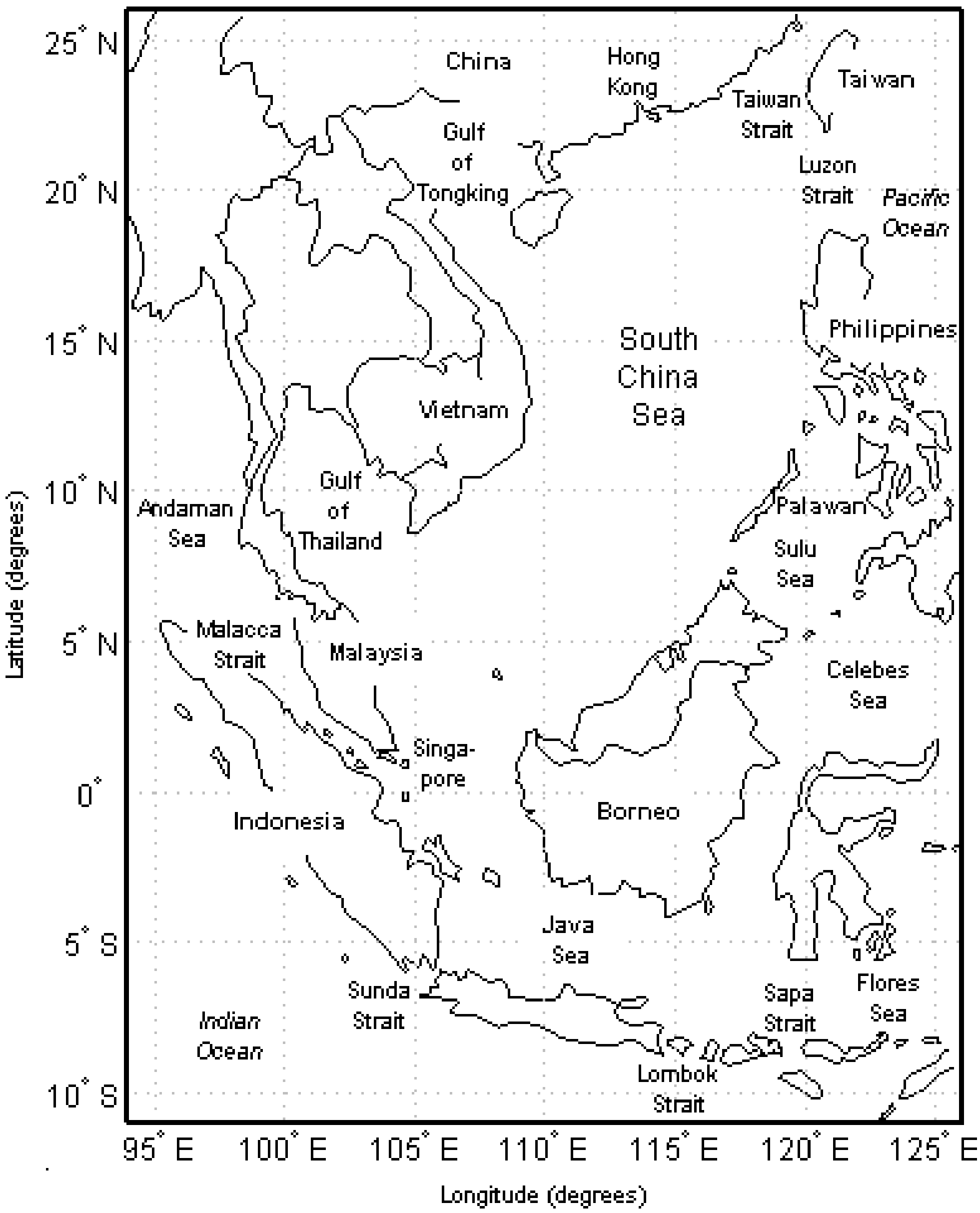

Figure G.1: Overview of South China Sea topography.

G.2 South China Sea bathymetry

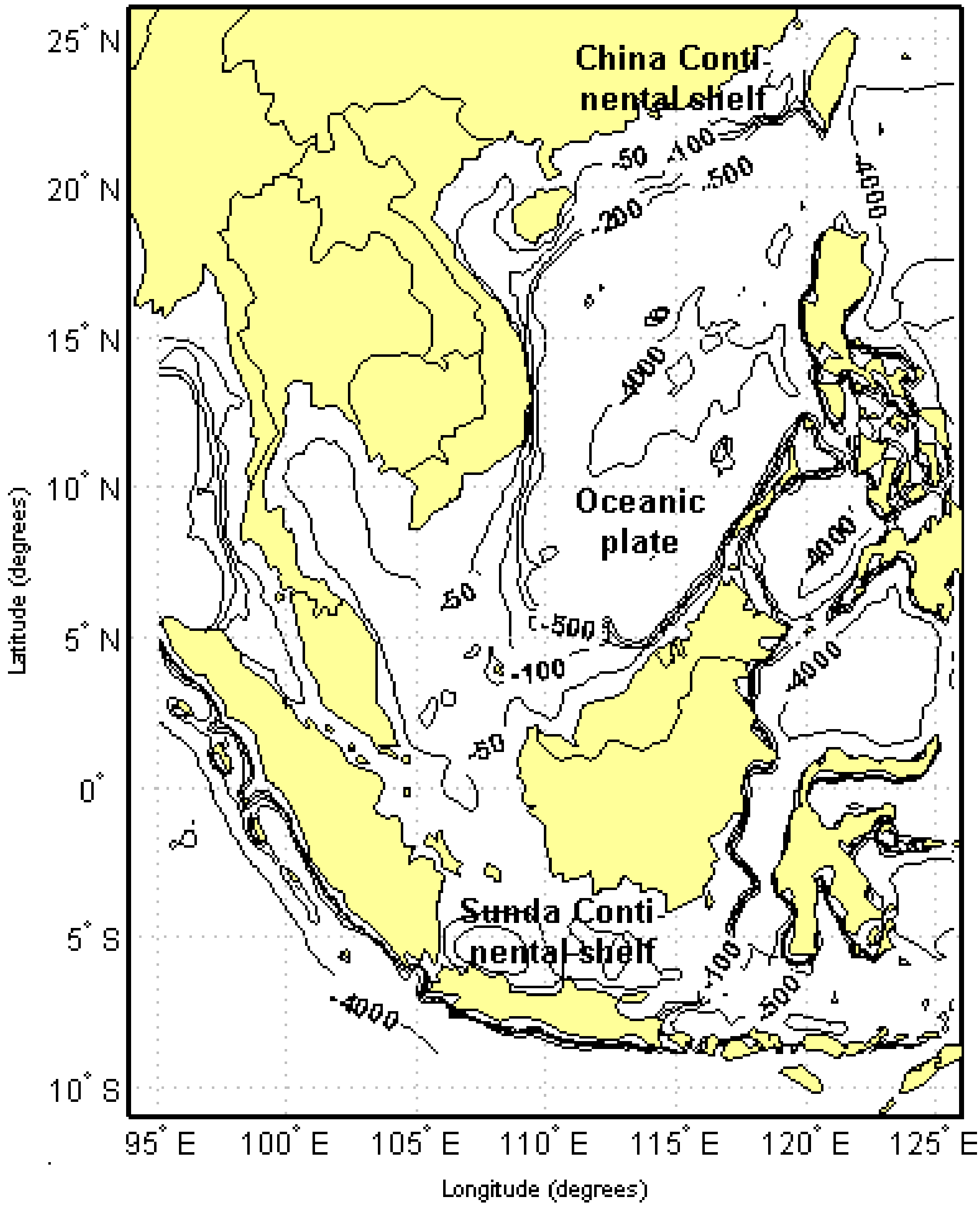

Figure G.2: Overview of South China Sea bathymetry, obtained from the ETOPO5 dataset.

G.3 Climatological wind fields: NE monsoon period

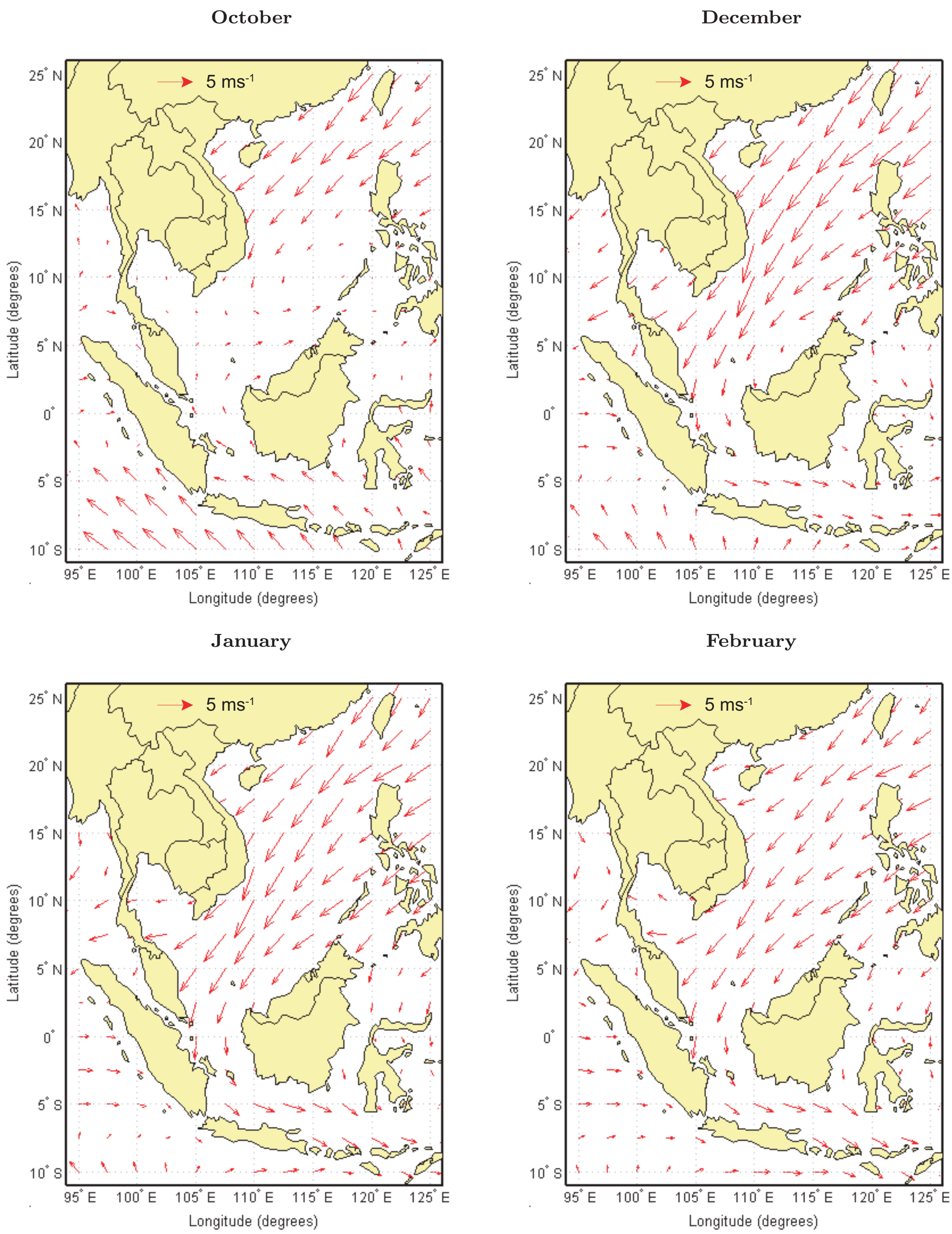

Figure G.3: Monthly-mean climatological wind fields, determined from 13 years of ECWMF ERA-40 data: NE monsoon period

G.4 Climatological wind fields: SW monsoon period

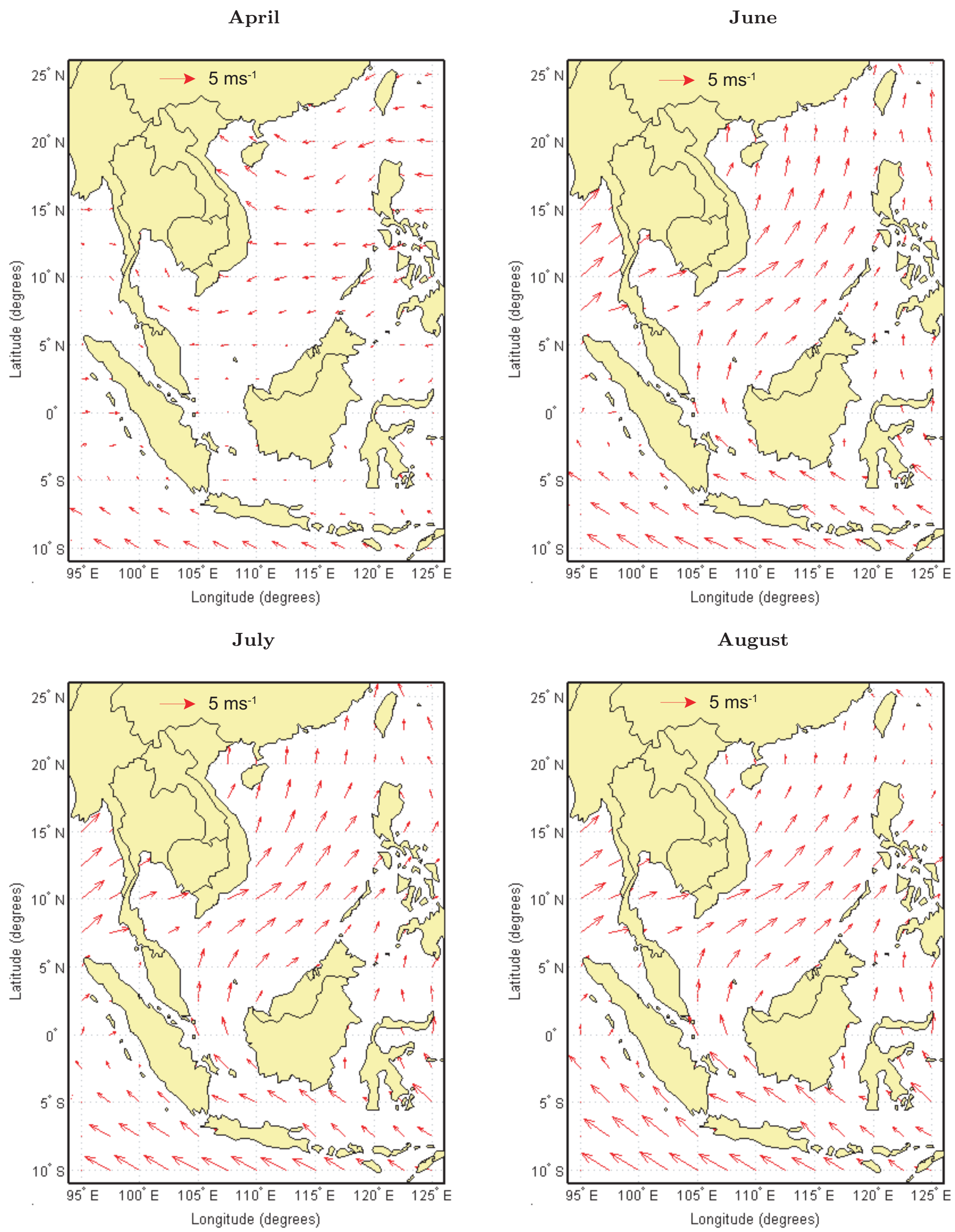

Figure G.4: Monthly-mean climatological wind fields, determined from 13 years of ECWMF ERA-40 data: SW monsoon period

G.5 Climatological sea surface anomaly fields

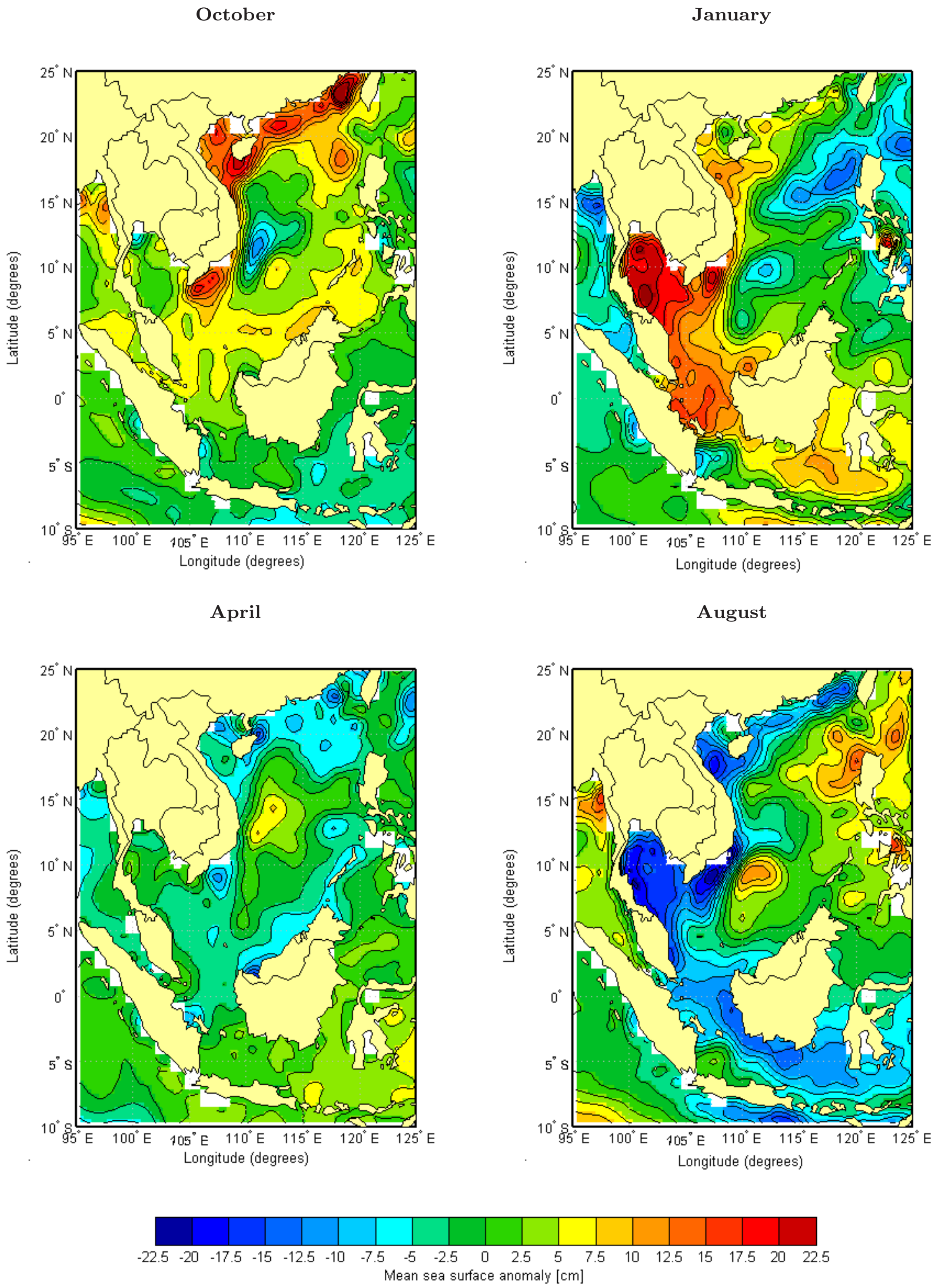

Figure G.5: Monthly-mean climatological sea surface anomaly (SSA) fields, determined from 14 years of DUACS SSA data

G.6 Climatological absolute dynamic topography fields

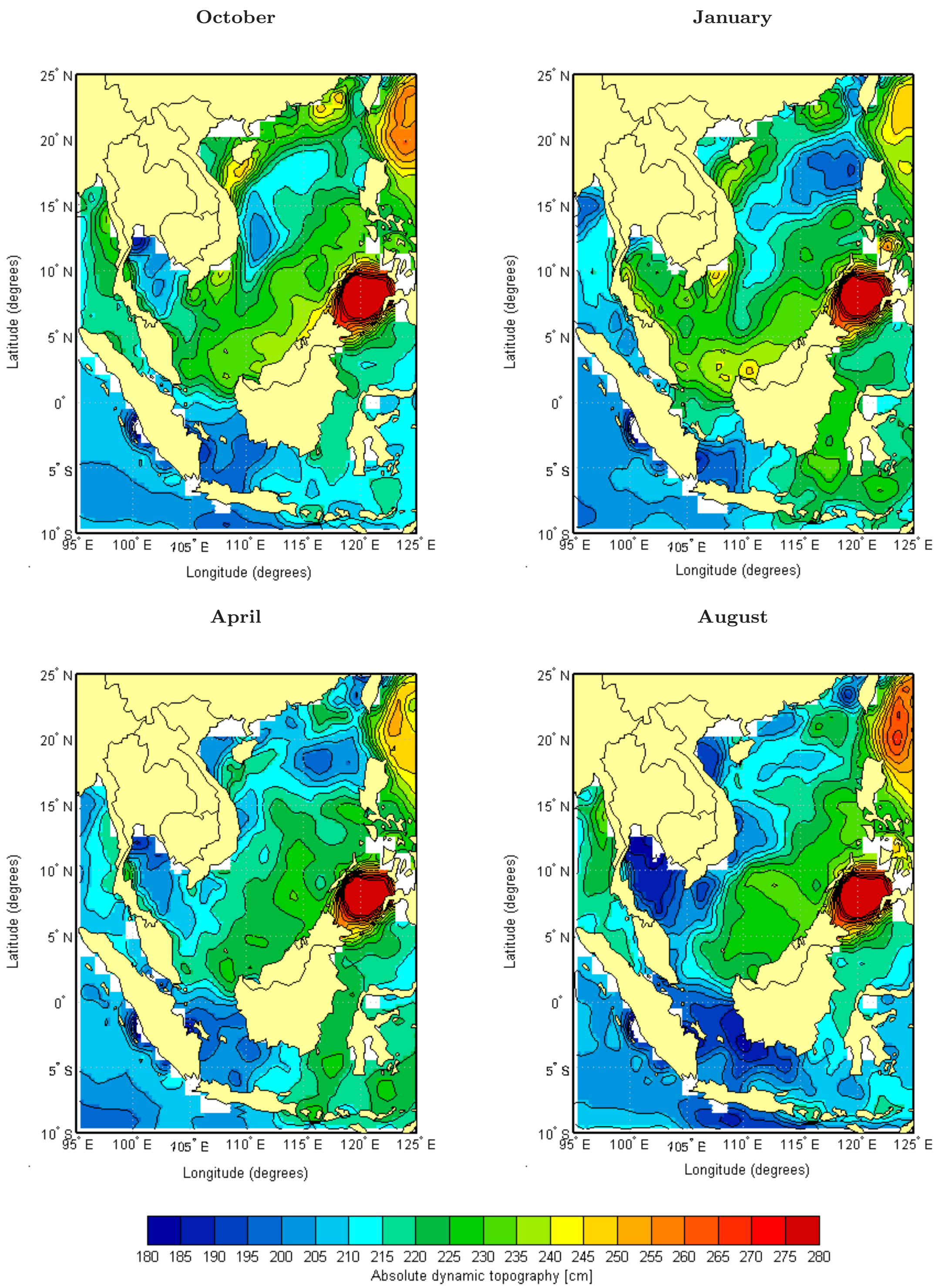

Figure G.6: Monthly-mean climatological absolute dynamic topography (ADT) fields, determined from 4 years of DUACS ADT data

G.7 Climatological sea surface temperature fields: NE monsoon period

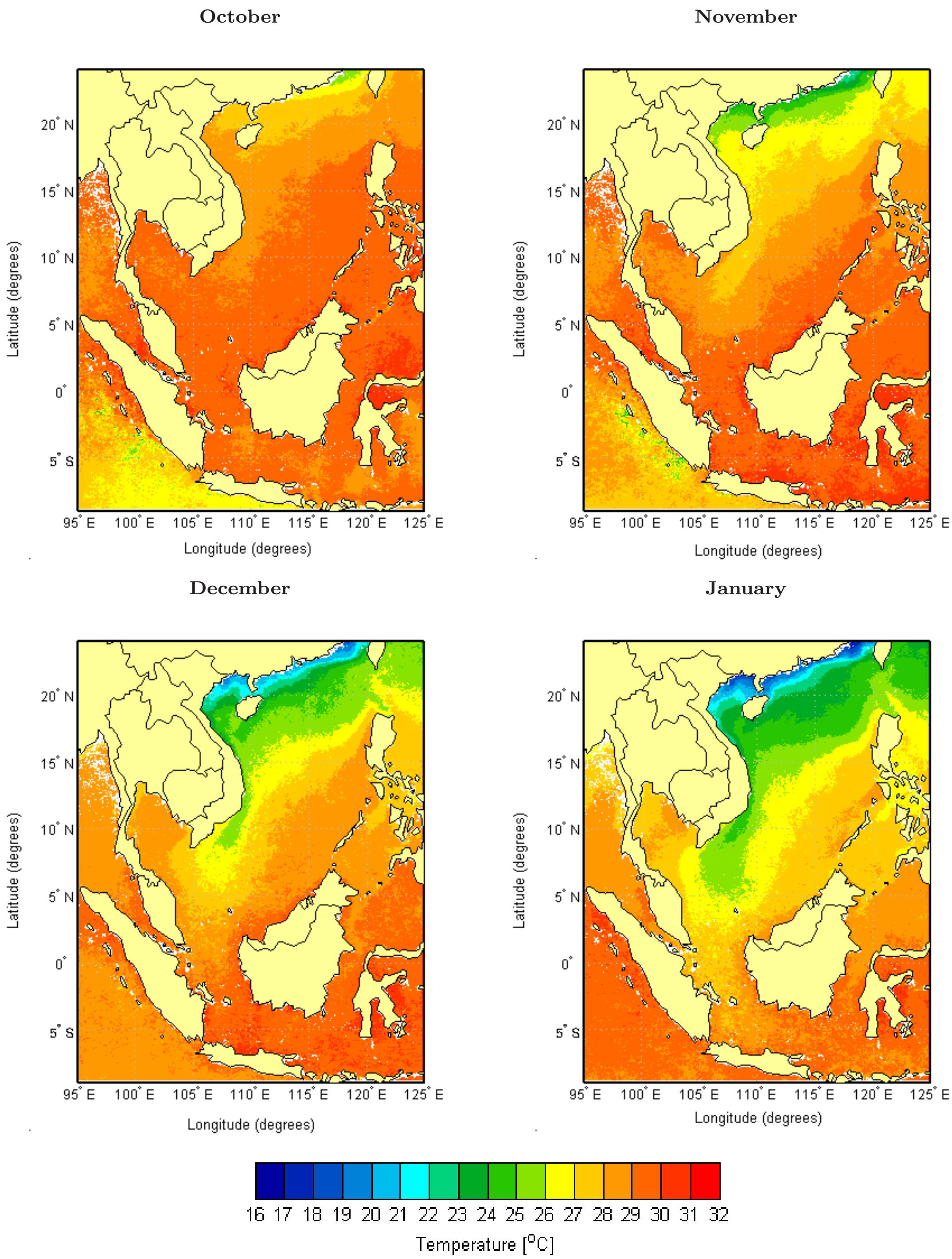

Figure G.7: Monthly-mean climatological sea surface temperature (SST) fields, determined from 10 years of AVHRR Oceans Pathfinder SST data: NE monsoon period

G.8 Climatological sea surface temperature fields: SW monsoon period

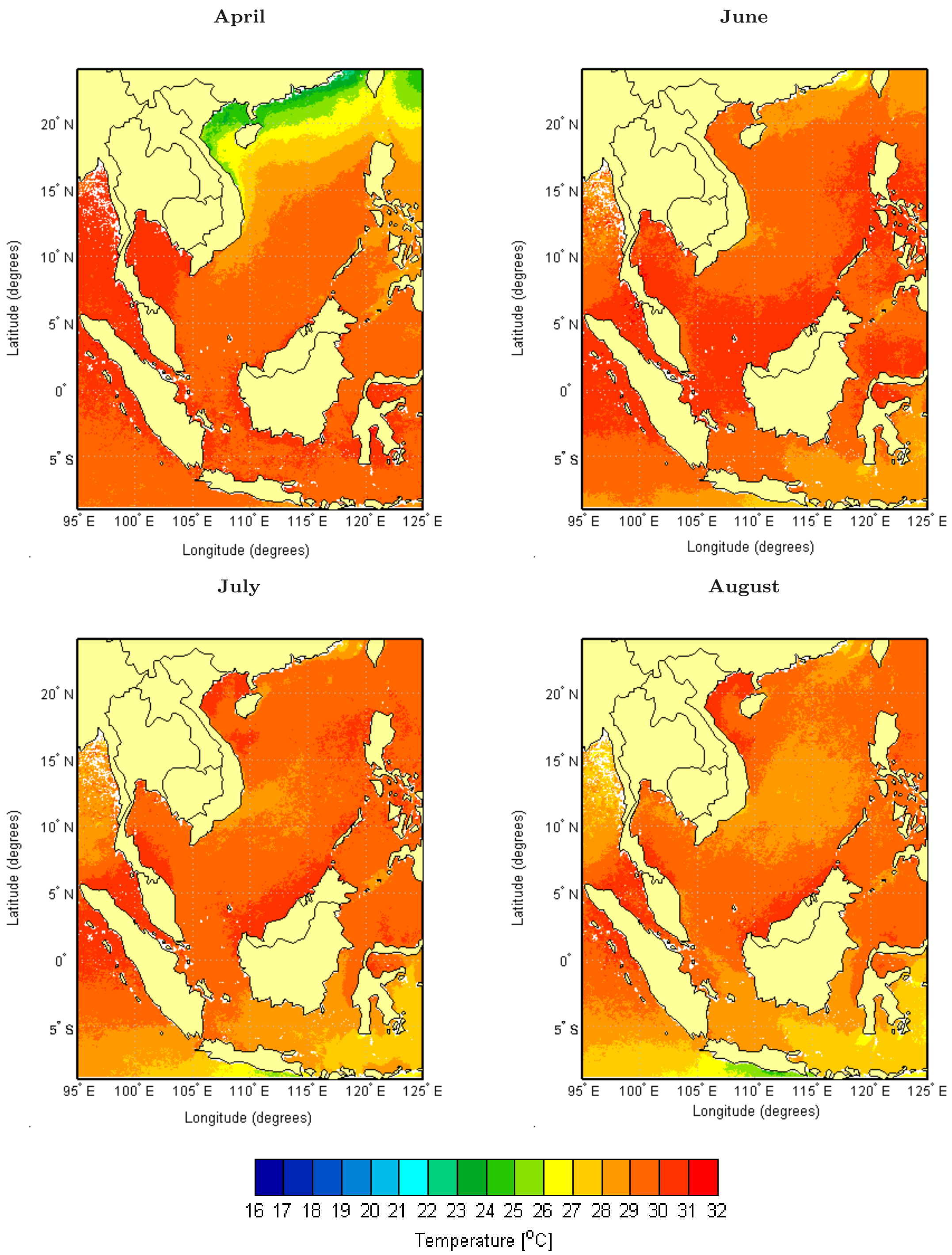

Figure G.8: Monthly-mean climatological sea surface temperature (SST) fields, determined from 10 years of AVHRR Oceans Pathfinder SST data: SW monsoon period

Appendix H

Data acquisition and assessment

H.1 Overview of datasets used for the SAT2SEA2 project

Dataset	*Spatial coverage*	*Spatial resolution*	*Temporal coverage*	*Temporal res.*
Climatological data				
WOA01	Global	1 degree	Climatological year	Monthly
WOA01 1/4	Global	0.25 degree	Climatological year	Monthly
Sea surface temperature data (remote sensing)				
AVHRR	Global	4.9 km	1985 - current	24 hrs
Reynolds	Global	1 degree	1981 - current	Weekly
Water level data (remote sensing)				
DUACS DT	Global	1/3 degree	1992 - 2005	Weekly
DUACS NRT	Global	1/3 degree	2001 - 2006	Weekly
In-situ data				
ASIAEX	21.8°N, 117.3°E	N.A.	April - May 2000	Daily
SCSMEX	13°N - 18°N, 114°E - 116°E	N.A.	April 1997 - May 2000	Daily
Meteorological data				
ECMWF	Global	2.5 degree	1957 - 2002	6 hrs
NCEP/NCAR	Global	2.5 degree	1948 - current	6 hrs
COADS (SOC)	Global	1 degree	1960 - current	Monthly

Dataset	*Variables*	*Data statistics*	*Accuracy*
Climatological data			
WOA01	Temperature, Salinity	Mean, STD, error	N.A.
Sea surface temperature data (remote sensing)			
AVHRR	SST	Mean, quality index	0.3 - 0.5 K.
Reynolds	SST	Mean, error	0.3 - 0.5 K.
Water level data (remote sensing)			
DUACS DT	SSA	Mean, error	N.A.
DUACS NRT	SSA, ADT	Mean, error	N.A.
In-situ data			
ASIAEX	See table 4.3	N.A.	N.A.
SCSMEX	See table 4.4	N.A.	See table 4.4
Meteorological data			
ECMWF	See table 4.6	Mean	N.A.
NCEP/NCAR	See table 4.7	Mean, STD	N.A.
COADS (SOC)	See table 4.8	Mean, STD	N.A.

Table H.1: Overview of datasets used for the SAT2SEA2 project

Note that spatial and temporal resolutions mentioned in table H.1 refer to the highest available for the described dataset. Also, accuracy mentioned in this table relates to accuracy statements by the dataset provider based on sensor characteristics. In most cases, no such values are available. Finally, most datasets described are pre-processed, meaning they are averaged in both space and time. Also, they are mapped on a specified grid.

Acronyms: WOA01 = World Ocean Atlas 2001; WOA01 1/4 = World Ocean Atlas, 1/4 degree resolution; AVHRR = AVHRR Oceans Pathfinder; Reynolds = Reynolds OI SST; ECMWF = ECMWF ERA-40; NCEP/NCAR = NCEP/NCAR Reanalysis; SOC = SOC heat flux climatology.

H.2 Overview of dataset applications during the SAT2SEA2 project

Dataset	*Application*
Climatological data	
WOA01	Assessment of temperature and salinity processes in SCS region (chapter 2); Model initial conditions (chapter 8); Model lateral boundary forcing (chapter 8); Model assessment using goodness-of-fit (appendix D); Model validation (chapter 10 and 11)
Sea surface temperature data (remote sensing)	
AVHRR	Assessment of temperature processes in SCS region (chapter 2); Assessment of inter-dataset consistency (chapter 6); Model validation (chapter 11)
Reynolds	Statistical (EOF) analysis of SCS temperature variability (chapter 3); Synthetic temperature profile reconstruction (chapter 7); Assessment of inter-dataset consistency (chapter 6); Data-assimilation by SST nudging (appendix D)
Water level data (remote sensing)	
DUACS	Assessment of large-scale SCS circulation (chapter 2); Statistical (EOF) analysis of SCS temperature variability (chapter 3); Synthetic temperature profile reconstruction (chapter 7); Model water level boundary forcing (chapter 8); Validation of model large-scale circulation (chapter 10)
In-situ data	
ASIAEX	Assessment of inter-dataset consistency (chapter 6); Model validation (chapter 11)
SCSMEX	Assessment of inter-dataset consistency (chapter 6); Synthetic temperature profile reconstruction (chapter 7); Model validation (chapter 11)
Meteorological data	
ECMWF	Assessment of SCS region (chapter 2); Statistical (EOF) analysis of SCS temperature variability (chapter 3); Assessment of inter-dataset consistency (chapter 6); Model momentum (wind) forcing (chapter 8); Model heat flux forcing (chapter 8)
NCEP/NCAR	Assessment of inter-dataset consistency (chapter 6)
COADS (SOC)	Assessment of inter-dataset consistency (chapter 6)

Table H.2: Overview of data applications during the SAT2SEA2 project

Acronyms: WOA01 = World Ocean Atlas 2001; WOA01 1/4 = World Ocean Atlas, 1/4 degree resolution; AVHRR = AVHRR (Oceans) Pathfinder; Reynolds = Reynolds OI SST; ECMWF = ECMWF ERA-40; NCEP/NCAR = NCEP/NCAR Reanalysis; SOC = SOC heat flux climatology.

H.3 Overview of SCSMEX data availability

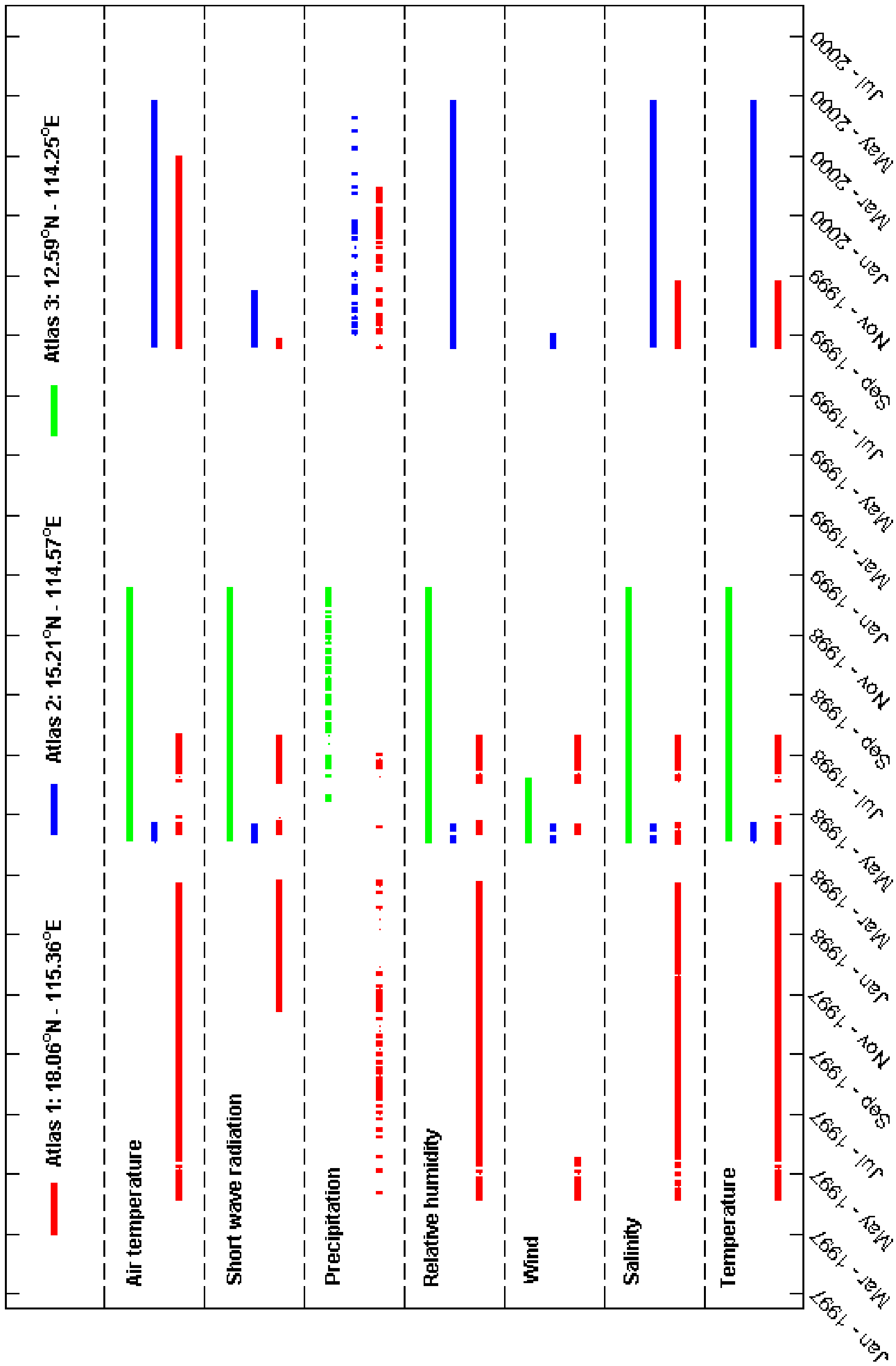

Figure H.1: Overview of in-situ data available from the SCSMEX Atlas buoys

H.4 Overview of DUACS altimeter products

Product	Description
Dataset	
SSA	Sea Surface Anomaly, with $< SSH >$ the mean distance above the T/P reference ellipsoid derived from seven years of T/P, five years of ERS and two years of Geosat data. This $< SSH >$ is referred to as CLS01 MSS [Hernandez *et al.* , 2001]
ADT	Absolute Dynamic Topography, with MDT computed from a multivariate analysis using hydrographic data, surface drifter velocities and altimetry, using a first guess based on both the CLS01 MSS - EIGEN2 (CHAMP) geoid and the Levitus '98 climatology (referenced to 1500 dbar) [Rio & Hernandez, 2003]
Satellite	
Merged	Merged data from T/P, Jason-1, ERS-1 and 2, Envisat and GFO.
Single Satellite	Data from T/P, Jason-1, ERS-1 and 2, Envisat or GFO.
Along track	Data are chronologically ordered, following the satellite ground track.
Gridded	Data is mapped on either a 1/3 degree mercator grid or a 1 degree equidistant grid using a global objective analysis. 1/3 degree data is available at weekly intervals. 1 degree data is available at monthly intervals.
Processing / Time frame	
NRT	Near real time. Available for period August 2001 - ongoing.
DT	Delayed time. This product has higher quality than the NRT product because of the higher precision of the satellite orbit used, and by using a centered computation time window. Available for period October 1992 - ongoing.
Product	
H	SLA or ADT in cm.
UV	Geostrophic velocities derived from SLA or ADT fields in cm/s.
Corrections	
	All measurements are corrected for tropospheric and ionospheric signal delay, sea state bias, ocean tide and loading tide, solid earth tide, polar tide and atmospheric loading.

Table H.3: Overview of altimeter products from the DUACS dataset [DUACS, 2005] [DUACS, 2004]

H.5 Mean error of DUACS sea surface anomaly

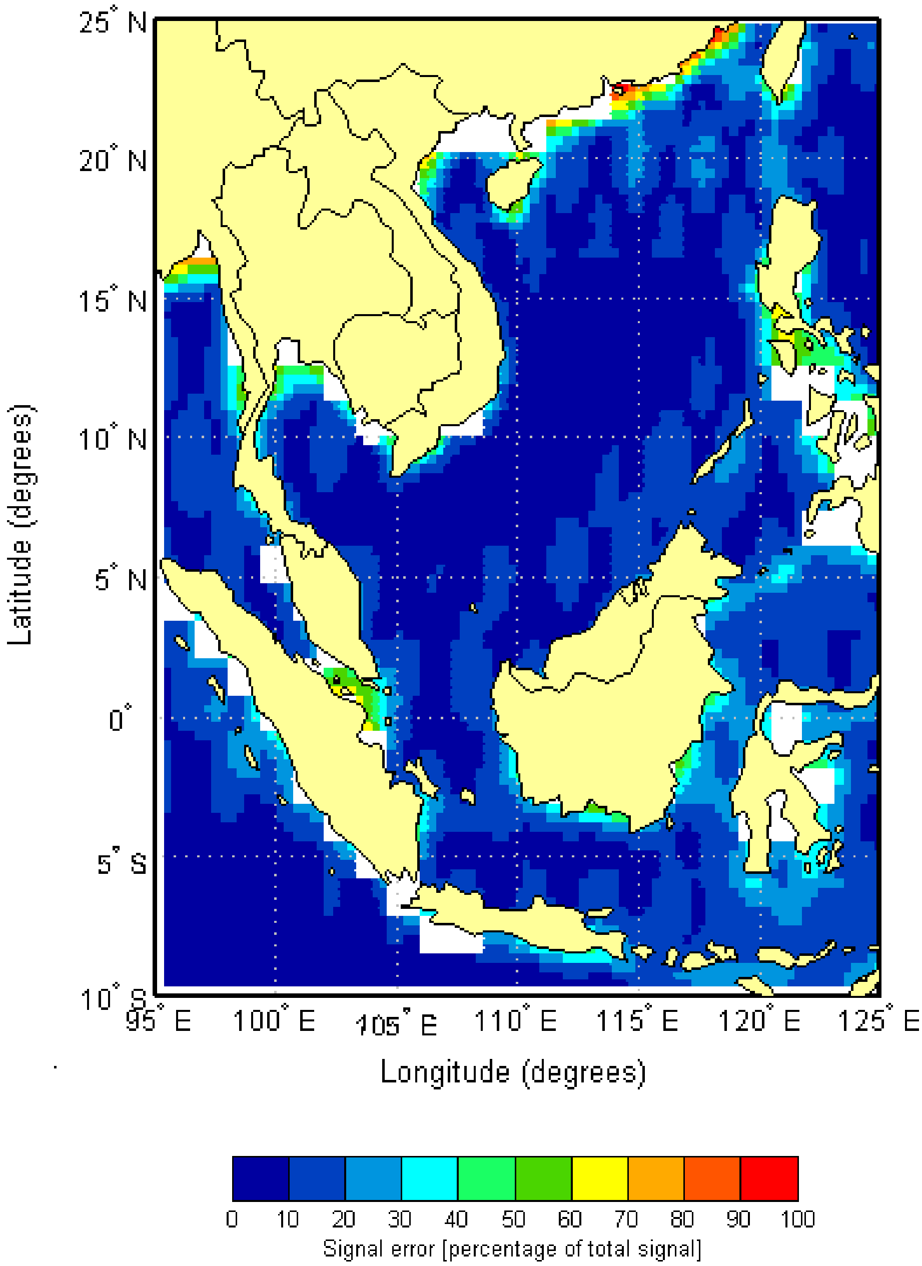

Figure H.2: Mean error of DUACS sea surface anomaly (SSA) data, determined by averaging 4 years of SSA error data

H.6 Standard deviation from DUACS sea surface anomaly climatology

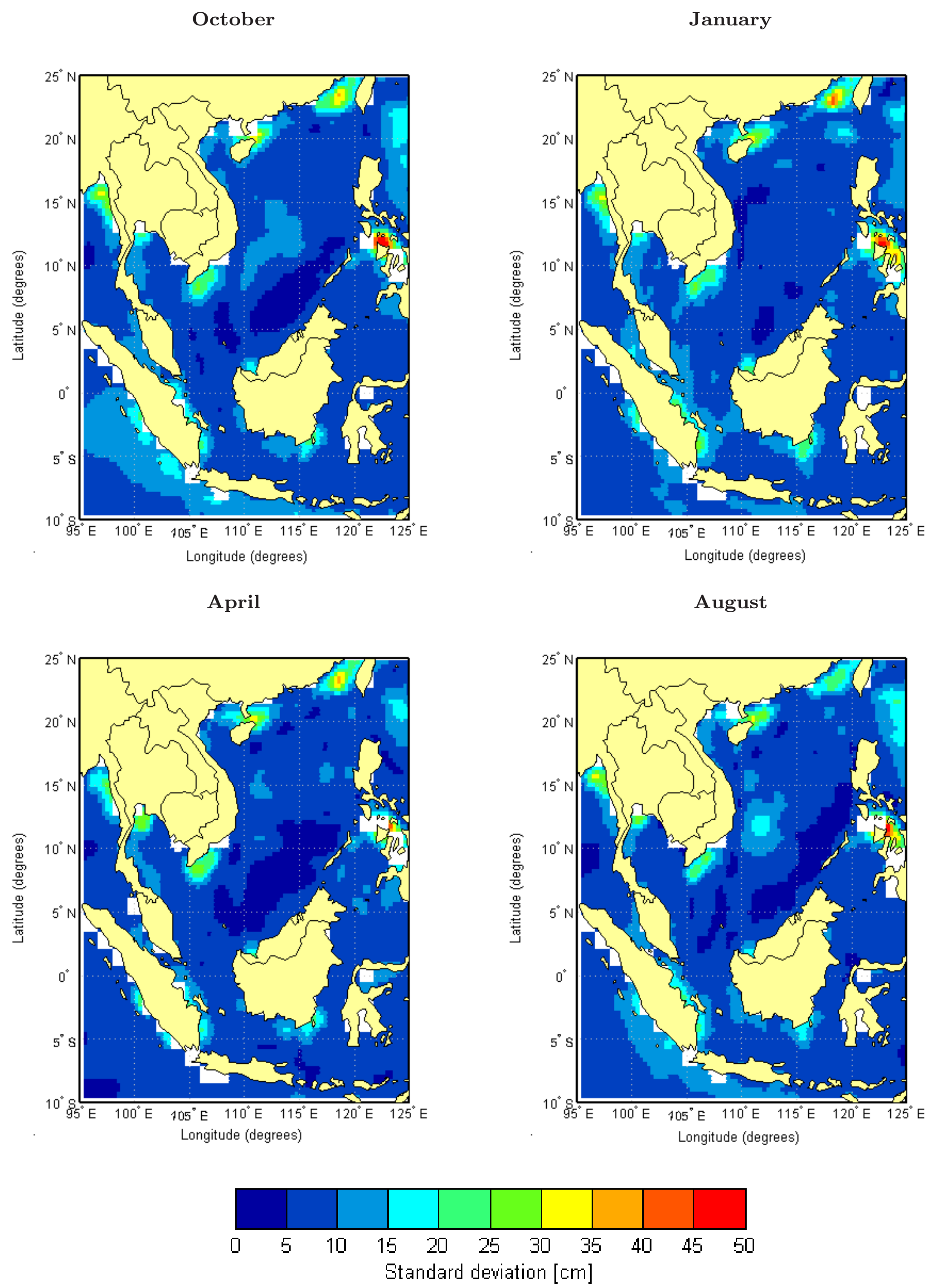

Figure H.3: Monthly-mean standard deviation from the DUACS sea surface anomaly (SSA) climatology, determined from 14 years of SSA data

H.7 Comparison of daily, weekly and monthly sea surface temperature composites

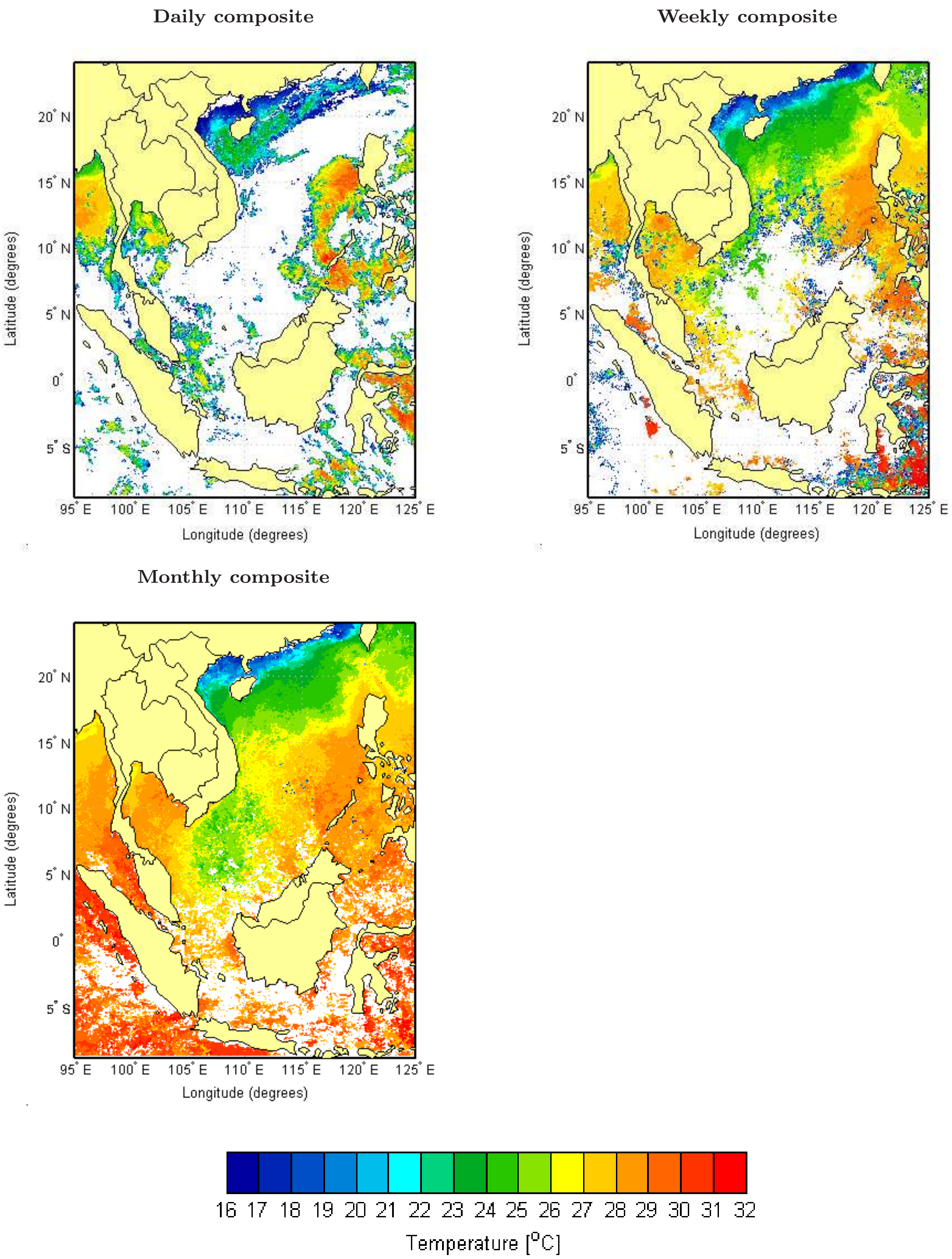

Figure H.4: Comparison between daily, weekly and monthly composites of remotely sensed sea surface temperature (SST) data from the AVHRR Pathfinder dataset

H.8 Temperature and salinity profile comparison

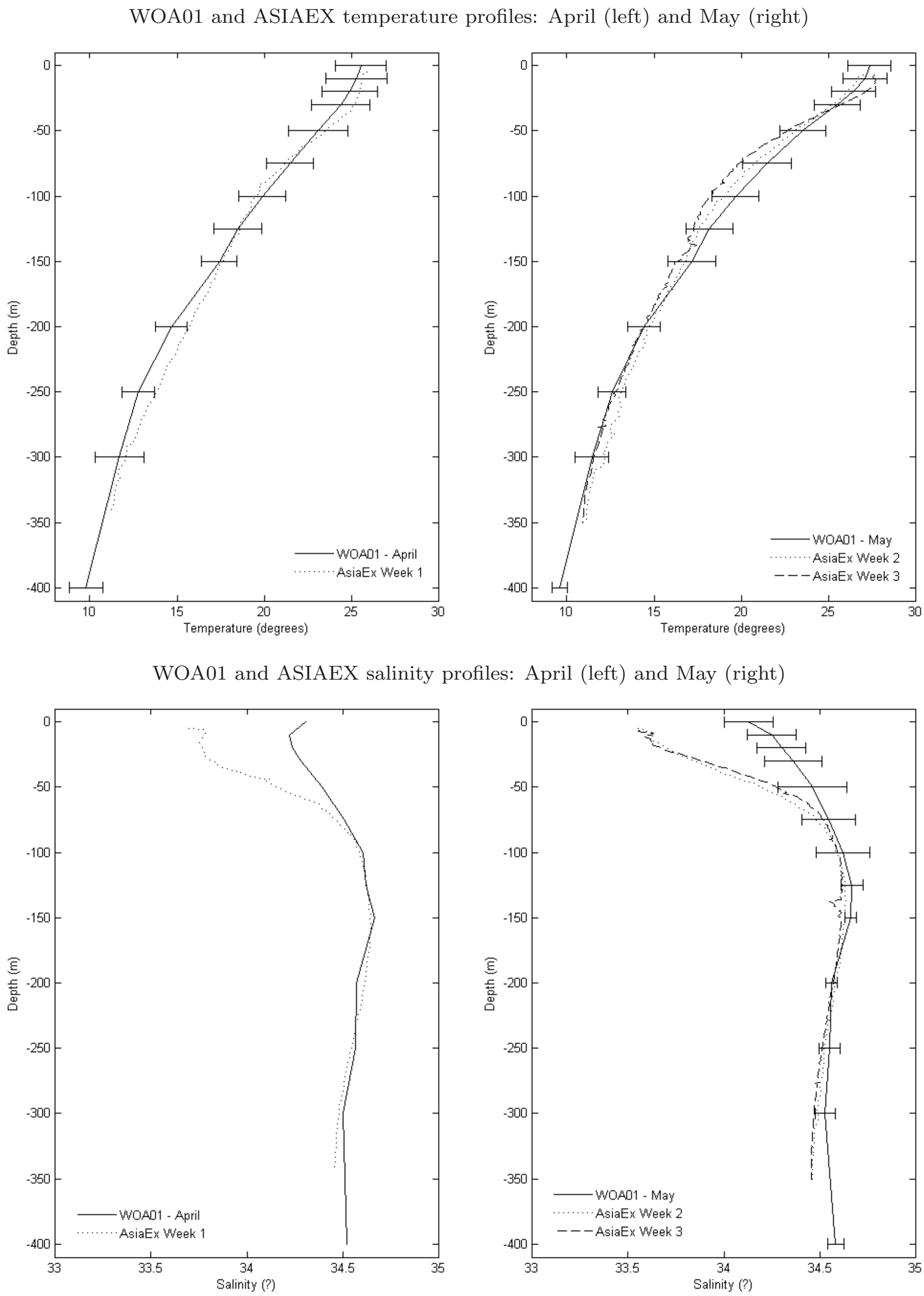

Figure H.5: Comparison between climatological temperature and salinity profiles from the World Ocean Atlas 2001 (WOA01) and historic (year 2000) profiles from the ASIAEX project. The WOA01 standard deviation from the climatological mean is included. For April no salinity standard deviation data is available.

H.9 Sea surface temperature data comparison

SST Comparison: 15.21°N - 114.57°E

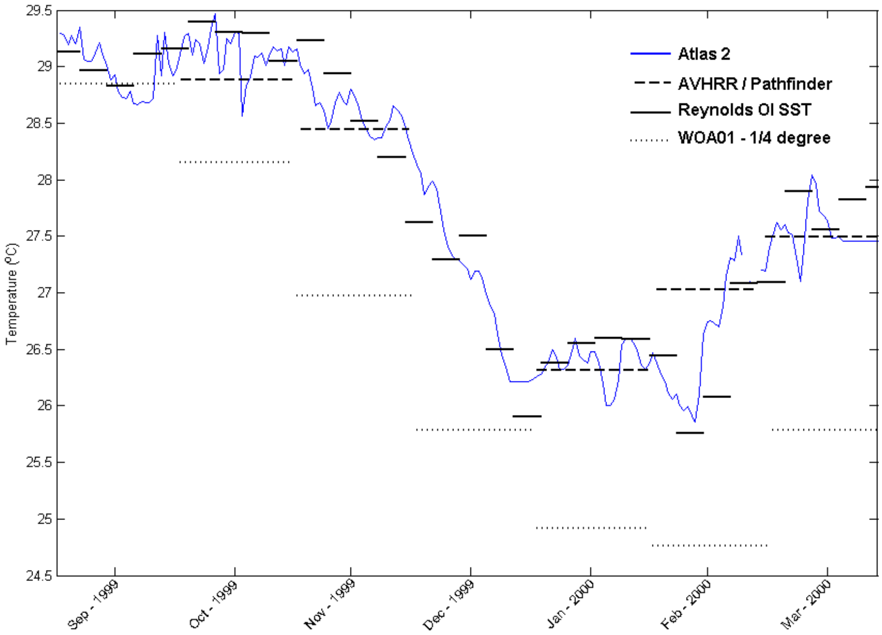

SST Comparison: 12.59°N - 114.25°E

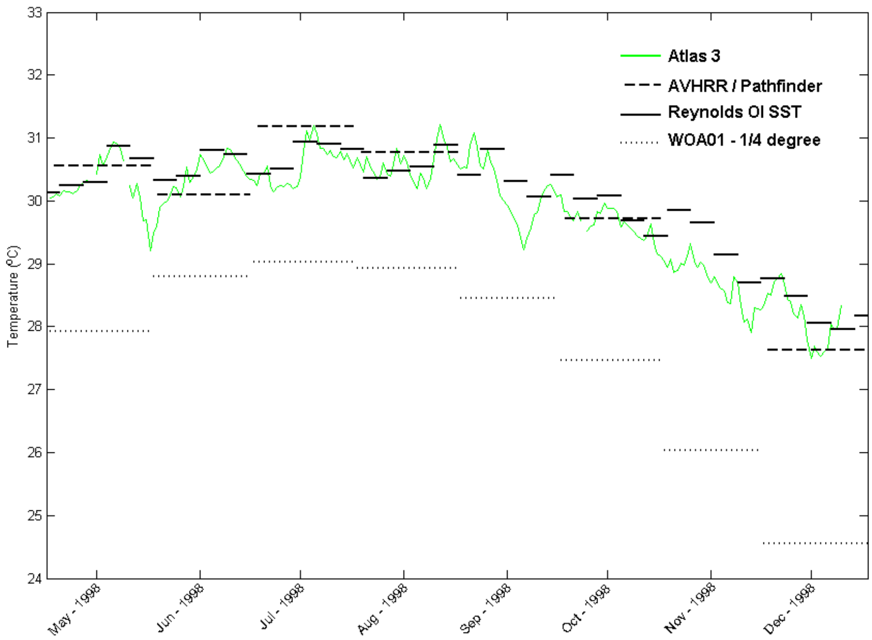

Figure H.6: Sea surface temperature (SST) data comparison: in-situ buoy data from the SCSMEX project (Atlas buoys), remotely sensed SST data from AVHRR Pathfinder and Reynolds OI SST and climatological SST data from the World Ocean Atlas 2001

Appendix I

Model setup, sensitivity analysis and validation

I.1 Model geographic extent, boundaries and truncated bathymetry

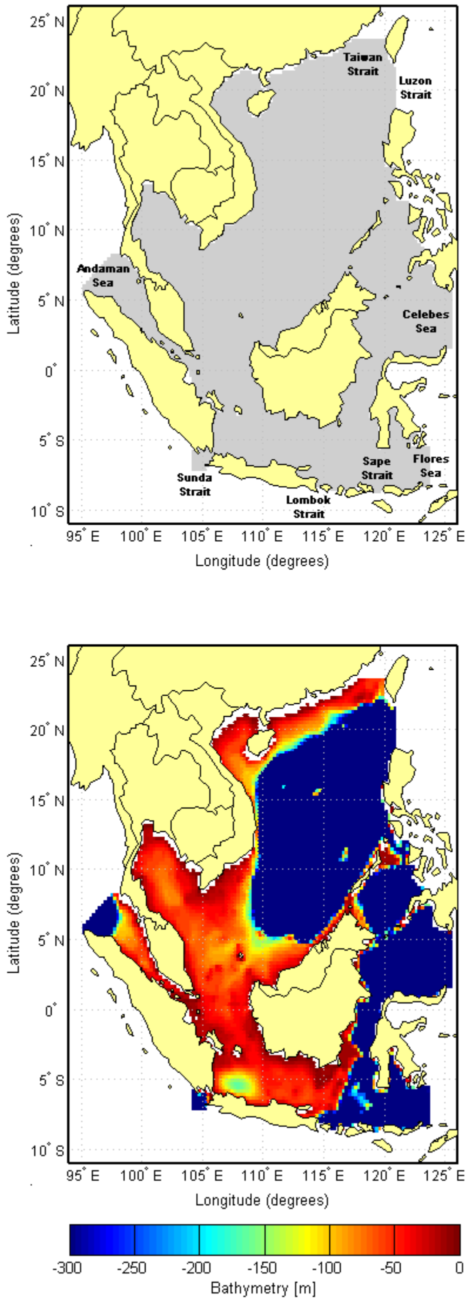

Figure I.1: Geographical extent of the Delft3D-FLOW SCS model and its open boundaries (upper panel). The model bathymetry truncated at 300 meters depth, based on the reduced-gravity approach (lower panel).

I.2 Model test basin and GoF domain

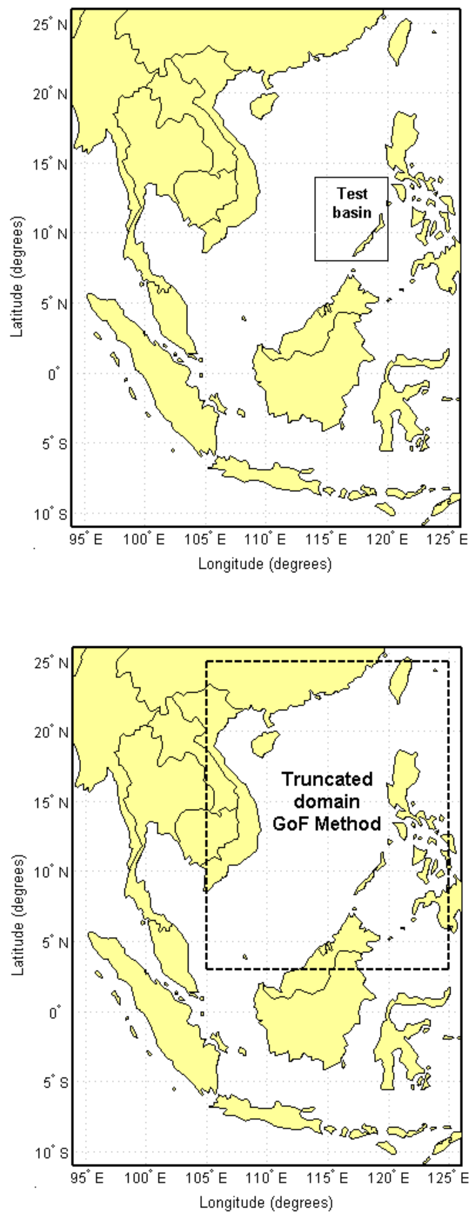

Figure I.2: Extent of test basin used to optimize the models heat flux coefficients (upper panel). The truncated model extent assessed using a goodness-of-fit method (lower panel).

I.3 Model test stations

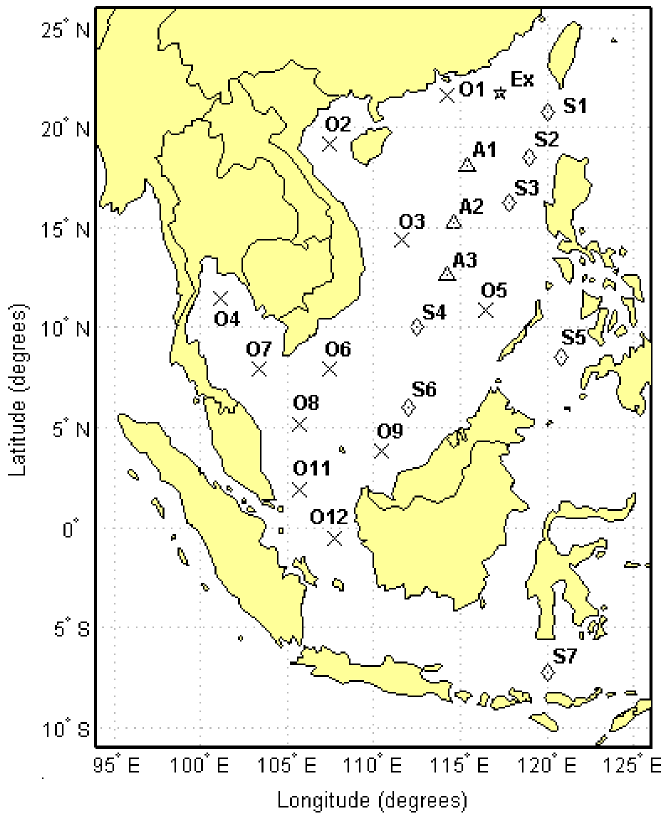

Figure I.3: Overview of test stations used for model validation.

Station	Latitude	Longitude	Station	Latitude	Longitude
A1	115.4	18.2	O2	107.4	19.21
A2	114.7	15.1	O3	111.6	14.4
A3	114.1	12.7	O4	101.1	11.4
S1	120.1	20.9	O5	116.5	10.9
S2	118.9	18.5	O6	103.4	8.0
S3	118.0	16.4	O7	107.4	7.9
S4	112.7	10.1	O8	105.7	5.2
S5	119.9	8.64	O9	110.4	3.81
S6	111.9	6.2	O11	105.7	1.9
Ex	117.3	21.8	O12	107.7	-0.57
O1	114.2	21.6			

Table I.1: Coordinates of model test stations: A = SCSMEX Atlas buoys, Ex = ASIAEX, S = Synthetic profiles, O = Other.

I.4 Overview of model sensitivity runs

Run ID	Parameters				Trunc.	Forcing			Nudge	Other
	c_e	c_h	L_∞	D_h		B.C.	B.T.	S.	G	
	10^{-3}	10^{-3}	[cm]	$[m^2/s]$	[m]					
HF-C1a	1.5	0.9	N.A.	1	150	SAT2SEA	WOA01	ECMWF-C	N.A.	
HF-C1b	1.5	0.9	N.A.	1	300	SAT2SEA	WOA01	ECMWF-C	N.A.	
HF-C2a	2.4	0.9	N.A.	1	150	SAT2SEA	WOA01	ECMWF-C	N.A.	
HF-C2b	2.4	0.9	N.A.	1	300	SAT2SEA	WOA01	ECMWF-C	N.A.	
HF-C3a	2.1	2.1	7	1	150	SAT2SEA	WOA01	ECMWF-C	N.A.	
HF-C3b	2.1	2.1	7	1	300	SAT2SEA	WOA01	ECMWF-C	N.A.	
HF-C3c	2.1	2.1	7	10	300	SAT2SEA	WOA01	ECMWF-C	N.A.	
HF-C3d	2.1	2.1	7	100	300	SAT2SEA	WOA01	ECMWF-C	N.A.	
HF-C3e	2.1	2.1	7	250	300	SAT2SEA	WOA01	ECMWF-C	N.A.	
HF-C3f	2.1	2.1	7	1	300	N.A.	N.A.	ECMWF-C	N.A.	
HF-H1a	2.1	2.1	7	1	300	SAT2SEA	WOA01	ECMWF-CH	N.A.	Historic air temperature
HF-H1b	2.1	2.1	7	1	300	SAT2SEA	WOA01	ECMWF-CH	N.A.	Historic relative humidity
HF-H1c	2.1	2.1	7	1	300	SAT2SEA	WOA01	ECMWF-CH	N.A.	Historic cloud coverage
HF-H1d	2.1	2.1	7	1	300	SAT2SEA	WOA01	ECMWF-CH	N.A.	Historic wind and pressure
HF-H1e	2.1	2.1	7	1	300	SAT2SEA	WOA01	ECMWF-H	N.A.	All historic
HF-H1f	2.1	2.1	7	1	300	SAT2SEA	WOA01	ECMWF-H	N.A.	Increased wind drag coefficient
C-1	2.1	2.1	7	250	300	SAT2SEA	WOA01	ECMWF-H	100	
C-2	2.1	2.1	7	250	300	DUACS	WOA01	ECMWF-H	100	
C-3	2.1	2.1	7	250	300	SAT2SEA	WOA01	ECMWF-C	100	
C-4	2.1	2.1	7	250	300	SAT2SEA	WOA01	NCEP-C	100	
C-5	2.1	2.1	7	250	300	SAT2SEA	N.A.	ECMWF-H	N.A.	
C-6	2.1	2.1	7	250	300	N.A.	N.A.	ECMWF-H	N.A.	Pressure forcing only
C-7	2.1	2.1	7	250	300	N.A.	N.A.	ECMWF-H	N.A.	Pressure and wind forcing
C-8	2.1	2.1	7	250	300	SAT2SEA	WOA01	ECMWF-H	100	Increased wind drag coefficient
N-1	2.1	2.1	7	250	300	SAT2SEA	WOA01	ECMWF-H	1	
N-2	2.1	2.1	7	250	300	SAT2SEA	WOA01	ECMWF-H	5	
N-3	2.1	2.1	7	250	300	SAT2SEA	WOA01	ECMWF-H	10	
N-4	2.1	2.1	7	250	300	SAT2SEA	WOA01	ECMWF-H	25	
N-5	2.1	2.1	7	250	300	SAT2SEA	WOA01	ECMWF-H	50	
N-6	2.1	2.1	7	250	300	SAT2SEA	WOA01	ECMWF-H	100	
HF-F	2.1	2.1	7	250	300	SAT2SEA	WOA01	ECMWF-H	N.A.	
N-F	2.1	2.1	7	250	300	SAT2SEA	WOA01	ECMWF-H	100	

Table I.2: Overview of model sensitivity runs

Acronym	Description	Acronym	Description
B.C.	Open boundary circulation forcing	ECMWF-C	ECMWF climatological forcing
B.T.	Open boundary transport forcing	ECMWF-H	ECMWF year 2000 forcing
S.	Free surface forcing	ECMWF-CH	ECMWF blended climatological / 2000 forcing
Trunc.	Truncation depth	NCEP-C	NCEP/NCAR climatological forcing
Nudge	Nudging coefficient	DUACS	DUACS SSA forcing
SAT2SEA	SAT2SEA SSA forcing		

Table I.3: Acronyms used in table I.2

I.5 Sensitivity analysis on the heat flux coefficients

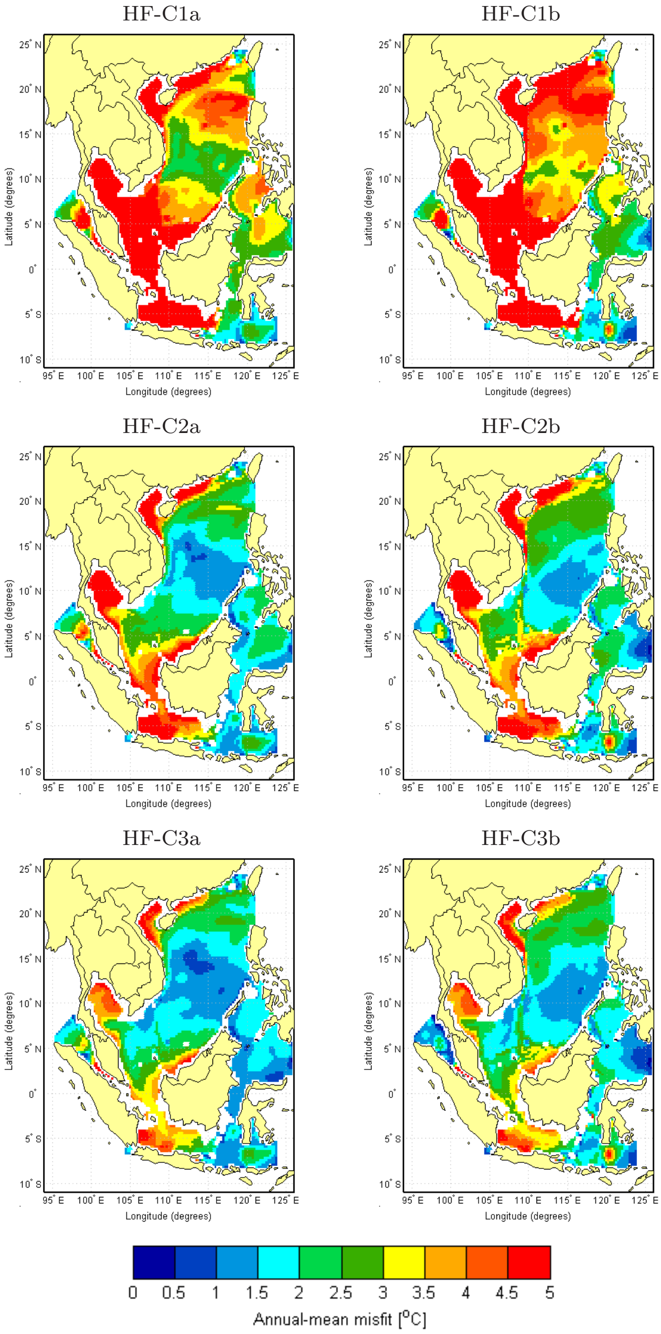

Figure I.4: Annual-mean misfit between the monthly-mean model and World Ocean Atlas 2001 temperature fields. This misfit is determined over the upper 6 model layers, representing the temperature up till 90 meters depth in the central SCS basin. It is specified at each model grid point.

I.6 Sensitivity analysis on horizontal diffusivity and wind drag

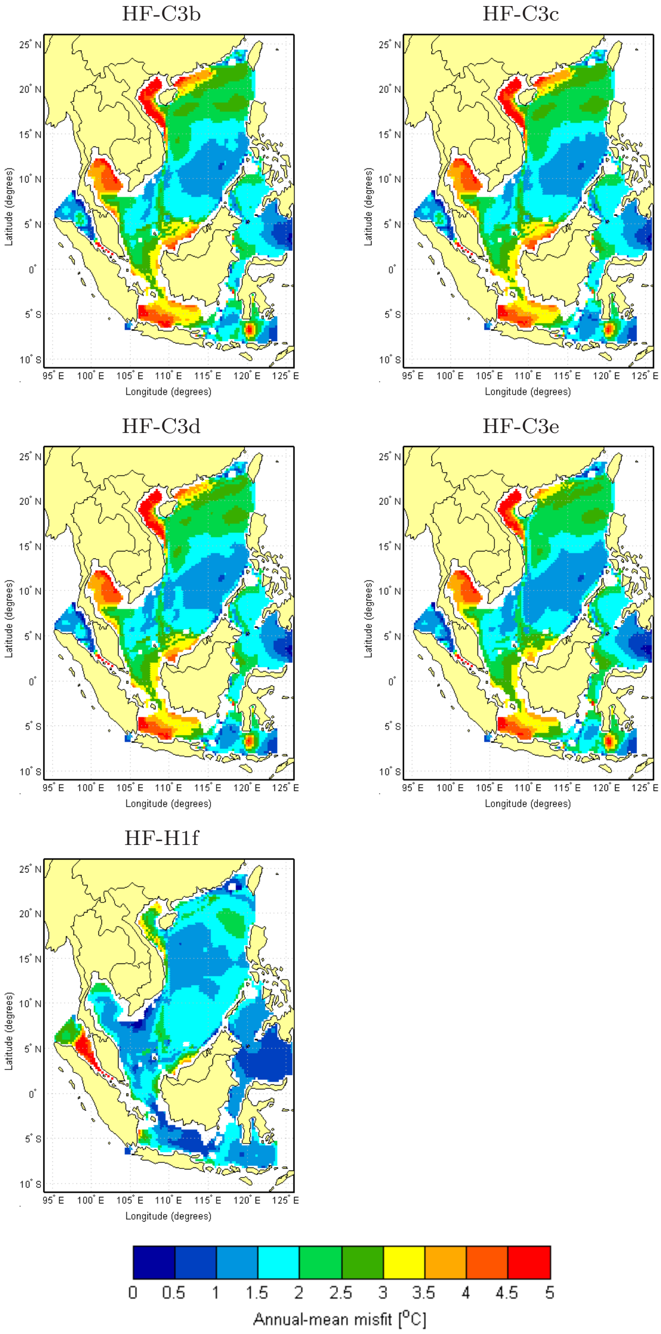

Figure I.5: Annual-mean misfit between the monthly-mean model and World Ocean Atlas 2001 temperature fields. This misfit is determined over the upper 6 model layers, representing the temperature up till 90 meters depth in the central SCS basin. It is specified at each model grid point.

I.7 Sensitivity analysis on temperature forcing

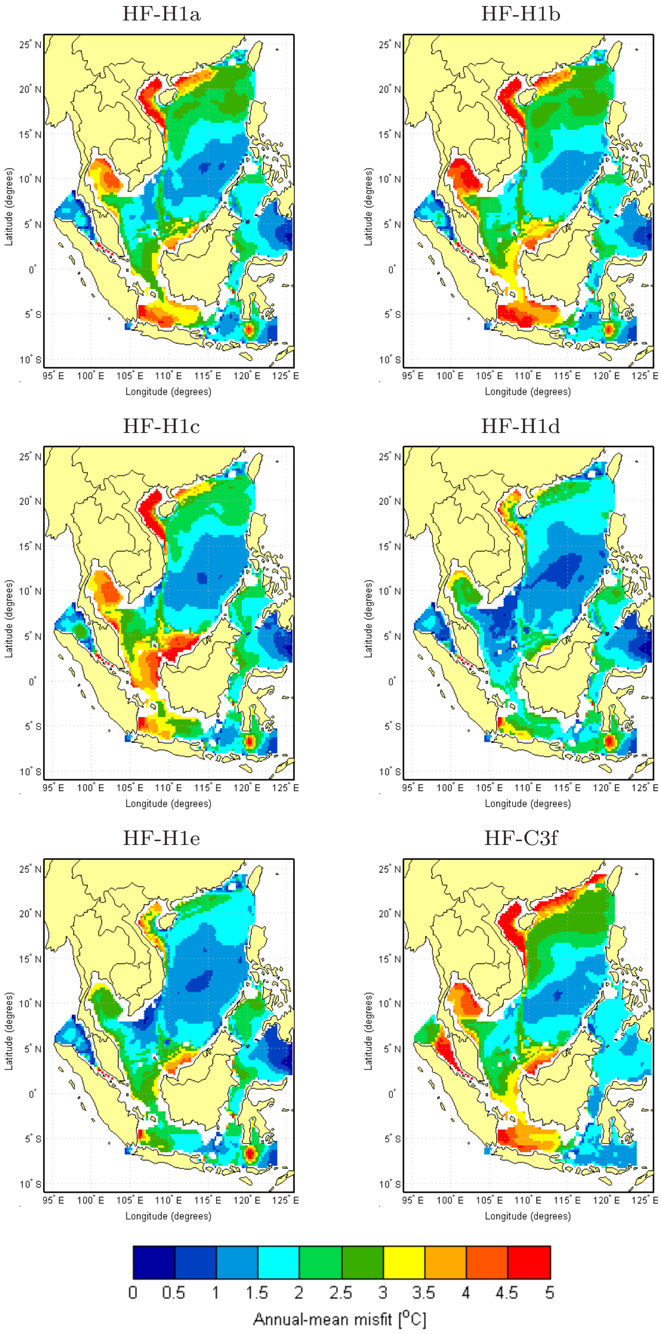

Figure I.6: Annual-mean misfit between the monthly-mean model and World Ocean Atlas 2001 temperature fields. This misfit is determined over the upper 6 model layers, representing the temperature up till 90 meters depth in the central SCS basin. It is specified at each model grid point.

I.8 Sensitivity analysis on model momentum forcing

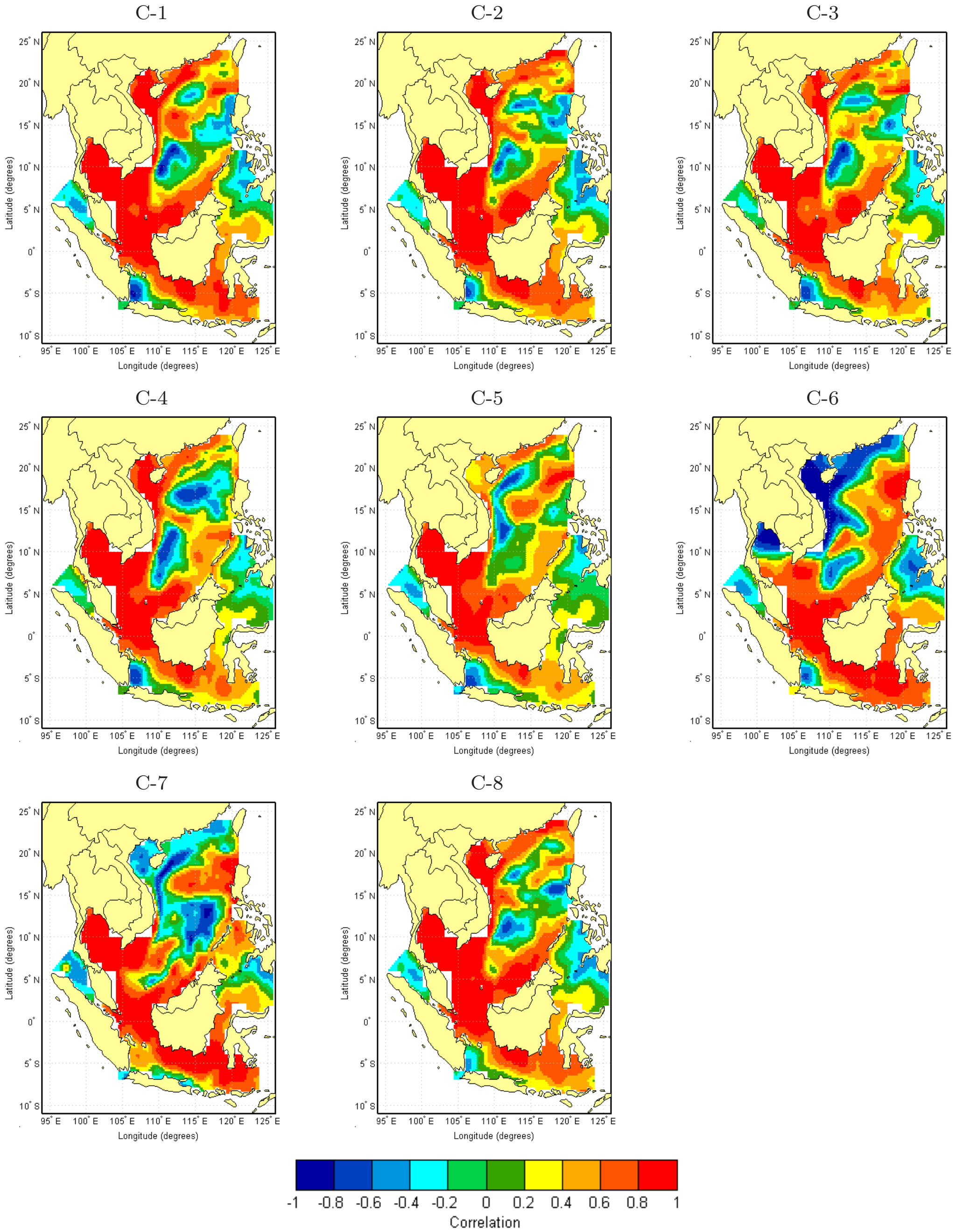

Figure I.7: Correlation between monthly-mean modeled water-level and altimeter Sea Surface Anomaly (SSA) data. Determined from yearly time-series of monthly-mean values at each model grid point. SSA data obtained from the DUACS dataset.

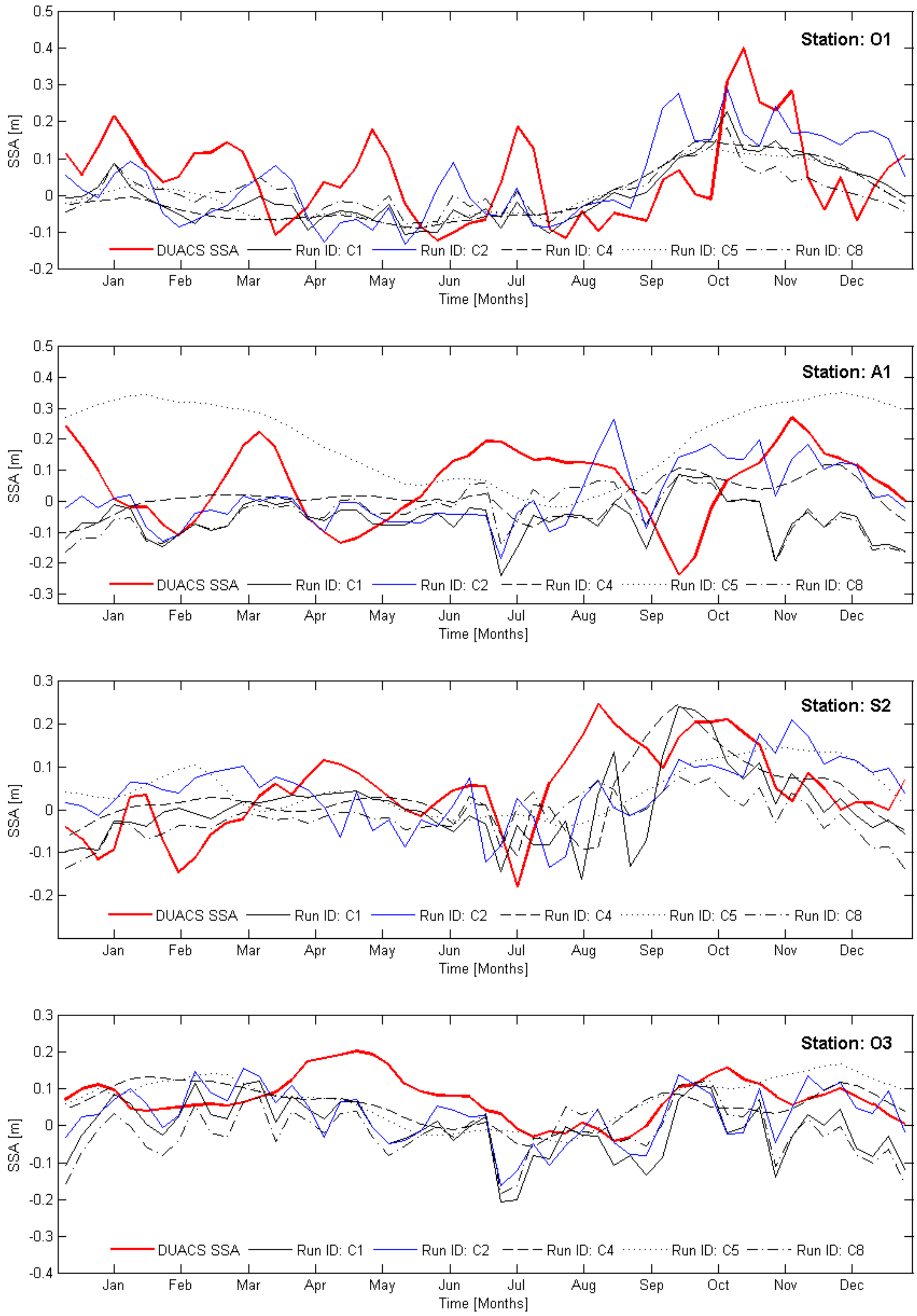

Figure I.8: Time series of modeled water-level and altimeter Sea Surface Anomaly (SSA) data at model test stations (1). SSA data obtained from the DUACS dataset.

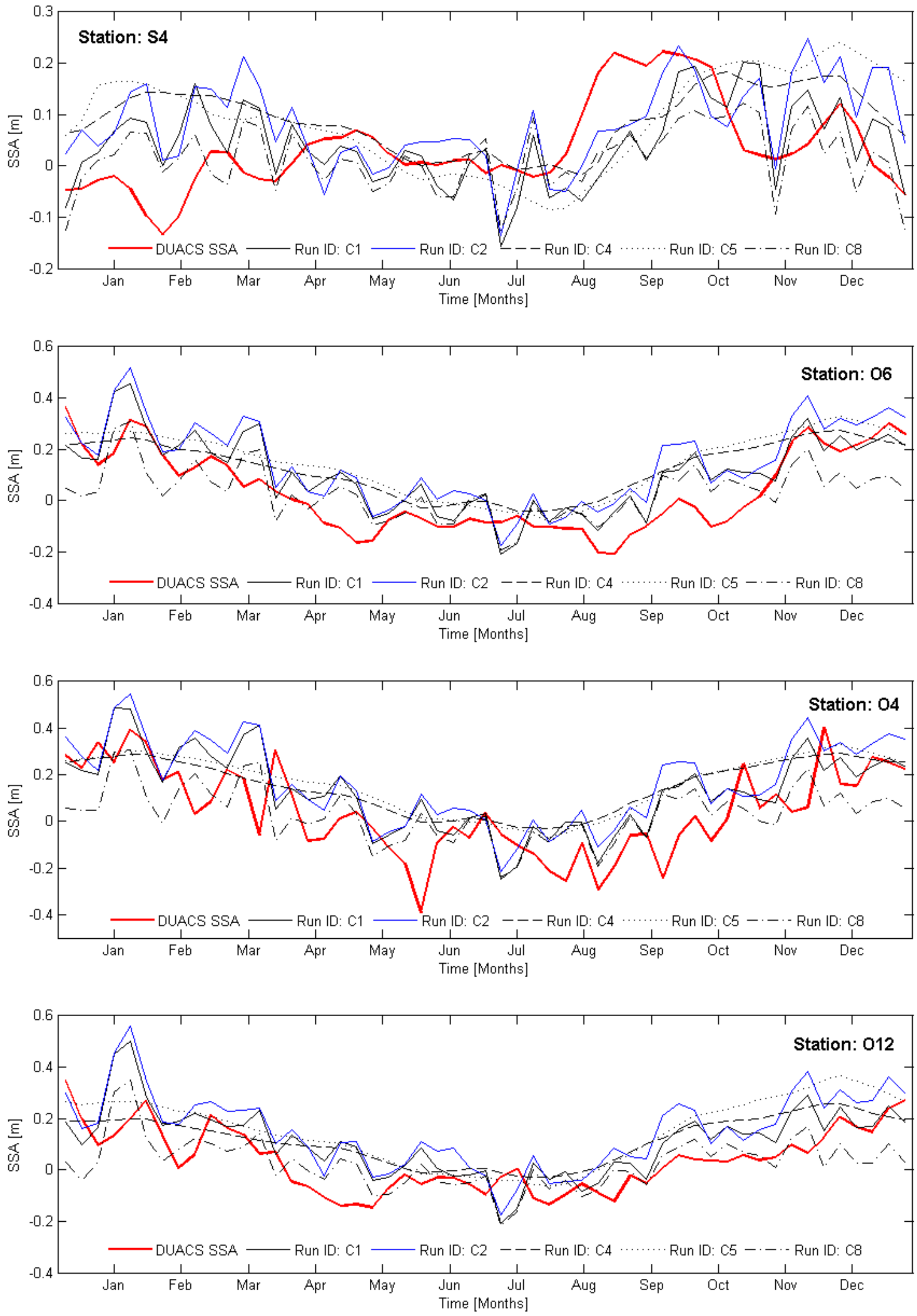

Figure I.9: Time series of modeled water-level and altimeter Sea Surface Anomaly (SSA) data at model test stations (2). SSA data obtained from the DUACS dataset.

I.9 Sensitivity analysis on SST nudging coefficient

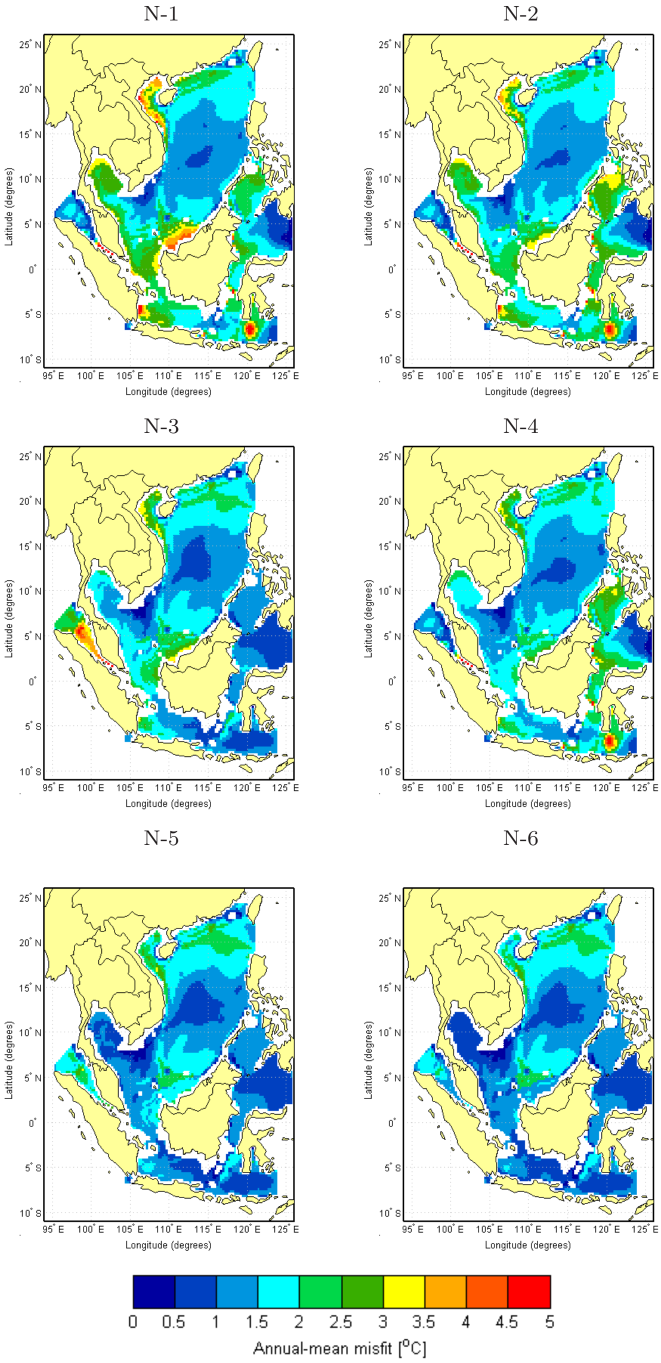

Figure I.10: Annual-mean misfit between the monthly-mean model and World Ocean Atlas 2001 temperature fields. This misfit is determined over the upper 6 model layers, representing the temperature up till 90 meters depth in the central SCS basin. It is specified at each model grid point.

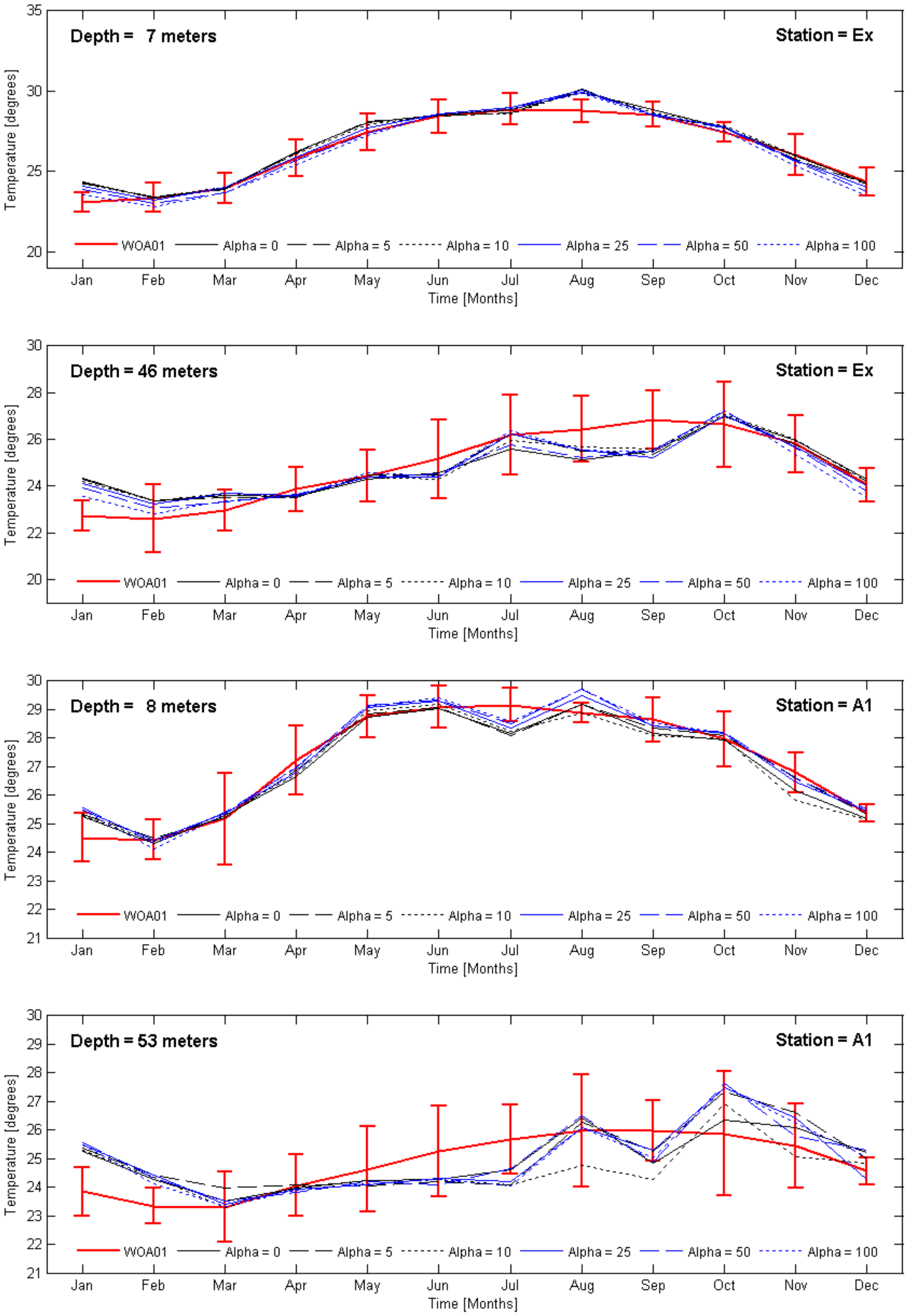

Figure I.11: Time-series of modeled and World Ocean Atlas 2001 temperature at model test stations (1). Model results for an increasing nudging coefficients.

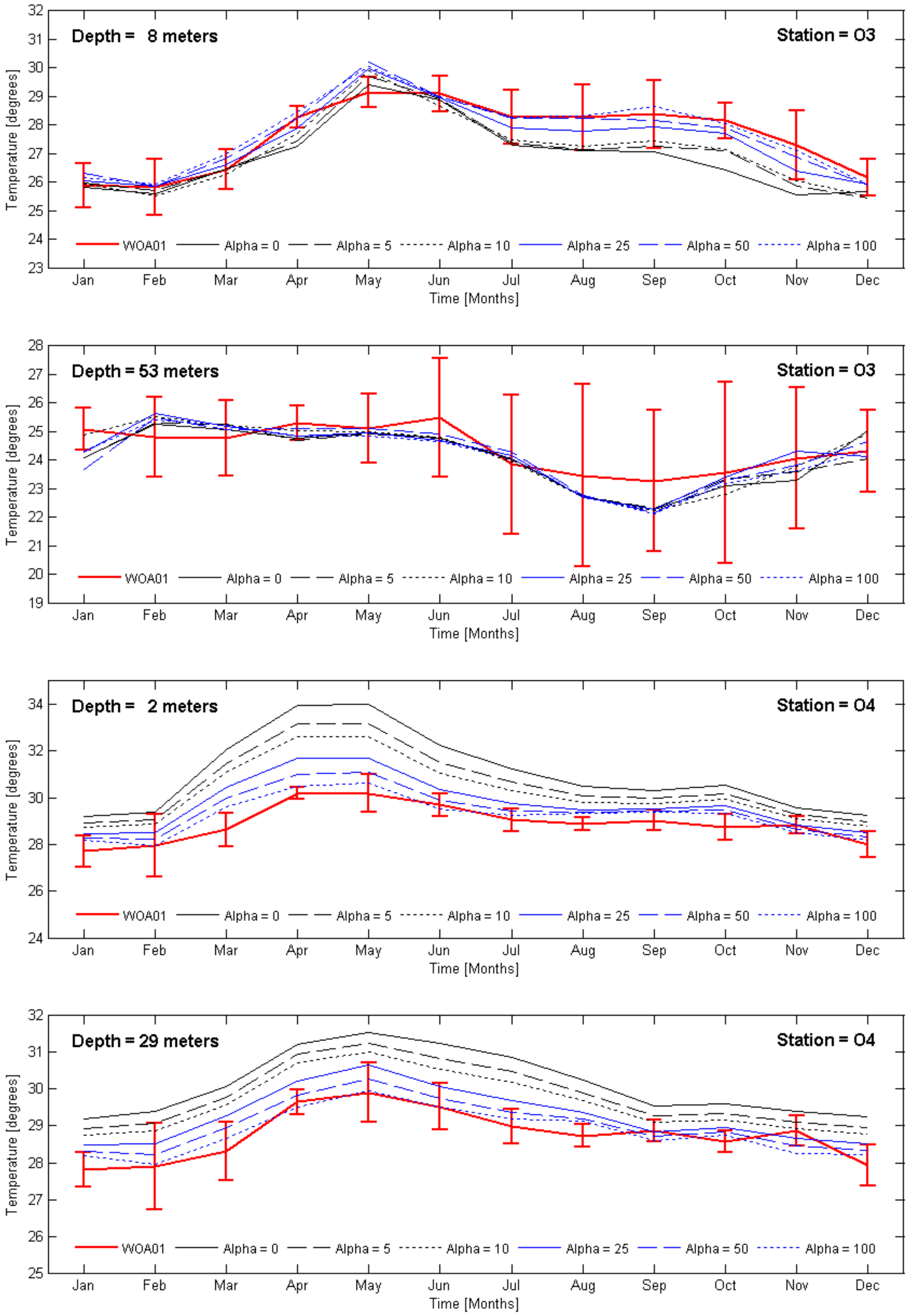

Figure I.12: Time-series of modeled and World Ocean Atlas 2001 temperature at model test stations (2). Model results for an increasing nudging coefficients.

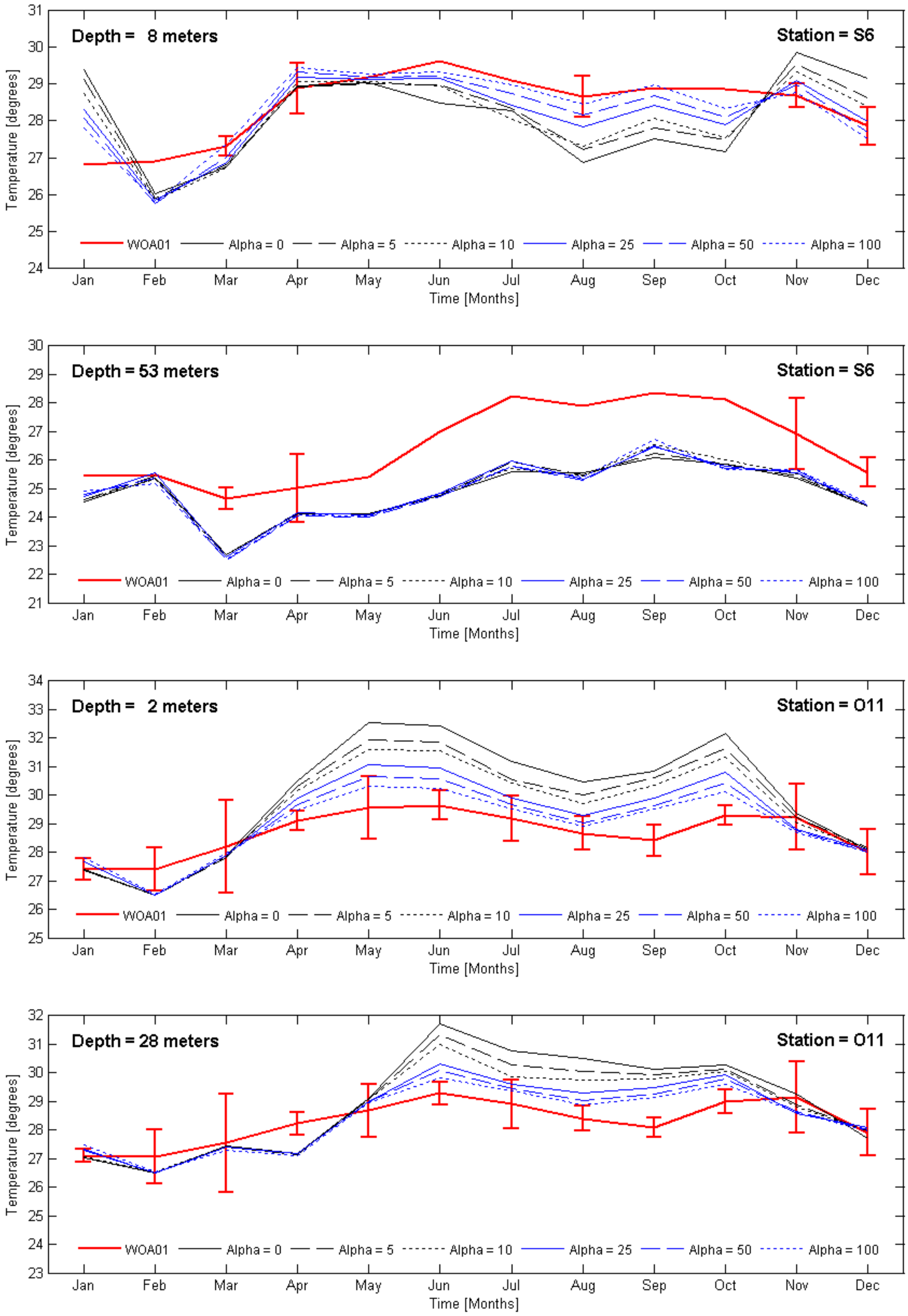

Figure I.13: Time-series of modeled and World Ocean Atlas 2001 temperature at model test stations (3). Model results for an increasing nudging coefficients.

I.10 Validation of model surface layer temperature using AVHRR SST data

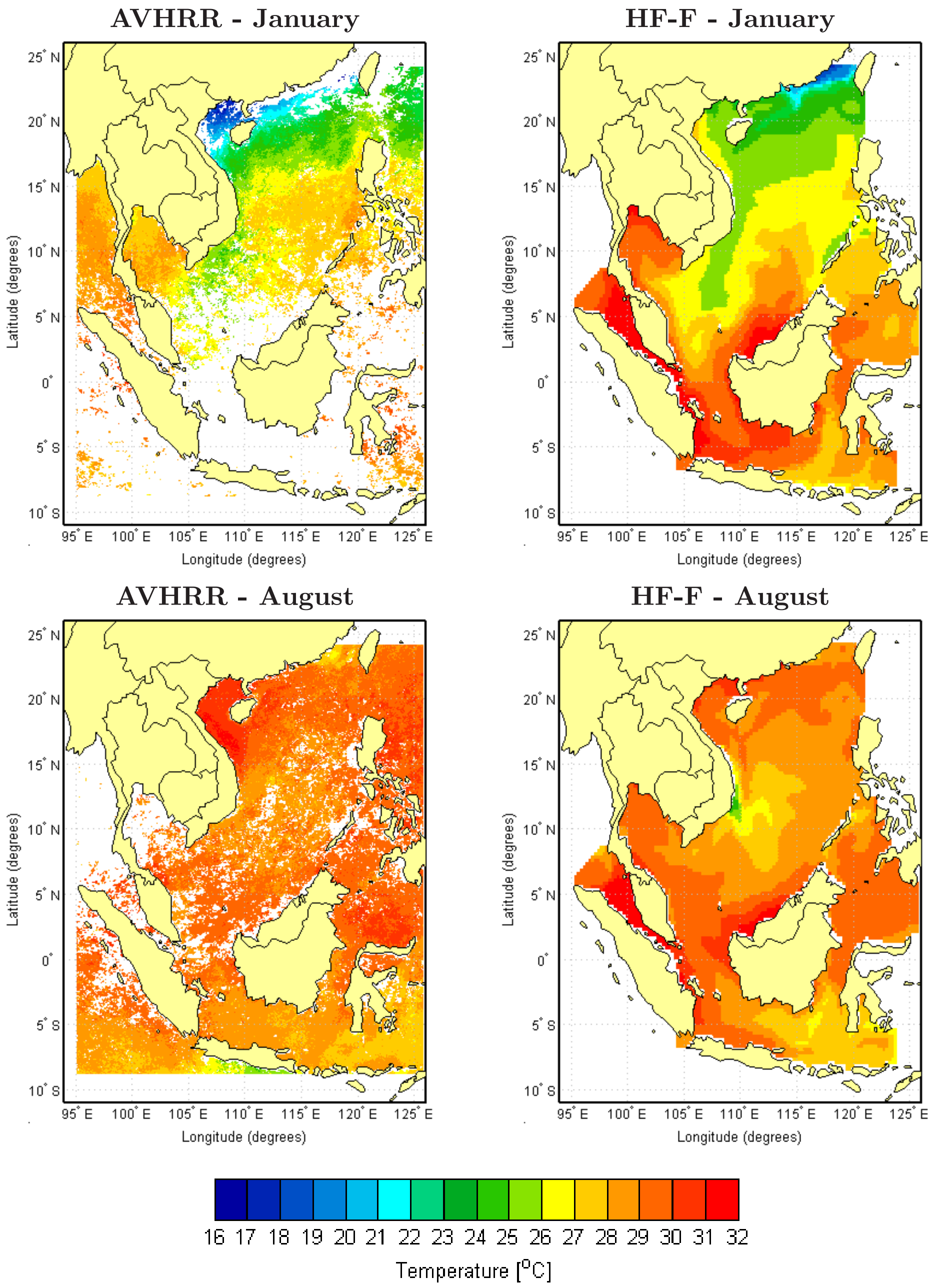

Figure I.14: Monthly-mean model surface-layer temperature, compared with monthly-mean Sea Surface Temperature (SST) data from AVHRR / Pathfinder: representing the SST state during the NE (January) and SW (August) monsoon highs (1).

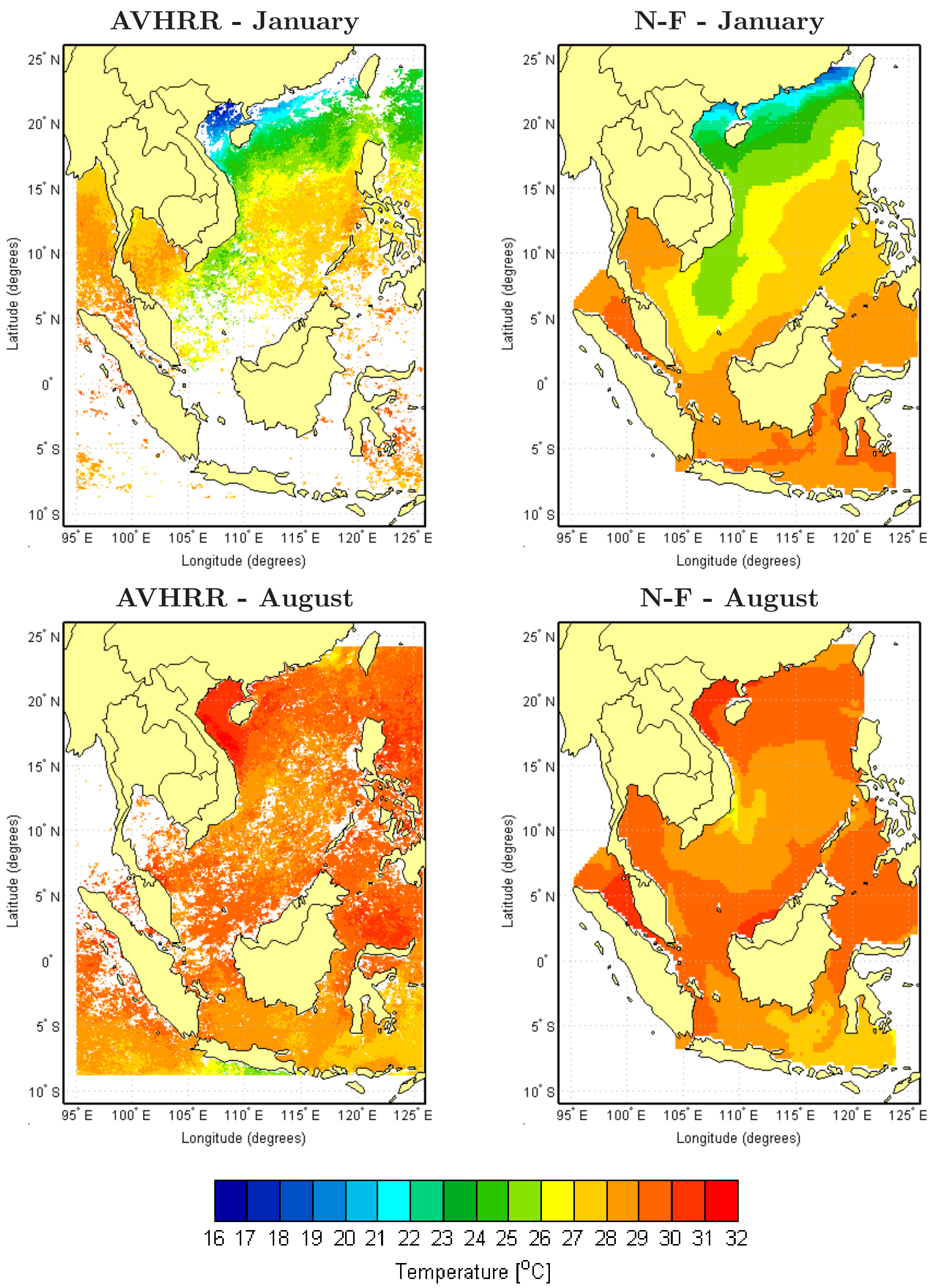

Figure I.15: Monthly-mean model surface-layer temperature, compared with monthly-mean Sea Surface Temperature (SST) data from AVHRR / Pathfinder: representing the SST state during the NE (January) and SW (August) monsoon highs (2).

I.11 Validation of modeled temperature using WOA01 data (1)

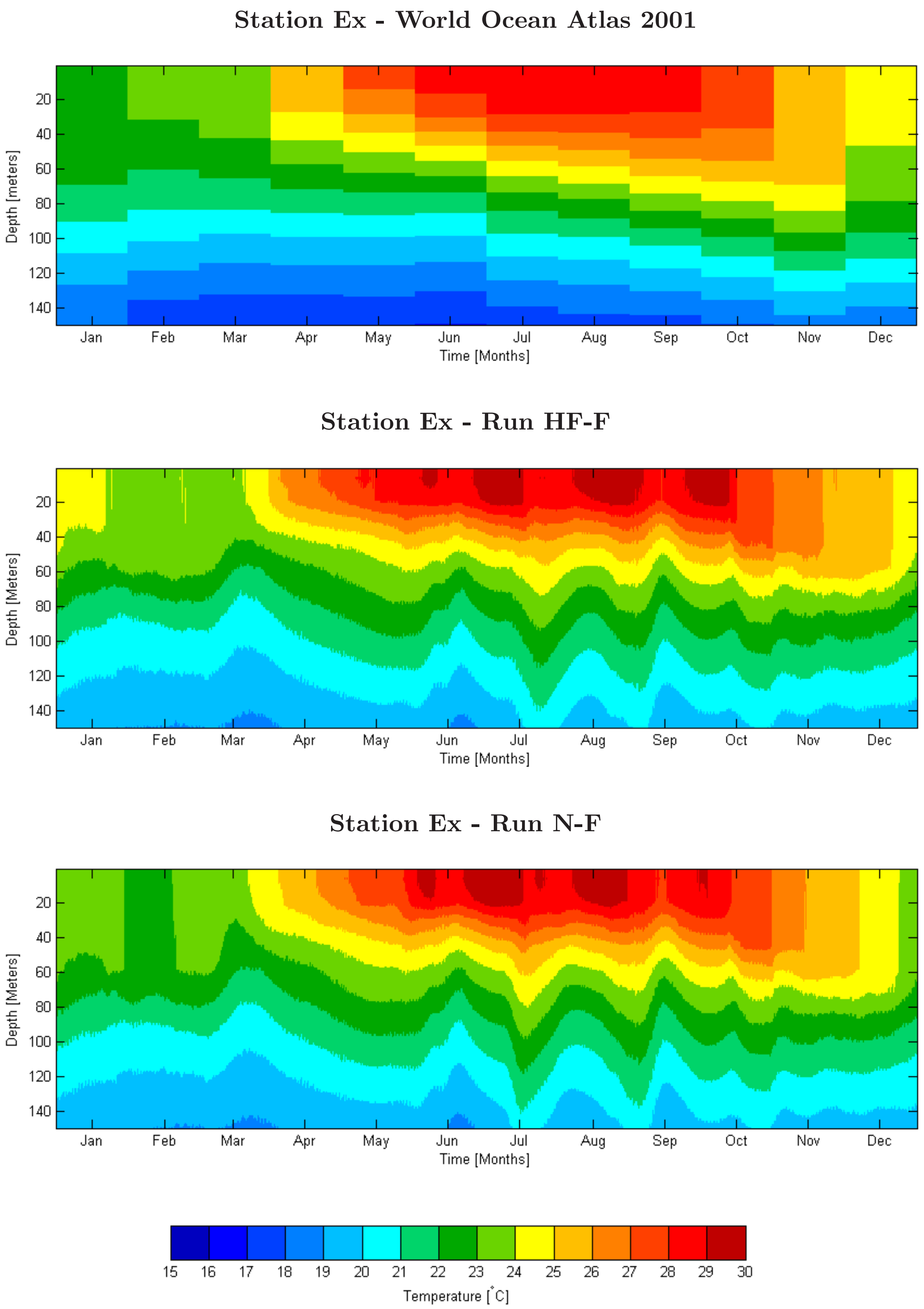

Figure I.16: Time-series of modeled and World Ocean Atlas 2001 temperature profiles at model test station Ex.

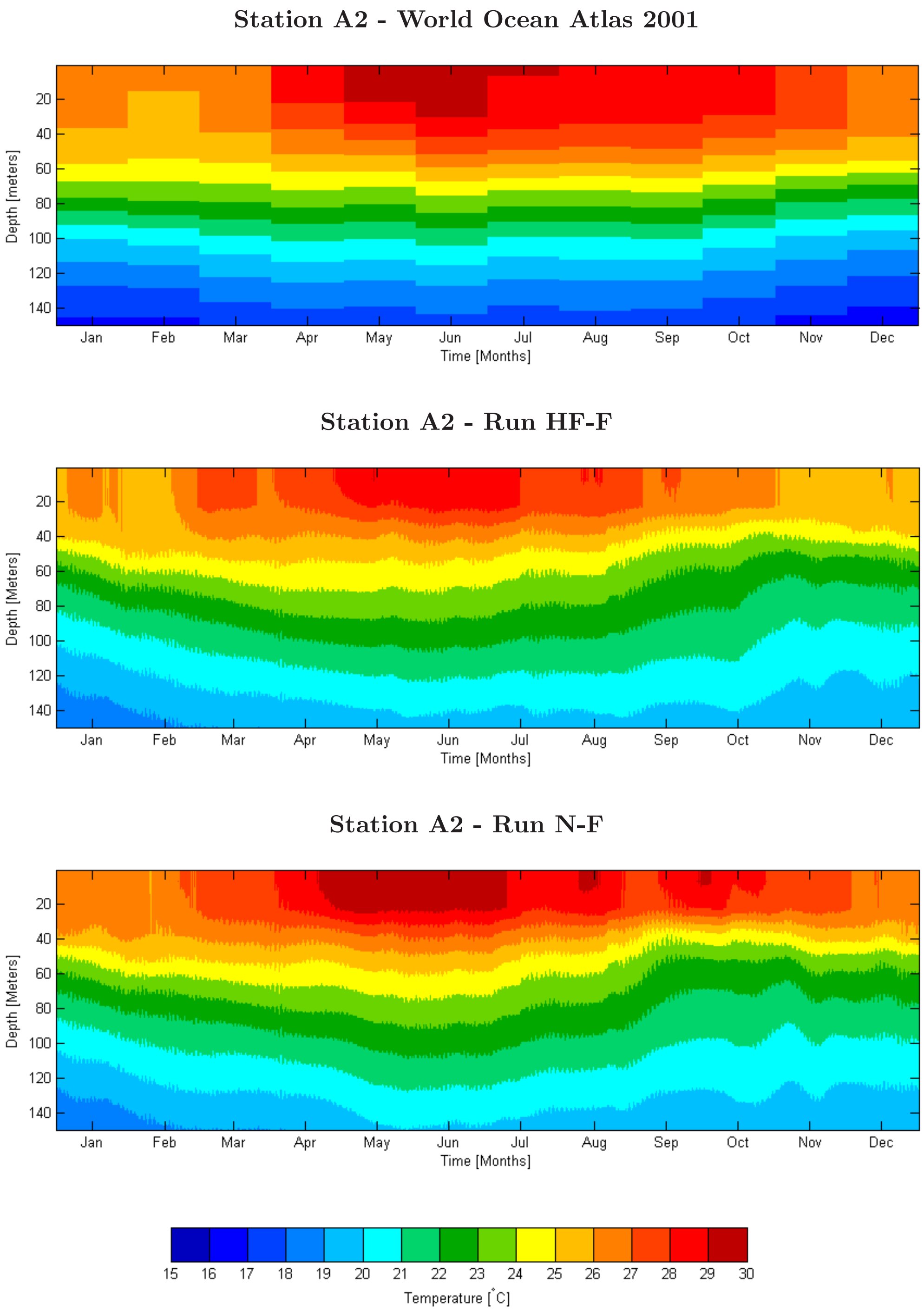

Figure I.17: Time-series of modeled and World Ocean Atlas 2001 temperature profiles at model test station A2.

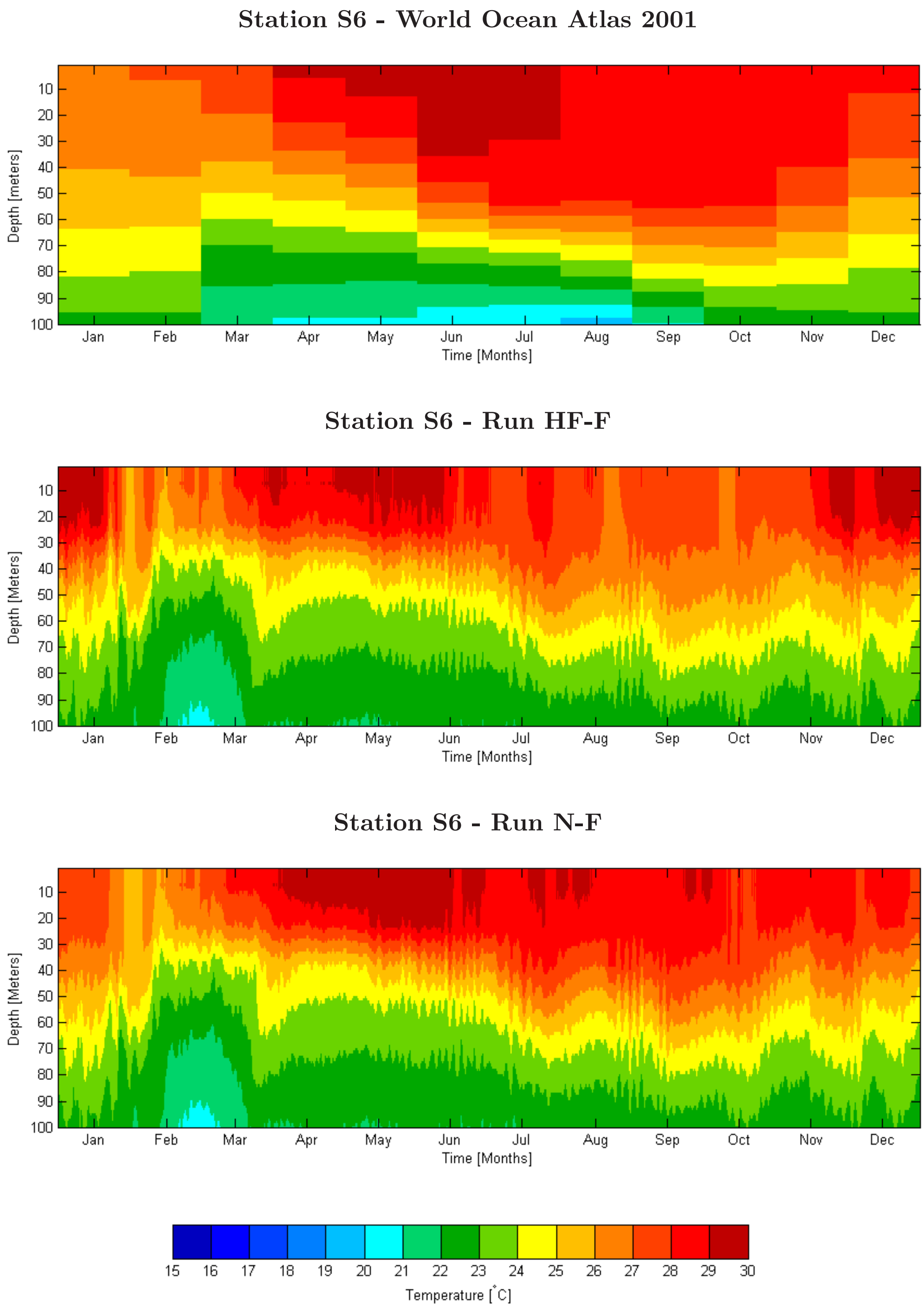

Figure I.18: Time-series of modeled and World Ocean Atlas 2001 temperature profiles at model test station S6.

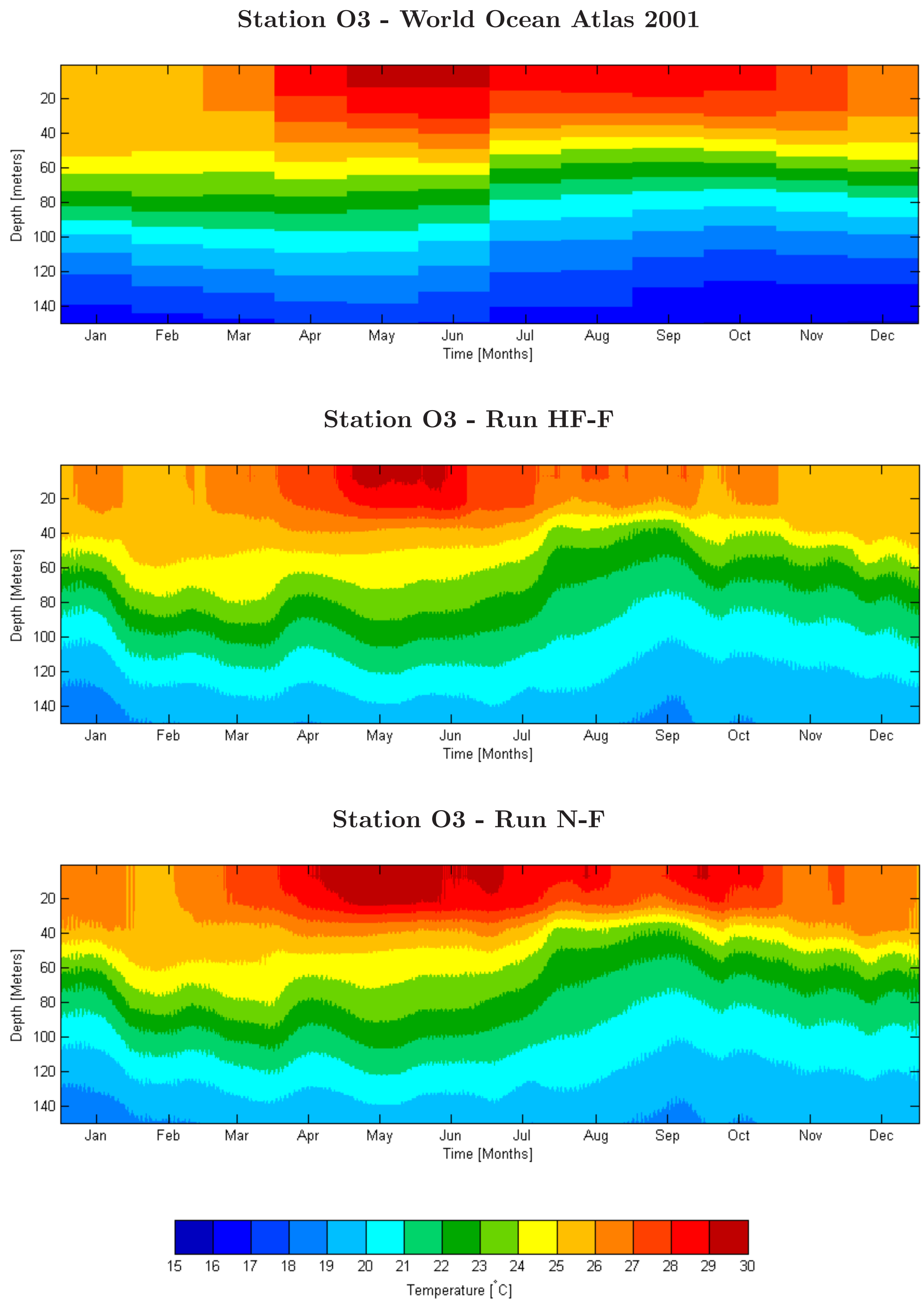

Figure I.19: Time-series of modeled and World Ocean Atlas 2001 temperature profiles at model test station O3.

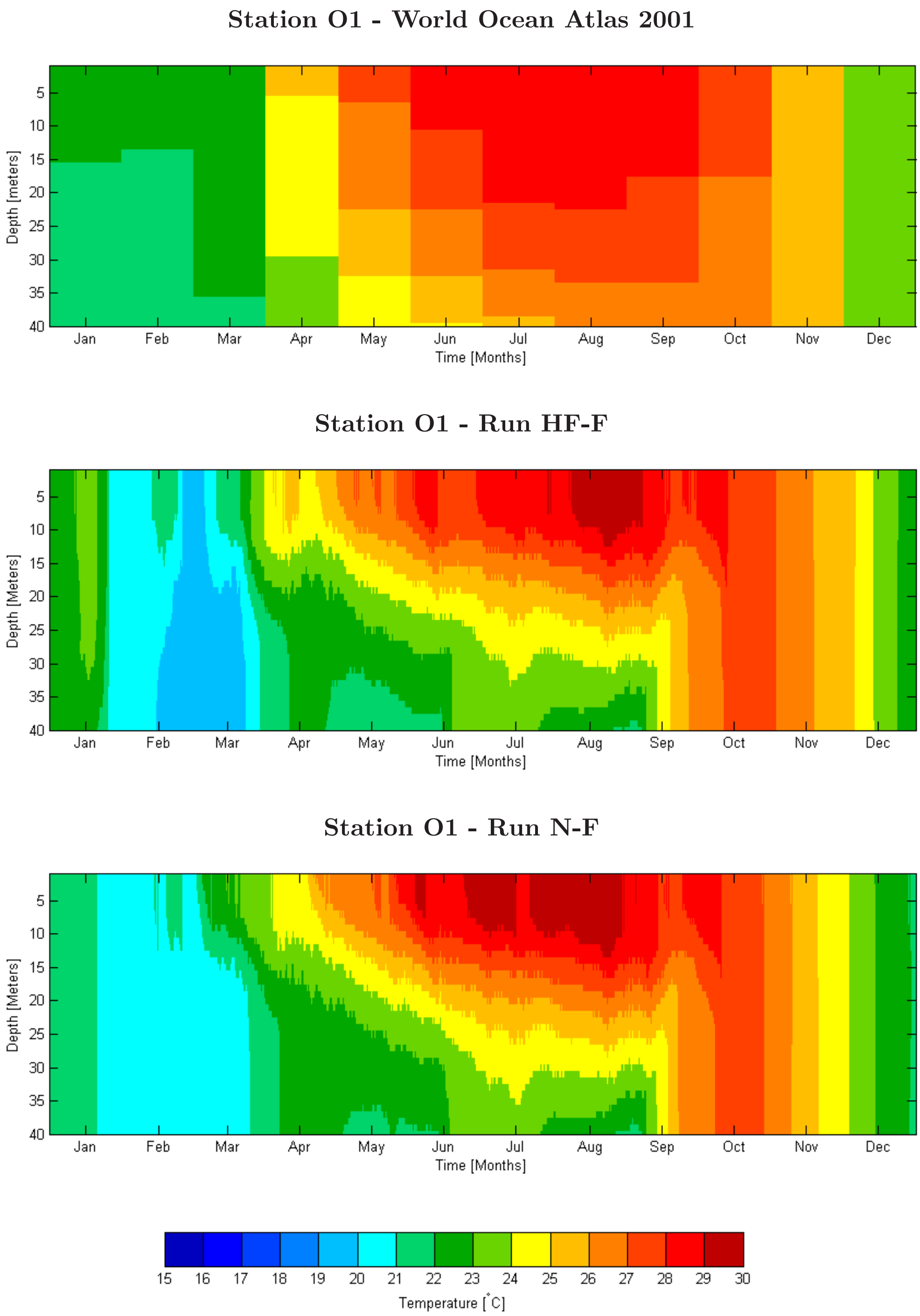

Figure I.20: Time-series of modeled and World Ocean Atlas 2001 temperature profiles at model test station O1.

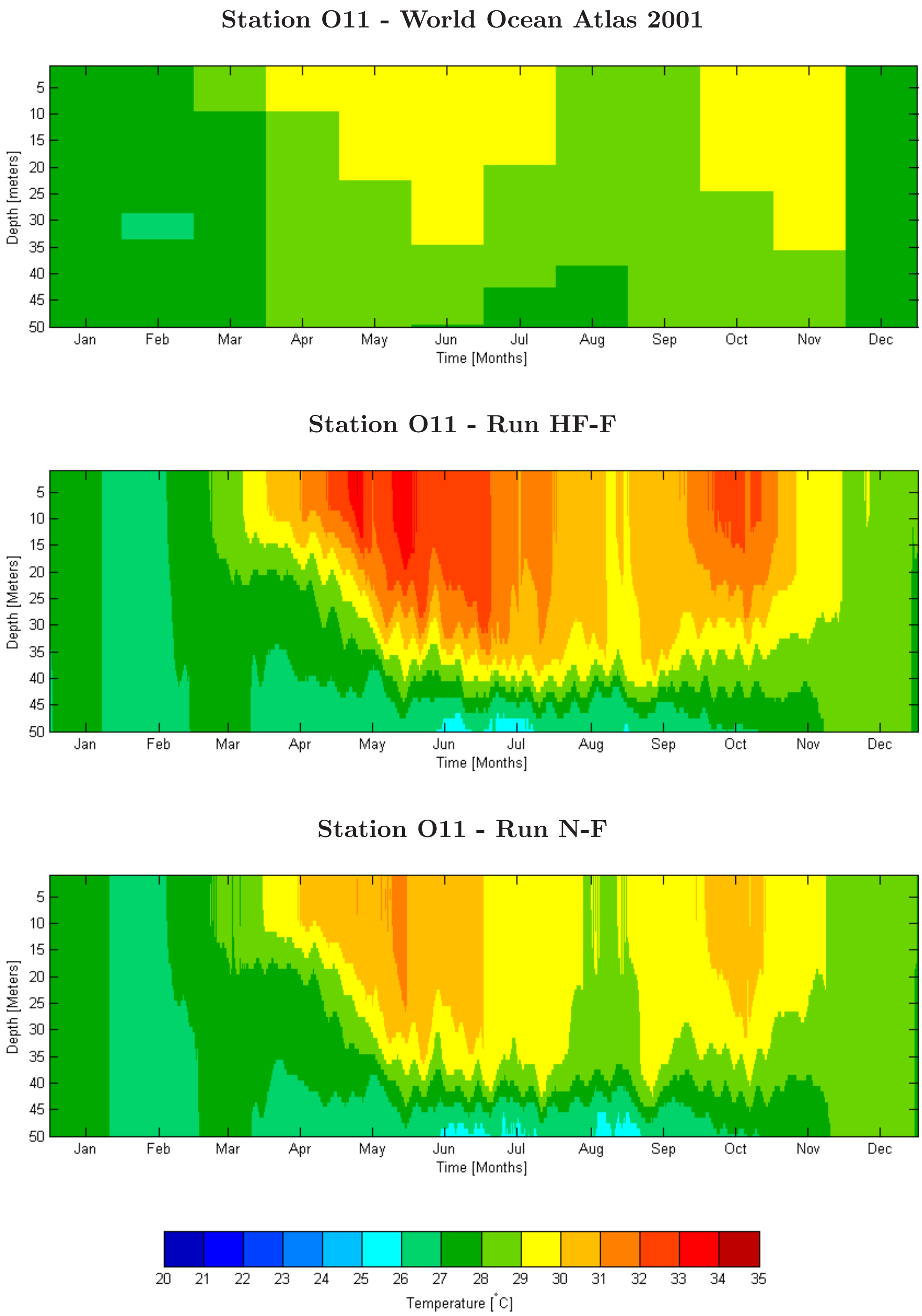

Figure I.21: Time-series of modeled and World Ocean Atlas 2001 temperature profiles at model test station O11.

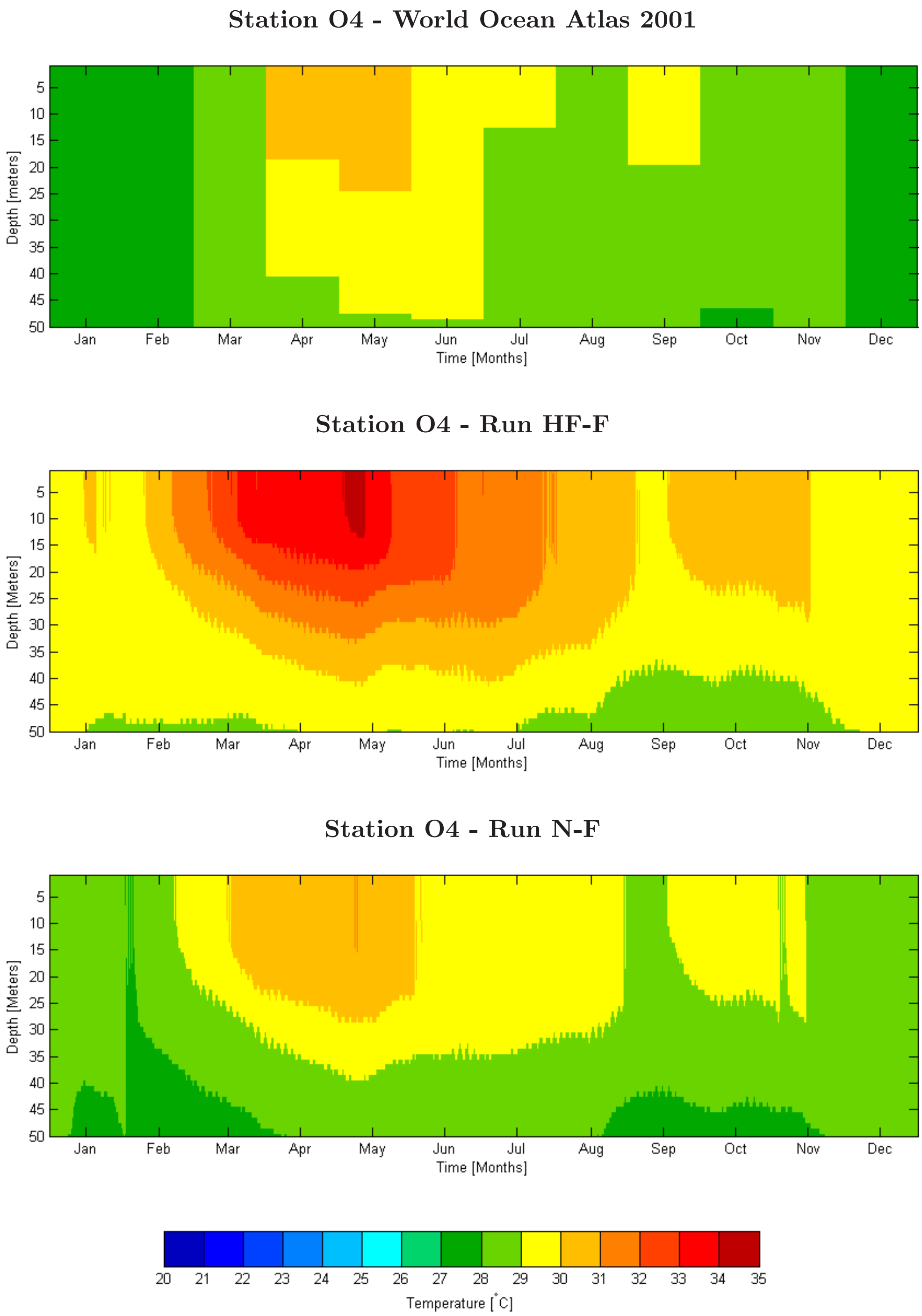

Figure I.22: Time-series of modeled and World Ocean Atlas 2001 temperature profiles at model test station O4.

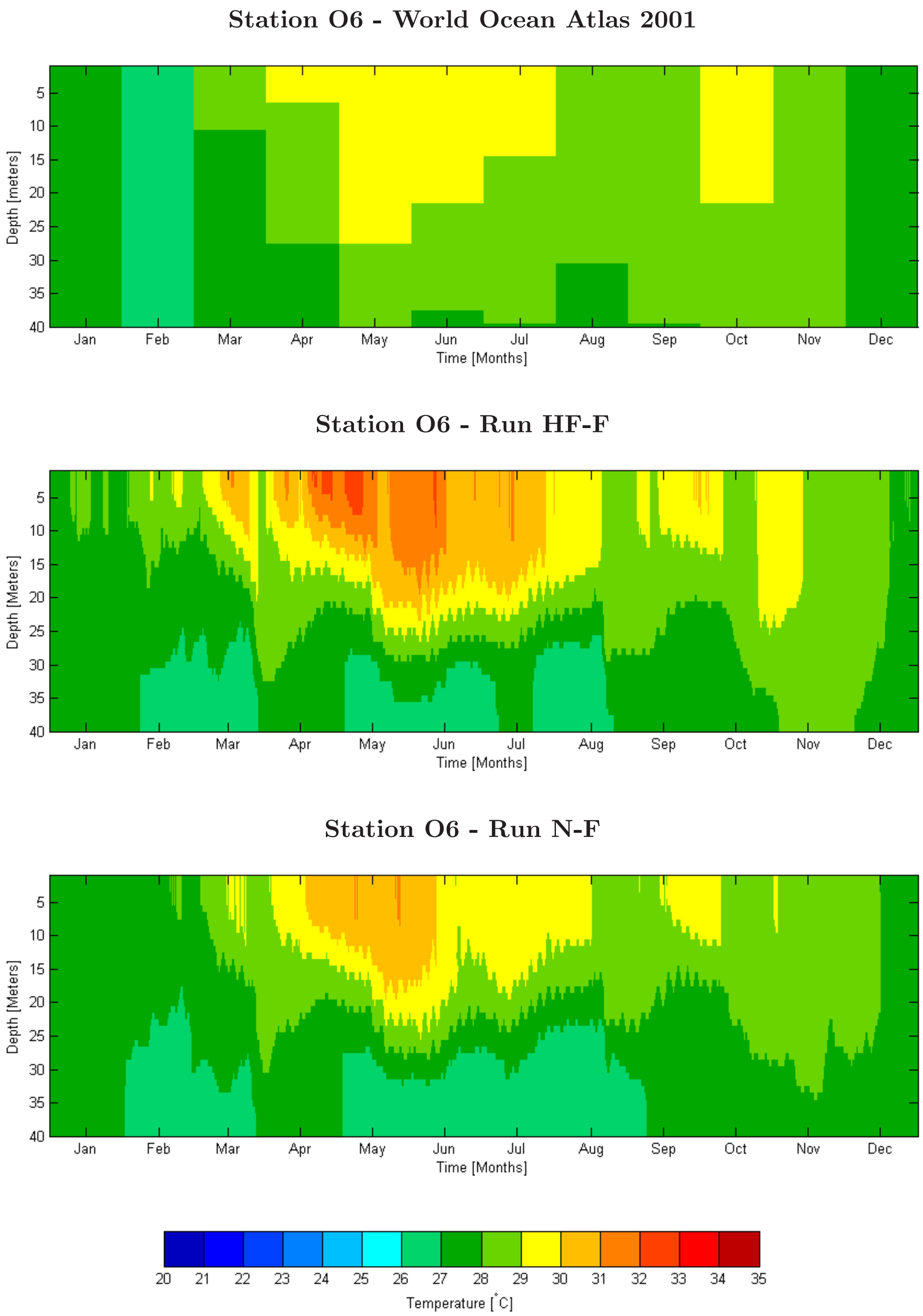

Figure I.23: Time-series of modeled and World Ocean Atlas 2001 temperature profiles at model test station O6.

I.12 Validation of modeled temperature using WOA01 data (2)

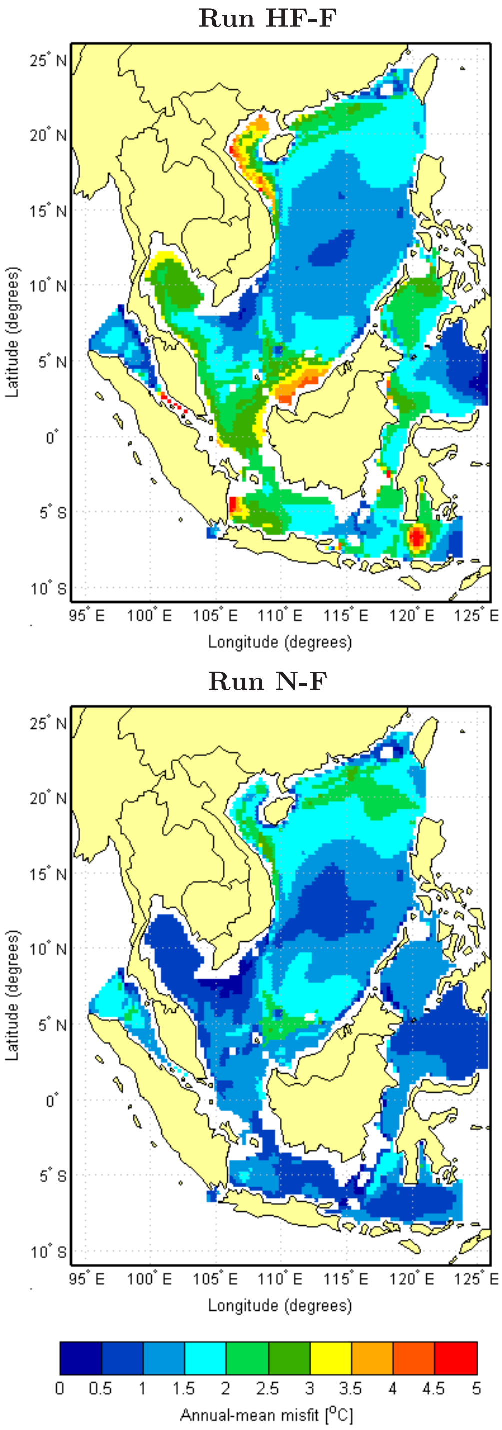

Figure I.24: Annual-mean misfit between the monthly-mean model and World Ocean Atlas 2001 temperature fields. This misfit is determined over the upper 10 model layers, representing the temperature up till 150 meters depth in the central SCS basin. It is specified at each model grid point.

I.13 Validation of modeled temperature using in-situ data

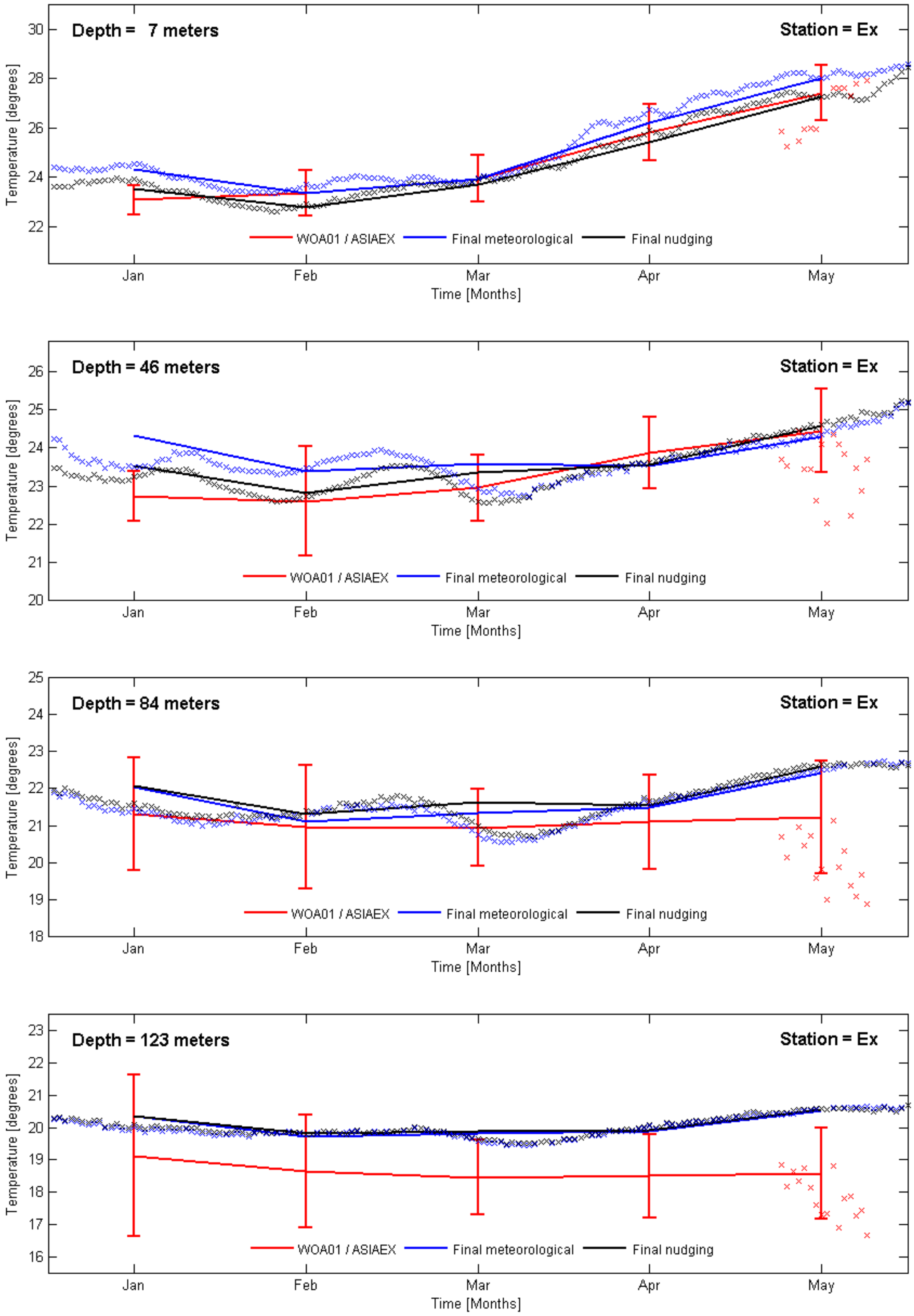

Figure I.25: Time-series of modeled and in-situ temperature data at model test station Ex. In-situ temperature data from the ASIAEX dataset.

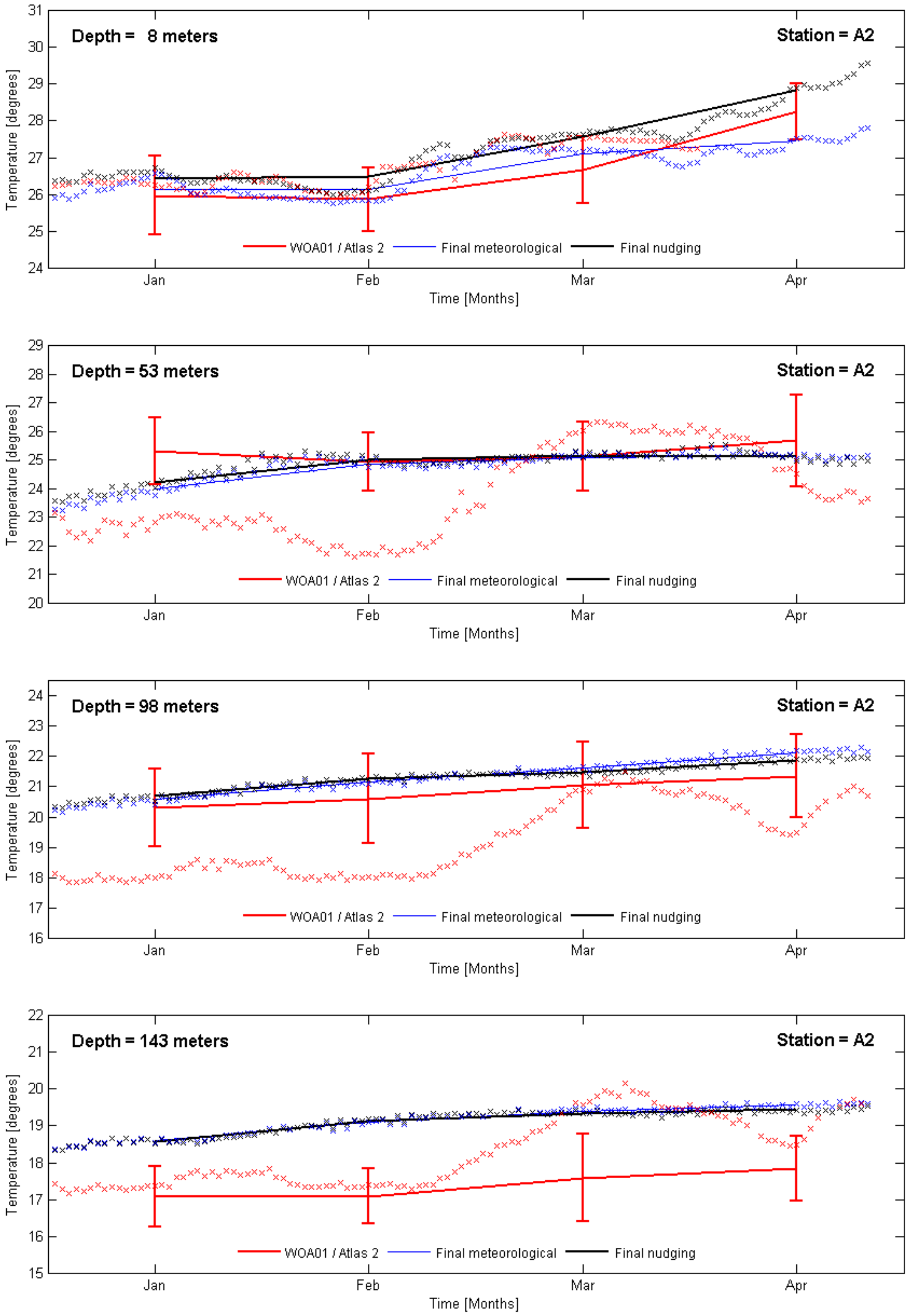

Figure I.26: Time-series of modeled and in-situ temperature data at model test station A2. In-situ temperature data from the SCSMEX dataset.

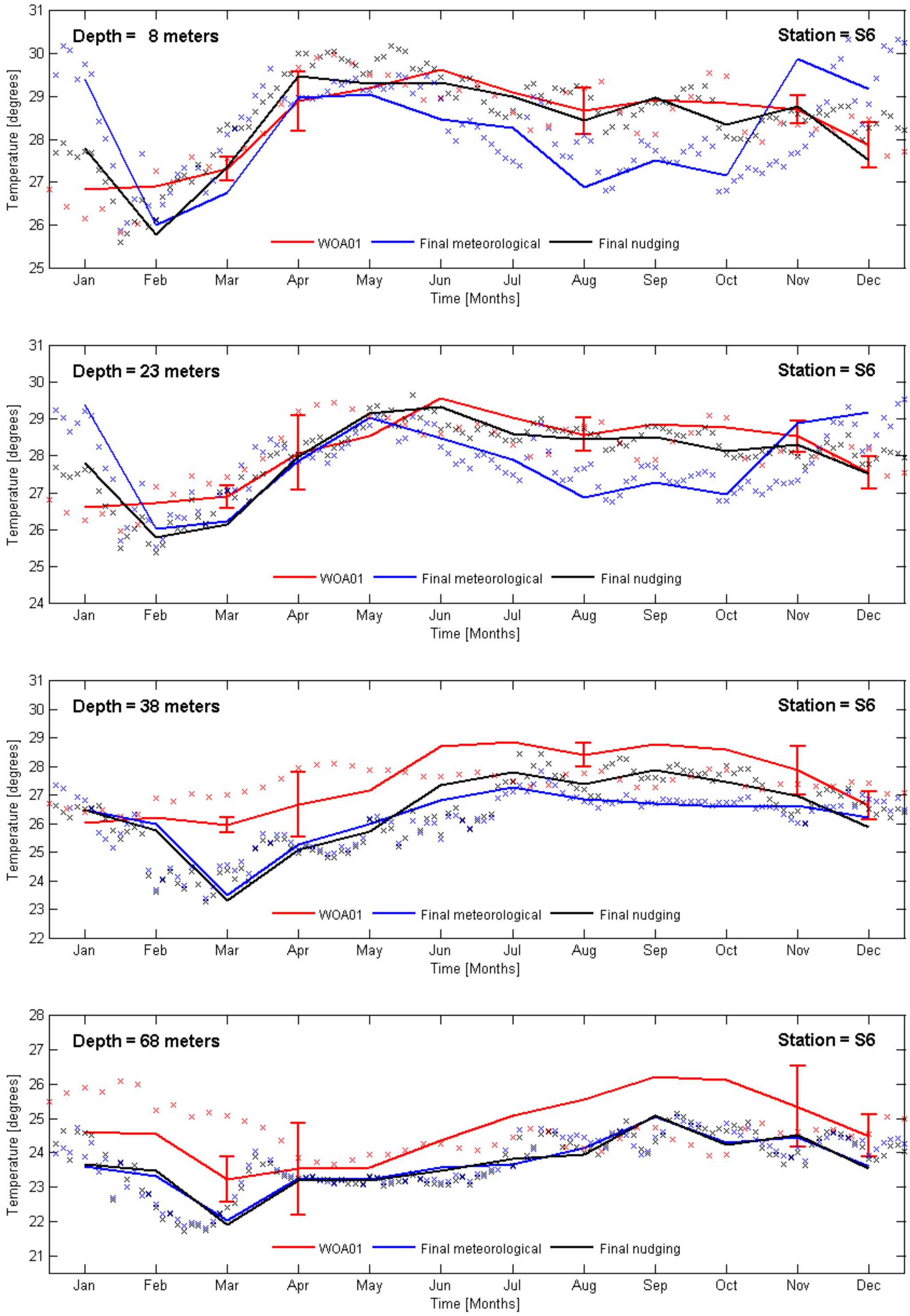

Figure I.27: Time-series of modeled and synthetic temperature data at model test station S6. Synthetic temperature profiles determined using profile data from the World Ocean Atlas 2001, sea surface anomaly data from the DUACS dataset and sea surface temperature data from the Reynolds OI SST dataset, based on a methodology described by [Nardelli & Santoleri, 2004].